

**Developments towards time-resolved
electron diffraction: Roadmap to
“molecular movies”**

João Pedro Figueira Nunes

PhD

University of York

Chemistry

November 2017

“I don’t believe any experiment until it is confirmed by theory. I find this is a witty inversion of conventional wisdom.”

Sir Arthur Stanley Eddington

Abstract

The imaging of molecular motions has long been a *gedanken* experiment in the development of models explaining structure-function relationships and chemical reactivity. In this thesis, a roadmap to molecular movies proposes an interdisciplinary approach to these experiments, combining the three experimental techniques of gas electron diffraction (GED), time-resolved electron diffraction (TRED), and ultrafast electron diffraction (UED), and the computational fields of quantum chemistry, and software development.

At York a time-averaged GED apparatus, the only one of its kind in the UK, was relocated and recommissioned, allowing the equilibrium ground-state structures of 1,2-dithiane and 4-(*N,N*-dimethylamino)benzotrile in the gas phase to be resolved. Furthermore, our TRED apparatus was upgraded with a new ultrafast laser system, custom-built solenoid lens, and optimised detector geometry, resulting in a 60% increase in the signal-to-noise ratio and improved spatial resolution.

Through collaboration with the UED group at the Stanford Linear Accelerator Center (SLAC), the ring opening dynamics of 1,2-dithiane were captured with sub-200 fs temporal resolution, using the MeV UED apparatus at SLAC. Combined with non-adiabatic multi-reference molecular dynamics simulations, these results revealed an oscillatory ring-opening motion with a period of ~ 400 fs, and the presence of transient straight-chain species.

Molecular dynamics simulations were also used to investigate the photostability of asparagusic acid, the ring-opening motion of which was found to be mediated by the dynamics of the carboxylic acid group. Similar studies for 1,2-dibromotetrafluoroethane predicted the sub-100 fs cleavage of the C–Br and the formation of non-bridging radical intermediate, followed by a secondary C–Br cleavage of the *anti* conformers.

A suite of software tools has been designed to extract experimental data, analyse computational results, and combine the experimental and simulated domains into interpretable descriptions of molecular motion. This synergistic relationship between experimental and computational chemistry has allowed the capture of previously unseen motions.

Table of Contents

Abstract	3
Table of Contents	4
List of Tables	10
List of Figures	11
List of Accompanying Material	21
Acknowledgements	22
Declaration	23
Chapter 1. Introduction	24
1.1 The importance of temporal resolution in the study of nature	25
1.2 The role of electron diffraction in structure determination	26
1.3 Overview on time-resolved electron diffraction	27
1.4 Historical overview of time-resolved electron diffraction	29
1.5 Current work in the field	33
1.6 Roadmap to molecular movies	38
1.7 Case studies	41
1.7.1 Study of the ground-state structure of DMABN	41
1.7.2 Study of the internal conversion dynamics of 1,2-dithiane	42
1.7.3 Study of the photoinduced dynamics of asparagusic acid	43
1.7.4 Study of the photodissociation of Halon-2402	44
Chapter 2. Background theory	46
2.1 Introduction to electron diffraction	46
2.1.1 Electron diffraction theory	46
2.1.2 Challenges in gas electron diffraction	50
2.1.3 Structure determination in gas electron diffraction	54
2.2 Introduction to time-resolved electron diffraction	56
2.2.1 Challenges in time-resolved electron diffraction	57
2.2.2 Overcoming temporal broadening in TRED	61
2.2.3 Challenges in data analysis	62
2.3 Summary in apparatus design	62
2.3.1 Electron gun	62

2.3.2	Sample delivery	64
2.3.3	Detector	65
Chapter 3.	Methods.....	67
3.1	Gas-phase electron diffraction at York	67
3.1.1	York GED apparatus overview	67
3.1.2	Apparatus commissioning	68
3.1.3	The York GED apparatus scope	71
3.2	Time-resolved electron diffraction at York.....	71
3.2.1	Electron beam characterisation	73
3.2.1.1	Charge vs drive UV	73
3.2.1.2	Charge vs full width half maximum	74
3.2.1.3	Spatial profile	75
3.2.1.4	Beam FWHM vs accelerating potential.....	76
3.2.2	Electron optics calibration.....	76
3.2.3	Deflector-plate calibration.....	79
3.2.4	MCP gain optimisation.....	80
3.2.5	Detector geometry optimisation	81
3.2.6	Magnetic distortion corrections	83
3.2.7	Determining time zero	84
3.2.8	Sample delivery system.....	86
3.2.9	Design improvements to the high-voltage coupling.....	88
3.3	Ultrafast electron diffraction at SLAC	89
3.3.1	MeV UED experiment workflow	89
3.4	Computational chemistry	90
3.5	Software tools.....	93
3.5.1	GED extraction package (<i>XTRACT</i>).....	94
3.5.1.1	<i>XTRACT</i> workflow and subroutine description	94
3.5.1.2	<i>XTRACT</i> input format.....	97
3.5.1.3	<i>XTRACT</i> output format.....	98

3.5.1.4	<i>XTRACT</i> benchmark against XPKG	98
3.5.2	Molecular intensity curve simulator (<i>SIMMIC</i>)	99
3.5.2.1	<i>SIMMIC</i> workflow and subroutine description	99
3.5.2.2	<i>SIMMIC</i> interface with ELSEPA	101
3.5.3	Time-dependent molecular intensity curve simulator (<i>TD-SIMMIC</i>)	101
3.5.3.1	<i>TD-SIMMIC</i> workflow and subroutine description	101
3.5.4	Molecular dynamics trajectory analysis package (<i>TRAVIS</i>)	102
3.5.4.1	Internal coordinate visualisation tool (<i>TRAVIS-ICV</i>)	102
3.5.4.2	Internal coordinate extraction tool (<i>TRAVIS-ICX</i>)	103
3.5.4.3	Heat-map representation of phase space (<i>TRAVIS-HM</i>)	103
3.5.4.4	Geometry overlay (<i>TRAVIS-GO</i>)	104
3.5.5	UED data-analysis package (<i>UEDEXTRA</i>)	104
3.5.5.1	<i>UEDEXTRA</i> workflow and subroutine description	104
3.5.5.2	<i>UEDEXTRA</i> noise reduction	105
3.5.5.3	<i>UEDEXTRA</i> data extraction	107
3.5.6	Future work and outlook	107
Chapter 4.	GED study of DMABN	109
4.1.1	Aims and considerations	109
4.1.2	GED experiment	109
4.1.3	Theoretical methods	110
4.1.4	Geometric model	111
4.1.5	Structure refinement	113
Chapter 5.	Experimental study of 1,2-dithiane	118
5.1	Literature on 1,2-dithiane	118
5.2	Aims and motivation	120
5.3	GED study of 1,2-dithiane	121
5.3.1	Synthesis and characterisation	121
5.3.2	GED experiment	122
5.3.3	Theoretical methods	123
5.3.4	Geometric model	124

5.3.5	Structure refinement.....	125
5.4	UED simulation of 1,2-dithiane.....	128
5.5	UED study of 1,2-dithiane.....	130
5.5.1	Synthesis and characterisation.....	130
5.5.2	Experimental parameters.....	131
5.5.3	Sample delivery.....	132
5.5.4	Time-zero determination.....	133
5.5.5	Time-dependent diffraction data acquisition.....	134
5.5.6	Reduction, extraction and manipulation of UED data.....	134
5.5.7	Molecular movie of 1,2-dithiane.....	139
5.5.8	Publication of the UED study of 1,2-dithiane.....	140
Chapter 6.	Computational study of asparagusic acid.....	141
6.1	Static electronic structure calculations for asparagusic acid.....	141
6.1.1	Conformational space search.....	142
6.1.2	Active-space selection.....	143
6.1.3	Interpolated internal coordinate potential energy surface scans.....	144
6.2	Molecular dynamics simulations.....	145
6.3	Trajectory analysis.....	145
6.4	Comparative analysis: asparagusic acid vs. 1,2-dithiane.....	152
6.5	UED simulations.....	154
Chapter 7.	Computational study of Halon-2402.....	157
7.1	Static electronic structure calculations for Halon-2402.....	157
7.1.1	Conformational space search.....	157
7.1.2	Active-space selection.....	158
7.1.3	Interpolate internal coordinate potential energy surface scans.....	159
7.2	Molecular dynamics simulations.....	160
7.3	Trajectory analysis.....	161
7.4	UED simulations.....	163
Chapter 8.	Conclusion and future work.....	166
8.1	Achievements prompt by the roadmap to molecular movies.....	166

8.2	Challenges and future work.....	166
8.2.1	Challenges and future work in GED	167
8.2.2	Challenges and future work in TRED	169
8.2.2.1	Temporal resolution	169
8.2.2.2	Detector performance.....	169
8.2.2.3	Transverse coherence of the electron beam	170
8.2.3	Future UED studies	171
8.2.3.1	Ring opening dynamics of asparagusic acid	171
8.2.3.2	Photodissociation of Halon-2402	172
8.2.3.3	<i>E/Z</i> isomerisation of E-Cinnamionitrile	173
8.3	Complementary projects.....	174
8.3.1	Laser Induced Fluorescence of supersonic molecular beams	174
8.3.2	High transverse coherence electron source	175
8.4	Outlook in UED: beyond molecular movies	176
8.4.1	Towards 4D-UEM.....	176
Appendix A.	Overview on computational chemistry	178
A.1.	Introduction to quantum mechanics	178
A.2.	Hartree-Fock theory	179
A.3.	Møller-Plesset perturbation theory.....	180
A.4.	Coupled-cluster methods.....	181
A.5.	Density functional theory	181
A.6.	Time-dependent density functional theory.....	182
A.7.	Multireference configuration interaction theory	182
A.8.	Multi-configurational self-consistent-field theory	182
A.9.	Molecular dynamics simulations.....	183
A.10.	Basis sets	184
Appendix B.	York GED apparatus	186
B.1.	Electron gun	186
B.2.	Sample delivery	186
B.3.	Detector	189

B.4. Vacuum system	190
B.5. Controls and electronics	191
Appendix C. York TRED apparatus	192
C.1. Apparatus assembly and history	192
C.2. Electron gun	192
C.3. Laser set-up	194
C.3.1. Light sources	194
C.3.2. Layout	195
C.3.3. Electron generation path	196
C.3.4. Pump path	196
C.3.5. Libra optics layout	197
C.3.6. Solstice optics layout	198
C.4. Electron optics	199
C.5. Sample delivery	201
C.6. Detector	202
C.7. Vacuum system	204
C.8. Apparatus accessibility	204
C.9. Data acquisition workflow	205
Appendix D. SLAC UED apparatus	207
D.1. Electron gun	207
D.2. Laser layout	207
D.3. Sample delivery	208
D.4. Detector	210
Abbreviations	211
References	214
Associated Publications	234

List of Tables

Table 3.1: Refined (r_{hi}), theoretical ^a (r_e), and literature ^b geometric parameters and SARACEN restraints ^b applied in the least-squares refinement of benzene. Distances are tabulated in picometers.	70
Table 3.2: Selected interatomic distances (r_a), refined (u_{GED}), and theoretical ^a (u_{hi}) amplitudes of vibration, and distance corrections (k_{hi}) for the GED refinement of benzene.	70
Table 4.1: Summary of experimental parameters for the GED study of DMABN.	110
Table 4.2: List of parameters used to refine the structure of DMABN. ^a	112
Table 4.3: Selected ^a refined (r_{hi}) and theoretical ^b (r_e) geometric parameters ^c and SARACEN restraints ^d applied in the refinement of DMABN.	113
Table 4.4: Selected ^{a,b} interatomic distances (r_a), refined (u_{GED}) and theoretical (u_{hi}) amplitudes of vibration and distance corrections (k_{hi}) for DMABN.	114
Table 4.5: Refined GED and theoretical geometric parameters obtained from <i>ab initio</i> geometry optimisations of DMABN.	116
Table 5.1: X-ray crystallography experimental parameters for 1,2-dithiane.	121
Table 5.2: Unit cell dimension for 1,2-dithiane.	122
Table 5.3: Summary of experimental parameters for the GED data collection and refinement of 1,2-dithiane.	123
Table 5.4: List of parameters used to refine the structure of 1,2-dithiane.	124
Table 5.5: Refined (r_{hi}) and theoretical ^a (r_e) geometric parameters ^b and SARACEN restraints ^c applied in the refinement of 1,2-dithiane.	126
Table 5.6: Selected ^{a,b} interatomic distances (r_a), refined (u_{GED}) and theoretical (u_{hi}) amplitudes of vibration and distance corrections (k_{hi}) for 1,2-dithiane.	127
Table 5.7: Refined GED and X-ray ^a and theoretical geometric parameters <i>ab initio</i> geometry optimisations of 1,2-dithiane.	127
Table 6.1: Conformer ratios for asparagusic acid at room temperature (293 K), melting point (350 K), and in a supersonic molecular beam (<100 K).	142
Table 6.2: Conformer specific S-termini collision and disulfide bond recombination ratios for asparagusic acid.	147
Table 6.3: Average <i>r</i> S–S elongation velocities for 1,2-dithiane and asparagusic acid.	152
Table 6.4: Comparison table showing the percentage of collision and recombination events for 1,2-dithiane and asparagusic acid.	153
Table 7.1: Conformer ratios for Halon-2402 under effusive nozzle (293 K) and supersonic expansion (<100 K) conditions.	158

List of Figures

Figure 1.1: 1878 poster of “ <i>Sallie Gardner at a Gallop</i> ”, also known as <i>The Horse in Motion</i> by photographer and inventor Eadweard Muybridge. Adapted from Reference 12.	25
Figure 1.2: Rotating fan photographed at a) 1/1000 s, b) 1/500 s, and c) 1 s shutter speed. Adapted from Reference 51.	28
Figure 1.3: a) Photograph and b) schematic cross-section of the electron diffraction apparatus used to record the world’s first electron diffraction pattern. The electron gun, filament, target, and detector are denoted with the letters, G, F, T and D, respectively. Adapted from Reference 61.	30
Figure 1.4: First recorded gas electron diffraction pattern for CCl ₄ . Adapted from Reference 65.	30
Figure 1.5: Schematic representation of Ischenko’s “stroboscopic” electron diffraction apparatus, the world’s first time-resolved GED apparatus. Adapted from Reference 66.	31
Figure 1.6: Schematic representation of Zewail’s third-generation UED apparatus, UED-3. Adapted from Reference 78.	32
Figure 1.7: Examples of a) bright-field image, b) diffraction pattern at 90 K and c) phase-transition behaviour of an ensemble of Fe(pyrazine)Pt(CN) ₄ nanoparticles. Adapted from Reference 83.	34
Figure 1.8: Reversible ring-opening/closing reaction of 1,2-bis(2,4-dimethyl-5-phenyl-3-thienyl)perfluorocyclopentene. Adapted from Reference 1.	35
Figure 1.9: Diffraction patterns for polycrystalline gold a) accumulated over 1000 shots, b) recorded in single-shot mode, and c) a single-shot single-crystal diffraction pattern for gold. Adapted from Reference 91.	35
Figure 1.10: CAD drawing of the MeV UED beamline at SLAC’s ASTA facility. Adapted from Reference 41.	36
Figure 1.11: Block diagram of Centurion’s 90 keV UED apparatus at Lincoln, Nebraska. Adapted from Reference 96.	37
Figure 1.12: Schematic representation of Ropers’ ultrafast point projection microscopy (UPPM) remotely driven electron emission. Surface plasmon polaritons produced by near-IR illumination of a lithographically etched waveguide or grating coupler propagate towards the nanotaper apex where plasmon-induced electron emission takes place. A 250 V bias between the tip and the micro-channel plate (MCP) accelerates newly formed electrons away from the apex, towards the detector, producing shadow images of the sample. Adapted from Reference 100.	38
Figure 1.13: Diagrammatic representation of the roadmap to molecular movies.	39

Figure 1.14: Molecular structure of DMABN.	41
Figure 1.15: Molecular structure of 1,2-dithiane.	42
Figure 1.16: Molecular structure of asparagusic acid.	43
Figure 1.17: Molecular structure of Halon-2402.	44
Figure 2.1: Illustration of change in momentum, \mathbf{s} , where \mathbf{k}_0 is the incident vector, \mathbf{k} is the scattered electron vector, and θ is the angle between them.	47
Figure 2.2: Schematic illustrations of Young’s a) single-slit, and b) double-slit experiments. Adapted from Reference 123.	48
Figure 2.3: Example of a) a GED diffraction pattern, and b) an MIC for benzene, recorded during the commissioning of the York GED apparatus (see Section 3.1.2).	48
Figure 2.4: Experimental (red), theoretical (blue), and difference (experimental-minus-theoretical, black) RDCs obtained from the inverse Fourier transform of GED data for benzene.	50
Figure 2.5: Illustration of the “shrinkage effect” resulting from the vibration of the linear triatomic ABC.	51
Figure 2.6: Illustration of the differences between a) curvilinear and b) rectilinear corrections.	52
Figure 2.7: Schematic representation of the incident electron beam (A), interaction region (B) and diffraction cone (C), from where diffraction patterns are acquired at short (D) or long (E) nozzle-to-detector distances.	54
Figure 2.8: Schematic representation of linear pulse chirping in a non-relativistic electron bunch. Adapted from Reference 152.	58
Figure 2.9: Schematic representation of the interaction region between the pump laser (purple vertical lines) and probe electron beam (yellow diagonal lines) passing through a molecular beam sample (solid blue). Adapted from Reference 152.	59
Figure 2.10: Schematic representation of the interaction region between the tilted wavefront pump laser (purple vertical lines) and probe electron beam (yellow diagonal lines) passing through a molecular beam sample (solid blue). Adapted from Reference 152.	60
Figure 2.11: Schematic representation of the filament (A), the Wehnelt cylinder (B), and (C) the anode geometry in a triode electron gun. Adapted from Reference 159.	63
Figure 2.12: Schematic representation of a DC electron gun showing the drive ionisation laser pulse (A), the photocathode (B), the anode (C), and the expanding electron bunch (D).	63
Figure 2.13: Schematic representation of an RF electron gun showing the drive ionisation laser pulse (A), the photocathode (B), the RF cavities (C), and the electron bunch (D).	64
Figure 3.1: Photograph of the York GED apparatus.	68

Figure 3.2: Scanned image plates showing the diffraction patterns of benzene at a) long, and b) short nozzle-to-detector distances.....	69
Figure 3.3: Experimental (red), theoretical (blue), and difference (experimental-minus-theoretical, black) a) MICs, and b) RDCs for benzene. The MICs for the long (top) and short (bottom) nozzle-to-detector datasets are offset. The overlap between the two datasets serves as an indicator of data quality. Experimental and theoretical MICs were multiplied by $s.\exp(-2s^2.10^{-5}/[(Z_C - f_C)(Z_H - f_H)])$ prior to Fourier inversion. f_C and f_H denote the atomic scattering factors for carbon and hydrogen taken from Reference 176.	70
Figure 3.4: Photograph of the TRED apparatus at York.	72
Figure 3.5: Diagrammatic illustration of the TRED apparatus showing the electron gun (A), the laser set-up (B), the electron beam optics (C), the sample delivery system (D), the detector module (E), and the vacuum system (F).	72
Figure 3.6: Photograph of the TRED apparatus beam mask. The mask contains two orifices, 200 μm and 500 μm in diameter.	73
Figure 3.7: Calibration curve for the number of electrons per pulse and beam charge as a function of BBO crystal angle.	74
Figure 3.8: FWHM of an electron beam as a function of charge density.....	74
Figure 3.9: Two-dimensional profile of a) an unfocused, and b) a focused electron beam..	75
Figure 3.10: FWHM of an electron beam as a function of accelerating voltage. All measurements were recorded for a 1.6 fC electron beam.	76
Figure 3.11: Evolution of the FWHM of an electron beam as a function of solenoid current for the York solenoid lens and its predecessor. All FWHM measurements were taken at the interaction region using the technique introduced in Section 3.2.1.....	77
Figure 3.12: Diffraction of a polycrystalline platinum sample captured using an electron beam with a FWHM of a) 800 μm , and b) 400 μm	78
Figure 3.13: Evolution of the FWHM of an electron beam at the detector position as a function of solenoid current for the York solenoid lens and its predecessor. The FWHM measurements were extrapolated from the calibration curve in Figure 3.11, assuming a linearly divergent electron beam.....	78
Figure 3.14: Plot of electron beam shift as a function of the voltage applied to the deflector plates along the x and y directions. Voltages varied between -1 kV and $+1$ kV in 100 V increments.	79
Figure 3.15: Diagram of a typical MCP, showing the first MCP layer (A), the second MCP layer (B), and the scintillator screen (C).	80
Figure 3.16: Diffraction curves recorded for a sample of polycrystalline platinum using a) three different difference scintillator voltages, and b) four different MCP voltages.....	81

Figure 3.17: Schematic illustration of the spatial resolution of an MCP-based detector with a) a short, and b) a long MCP-to-scintillator distance.	82
Figure 3.18: Diffraction pattern of a polycrystalline platinum standard acquired using a) the original, and b) the optimised detector configuration.	82
Figure 3.19: Plot of the simulated (circles) and measured (squares) Bragg peak positions for diffraction from polycrystalline platinum, showing the direction of distortion. Data points are spread over four quadrants identified as 1 to 4.	83
Figure 3.20: Illustration of a) the orientation of the Earth’s magnetic field with respect to the orientation of the TRED apparatus and the geographic north, and b) the projection of the Earth’s magnetic field on the Bragg peak distortion plot.	84
Figure 3.21: Schematic representation of time-zero finder device used in the PIL experiment, showing a fine copper mesh (A), the electron and laser beams (B and C, respectively), and the copper plasma (D).....	85
Figure 3.22: Image frame recorded during PIL time-zero determination experiments with a) poor, and b) optimum temporal overlap.....	85
Figure 3.23: Series of frames showing the evolution in electron beam distortion as a function of time delay.	86
Figure 3.24: Photograph of the TRED apparatus sample holder, showing the polycrystalline platinum internal standard at position 1. The diffraction signal from the internal standard is routinely used to optimise the solenoid lens focusing.	87
Figure 3.25: Photograph of the TRED apparatus a) effusive and b) pulsed nozzle.....	87
Figure 3.26: Drawings showing the cross-section of a) the nozzle head, and b) an exploded view of the time-zero finder.....	88
Figure 3.27: CAD drawing of the enclosure surrounding the high-voltage feedthrough in the TRED apparatus electron gun, showing the HV feedthrough (A), HV connector (B), the PTFE flange fitting (C), the HV cable (D), the steel cylinder enclosure (E), the PTFE cable fitting (F), and end plate (G).	88
Figure 3.28: Schematic illustration of the UED apparatus at SLAC showing the RF electron gun (A), the main solenoid (B), the beam diagnostic module (C), the diffraction chamber (D), the sample delivery system (E), the near detector (F), and the EMCCD far detector (G).	89
Figure 3.29: Schematic depiction of the experimental protocol developed by the UED group at SLAC and used to acquire UED data for 1,2-dithiane.....	90
Figure 3.30: Flowchart representation of a typical data extraction using <i>XTRACT</i>	95
Figure 3.31: Diffraction pattern of benzene a) before, and b) after, the application of a Wiener filter. The zoomed section on the upper-right corner of each pattern illustrates the reduction in image graining before and after the Wiener filter.....	95

Figure 3.32: Examples of a) a diffraction pattern divided into quadrants, and b) the output of the <i>azimean</i> code, showing the overlap between quadrants. The similarity between all four detector quadrants is indicative of the adequate selection of the centre of the diffraction pattern.....	96
Figure 3.33: MICs before least-squares refinement for benzene shown a) separately for each quadrant, and b) spline fitted and compared against simulated data. Agreement between experimental and simulated MICs is indicative of data quality.....	97
Figure 3.34: Comparison of MICs generated using <i>XTRACT</i> and <i>XPKG</i> for the diffraction patterns of benzene recorded using the Edinburgh GED apparatus.....	99
Figure 3.35: Flowchart representation of a typical MIC simulation using <i>SIMMIC</i>	99
Figure 3.36: <i>SIMMIC</i> simulation of the atomic scattering of benzene, generated from the sum of the atomic scattering of six carbon and six hydrogen atoms.	100
Figure 3.37: <i>SIMMIC</i> simulation of the MIC for benzene.....	100
Figure 3.38: Schematic depiction of a typical time-dependent MIC simulation using <i>TD-SIMMIC</i>	102
Figure 3.39: Flowchart showing a typical UED data extraction run using <i>UEDEXTRA</i> . ..	105
Figure 3.40: Flowchart showing the X-ray hit removal algorithm implemented in <i>UEDEXTRA</i>	106
Figure 3.41: Diffraction pattern for 1,2-dithiane before time zero a) before, and b) after X-ray hit removal. The zoomed at the top-right corner of each pattern clearly illustrated the reduction in image noise achieved by the X-ray hit removal routine.	106
Figure 4.1: Structure of DMABN with atom numbering.....	111
Figure 4.2: Experimental (red), theoretical (blue), and difference (experimental-minus-theoretical, black) MICs for DMABN.	114
Figure 4.3: Experimental (red), theoretical (blue), and difference (experimental-minus-theoretical, black) RDCs for DMABN. Before Fourier inversion, experimental and theoretical MICs were multiplied by $s.exp(-2s^2.10^{-5}/[(Z_N - f_N)(Z_C - f_C)])$ prior to Fourier inversion. f_N and f_C denote the atomic scattering factor for nitrogen and carbon taken from Reference 176.	115
Figure 4.4: Variation in measured (squares) and symmetry inferred (triangles) $R_G/R_G(\text{min.})$ as a function of $dC(5)C(4)N(1)C(2)$. Data were fitted to a quadratic function (red line). The horizontal line denotes the 95% confidence limit.....	116
Figure 5.1: Diagrammatic representation of the potential energy surface of 1,2-dithiane along the S–S coordinates. Adapted from reference 108.....	118
Figure 5.2: Evolution of rS –S internal coordinate as a function of simulation time. Adapted from Reference 249.....	119

Figure 5.3: a) series of snapshots from a single trajectory simulation depicting the “molecular clackers” motion, and b) photograph of the clackers toy. ²⁵⁰	120
Figure 5.4: Crystal packing of 1,2-dithiane viewed along the a) <i>a</i> , b), <i>b</i> and c) <i>c</i> axes of the unit cell.....	122
Figure 5.5: Structure of 1,2-dithiane with atom numbering.	124
Figure 5.6: Experimental (red), theoretical (blue), and difference (experimental-minus-theoretical, black) MICs for 1,2-dithiane.....	125
Figure 5.7: Experimental (red), theoretical (blue), and difference (experimental-minus-theoretical, black) RDCs for 1,2-dithiane. Experimental and theoretical MICs were multiplied by $s \cdot \exp(-2s^2 \cdot 10^{-5} / [(Z_S - f_S)(Z_C - f_C)])$ prior to Fourier inversion. f_S and f_C denote the atomic scattering factors for sulfur and carbon taken from Reference 176.	126
Figure 5.8: Simulated time-dependent MIC matrix for 1,2-dithiane a) before, and b) after convolution with a 200 fs instrument-response function.	129
Figure 5.9: Simulated time-dependent RDC matrix for 1,2-dithiane a) before and b) after convolution with a 200 fs instrument-response function.	130
Figure 5.10: Simulated and recorded UV absorption spectra of 1,2-dithiane, showing four absorption bands centred at approximately 202, 211, 238, and 286 nm, corresponding to two $n_S \rightarrow \sigma_{C-S}^*$ and two $n_S \rightarrow \sigma_{S-S}^*$ transitions, respectively.	131
Figure 5.11: a) Diffraction pattern and b) Bragg peak assignment for crystalline gold.	132
Figure 5.12: Comparison between the experimental and simulated MICs for 1,2-dithiane recorded before time zero, and simulated for a ground-state structure.....	133
Figure 5.13: Evolution of the $I(4-5)/I(3.5-4)$ as a function of delay time, showing the onset of the ring-opening motion. Representative error bars are included in the 200 fs datapoint.	134
Figure 5.14: Time-dependent diffraction patterns of 1,2-dithiane a) before the subtraction of the EMCCD background, and b) before and c) after the removal of X-ray noise. Zoomed areas at the top-right corner of each frame, clearly show the reduction in noise.....	135
Figure 5.15: Time-dependent a) scattering intensity curves, and b) MICs for 1,2-dithiane.	136
Figure 5.16: Time dependent MIC matrix for 1,2-dithiane a) before and b) after the Gaussian envelope convolution.	137
Figure 5.17: Time-dependent RDC matrix for 1,2-dithiane, showing the evolution of interatomic distances between 1.5 and 2.5, 2.5 and 3.5, and 4.0 and 6.5 Å, labelled A, B and C, respectively.....	138

Figure 5.18: Molecular structure of 1,2-dithiane with labelled interatomic distances. Interatomic distances are shown in Å, and for clarity purposes distances to hydrogens atoms are not included.	138
Figure 5.19: Diagram showing the time-dependent RDC matrix of 1,2-dithiane with a schematic representation of the “molecular clackers” motion.	140
Figure 6.1: Numbering scheme used in the computational study of asparagusic acid.	141
Figure 6.2: Relaxed potential energy surface scan of asparagusic acid along the $dC(4)C(5)C(6)O(7)$ internal coordinate.	142
Figure 6.3: Choice of active space for asparagusic acid (conformer B).	143
Figure 6.4: Linearly interpolated internal coordinate (LIIC) scans at the SA4-CASSCF(10,8)/cc-pVDZ and SA4-CASPT2/cc-pVDZ levels for asparagusic acid (conformer B). Identical plots for conformers A and C can be found in Appendix F.	144
Figure 6.5: Schematic depiction of the elongation of the $rS-S$ internal coordinate, and the rotation of the two dihedral angles along the ring carbon backbone, $dS(1)C(4)C(5)C(3)$ and $dS(2)C(3)C(5)C(4)$	145
Figure 6.6: Plot of the evolution of a) the $rS-S$, b) the $dS(1)C(4)C(5)C(3)$, and c) the $dS(2)C(3)C(5)C(4)$ internal coordinates as a function of time for conformer A (grey), B (red) and C (yellow). The mean value and standard deviation of the internal coordinates are denoted as \bar{x} and σ , respectively.	146
Figure 6.7: Schematic representation of the van der Waals radii of asparagusic acid at a) 122, b) 168, and c) 215 fs, corresponding to $S \cdots S$ separations of 5.49, 5.46 and 5.87 Å, respectively.	147
Figure 6.8: Heat-map representation of the $rS-S/dSCCS$ phase space for conformer B, at a) 100, b) 200, c) 400, and d) 1500 fs. For clarity purposes $dS(1)C(4)C(3)S(2)$ is expressed in terms of relative dihedral angle normalised between 0 and 360°.	148
Figure 6.9: Heat-map representation of the $rS-S/dSCCS$ phase space for conformers a) A, and b) C.	149
Figure 6.10: Schematic depiction of the elongation of the $rS-S$ internal coordinate, and the rotation of the two dihedral angles along the ring carbon backbone, $dS(1)C(4)C(5)C(3)$ and $dS(2)C(3)C(5)C(4)$	150
Figure 6.11: Average evolution of the $apCCCpOCO$ angle for asparagusic acid.	151
Figure 6.12: Heat-map representation of the $rS-S/apCCCpOCO$ phase space for conformers a) A, b) B, and c) C. Angles were normalised between 0 and 180°.	151
Figure 6.13: Heat-map representation of the $rS-S/dSCC\beta$ phase space for a) 1,2-dithiane, and b) asparagusic acid.	154
Figure 6.14: Simulated time-dependent MIC matrix for asparagusic acid a) before, and b) after the convolution with a 200 fs instrument-response function.	155

Figure 6.15: Simulated time-dependent RDC matrix for asparagusic acid a) before and b) after the convolution with a 200 fs instrument-response function, assuming the A/B/C conformer ratio of 11/53/36%.....	156
Figure 7.1: Numbering scheme used in the computational study of Halon-2402.	157
Figure 7.2: Relaxed potential energy surface scan of Halon-2402 along the <i>d</i> BrCCBr internal coordinate.....	158
Figure 7.3: Choice of active space for the <i>anti</i> conformer in Halon-2402.	159
Figure 7.4: Linearly interpolated internal coordinate scans at the CASSCF and CASPT2 levels for the a) <i>anti</i> and b) <i>gauche</i> conformers of Halon-2402.	160
Figure 7.5: Plot of the evolution of the <i>r</i> C–Br internal coordinate as a function of time for the a) <i>anti</i> , and b) <i>gauche</i> conformers. For clarity purposes, the two <i>r</i> C–Br internal coordinates are labelled <i>r</i> C(1)–Br(7) and <i>r</i> C(2)–Br(8).	161
Figure 7.6: Structure of a) a non-bridging and b) bridged bromotetrafluoroethane radical intermediate.....	162
Figure 7.7: Simulated time-dependent MIC matrix for an <i>anti/gauche</i> conformer ratio of 75/25% of Halon-2402 a) before and, b) after the convolution with a 200 fs instrument-response function.	163
Figure 7.8: Simulated time-dependent RDC matrix for Halon-2402 a) before, and b) after the convolution with a 200 fs instrument-response function.	164
Figure 8.1: A schematic representation of the proposed beam diagnostic tool view from the a) the front and b) side showing: the retractable rod (A), the rotating sector (B), the beam stop (C), the nozzle (D), the interaction region between the electron beam and the sample (E), the image plate holder (F), the Faraday cup (G), the Gd ₂ O ₂ S imaging screen (H), the electron beam (I), electrons scattered from the sample (J), and CCD camera (K).	168
Figure 8.2: CAD drawing of the TRED apparatus future detector modules, showing the interaction region (A), the 1 kHz pulsed nozzle (B), the elongated detector module (C), the flange-mounted optical taper (D), and the EMCCD camera (E).	170
Figure 8.3: Plot of the evolution in carbon halogen separation as a function of time for a) the <i>anti</i> , and b) the <i>gauche</i> conformers of Halon-2402 and C ₂ F ₄ I ₂	172
Figure 8.4: Schematic depiction of the main internal conversion pathways, A and B, and isomerisation pathways, C and D, for <i>E</i> -cinnamionitrile.....	173
Figure 8.5: Photograph of the York laser-induced fluorescence apparatus.....	175
Figure 8.6: Photograph of the York ultrafast point-projection microscopy apparatus.	176
Figure A.1: Flowchart illustration of a typical molecular dynamics simulation in NEWTON-X.	183

Figure B.1: Photographs of the York GED apparatus: a) the filament, b) a solenoid deflector, and c) the shutter mechanism. The shutter mechanism includes a lead beam dump and lead shielding.....	186
Figure B.2: Photographs of the York GED apparatus: a) the effusive nozzle, b) the nozzle and cold trap, and c) the electron beam viewed through the lead-glass viewport.	187
Figure B.3: Schematic depiction of the heated nozzle. The main components in the nozzle are: the copper tip (A), the sample tube (B), the compressed air inlets (C), the valve casing (D), the valve (E), and the sample holder (F). Red and blue arrows indicate the direction of the hot compressed air and sample flow, respectively.....	188
Figure B.4: Photograph of the heated nozzle adapted for the York GED apparatus.	188
Figure B.5: Photographs of the York GED apparatus: a) the plate box, b) the rotating sector, and c) the flat-bed scanner. In the centre of the rotating sector, a beam stop collects unscattered electron, preventing detector damage. The edges of the beam-stop are coated with a thin layer of ZnS-based scintillator to facilitate the visual alignment of the electron beam.	190
Figure B.6: Photograph of the York GED apparatus control panel.	191
Figure C.1: CAD drawing of the TRED apparatus electron gun showing the high-voltage connector rod (B), connecting the high-voltage feedthrough (A) to the steel electrode (E), which is supported by a MACOR ceramic tube (D). The viewport (C) allows a laser to illuminate the photocathode (F), which together, with the anode plate (G) establishes the effective accelerating structure for the electrons.	193
Figure C.2: Photograph of the York TRED photocathode.	194
Figure C.3: Diagram of the Libra optics set-up, showing the layout of the electron generation and pump paths in red and blue, respectively.	197
Figure C.4: Diagram of the Solstice optics set-up, showing the layout of the electron generation and pump paths in red and blue, respectively.	198
Figure C.5: Photograph of the York Solenoid lens inside the TRED apparatus diffraction chamber.....	200
Figure C.6: CAD drawing of the TRED apparatus beam deflector, showing the mounting plates (A and F), the deflector plate pairs (B and D), and the MACOR spacers (C and E).	200
Figure C.7: CAD drawing of the TRED apparatus sample holder, showing the brass plate (A), the copper frame (B), the brass outer plate (C), the translator mount (D), and internal standard position (E).	201
Figure C.8: TRED apparatus sample reservoir, showing the inlet of helium and the outlet of a mixture of helium and sample gas.....	202
Figure C.9: Photograph of the TRED apparatus electron detector, showing the detector flange (A), scintillator mount (B), MCP (C), and beam stop (D).	203

Figure C.10: Photograph of the TRED apparatus Faraday cup and beam stop assembly viewed from a) the side, and b) the top.....	203
Figure C.11: CAD drawing of the second-generation TRED apparatus showing a) the top, and b) the side flanges. Both flanges consist of a zero-length 12' ' to 8' ' reducer with opposing knife edges and an offset centre, coupled to either a) an 8' ' spacer, or b) an 8' ' to two 2 ³ / ₄ ' ' zero-length reducer.	205
Figure C.12: Diagram of a data-acquisition routine implemented in the <i>TRED.run</i> software package.....	206
Figure D.1: Schematic representation of the layout of the MeV UED apparatus, showing the MeV electron beam (A), the two bored mirrors (B), the solid-state sample holder (C), the CCD camera imaging the interaction region (D), the incident pump beam (E), the molecular beam (F), and the scattered electron beam (G).	208
Figure D.2: Schematic representation of the MeV UED apparatus sample delivery system, showing the μ -metal shield (A), nozzle head (B), nozzle solenoid (C), in-vacuum transport line (D), three-axis manipulator (E), feedthrough for the nozzle drive (F), feedthrough for the in-vacuum heaters (G), Kapton in-vacuum heaters (H), out-of-vacuum transport line (I), out-of-vacuum rope heaters (J), and valve (K).	208
Figure D.3: Schematic representation of the solid-state holder developed during the 2016 gas-phase run, showing the intake needle valve (A), the Swagelok-to-conflat flange (CF) adaptors (B), 1 ¹ / ₂ ' ' CF elbow fittings (C), quarter-turn valve (D), and glass-wool plug (E).	209
Figure D.4: Schematic representation of the MeV UED apparatus detector, showing the scintillator (A), 45° mirror (B), EMCCD camera (C), f/0.85 collection lens (D), unscattered electron beam (E), scattered electron beam (F), fluorescence from the scintillator (G), and reflected fluorescence (H).	210

List of Accompanying Material

The Appendices attached to the end of this thesis contain: a summary of the theoretical background underpinning the computational methods used in electron diffraction, a detailed description of the functionality, design and layout of electron diffraction apparatus, annotated code, and tables, plots and drawings summarising the most relevant results of this project. The methods and designs described in Appendices A to D are not of my authorship, unless stated otherwise; and therefore are only included for consultation purposes, as they provide the reader with a wider context to my research goals and achievements (presented in Chapters 4 to 7). On the other hand, Appendices E to H contain several hundred pages of supplementary information supporting the results of my PhD project. These are presented in in electronic format, as a DVD attached to the back cover of this book.

Appendix A – Summary of computational methods used in GED and TRED studies.

Appendix B – York GED apparatus design and layout.

Appendix C – York TRED apparatus design and layout.

Appendix D – SLAC UED experimental setup.

Appendix E – Functions, libraries and scripts for software packages.

Appendix F – Active-spaces, optimised structures, linearly interpolated internal coordinate scans and coordinate evolution plots for computational studies.

Appendix G – Refinement of gas electron diffraction data.

Appendix H – Technical drawings of the components added to the York time-resolved electron diffraction apparatus.

Acknowledgements

First and foremost, I would like to thank my supervisor, Dr Derek Wann, for giving me the opportunity to undertake this project, and for his patient guidance, encouragement, and support throughout all its stages.

I thank all members of the Wann group, past and present – Dr Paul Lane, Dr Stuart Young, Robin Virgo, Matthew Fancy, Fiona Whiting, and Tomas Lock Feixas – for their good advice and enlightening discussions. A special thanks to Dr Matthew Robinson for teaching me about time-resolved electron diffraction, and for reassuring me that “the success of a PhD in science comes down to one’s ability troubleshoot small problems daily”. I would also like to thank Conor Rankine for introducing me to molecular dynamics, and for his dedication in maintaining and debugging the computational packages used in this project. To everyone in the A057 office, I am thankful for these three years of flawless weekly cakes, and for a welcoming work environment.

I would like to thank to Prof. Xijie Wang and the rest of the UED team at SLAC for allowing me to take part in the UED experiments. I am especially grateful to Dr Jie Yang and Dr Thomas Wolf for their dedication to the UED study of dithiane, and for helping me to operate the UED apparatus through sleepless nights.

I would like to thank the Department of Chemistry mechanical, electronics and glass-blowing workshop staff, without whom the custom components described in this thesis could not have been manufactured. I am especially grateful to Dr Chris Rhodes and Chris Mortimer for educating me in the ways of electronics and machining, respectively

I acknowledge the University of York for funding my project, and the Wild Overseas Scholars Fund for funding my visit to SLAC; the Central Laser Facility provided the Wann group with a laser loan pool laser during the first year of my PhD.

On a more personal note, I thank my parents and brother, Fátima Nunes, Bernardo Nunes, and Diogo Nunes, whose love and unconditional support knows no borders, and have made my academic pursuits possible. I owe special thanks to my partner in all things, Filipa Fernandes, for making York a warmer place, and for her willingness to proof read countless iterations of scientific rambling. These people have experienced the ups and down of my research. This thesis is dedicated to them.

Declaration

I declare that this thesis is a presentation of original work, and that I am the sole author. Moreover, this work has not previously been presented for an award at this, or any other, University. All sources are acknowledged as References.

João Pedro Figueira Nunes

Chapter 1. Introduction

For centuries, chemists have studied the response of molecular structures to external stimuli, such as heat and light, using innovative experiments and an imagination of the mechanisms underpinning chemical reactivity. This approach, based on indirect observation of molecular structures and motions, allowed chemists to construct models of molecular interactions and reactions, despite having never observed such phenomena directly. Throughout this time, chemists dreamed of capturing molecular motions in real time, using so-called molecular movies. At the turn of the 21st century, developments in femtosecond technology and structure determination methods allowed the molecular movie to transcend the thought experiment and become a tool for the study of molecular motions. For the first time, chemists could observe molecules move and react; they no longer had to rely solely on imagination to predict chemical reactivity or to explain the physical properties of materials. Modern time-resolved structure determination techniques, such as time-resolved electron diffraction (TRED), allow molecular motions to be recorded with sub-picosecond temporal resolution.¹⁻⁵ These molecular movies provide an unambiguous, albeit classical, slow-motion representation of the evolution of interatomic distances within molecules.⁶ The ability to follow structural rearrangements and chemical reactions in real time has sparked a renaissance in the field of time-resolved structural dynamics, the results of which continue to challenge chemists' understanding of the natural world.^{7,8}

The project presented in this thesis aims to develop new strategies for recording molecular movies, using a combination of time-resolved imaging tools, computational methods, and traditional structure determination techniques for the study of molecular motions. The Wann group expertise in both gas electron diffraction (GED) and quantum chemistry has allowed me to explore the synergy between experimental and theoretical chemistry, a combination that is crucial to the study of molecular dynamics. Developments towards the realisation of molecular movies are presented in Chapters 4 to 7, where case studies showcase the different stages of a roadmap to molecular movies presented in Section 1.6.

1.1 The importance of temporal resolution in the study of nature

Decades before the discovery of atoms, and at a time where the concept of “molecular movies” would have seemed utterly nonsensical, American magnate and racehorse owner Leland Stanford realised the competitive advantage that would be gained by understanding how a horse gallops. Aware that the human eye could not capture the quick movements of the horse’s legs, Stanford hired the help of Eadweard Muybridge, an English photographer, to find out if a galloping horse could have all four hooves off the ground.⁹ To answer Stanford’s challenge, Muybridge placed 24 cameras along the edge of the track to capture the horse’s silhouette as a series of still frames, one twenty-fifth of a second apart. Trip wires placed along the racetrack ensured shutter synchronicity. Muybridge used one of his inventions, the zoopraxiscope – credited as the first movie projector – to visualise these images of a galloping horse, in what can be thought of as the world’s first slow-motion movie.¹⁰ The twelve-image sequence depicted in Figure 1.1 shows Stanford’s horse, Sallie Gardner, mid-gallop with all four hooves off the ground. In settling an age-old argument in the horse-racing community, Muybridge demonstrated the importance of temporal resolution in the study of fast motion. The scientific relevance of what came to be known as the world’s first time-resolved experiment did not go unnoticed and in 1878 Muybridge’s findings were published in the article entitled “The science of horse’s motion”.¹¹ The development of time-resolved imaging tools to study increasingly small features and faster motions has remained one of science’s great driving forces.

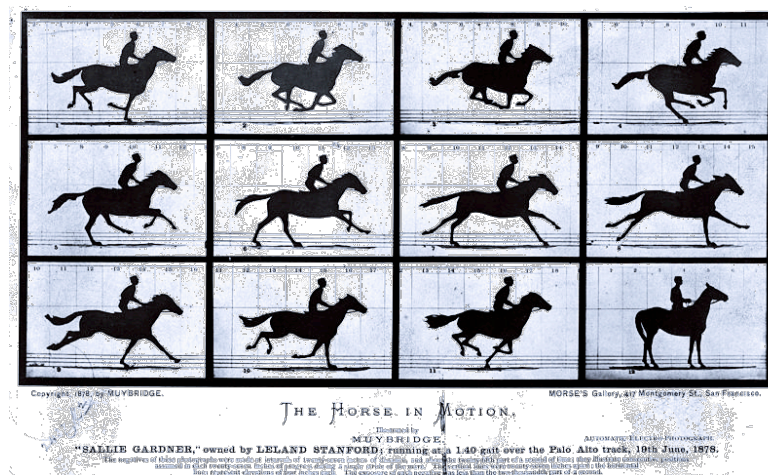


Figure 1.1: 1878 poster of “Sallie Gardner at a Gallop”, also known as *The Horse in Motion* by photographer and inventor Eadweard Muybridge. Adapted from Reference 12.

Ubiquitous throughout nature, ultrafast motions have been found to be integral to some fundamental mechanisms. For instance, the ability of an eye to see relies on the sub-200 fs irreversible *cis-trans* isomerisation of the retinal chromophore 11-*cis*-rhodopsin, and also on the structural integrity of DNA so that its deoxyribose-phosphodiester backbone can dissipate excess energy through ultrafast vibrational relaxation.¹³⁻¹⁶ In both cases, system functionality is controlled by both static and dynamic structure, illustrating the importance of molecular motion and timescale on the structure-function relationships governing chemical reactivity. The use of time-averaged methodologies to study the dynamic world has resulted in misinterpretations and the construction of misrepresentative models, usually derived from assumptions rather than observations. Therefore, modern time-resolved techniques, such as TRED and time-resolved X-ray diffraction (TRXD), record molecular motions in four dimensions (x, y, z, t), with the first three corresponding to the Cartesian coordinates (xyz) and the fourth dimension being time.¹⁷⁻¹⁹

1.2 The role of electron diffraction in structure determination

For many decades, spectroscopy has dominated the study of time-resolved dynamics, thanks to the development of techniques such as transient-absorption spectroscopy, time-resolved infrared spectroscopy, and time-resolved photoemission spectroscopy.²⁰⁻³³ Despite their unparalleled temporal resolution, these methods cannot image molecular motions directly, instead inferring molecular structure and how it changes over time. This limitation can be overcome with the use of time-resolved diffraction techniques, such as TRED, which capture molecular motions as sequences of unique molecular structures recorded with sub-Ångström spatial resolution.³⁴⁻³⁶ Recent breakthroughs in accelerator design and the advent of femtosecond laser technology have allowed diffraction sources to achieve unprecedented brightness and temporal profiles.³⁷⁻⁴¹ Modern studies of excited-state dynamics use time-resolved spectroscopy and diffraction methods in a complementary fashion to explore the behaviour of electronic and nuclear wavepackets, respectively.⁴²⁻⁴⁵

Time-resolved diffraction techniques have been developed using the three most common diffraction probes: X-rays, electrons, and neutrons, each of which uses a fundamentally different interaction to induce scattering. X-rays and neutrons interact with the electron cloud and nuclei, respectively, whereas electrons interact with the

charge gradients around the nuclei.⁴⁶ Though conceptually more suitable as a probe of molecular motion, time-resolved neutron diffraction is far less common than its X-ray and electron counterparts. Difficulties in generating pulsed neutron beams using spallation processes have restricted neutron scattering to the time-averaged domain. Modern X-ray and electron sources use far subtler processes to control the temporal profile. Although, X-rays and electrons have been used to study molecular motions of small molecules in both condensed and gas phases, when it comes to sample damage, X-rays are more destructive than electrons.⁴⁷ More susceptible to inelastic scattering, X-rays are known to deposit far more energy to the sample, resulting in irreversible radiation damage.⁴⁸ Furthermore, as charged particles, electrons interact more strongly with atoms than X-rays, requiring lower fluency to achieve similar signal-to-noise ratios (SNRs). In fact the scattering cross-section for an electron is several orders of magnitude larger than that of an X-ray.⁴⁹ Moreover, X-ray beams bright enough to yield adequate SNR at the desired temporal resolution can only be generated using synchrotrons and free-electron lasers (FELs). High operational cost and lengthy application processes for beam-time allocation at these facilities can significantly hamper the research output of time-resolved X-ray diffraction. Although table-top X-ray sources have been developed for time-resolved studies, they are much less reliable than their electron-driven counterparts.⁵⁰ The table-top TRED apparatus allows molecular dynamics studies to be carried out cost-effectively by university research groups.

1.3 Overview on time-resolved electron diffraction

Time-resolved electron diffraction combines the temporal resolution of spectroscopic methods with the structural accuracy of direct imaging techniques. In fact TRED is a pump-probe experiment where a pulsed electron beam replaces the optical probe and time-dependent information is recorded in the form of diffraction patterns.

Electron bunches generated *via* ionisation of a metal photocathode are accelerated across a potential to produce a bright, collimated electron beam (see Chapter 2 and Appendix C for details regarding beam generation and dynamics). Electron optics reshape the beam and direct it towards a chemical target. Examples of gaseous target samples are presented in Chapter 4 and 5. The charge gradients around atomic nuclei cause incident electrons to scatter at an angle proportional to the interaction magnitude (see Chapter 2 for a full explanation). An electron detector, downstream

from the sample-probe interaction region, records the intensities and positions of scattered electrons as diffraction patterns. From these images, molecular structures are retrieved using sophisticated data-reduction and structure-refinement methods, which are described in Chapter 2. Prior to the arrival of the electron probe at the sample, a pulsed laser pump optically excites the sample, inducing structural changes. By altering the time delay between the optical pump and the arrival of the electron beam one can capture the molecular structure at different stages during its excited-state motion. In these experiments, data quality is not only dependent on the brightness of the electron beam, but also its longitudinal profile, *i.e.* its duration, as the use of pulses longer than the timescales of the motions being studied will result in “blurred” diffraction patterns and loss of dynamical information. In photography, this would be analogous to photographing a fast-moving object using a long camera exposure, *i.e.* a slow shutter speed. The effect of exposure on photographic image resolution is illustrated in Figure 1.2. In electron diffraction, exposure is controlled by the duration of the probe electron beam. To achieve shutter speeds of a few hundred quadrillionths of a second, *i.e.* hundreds of femtoseconds, electron diffraction uses ultrafast laser systems to produce ultra-short electron bunches and to photoexcite the sample. Diffraction data are recorded at varying pump-probe time delays and sorted chronologically to produce a “molecular movie”.⁶

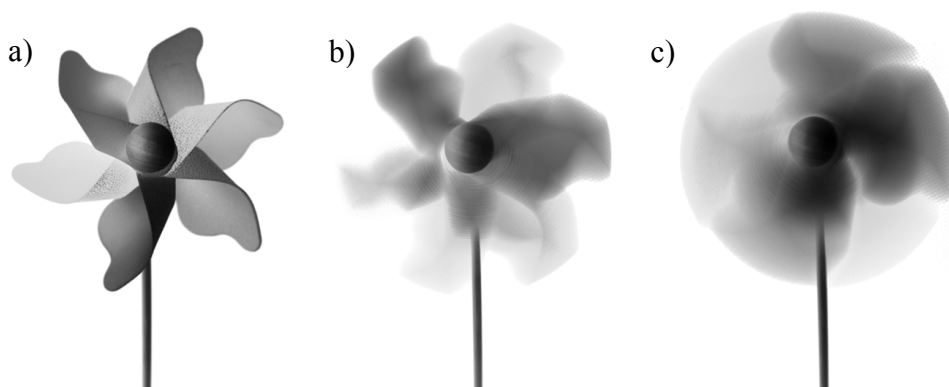


Figure 1.2: Rotating fan photographed at a) 1/1000 s, b) 1/500 s, and c) 1 s shutter speed. Adapted from Reference 51.

In 1994, the experimental feasibility of the molecular movie concept was demonstrated in the study of myoglobin using X-ray crystallography allowing “crystallographers to discover what Hollywood has discovered long ago – that there’s nothing like action to draw the crowds”.^{52,53} Simply put, “molecules have

become the world's smallest movie stars" and modern time-resolved imaging techniques such as TRXD and TRED "the next big hit in molecular Hollywood".⁵⁴ In over two decades of existence, TRED has progressed from capturing phase transitions in metal films and the photodissociation of small molecules, to the study of far subtler motions, such as *cis-trans* isomerisations and ring-opening processes in biologically relevant systems.⁵⁵ Given the community's enthusiasm and the potential of TRED, far more complex and ground-breaking experiments are to be expected in the years to come.

1.4 Historical overview of time-resolved electron diffraction

In 1897, Nobel laureate Sir Joseph J. Thomson reported the existence of "corpuscles" (Latin for small body), 1836 times lighter than hydrogen and negatively charged.⁵⁶ Thomson's "Cathode Tubes" paper marks the discovery of the first subatomic particle, describing what is now known to be the electron. Two years earlier, German physicist Wilhelm Röntgen, in the paper "On a new kind of ray: a preliminary communication", coined the term "X-ray", following the observation of a faint green glow emanating from a fluorescent screen in the vicinity of a Crookes tube – a primitive form of cathode-ray tube (CRT) – stored inside a cardboard box. This invisible ray could pass through glass, cardboard, books and, to Röntgen's astonishment, even his desk.⁵⁷ In 1912, twenty-two year old William Lawrence Bragg and his father Sir William Henry Bragg discovered that crystalline solids reflected X-rays at discrete angles forming interesting patterns.⁵⁸ For their contribution to structural chemistry, namely the discovery of the laws of diffraction and the determination of the crystal structures of NaCl, ZnS and diamond, father and son were awarded the Nobel Prize in Physics in 1915. William Lawrence Bragg, to this day the youngest Physics Nobel laureate, expanded on the "wave theory of light" proposed by Thomas Young in the early nineteenth century,⁵⁹ to demonstrate how the constructive and destructive interference of specularly reflected waves could be used to determine the structures of crystal lattices. In 1924, Louis de Broglie's PhD thesis "Recherches sur la théorie des quanta" (Research on Quantum Theory) postulated the wave nature of electrons, proposing a universal duality between particle and waves.⁶⁰ Three years later, two independent observations of electron diffraction confirmed de Broglie's hypothesis. At the University of Aberdeen, George Thomson recorded the first electron diffraction of a thin film. Meanwhile at

Bell Labs, Clinton Davisson and Lester Germer observed the first electron diffraction pattern from a crystalline sample, for which they shared the 1937 Nobel Prize for Physics.^{61,62} Davisson and Germer described their apparatus, shown in Figure 1.3, as a “ship in a bottle, with a gun for a ship, firing electrons at a nickel crystal target with a collector detecting any reflected electrons”.

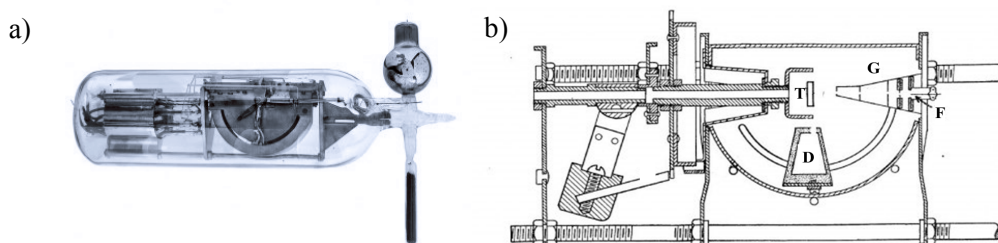


Figure 1.3: a) Photograph and b) schematic cross-section of the electron diffraction apparatus used to record the world’s first electron diffraction pattern. The electron gun, filament, target, and detector are denoted with the letters, G, F, T and D, respectively. Adapted from Reference 61.

In Davisson and Germer’s paper “The scattering of electron by a single crystal of nickel”, peaks in the diffraction pattern for nickel are shown to match the reflections predicted by the Bragg laws of diffraction.^{61,63} In 1928, inspired by Davisson and Germer’s ground-breaking work, as well as Peter Debye’s use of X-rays to study molecular structures in gaseous samples, Herman Mark and Von R. Wierl carried out the first gas electron diffraction (GED) experiment, shown in Figure 1.4.^{64,65}

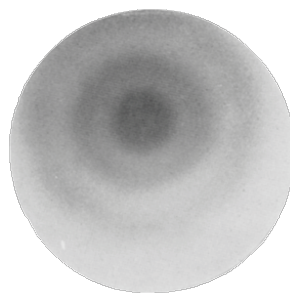


Figure 1.4: First recorded gas electron diffraction pattern for CCl₄. Adapted from Reference 65.

Improvements in the reliability of continuous electron sources, built on the legacy of CRT technology, allowed GED to become the staple technique for the determination of ground-state structures in the gas phase throughout the 1960s and 1970s.

Demand for time-resolved information led to advances in GED in the early 1980s. In 1983, Anatoly Ischenko used a set of electromagnetic deflector plates to chop an electron beam generated by thermionic emission, producing the world's first pulsed electron beam.⁶⁶ Ischenko's "stroboscopic" electron diffraction apparatus, schematically depicted in Figure 1.5, was used to study the photodissociation of trifluoroiodomethane (CF_3I) with microsecond temporal resolution. These experiments used a laser-pump pulse to photoexcite CF_3I molecules and GED to structurally resolve the C-I separation.⁶⁶

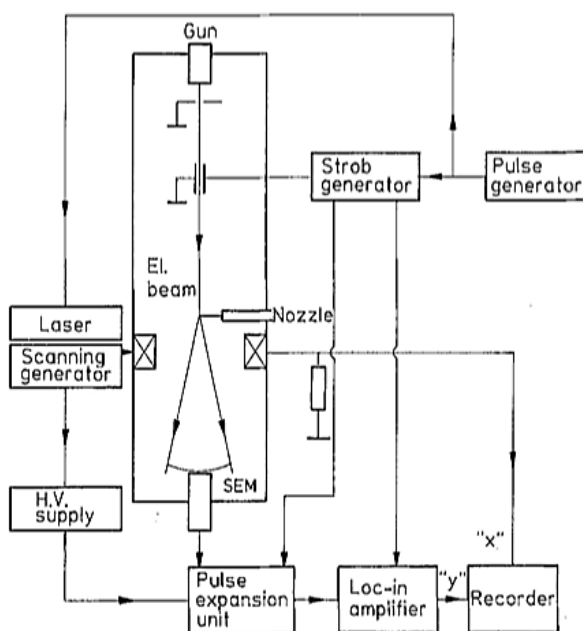


Figure 1.5: Schematic representation of Ischenko's "stroboscopic" electron diffraction apparatus, the world's first time-resolved GED apparatus. Adapted from Reference 66.

Williamson and Morou replaced the thermionic electron source in Ischenko's design by a light-driven photocathode electron gun, which could operate at higher repetition rates and ensure the synchronicity between pump and probe beams.⁶⁷ Williamson and Morou's 1984 publication, "Picosecond electron diffraction", reporting on the lattice dynamics of a thin film of aluminium with picosecond resolution, represents a landmark in the development of modern TRED.⁶⁸ Early TRED studies recorded time-dependent diffraction data as a series of unique exposures on photographic film, each corresponding to a different pump-probe time delay, making data visualisation and extraction a painstakingly slow process. In an attempt to streamline the acquisition and handling of TRED data, Ewbank *et al.* demonstrated the use of

phosphor-screen scintillators and photodiode arrays for electron detection.⁶⁹ Ewbank's electron detector, quickly superseded by charge-coupled device (CCD) chip technology, eliminated the need to replace and develop the photographic medium after each exposure. Furthermore, it allowed data to be viewed in real time on a computer, drastically reducing downtime associated with TRED experiments. Insensitive to low-energy particles, such as ambient light or stray photons, scintillator-based detectors eliminate the need to carry out experiments under safelight conditions, whilst preserving image quality. Ewbank's contribution to TRED culminated in the study of the photofragmentation of carbon disulfide with nanosecond resolution using an excimer laser to drive a photocathode electron gun similar to that of Williamson and Morou.⁷⁰

The development of photocathode technology and the advent of commercial femtosecond lasers in the early 1990s allowed TRED to transcend into the femtosecond timescale.⁷¹ Nobel laureate Ahmed H. Zewail, known as the "father of femtochemistry", pioneered the use of TRED to study femtosecond dynamics in molecules, coining it ultrafast electron diffraction (UED).⁷² Zewail *et al.* built several UED apparatus to investigate molecular motions in the gas phase and developed the theoretical knowledge required to interpret time-dependent diffraction data.⁷³⁻⁷⁶ A schematic representation of Zewail's third-generation UED apparatus, used to resolve the photodissociation of 1,2-diodotetrafluoroethane with picosecond temporal resolution, is shown in Figure 1.6.⁷⁷

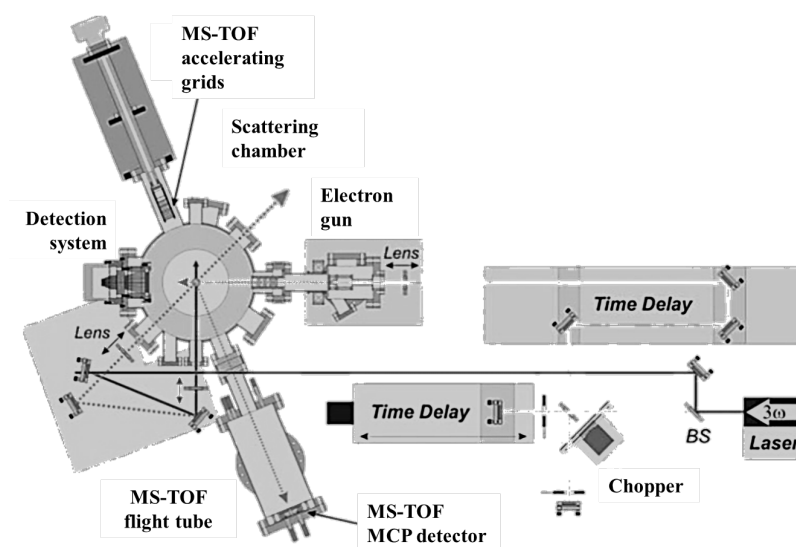


Figure 1.6: Schematic representation of Zewail's third-generation UED apparatus, UED-3. Adapted from Reference 78.

The detrimental effect of Coulombic repulsion on the duration of electron pulses meant that the temporal resolution of early UED experiments was limited to a few picoseconds. However, in 2007 Bradley Siwick and Jom Luiten demonstrated the use of radio frequencies (RF) to longitudinally compress electron pulses, overcoming the effects of space-charge broadening on the temporal resolution of UED experiments.⁷⁹ Their experiments with RF-pulse modulation pioneered the use of RF electron guns and RF bunch compressors (see Chapter 2) in electron diffraction. A year earlier, Hastings *et al.* had overcome Coulombic repulsion with the use of relativistic electrons at the Stanford Linear Accelerator Center (SLAC), successfully resolving the phase transition of aluminium with sub-picosecond temporal resolution.⁸⁰

More recently, the group of R. J. Dwayne Miller has used TRED to study much more subtle motions in large organic and biological molecules, demonstrating the relevance and applicability of electron diffraction to the wider chemical and biological communities.^{55,81}

The ability of TRED to capture and unambiguously resolve molecular motions in photochemically rich systems has attracted researchers at universities and also at central facilities to contribute to the development of the technique.

1.5 Current work in the field

Contributions from the Zewail, Miller, Siwick, and more recently the Ropers, Küpper, and Centurion groups have redefined the state-of-the-art in TRED, securing its place at the forefront of structural dynamics.

In 2013, Zewail *et al.* used TRED to measure the force constants associated with DNA nanostructures mounted across thin porous carbon, demonstrating the applicability of TRED to the study of large biological samples.⁸² In the same year, Zewail *et al.* explored the thermal contraction of Fe(pyrazine)Pt(CN)₄ nanoparticles mounted on a graphite substrate (see Figure 1.7), using a train of laser pulses to rapidly heat the substrate, inducing the contraction of the cyanide nanoparticle. Changes in nanoparticle size were recorded with nanosecond temporal resolution using TRED.⁸³

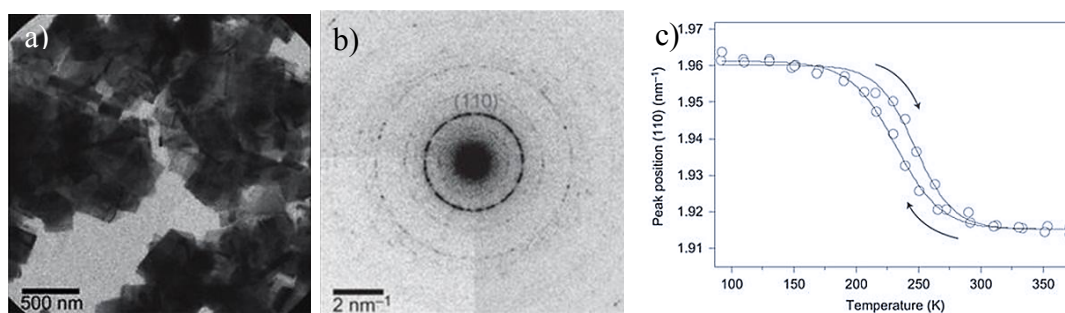


Figure 1.7: Examples of a) bright-field image, b) diffraction pattern at 90 K and c) phase-transition behaviour of an ensemble of Fe(pyrazine)Pt(CN)₄ nanoparticles. Adapted from Reference 83.

Miller and Siwick developed much of the theory underpinning the generation and manipulation of electrons from kilo-electron-volt (keV) sources.⁷⁴ In their study of electron beam dynamics, Miller *et al.* describe the effect of Coulombic repulsion and velocity distribution in a non-relativistic electron bunch on the temporal resolution of TRED experiments and demonstrate the use of electric fields in the control of beam properties.⁸⁴ Miller *et al.* have also contributed to the development of beam characterisation and diagnostic tools, the most remarkable of which is the ponderomotive scattering method for the determination of electron bunch duration. Following the observation of the phase transitions of aluminium⁷⁶ and bismuth with picosecond temporal resolution, the Miller group changed its focus to the study of the photoinduced dynamics of organic molecules. Developments in TRED design and beam characterisation tools culminated in the commissioning of Miller's 95 keV apparatus and the observation of 1,2-bis(2,4-dimethyl-5-phenyl-3-thienyl)perfluorocyclopentene ring-opening dynamics in 2013 (see Figure 1.8).¹ Miller *et al.* were able to confirm the formation of an excited transition state and “unambiguously witness convergence towards the structure of the closed-ring molecule” on the sub-200 fs and 5 ps timescales, respectively. In the same year, Miller *et al.* resolved the motion associated with the insulator-to-metallic phase transition in an ethylenedioxytetrathiafulvalene complex.⁵⁵ At McGill University, Siwick started his own research group that focused, almost exclusively, on UED studies of solid-state samples. In 2014, Siwick *et al.* published a UED study of the semiconductor-to-metal transition in polycrystalline VO₂ and since then have remained at the forefront of condensed-phase UED.⁸⁵

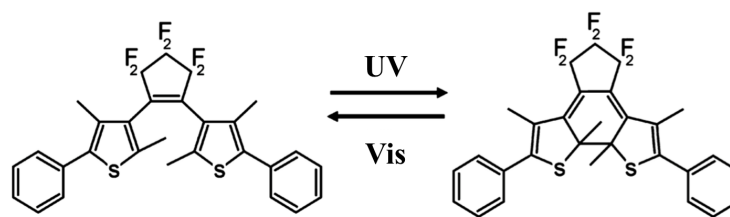


Figure 1.8: Reversible ring-opening/closing reaction of 1,2-bis(2,4-dimethyl-5-phenyl-3-thienyl)perfluorocyclopentene. Adapted from Reference 1.

Four years after Hastings successfully studied the phase transition of aluminium using relativistic electrons at SLAC, Musumeci *et al.* recorded the same phenomenon for a gold sample, using a 3.5 MeV UED apparatus at the University of California Los Angeles (UCLA).⁸⁶ At the Tsinghua Thomson X-ray scattering (TTX) source, Li *et al.* carried out a similar experiment, although using an RF deflection cavity to streak the electron bunch and capture the entire phase-transition dynamics in a single shot.⁸⁷ This approach to UED was inspired by Schwoerer's streak camera apparatus⁸⁸ developed years earlier and Weber's 1995 theoretical study of reflectron guns.^{89,90 82,83} At the versatile electron linear accelerator (VELA) the UK's first relativistic UED apparatus was commissioned as part of a collaboration between Daresbury laboratories and the Wann group. In 2014, the MeV VELA-UED apparatus at Daresbury captured its first static diffraction pattern for polycrystalline and single-crystal gold, shown in Figure 1.9.⁹¹

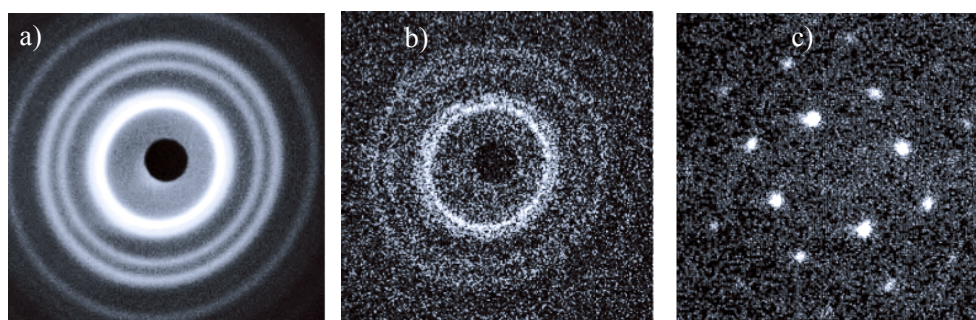


Figure 1.9: Diffraction patterns for polycrystalline gold a) accumulated over 1000 shots, b) recorded in single-shot mode, and c) a single-shot single-crystal diffraction pattern for gold. Adapted from Reference 91.

In the autumn of 2014, a strategic plan set out by the US Department of Energy (DOE) launched an initiative to develop a UED facility at SLAC for the study of “ultrafast processes in highly complex system”.⁹² An MeV UED apparatus, shown in

Figure 1.10, has been built at SLAC's accelerator structure test area (ASTA) to capture molecular motions in gaseous and condensed phases.⁴¹ Spearheaded by Xijie Wang, this initiative has led to the creation of the UED group at SLAC and, through collaboration with Martin Centurion at Nebraska and Markus Gühr at Potsdam, yielded major breakthroughs in UED. Furthermore, through collaboration with the Lindenberg group and the PULSE Institute at Stanford, and the Wann group at York, UED at SLAC is now the world leader in technical and scientific developments and the use of UED as a tool for the study of time-resolved molecular structures in gaseous and condensed phases.

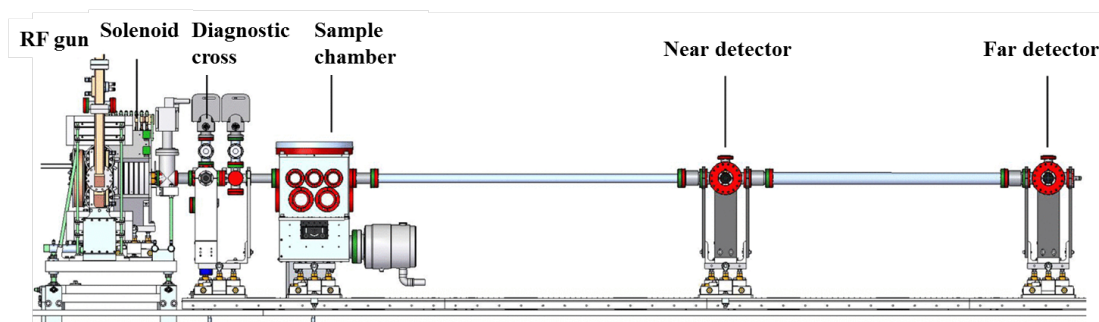


Figure 1.10: CAD drawing of the MeV UED beamline at SLAC's ASTA facility. Adapted from Reference 41.

Whilst most UED studies use one-dimensional diffraction data, the work of Centurion and, more recently, Küpper has attempted to expand the dimensionality of UED data. Centurion *et al.* use polarised laser pulses to induce rotational wavepackets onto molecules in the gas phase, non-adiabatically aligning them in a field-free region.^{3,93,94} Diffraction patterns acquired using this technique consist of two-dimensional projections of the molecule in reciprocal space. Structural information can be retrieved directly from the Fourier transform of these diffraction patterns, without the need for further structural refinement. Moreover, using the 25 keV UED apparatus at Nebraska, Centurion *et al.* have recently been able to resolve the molecular alignment of CS₂ with picosecond temporal resolution.⁹⁴ In 2016, through collaboration with the UED group at SLAC, the Centurion group successfully resolved the motion of the vibrational wavepacket in isolated iodine molecules using relativistic electrons.⁹⁵ These experiments demonstrate the ability of UED to record time-resolved diffraction data in more than one dimension, paving the way for more complex align-pump-probe experiments. Furthermore, Centurion's

table-top 90 keV UED apparatus, shown in Figure 1.11, has recently achieved sub-400 fs temporal resolution using an RF bunch compressor.⁹⁶ At the Deutsches Elektronen-Synchrotron (DESY) facility in Hamburg, the Küpper group has recently commissioned a 15 keV UED apparatus for the study of impulsively aligned molecules.⁹⁷ Elegant work by the Küpper and Centurion groups has revolutionised the very nature of diffraction data and has led to new schools of thought in UED.

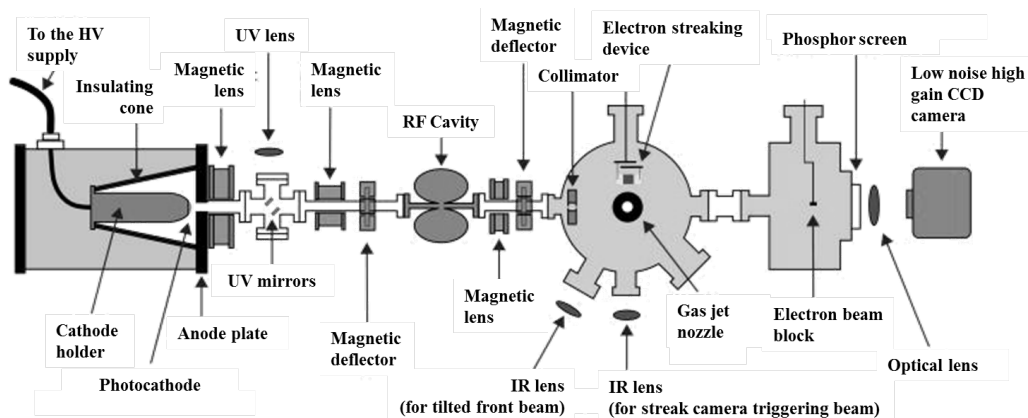


Figure 1.11: Block diagram of Centurion's 90 keV UED apparatus at Lincoln, Nebraska. Adapted from Reference 96.

To allow UED, and the related field of ultrafast electron microscopy (UEM), to study the dynamics of larger biological systems and macromolecules, the Ropers group at Göttingen is currently developing a point-like source for the generation of highly coherent electrons. In 2007, Ropers *et al.* recorded the first evidence of sustained multiphoton single-electron emission from an atomically sharp gold nanotaper using remotely driven surface-plasmon nano-focusing, rather than the more traditional far-field apex-illumination method.⁹⁸ In Ropers' ultra-compact electron gun, schematically depicted in Figure 1.12, surface plasmon polaritons (SPP) are generated at the shaft of the nanotaper using a tightly focused near-IR ultrafast laser. A nanoscale waveguide, lithographically etched along the conical nanotaper, launches these plasmon wavepackets towards the apex, where spatial contraction induces adiabatic nano-focusing and electron emission.⁹⁹ The applicability of these sources in imaging has been demonstrated in the point projection microscopy (PPM) study of silver nanowires.¹⁰⁰ Due to their unique transverse coherence and temporal resolution, plasmon-driven nanoscale emitters are driving interest in this new generation of point-source UED and UEM apparatus.

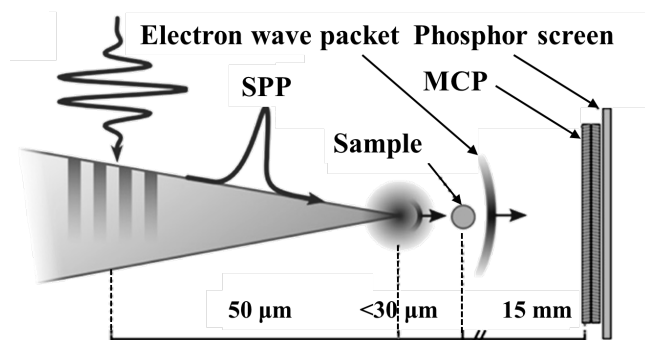


Figure 1.12: Schematic representation of Ropers' ultrafast point projection microscopy (UPPM) remotely driven electron emission. Surface plasmon polaritons produced by near-IR illumination of a lithographically etched waveguide or grating coupler propagate towards the nanotaper apex where plasmon-induced electron emission takes place. A 250 V bias between the tip and the micro-channel plate (MCP) accelerates newly formed electrons away from the apex, towards the detector, producing shadow images of the sample. Adapted from Reference 100.

The study of molecular motions with unprecedented spatio-temporal resolutions, and the development of novel sources for the imaging of previously unseen events, have kept TRED and associated techniques relevant in the search for the ultimate visualisation tool. Nearly a century after the first experiments, electron diffraction is undergoing yet another reinvention, pushing frontiers of imaging into unprecedented time domains.

1.6 Roadmap to molecular movies

The advent of TRED, UED, and UEM brought the concept of “molecular movies” into the spotlight of modern chemistry, completely changing the way in which chemists approach the study of molecular dynamics. Molecular movies have transcended the *in-silico* domain and become a tool for the exploration of molecular motions, benchmarking of computational methods, and validation of spectroscopic observations. In practical terms, molecular movies are the results of careful combination of complementary information acquired using computational, spectroscopic, time-averaged, and time-resolved structural methods. Before running TRED experiments, molecular motions are often explored using static quantum chemical calculations and molecular dynamics simulations. Furthermore, traditional GED studies are routinely used to determine the time-averaged ground-state structures of the species involved. These satellite studies provide the preliminary body of work required to increase the likelihood of the success of TRED

experiments. During the analysis and interpretation of TRED results, external datasets from *a posteriori* computational and spectroscopic investigations are used to deconvolute diffraction data. Theoretical and other experimental data are combined to supplement diffraction data, considerably improving the reliability of TRED studies.

In this Section, the roadmap shown in Figure 1.13 is proposed as a robust strategy for the recording of molecular motions. The synergy between experimental and theoretical methods is clearly illustrated in the roadmap with its “computational” building block placed alongside electron diffraction experiments. Computational studies are shown to support all stages of the roadmap, from the identification of suitable sample candidates, to the recording of molecular motions, and the analysis of datasets. The roadmap also illustrates the dependencies and relationships between different experimental techniques, emphasising the importance of the use of complementary techniques in the capture of molecular motions. In addition to proposing a methodology for the study of molecular dynamics, the roadmap was used to identify research goals and define research strategies throughout this PhD project.

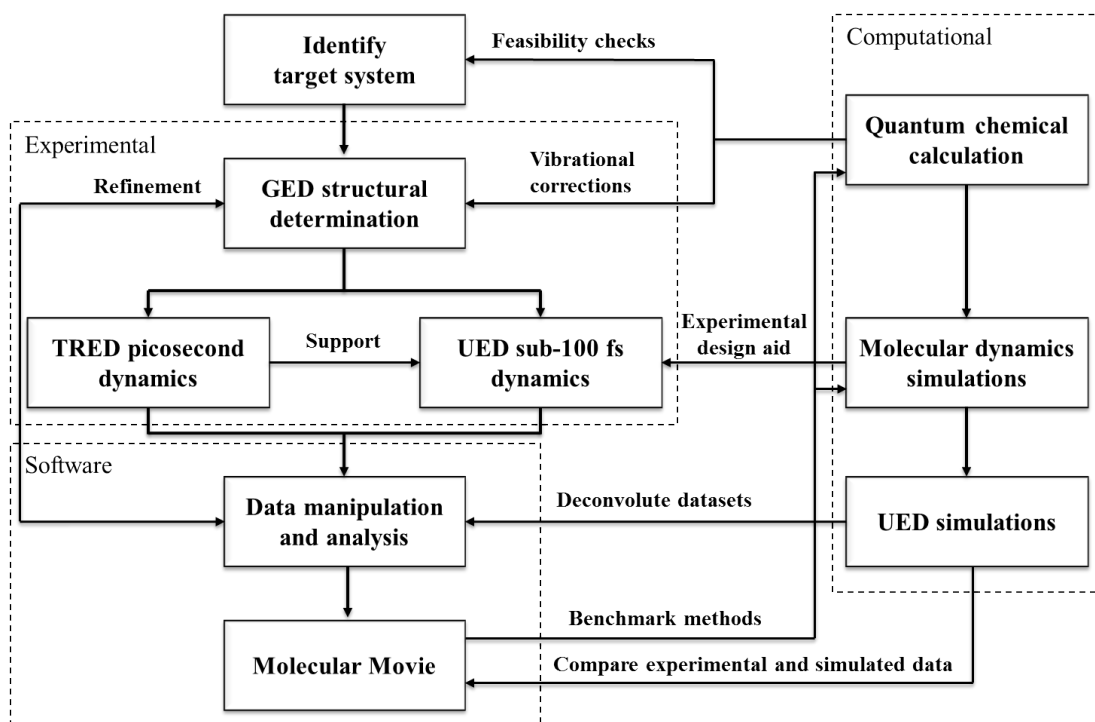


Figure 1.13: Diagrammatic representation of the roadmap to molecular movies.

The first step towards recording a molecular movie is the selection of a suitable target sample, a process that usually starts with the identification of fast molecular motions through time-resolved spectroscopy and/or computational studies. Potential energy surface (PES) scans and molecular dynamics (MD) simulations can also be used to investigate the timescales and motions of interest, as well as to assess experimental feasibility in the context of diffraction. Systems deemed suitable for TRED studies are allowed to enter the experimental section of the roadmap, in which GED studies are used to determine time-averaged ground-state structures, helping to define a before-excitation baseline. Being relatively inexpensive, these studies are used to optimise experimental parameters such as exposure time, sample delivery, and gas density. GED studies can also be used as a diagnostic tool in TRED experiments. TRED studies use pulsed electron beams to capture molecular motions with picosecond temporal resolution, projecting structural information recorded using GED into the time domain. Ahead of these experiments, preliminary quantum chemical calculations and MD simulations, are used to predict the optimum excitation wavelength, observation window, and experimental timescale. In the event of molecular motions being faster than the temporal resolution of the TRED apparatus, either identified through the detection of motion blur in datasets or from MD simulations, the system is flagged as a potential candidate for UED studies using MeV electrons. Typically carried out at large central facilities, UED studies tend to depend on beam-time allocation, subject to competitive application processes, and approval by scientific and feasibility panels. The experimental track record from GED and TRED studies and the theoretical support of MD simulations can be used to facilitate this process. UED studies focus on the imaging of motions outside of the scope of TRED, *i.e.* timescales between 100 and 1000 fs. The experimental investigation of the internal conversion dynamics of 1,2-dithiane, presented in Chapter 5, illustrates the importance of experiment complementarity in the study ultrafast motions. Purpose-built software packages, discussed in Section 3.5, are used to extract time-dependent data from TRED and UED experiments and compare the output to simulated datasets from MD simulations. To differentiate between ground-state and excited-state dynamics, data from GED studies are used to deconvolute diffraction data and facilitate the identification of time-dependent signals. The resulting dataset is then dimensionally reduced to an ensemble of time-

dependent interatomic distances used to reconstruct molecular motions. Therefore, molecular movies are, at least in the context of electron diffraction, expressed as one-dimensional projections of three-dimensional motions onto time-dependent distance matrices, providing us with an unprecedented insight into molecular motions.

In this thesis, contributions to instrument and software development are accompanied by the experimental and computational investigation of four case studies – 4-(*N,N*-dimethylamino)benzonitrile, 1,2-dithiane, 1,2-dithiolane-4-carboxylic acid and 1,2-dibromotetra-fluoroethane – showcasing the role of each building block of the roadmap in the study of molecular dynamics. A brief introduction on the scientific relevance of these studies can be found in Section 1.7.

1.7 Case studies

1.7.1 Study of the ground-state structure of DMABN

In the field of photochemistry DMABN, shown in Figure 1.14, is known as a staple system for the study of dual fluorescence,¹⁰¹ as it fluoresces at two different energies depending on temperature and solvent polarity.¹⁰² In polar solvents the DMABN fluorescence spectrum is dominated by the locally excited (LE) band, whereas, in the presence of apolar solvents, this dominance is shifted to the lower-energy intramolecular charge transfer (ICT) band. DMABN has been found to non-adiabatically relax to its S_1 state 25 fs after excitation. In the S_1 state, a much slower adiabatic equilibration process dominates, twisting DMABN towards two S_1 minima, referred to as S_1 -LE and S_1 -ICT. The dimethylamino group, which is coplanar with the phenyl moiety in S_0 -DMABN, twists to 150° and 90° to access the S_1 -LE and S_1 -ICT minima, respectively.¹⁰³ Despite extensive spectroscopic and computational studies, the DMABN relaxation mechanism and associated molecular dynamics have not yet been unambiguously resolved, making it a potential candidate for future TRED studies.

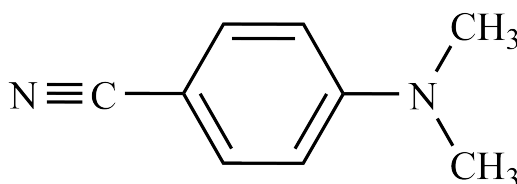


Figure 1.14: Molecular structure of DMABN.

In Chapter 4, the ground-state structure of DMABN in the gas-phase is studied using time-averaged GED, paving the way for future time-resolved studies. Moreover, experimental challenges encountered during this study, were overcome through the development of the sample delivery solutions presented in Appendix B, which were later implemented in both time-averaged and time-resolved electron diffraction apparatus.

1.7.2 Study of the internal conversion dynamics of 1,2-dithiane

Ubiquitous in nature, disulfide bonds have been found to play a key role in the adaptation and survival of proteins in hostile environments.^{104,105} In the extreme conditions of hot springs and hydrothermal vents, proteins use these disulfide bonds to retain their structure and functionality. Furthermore, disulfide bonds have been found to act as photochemical sinks, quenching harmful UV-induced fluorescence from tryptophan residues.¹⁰⁶ Commonly found as part of cyclic moieties in nature, these disulfide bonds are far more stable to heat and light than their acyclic counterparts. A simple model for such species is 1,2-dithiane, shown in Figure 1.15.

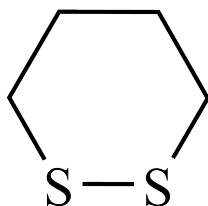


Figure 1.15: Molecular structure of 1,2-dithiane.

Illumination of 1,2-dithiane with mid-UV light has been found to produce transient $\cdot\text{S}-(\text{CH}_2)_4-\text{S}\cdot$ diradical species as a result of disulfide bond fission in the S_1 state. Along the S—S stretching coordinate, a minimal-energy conical intersection (MECI) allows S_1 -1,2-dithiane to return non-radiatively to its S_0 state. In the ground state, the S-termini can recouple and excess electronic energy is converted into vibrational energy and dissipated to the environment, giving 1,2-dithiane its apparent photostability.¹⁰⁷

Time-resolved mass spectrometric (TRMS) studies by the Sølling group have showed that S_1 -1,2-dithiane “rocks” between the S_1 minimum and the MECI, making multiple passes over the S_1/S_0 coupling region.¹⁰⁸ Stephansen *et al.* proposed a model in which a “wiggling” 1,2-dithiane carbon backbone causes the S-termini to

move past each other every 400 fs, according to the periodicity of the ion-current signal arising from the S–S internal coordinate.¹⁰⁹ Stephansen’s model used TRMS measurements and high-level quantum chemical calculations to infer S–S separation and resolve the relative motions of S-termini.¹⁰⁷

This thesis explores the internal-conversion dynamics of 1,2-dithiane from a structural point of view, using combination of MD simulations, GED and UED experiments to challenge our current understanding of this class of compounds. Moreover, the study of 1,2-dithiane will explore and test all aspect of the roadmap under real experimental conditions, as reported in Chapter 5.

1.7.3 Study of the photoinduced dynamics of asparagusic acid

The computational study of the photoinduced dynamics of asparagusic acid was designed to explore the impact of functional-group position and motion in the photostability of disulfide bonds. Asparagusic acid, shown in Figure 1.16, is a naturally occurring compound in asparagus – hence the name – consisting of a 1,2-dithiolane ring, functionalised at the *para* position by a carboxylic acid group.^{110,111} Asparagusic acid has been identified as a bio-photosystem precursor and its 1,2-dithiolane moiety is believed to be involved in primary photon trapping in photosynthesis.^{112,113} In aerobic organisms, asparagusic acid has been found to replace lipoic acid in the α -keto-acid oxidation steps of the Krebs cycle responsible for the synthesis of adenosine triphosphate.¹¹⁴ Despite its ubiquity in nature, and its importance to aerobic metabolism, little is known about the photostability and photochemistry of asparagusic acid.

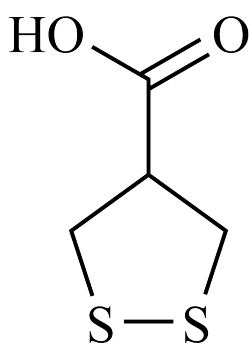


Figure 1.16: Molecular structure of asparagusic acid.

In this thesis, quantum chemical calculations and MD simulations (see Chapter 6), will be used to investigate the role of the carboxylic acid group in the ring-opening dynamics of asparagusic acid. The use of functional groups aims to mimic the sterics of the protein environment, believed to regulate the molecular dynamics of protein-active sites and promote photostability. Moreover, the computational study of asparagusic acid aims to showcase the roadmap's ability to predict molecular motions and assess the experimental feasibility of future TRED studies.

1.7.4 Study of the photodissociation of Halon-2402

The computational investigation of 1,2-dibromotetrafluoroethane, commercially known as Halon-2402 or Freon-114B2, was designed as a follow-up study to Zewail's TRED study of the iodinated analogue of Halon-2402, 1,2-diiodotetrafluoroethane.⁷⁵ Halon-2402, shown in Figure 1.17, was used as a fire suppressant, refrigerant, and leak detector in a wide range of industrial applications, until it was banned under the Montreal agreement in 1989. The ban on fluorocarbons (halons) was an attempt to reduce the concentration of bromine radical species in the atmosphere. On an atom-for-atom basis bromine was found to be nearly 100 times more destructive to stratospheric ozone than its better-known lighter neighbour, chlorine.¹¹⁵ Though banned nearly 30 years ago, Halon-2402 photoproducts still account for ~13% of all bromine detected in the tropical tropopause, the air mass responsible for troposphere-stratosphere exchange.¹¹⁶ From an environmental point of view the study of the photochemistry of Halon-2402, is still relevant today.

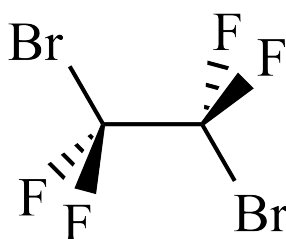


Figure 1.17: Molecular structure of Halon-2402.

In the presence of UV light in the stratosphere, Halon-2402 has been found to readily undergo C–Br bond fission, producing a monobromotetrafluoroethane radical and either a ground-state or excited-state bromine radical. Following this primary photodissociation, the radical fragment could, in some cases, have enough energy to induce a secondary C–Br bond fission, producing a second bromine radical and

tetrafluoroethene. In 2000, the relative branching ratios of primary and secondary photodissociation events were determined in a series of time-of-flight mass spectrometric (TOF-MS) experiments by Zou *et al.*¹¹⁷ Ten years later, a spectroscopic study by Reid *et al.* suggested a stepwise dissociation mechanism,¹¹⁸ corroborating the observation by Zewail *et al.* for Halon-2402 iodinated counterpart, C₂F₄I₂. These pioneering studies sparked the ultrafast community's interest in the photochemistry of this class of compound, hypothesising the existence of short-lived bridging photoproducts as part of this stepwise photodissociation mechanism.^{75,77} Although spectroscopic and computational studies on C₂F₄Br₂,¹¹⁸ and UED studies on C₂F₄I₂ have found no evidence of the formation of such species, ambiguities regarding the nature of the photodissociative mechanism and its products persist.⁷⁷

Chapter 7 of this thesis computationally explores the photodissociation of Halon-2402 using quantum chemical methods and MD simulations to understand better the UV-driven photochemistry of this class of compounds.

Chapter 2. Background theory

This Chapter introduces the concepts and theories underpinning the methods presented in the roadmap to molecular movies proposed in Section 1.6. The theoretical framework supporting the experimental studies in Chapters 4 and 5 is presented and discussed in Sections 2.1 to 2.2. In Section 2.3, the design features of the time-averaged and time-resolved GED apparatus are explored, contextualising the apparatus developments described in Chapters 3 (see Appendices B and C for more details).

2.1 Introduction to electron diffraction

2.1.1 Electron diffraction theory

The principle that electrons moving through a sample experience a change in momentum according to the charge gradient around the nuclei of the atoms in that sample, underpins all electron diffraction experiments. The numbers of electrons and protons in the atoms control the magnitude of this gradient, which, combined with the electron wavelength, dictates the degree of scattering observed. Therefore, heavy atoms are expected to diffract electrons more easily and have stronger diffraction signatures than their lighter, smaller counterparts. The wavelength of an electron probe can be calculated using the de Broglie equation (Equation 2.1):¹¹⁹

$$\lambda = \frac{h}{mv} , \quad \text{Eq. 2.1}$$

where h is Planck's constant, and m and v are the mass and speed of an electron, respectively. To model a beam containing electrons travelling close to the speed of light, a relativistic term is added to the electron velocity and mass, as shown by Equation 2.2:¹²⁰

$$\lambda = \frac{h}{\sqrt{2m_e eV \left(1 + \frac{eV}{2m_e c^2}\right)}} , \quad \text{Eq. 2.2}$$

where V is the accelerating potential, e is the electronic charge, c is the speed of light and m_e the mass of an electron. For a given scattering event the change in the momentum of the incident electron is expressed as the scattering vector, \mathbf{s} , illustrated in Figure 2.1.

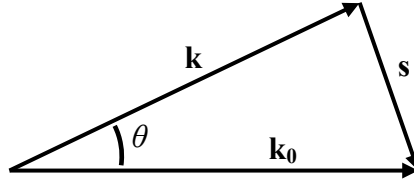


Figure 2.1: Illustration of change in momentum, \mathbf{s} , where \mathbf{k}_0 is the incident vector, \mathbf{k} is the scattered electron vector, and θ is the angle between them.

In GED experiments electrons are assumed to scatter elastically, and so it is reasonable to assume that the magnitudes of the incident, \mathbf{k}_0 , and scattered, \mathbf{k} , electrons are conserved, *i.e.* $|\mathbf{k}| = |\mathbf{k}_0|$. The magnitude of the scattered vector, $|\mathbf{k}|$, can be calculated using Equation 2.3:^{120,121}

$$|\mathbf{k}| = \frac{2\pi}{\lambda} . \quad \text{Eq. 2.3}$$

The trigonometric relationship shown in Figure 2.1 allows the scattering vector, \mathbf{s} , to be determined using Equation 2.4:

$$\mathbf{s} = \frac{4\pi}{\lambda} \sin\left(\frac{\theta}{2}\right) . \quad \text{Eq. 2.4}$$

To retrieve structural information from diffraction patterns, GED relies on a set of equations describing the relationship between interatomic distances in a molecule and the intensity of scattering as a function of the scattering vector.¹²² The most significant of which, the Wierl equation, was developed following Mark and Wierl's early attempts at interpreting diffraction data.⁶⁵ The scattering intensity, $I(s)$, at discrete s values can be calculated using Equation 2.5:

$$I(s) = \sum_i^N \sum_j^N F_i(s) F_j(s) \frac{\sin(sr_{ij})}{sr_{ij}} , \quad \text{Eq. 2.5}$$

where $F_i(s)$ is the scattering factor of atom i , and r_{ij} is the distance between atoms i and j . Therefore, Equation 2.5 implies two types of contribution to the overall scattering: molecular $i \neq j$ and atomic $i = j$, mathematically expressed in Equation 2.6:¹¹¹

$$I(s) = I_{\text{atomic}}(s) + I_{\text{mol}}(s) . \quad \text{Eq. 2.6}$$

The atomic scattering term, conceptually equivalent to Young's single-slit experiment, shown in Figure 2.2a, can easily be calculated and subtracted from the overall scattering intensity, allowing the more structurally relevant molecular scattering term to be extracted.⁶² This term can be conceptually related to Young's double-slit experiment shown in Figure 2.2b.

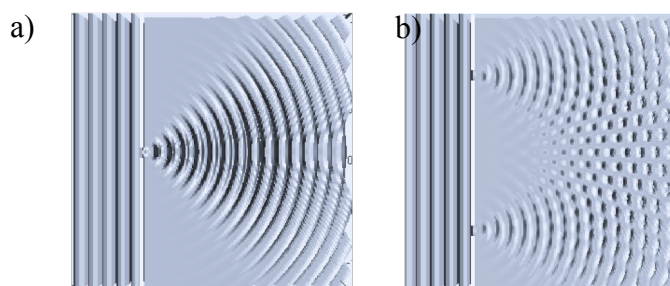


Figure 2.2: Schematic illustrations of Young's a) single-slit, and b) double-slit experiments. Adapted from Reference 123.

In both electron diffraction and Young's iconic double-slit experiments, waves diffracted from different scattering points (atoms or slits) interfere constructively and destructively, producing areas of higher and lower scattered intensity at the detector.¹²¹ Information about the size and spacing between scattering points can be determined from the interference patterns. In electron diffraction these patterns are typically recorded as two-dimensional intensity matrices, known as diffraction patterns (Figure 2.3a). The dimensional reduction of these diffraction patterns results in one-dimensional molecular intensity curves (MICs), an example of which is shown in Figure 2.3b.

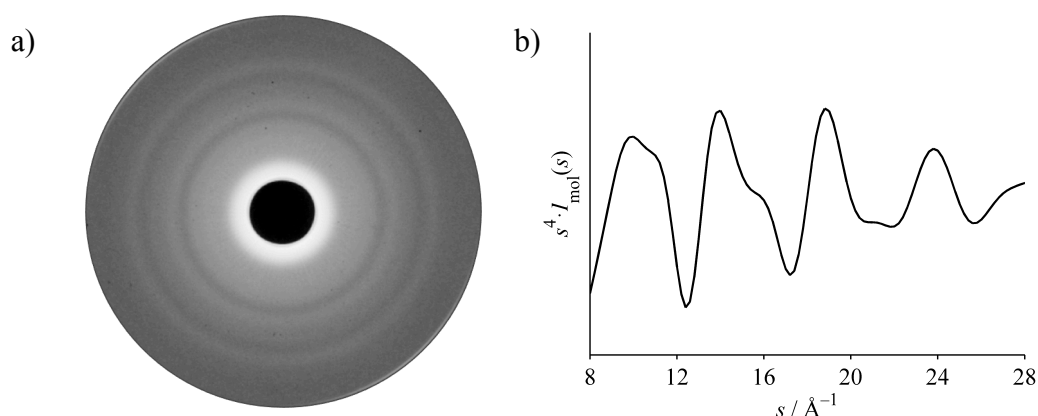


Figure 2.3: Example of a) a GED diffraction pattern, and b) an MIC for benzene, recorded during the commissioning of the York GED apparatus (see Section 3.1.2).

In a gaseous sample, the random orientation of molecules gives rise to a diffraction pattern consisting of diffuse concentric rings (Figure 2.3a), in contrast to the sharp diffraction spots observed in diffraction from single crystals, where molecules are oriented in a lattice.

The MIC used in GED structure determination can be mathematically represented as the sum of a series of sine functions (Equation 2.5), each accounting for the discrete scattering of a pair of atoms. A Fourier transform can, therefore, convert this sine-function series into a discrete set of interatomic distances.¹²⁰ Equation 2.7 shows the mathematical expression used to perform this operation:

$$\frac{P(r)}{r} = A \int_0^{\infty} \frac{s I_{\text{mol}}(s)}{|F(s)|^2} \sin(sr) ds, \quad \text{Eq. 2.7}$$

where A is a scaling factor, and $F(s)$ the scattering factor weighted according to the scattering cross-section magnitude of each atom. The inverse Fourier transform of GED data, in MIC format, yields a radial distribution curve (RDC), describing the relative probabilities of a certain interatomic distance, r , resulting in a scattering event, $P(r)$. Before Fourier inversion, data are multiplied by the damping function shown in Equation 2.8:

$$s \exp\left(\frac{-2 \times 10^{-5} s^2}{(Z_i - f_i)(Z_j - f_j)}\right), \quad \text{Eq. 2.8}$$

where Z_i and Z_j and f_i and f_j are the atomic numbers and scattering factors of two significant scatterers in the molecule, respectively. The intensities of the peaks in an RDC are proportional to the number of instances a given interatomic distance is present, and the scattering factors $[F(s)]$ of the atoms involved, and inversely proportional to r_{ij} .¹²⁰ Theoretical MICs and RDCs are generated from a computational model of the target molecule, built using geometric parameters, such as bond lengths, bond angles, and dihedral angles. These parameters are then varied using a least-squares refinement algorithm to achieve the best fit to the experimental data. An example of this refinement process, further discussed in Section 2.1.3, can be found in Chapter 4. The RDC, an example of which is shown in Figure 2.4, allows the GED data in Figure 2.3 to be visualised in a more intuitive format. Furthermore, comparing the experimental and theoretical RDC highlights which

interatomic distances are poorly described in the parameterised description of the molecule.

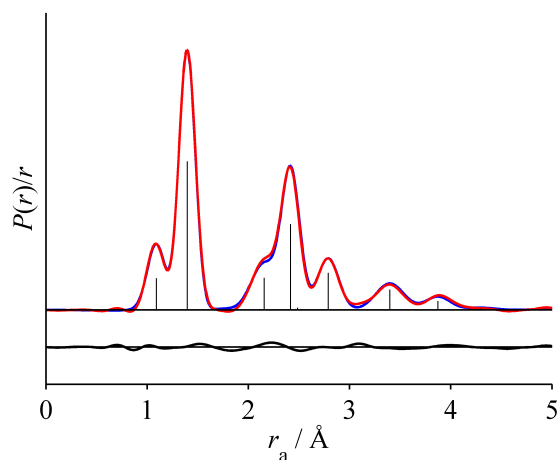


Figure 2.4: Experimental (red), theoretical (blue), and difference (experimental-minus-theoretical, black) RDCs obtained from the inverse Fourier transform of GED data for benzene.

2.1.2 Challenges in gas electron diffraction

To determine a molecular structure from electron diffraction data, the effect of molecular vibrations on the apparent geometry of a molecule must be taken into account. Molecules are dynamic species, constantly vibrating, in most cases with $3N-6$ vibrational modes (where N is the number of atoms in the molecule). In an electron diffraction experiment, regardless of whether a continuous or pulsed electron beam is used, each scattered electron will probe instantaneously the interatomic distance between a given atom pair. Therefore, the same atom pair will be probed multiple times at different points in its vibrational cycle, yielding an average interatomic distance (r_a), rather than an equilibrium distance (r_e). Formally, GED-determined distances, r_a , are defined as the inverse of the average inverse of the interatomic distance (r), as shown in Equation 2.9:

$$r_a = \left\langle r^{-1} \right\rangle^{-1} . \quad \text{Eq. 2.9}$$

This leads to the observation of the “shrinkage” effect, in which r_a appears shorter than r_e .^{124,125} In a linear triatomic, ABC, this “shrinkage” effect, schematically illustrated in Figure 2.5, causes the average distance A···C to appear shorter than AB+BC.

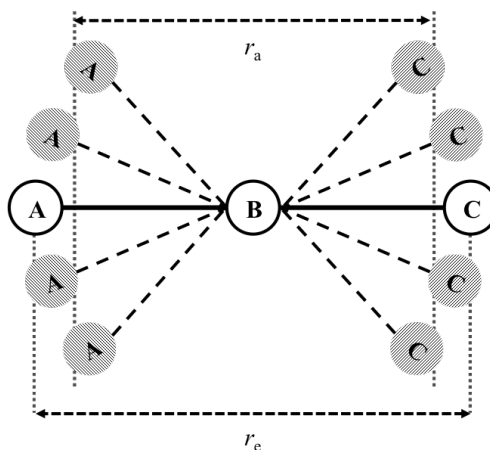


Figure 2.5: Illustration of the “shrinkage effect” resulting from the vibration of the linear triatomic ABC.

To account for the “shrinkage” effect, vibrational corrections are calculated from equations of motion coupled to force constants and applied to the GED structure, producing an approximate equilibrium structure, which can be meaningfully compared with structures derived from other experimental or theoretical methods. These vibrational force constants are usually calculated using *ab initio* methods and analysed using codes such as SHRINK¹²⁵ and VibModule.¹²⁶ The mathematical relationship between r_e and r_a is shown in Equation 2.10:

$$r_e - r_a \approx \frac{u^2}{r_a} - k - \delta A - \delta r, \quad \text{Eq. 2.10}$$

where u is the root-mean-square amplitude of vibration, k is the “shrinkage” correction for vibrational motions perpendicular to the interatomic vector (see Figure 2.5), and δA and δr are corrections for anharmonicity and centrifugal distortion arising from rotational motion, respectively. For simplicity, contributions from δA and δr terms to the overall correction are usually neglected, as these cannot be computed using the harmonic force-field methods in *ab initio* calculations. The perpendicular displacement, k , can be described using a rectilinear (implemented in the ASYM¹²⁷ code) or curvilinear (implemented in SHRINK¹¹⁶ code) approximation, leading to r_{h0} and r_{h1} solutions, illustrated in Figure 2.6. Based on a harmonic oscillator, first-order curvilinear distance corrections, mathematically described in Equation 2.11:

$$r_{\text{hl}} \approx r_{\text{a}} + \frac{u^2}{r_{\text{a}}} - k_{\text{hl}} \quad \text{Eq. 2.11}$$

are obtained from the SHRINK analysis of a set of calculated force constants. Although first-order curvilinear distance corrections are used in r_{hl} -type refinements to determine the majority of structures in GED, these have been found to describe poorly vibrations with large amplitudes as well as those that are particularly anharmonic. In these cases, the use of MD simulations provides an alternative. Various groups in the GED community,^{128–131} including the Wann group, have demonstrated the use of MD in the determination of corrections for molecules with large and anharmonic amplitudes of vibration.¹³² Moreover, in systems with freely rotating groups or with complex motions, MD simulations can be used to sample all potential motions, producing more complete corrections for use in the GED refinement.

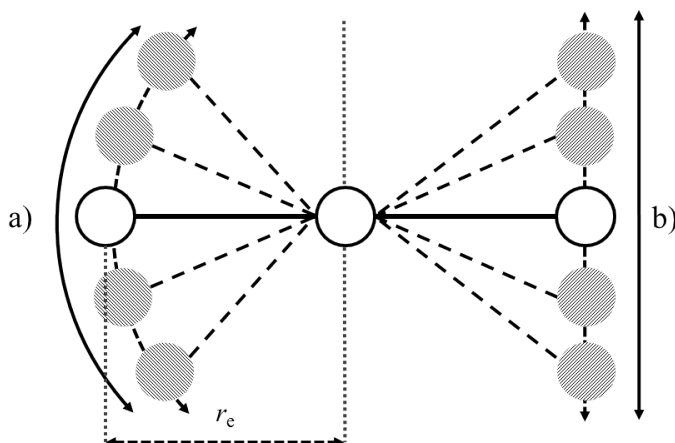


Figure 2.6: Illustration of the differences between a) curvilinear and b) rectilinear corrections.

In GED the three-dimensional structures of the target molecules are captured in one-dimensional MICs and thus, where interatomic distances are similar, they become difficult to differentiate from one another. In RDCs this is represented as clusters of interatomic distances under single peaks, resulting in the potential loss of structural information.

Another challenge associated with GED is that the area of a peak in the RDC, A_{RDC} , is proportional to the atomic number of the scattering centres involved, Z_i and Z_j , and

inversely proportional to the distance between them, r_{ij} , as show in Equation 2.12:^{125,133}

$$A_{\text{RDC}} \propto \frac{Z_i Z_j}{r_{ij}} . \quad \text{Eq. 2.12}$$

Therefore, hydrogen atoms are almost always poorly resolved in GED refinements.

Where insufficient data are available to solve the structure of a target molecule, additional information from sources other than GED can be used. An example of these externally aided refinement methods is STRADIVARIUS, which uses structural information from microwave spectroscopy and liquid-crystal nuclear magnetic resonance (NMR) to complement diffraction data.^{133–136} This approach allows the refinement of complex structures, despite the lack of information on light atoms and similar interatomic distances. On the other hand, the molecular orbital constrained electron diffraction (MOCED) method uses interatomic distances calculated using quantum chemical methods to constrain the refinement and improve structural accuracy.¹³⁷ The main disadvantage of the MOCED method is its inability to account for inaccuracies in *ab initio* calculations, relying too heavily on a single computational method. Built on the same principles as MOCED, the SARACEN method allows for theoretical parameters to be supplied to the refinement as flexible restraints.^{120,138} These restraints are derived from the ranges of values in a series of quantum chemical calculations using different methods and basis sets. In this approach, information aiding the refinement process does not rely on a single calculation, but rather in the wealth of quantum chemistry available. The SARACEN method revolutionised GED structure determination, allowing larger and more complex molecules to be studied. This synergistic relationship between theory and experiment has allowed both fields to thrive and its importance is no less relevant today, as illustrated by the roadmap in Chapter 1.

The GED study of molecules that exist in topologically shallow regions of the PES must be accompanied by a comprehensive exploration of the space surrounding the global minimum, as experimental temperatures might be sufficient to allow population to be distributed to neighbouring local minima, giving rise to multiple conformers. Therefore, relative conformer ratios must be described in the parameterised description of the molecule and taken into account in the refinement

process. *Ab initio* calculation can be used to determine the relative energies of stationary points on the PES and, using the Boltzmann distribution (Equation 2.13), determine the abundance ratio (N_i/N) for each conformer at the experimental temperature:¹³⁹

$$\frac{N_i}{N} = \frac{\exp\left(-\frac{E_i}{RT}\right)}{\sum_i \exp\left(-\frac{E_i}{RT}\right)}, \quad \text{Eq. 2.13}$$

where E_i is the relative energy of the conformer with respect to the minimum energy conformer, R is the gas constant, and T is the experimental temperature. In Chapters 6 and 7 this method is used to calculate the conformer ratios of asparagusic acid and Halon-2402. In GED refinements, conformer contributions are weighted according to the abundance ratio and adjusted to produce the best possible fit between theoretical and experimental data.

2.1.3 Structure determination in gas electron diffraction

In practical terms, the GED study of a system can be divided into four stages: recording of GED data, the theoretical study of molecular structure and associated vibrations, the building of a parameterised model, and the least-squares refinement.

Diffraction data are typically recorded at two nozzle-to-detector distances in order to sample both the narrower and wider parts of the diffraction cone and produce a more complete dataset, as shown in shown in Figure 2.7.

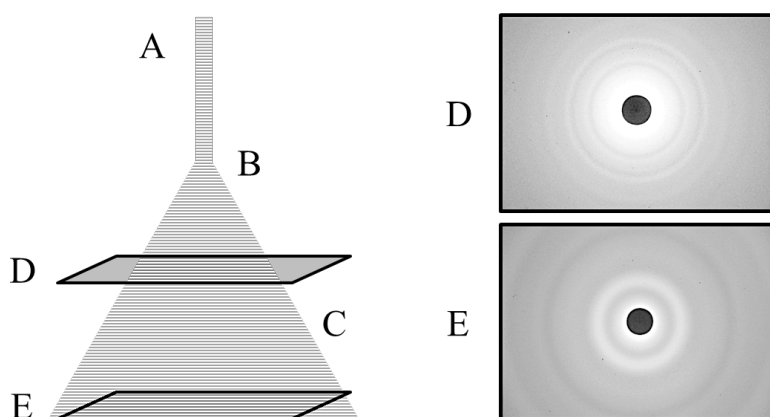


Figure 2.7: Schematic representation of the incident electron beam (A), interaction region (B) and diffraction cone (C), from where diffraction patterns are acquired at short (D) or long (E) nozzle-to-detector distances.

The narrow and wide scattering angles are recorded at the long and short nozzle-to-detector distances, respectively. The two nozzle-to-detector distances ensure the widest possible scattering-angle range, whilst preserving an overlap region between datasets. A selection of extraction packages, such as XPKG,¹⁴⁰ UNEX,¹⁴¹ and *XTRACT* (described in Section 3.5.1), transform diffraction patterns into MIC data, which can be used in the least-squares refinement process.

Ab initio calculations are routinely used to determine the equilibrium structures of the target molecules and calculate the force constants used in the “shrinkage effect” corrections. Equilibrium distances (r_e) determined from *ab initio* geometry optimisations are used as parameters in the model description of the target molecule. Vibrational corrections, required to produce approximate equilibrium structures from GED experiments, are generated from vibrational force constants computed in high-level *ab initio* frequency calculations. The methods and software packages used to carry out these theoretical studies are discussed in Section 3.5.

Target molecules are described as parameterised models, typically coded in FORTRAN, and written in terms of the trigonometric relationships between distances and angles in the molecule. These models can also be used to describe periodic rotations of functional groups, conformer abundance ratios, and the presence of any decomposition products in the sample.

At the beginning of the refinement routine, experimental data – multiple exposures at both short and long nozzle-to-detector distances – are scaled and combined to produce a single MIC dataset. The simulated scatterings from each pair of atoms described in the geometric model are used to generate a theoretical diffraction curve. The simulated and experimental diffraction curves are compared and parameters in the model are refined in a stepwise manner using a least-squares method, until the best fit is achieved. Restraints calculated from data external to electron diffraction (“non-ed”) – *ab initio* calculation or other structural methods – are applied to refinable parameters, aiding the refinement process. Amplitudes of vibration associated with interatomic distances under the same peak in the RDC are tied to the amplitude with the largest area and refined. After each refinement cycle, experimental and simulated MICs are compared and the goodness-of-fit reported as R_G and R_D factors.¹⁴² A comprehensive description of these refinement parameters can be found in Reference 142. A successful structure refinement should achieve an

R factor below 10% without breaking the restraints imposed on the parameters. Several least-squares refinement software packages have been developed to retrieve structural information from GED data; among the most widely used are KCED,¹⁴³ UNEX,¹⁴⁴ and ED@ED.¹⁴⁵ An example of GED structure refinement using ED@ED can be found in Chapter 4.

2.2 Introduction to time-resolved electron diffraction

In traditional GED experiments, molecular structures are determined using continuous electron beams, typically produced using thermionic emission from a tungsten filament. In these time-averaged experiments, dynamic information on molecular motion is lost. In modern TRED, the use of short electron pulses produced by light-driven photocathode electron guns allow dynamic information to be retained, resulting in the capture of molecular structures with sub-picosecond temporal resolution. Many processes and mechanisms in chemistry are mediated by structural rearrangements often involving molecules in the excited state. Therefore, TRED uses an optical pump to photoexcite target molecules into these excited states, inducing structural changes. Most TRED apparatus, including the one at York (see Section 3.2), use a single ultrafast laser system both to drive photoelectron emission at the electron gun and to pump the sample, keeping the probe and pump beams inherently synchronised. Modern optical parametric amplifiers (OPAs) allow the pump wavelength to be tuned, typically between 189 nm and 20 μm for Ti:Sapphire laser systems.¹⁴⁶ TRED datasets, acquired as series of diffraction images, are extracted and transformed using sophisticated software tools (see Section 3.5), before being combined with simulations to produce the molecular movies.

To capture molecular motion on the sub-picosecond timescale, one must first overcome the challenges associated with the scarce nature of scattering events and the instability of pulsed electron sources. In Section 2.2.1, challenges and limitations associated with the temporal broadening of electron bunches, the velocity-mismatch between probe electron and pump laser beam, and source time-jitter are presented in the context of the experimental scope of TRED. Recent technological developments in accelerator technology, briefly described in Section 2.2.2, have allowed TRED to overcome electron-bunch broadening effects and enter the sub-100 fs domain. In Section 2.2.3 limitations inherent to the nature of time-dependent diffraction data will be presented.

2.2.1 Challenges in time-resolved electron diffraction

In an electron beam, continuous or pulsed, the majority of electrons ($\sim 99\%$)¹²² will not scatter from a gas-phase sample; instead they pass directly through without interacting. Beam studies in UED apparatus have revealed that for a 1.6 fC electron beam (equivalent to 10^4 electrons per pulse) probing a molecular beam containing 10^3 molecules per cm^3 , ten electrons or fewer are expected to scatter elastically.¹⁴⁷ Therefore, the success of TRED experiments is strongly dependent on the brightness of electron sources and the efficiency of the detectors used. TRED employs two very different, yet complementary, strategies to overcome the poor SNR of diffraction datasets. The first one focuses on using high collection efficiency, high dynamic range detectors to improve the quality of diffraction patterns and minimise information loss. The range of detectors currently available to TRED is further discussed in Section 2.3.3. An alternative, more cost-effective, approach uses image post-processing algorithms to detect and then remove or correct imperfections in the data, boosting the signal levels, discussed in Section 3.5. These software-based solutions borrow concepts used in astrophotography to minimise the impact of detector-induced noise on the quality of data.

The main challenge in generating pulsed electron beams for diffraction is the preservation of temporal resolution. In photodriven electron guns (see Section 2.3.1), electrons are produced with a temporal profile similar to that of the incident laser.^{74,148} In most cases, this temporal profile is Gaussian shaped with a full-width-half-maximum (FWHM) of a few hundred femtoseconds. The number of electrons per pulse is kept above 10^4 to ensure that the diffraction pattern SNR is above the Rose criterion, which states that an SNR of at least 5 is needed to unambiguously distinguish features in an image.¹⁴⁹ At the high charge densities required to perform TRED experiments, the repulsion forces between electrons confined to such a small volume are enough to broaden the temporal and spatial profiles of pulses. Inside an electron bunch Coulombic repulsion accelerates electrons at the front of the bunch, whilst decelerating electrons at the back.¹⁵⁰ Present throughout the propagation lifetime of an electron pulse, these two effects induce a linear chirp (see Figure 2.8), stretching the bunch along the direction of travel, hence increasing the pulse duration. This phenomenon, known as space-charge repulsion, is responsible for the degradation in the temporal resolution of most TRED experiments.¹⁵¹ As pulses

become longer than the timescales of the motions being probed, the likelihood of the structures sampled by electrons at the front of the pulse being significantly different to those sampled by electrons at the back of the pulse increases. In practical terms, space-charge effects result in the motion blurring of TRED data and loss of structural information. Ingenious electron-gun designs, developed to mitigate the detrimental effects of temporal broadening, are presented briefly in Section 2.2.2.

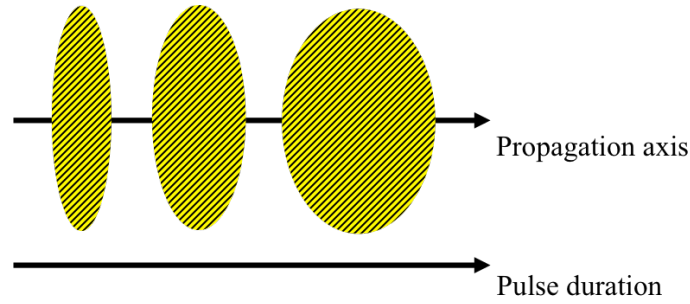


Figure 2.8: Schematic representation of linear pulse chirping in a non-relativistic electron bunch. Adapted from Reference 152.

The temporal resolution of TRED experiments using non-relativistic electrons is limited by the mismatch in pump and probe velocities.⁷³ In apparatus using direct current (DC) electron guns, such as the TRED apparatus at York, the velocity of an electron in the beam is described by Equation 2.14:

$$v_e = c \sqrt{1 - \left(1 + \frac{eV}{m_e c^2}\right)^{-2}}, \quad \text{Eq. 2.14}$$

where e is the electronic charge, V is the accelerating potential, c is the speed of light, and m_e is the mass of an electron. Equation 2.14 shows that, at a potential of 100 kV (typical working range of DC electron guns), electrons are accelerated to ~55% of the speed of light. This expression also shows that electrons cannot travel at the speed of light, regardless of the accelerating potential applied. In order to overcome this limitation, one must first understand how velocity mismatch affects TRED experiments. Figure 2.9 illustrates the interaction cross section between a pump laser beam, a molecular beam, and a probe electron beam.

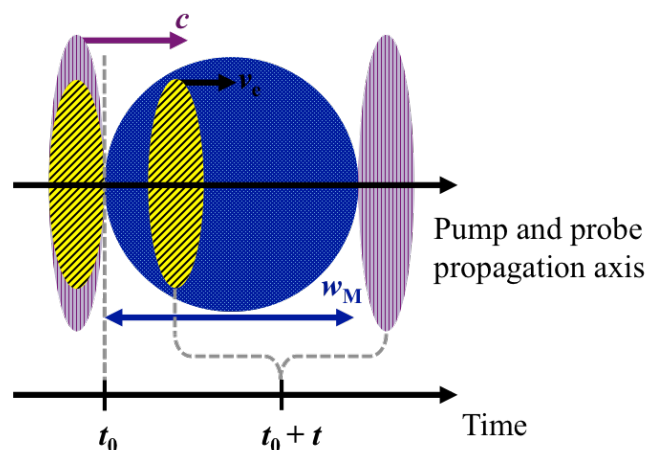


Figure 2.9: Schematic representation of the interaction region between the pump laser (purple vertical lines) and probe electron beam (yellow diagonal lines) passing through a molecular beam sample (solid blue). Adapted from Reference 152.

The discrepancy between the speed of light, c , and the velocity of the electrons, v_e , causes the electron pulse to lag behind the faster moving laser pulse as both pulses pass through a sample. The resulting time delay between the arrival of the pump and probe pulses inside the molecular beam limits the ability to probe a well-defined structure, as electrons encounter molecules at different points in their excited-state landscape.¹⁵² The simplest solution to this limitation involves reducing the molecular beam diameter using increasingly narrow apertures to skim excess beam diameter, thus minimising the impact of velocity mismatch at the expense of sample density. Alternatively, Baum and Zewail *et al.* proposed the use of a tilted-wavefront pump laser to increase the path length through the sample, and compensate for the velocity mismatch.¹⁵³ This elegant solution is illustrated schematically in Figure 2.10. The wavefront tilt, θ , at which the velocity component of the pump beam along the probe axis of propagation matches that of the electron beam, can be calculated using Equation 2.15:

$$\theta \approx \arccos\left(\frac{v_e}{c}\right). \quad \text{Eq. 2.15}$$

The velocity mismatch of a 100 keV electron beam is minimised at a pump wavefront tilt angle of 57° .¹⁵⁴ The UED apparatus at SLAC accelerates electrons to $\sim 99\%$ of the speed of light, and therefore only needs a 3° wavefront tilt to ensure the best possible overlap between pump and probe beams.¹⁵⁵

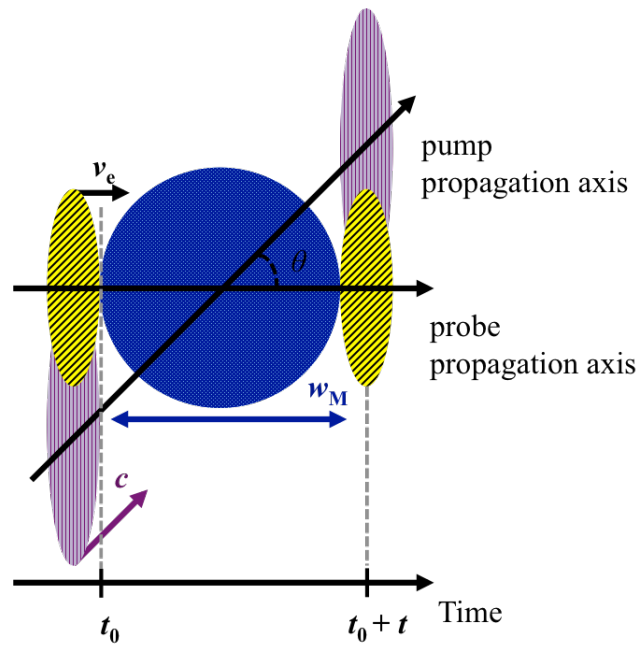


Figure 2.10: Schematic representation of the interaction region between the tilted wavefront pump laser (purple vertical lines) and probe electron beam (yellow diagonal lines) passing through a molecular beam sample (solid blue). Adapted from Reference 152.

In principle, the temporal resolution of a wavefront-tilted TRED experiment is dictated by the combined pulse durations of its pump and probe beams, assuming that, at time zero, they arrive at the sample simultaneously. However, under experimental conditions this assumption breaks down, as small changes in the laboratory environment strongly affect the arrival of the pump and probe beams at time zero, resulting in a time jitter. The main sources of time jitter in TRED experiments are inconsistencies in the nozzle timing and duty cycle, deformations in the laser path, and instabilities in the electron gun accelerating potential. Drifts in laboratory temperature and humidity have been found to significantly impact the stability of ultrafast laser sources and deform the shape of laser tables, inducing optical path deformations. Moving at the speed of light, a 0.1 mm deformation in optical pathway can result in over 300 fs of timing jitter. The detrimental effect of laser-timing-induced time jitter are minimised in climate-controlled laser laboratories (stable within 0.1 °C) and through the use of humidity-controlled enclosures. Time jitter associated with the probe electron beam, is dependent on both the timing stability of the drive laser and the homogeneity and stability of the accelerating field. In DC and RF electron guns, timing jitter is usually attributed to power instabilities

in the output from the high-voltage power supply and the klystron, respectively.¹⁵⁶ In special cases, external magnetic fields from nearby NMR instruments or solenoid-operated machinery can also disturb the flight path of electrons, increasing time jitter. In electron guns using RF bunch compressors, the arrival time of electron bunches at the sample is conditioned by the power, timing, and shape of the RF pulse used. These apparatus are usually fitted with timing tools, such as streak cameras,⁹⁶ which allow data to be time-stamped and resorted in post-processing.¹⁵⁵

2.2.2 Overcoming temporal broadening in TRED

Over the years, research groups in the fields of injector physics, particle acceleration, and electron diffraction have designed electron guns to overcome the limitations discussed in Section 2.2.1. Most modern electron guns employ one or more engineering solutions to minimise, prevent, or reverse the effects of space-charge broadening.

The simplest solution to space-charge broadening involves the use of a compact electron gun. By minimising the distance between the electron source and the sample, compact electron guns do not allow the electron bunches enough time to expand. A compact electron gun apparatus, such as the apparatus at York (see Section 3.2), allows for picosecond temporal resolution to be achieved cost-effectively; its small dimensions make it particularly suitable to the university laboratory environment.³⁷ An alternative to the use of compact electron guns involves accelerating electrons to speeds comparable to that of light and using relativistic effects to reduce temporal broadening in electron bunches. In these relativistic electron guns, electrons are accelerated using 3-5 MeV potentials to ~99% the speed of light. TRED experiments using this type of electron gun can achieve sub-100 femtosecond temporal resolution. However, the physical dimensions and safety implications of operating these systems are often only compatible with large research facilities.

The pulse duration of both non-relativistic and relativistic electron bunches can be significantly improved by the use of RF bunch compressors. These use RF modulations to induce a negative chirp in the freely expanding electron bunches, effectively reversing the effects of space-charge broadening.^{78,157} As an electron bunch enters the RF cavity, an oscillating electric field causes electrons at the front of the pulse to slow down, whilst the electrons at the back of the pulse are allowed to

catch up. The sudden deceleration of electrons at the front of the bunch results in a pulse compression along the propagation axis and a net gain in temporal resolution. RF bunch compressors are, in principle, capable of generating bunches shorter than 100 fs.¹⁵⁸ However, time-jitter events upstream of the cavity can cause electrons to arrive out of phase with the compression cycle, resulting in pulse elongation rather than compression.

2.2.3 Challenges in data analysis

Modern TRED apparatus can achieve sub-200 fs temporal resolution and record time-dependent diffraction signals well above background-noise levels. In the last decade developments in ultrafast lasers, accelerator structure, and detector technologies have expanded the experimental scope of TRED studies towards faster and more complex systems. However, the complex nature of time-dependent diffraction data has remained the biggest challenge in TRED. In addition to the loss of information associated with capturing three-dimensional information in one-dimensional datasets, discussed in Section 2.1.2, TRED data are convoluted further by temporal resolution of the apparatus used. Several data analysis routines and algorithms have been developed to disentangle these complex datasets into their structural components. Most of these software-based solutions take advantage of the synergistic relationship between experimental and computational results to deconvolute experimental data and extract dynamic information from TRED data. Examples of the data analysis algorithms used in the analysis of TRED data can be found in Section 3.5.

2.3 Summary in apparatus design

In the electron diffraction community, apparatus tend to be custom-built to overcome a specific experimental limitation or to address the challenges of a particular research topic. However, many features of apparatus design are ubiquitous, and so worth discussing in Sections 2.3.1 to 2.3.3.

2.3.1 Electron gun

Borrowed from the field of electronics, the term electron gun is applied to any accelerating structure capable of producing a narrow, collimated beam of electrons.

In time-averaged GED experiments, continuous electron beams are generated *via* the thermionic emission of electrons from a hot filament. Typically made out of

tungsten, this filament behaves as the cathode in a “triode system”, shown in Figure 2.11. The charge and shape of the electron beam is controlled by the position and potentials applied to the elements of the accelerating structure. The triode gun design is by far the most commonly used in GED.¹⁵⁹

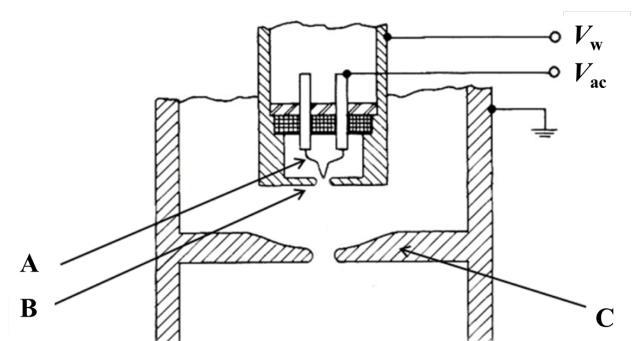


Figure 2.11: Schematic representation of the filament (A), the Wehnelt cylinder (B), and (C) the anode geometry in a triode electron gun. Adapted from Reference 159.

The two most common electron sources in TRED are the DC and RF electron guns. DC electron guns use a fixed potential to accelerate electron bunches produced by photo-ionisation of a metal-film cathode. These photoelectrons are accelerated over a few millimeters and directed towards the sample, usually placed a few centimeters from the source. The repetition rate, charge, and profile of the electron beam are controlled by the Ti:Sapphire ultrafast laser system driving the photoionisation process. Often made out of gold or copper, photocathode targets can be shallow-angle or retro-illuminated, depending on the apparatus geometry.^{73,153} DC electron guns operate with potentials of between 50 and 300 kV at repetition rates of between 1 and 5 kHz. A schematic diagram of a retro-illuminated DC electron gun, similar to the one installed in the TRED apparatus at York, is shown in Figure 2.12.

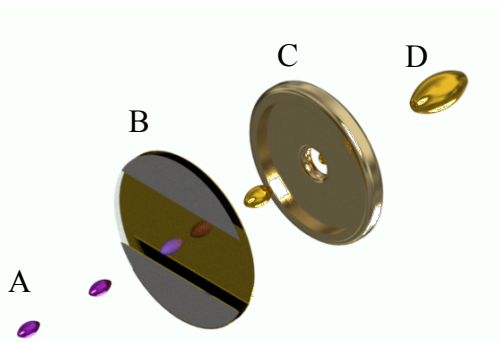


Figure 2.12: Schematic representation of a DC electron gun showing the drive ionisation laser pulse (A), the photocathode (B), the anode (C), and the expanding electron bunch (D).

Though cost-effective, DC electron guns are inherently limited to temporal resolutions of a few hundred femtosecond. In Section 2.2.2, klystron-powered MeV RF electron guns are presented as a possible solution to this limitation. These accelerate electrons to relativistic velocities and, depending on the RF phase used, compress the electron bunches simultaneously. MeV RF electron guns are classified as radiation-controlled accelerating structures and require large radiation-rated enclosures to stop the large amounts of X-rays generated. The UED study of 1,2-dithiane, presented in Chapter 5, was carried out using an MeV RF electron gun.⁴¹ A schematic representation of an angle-illuminated RF electron gun is shown in Figure 2.13.

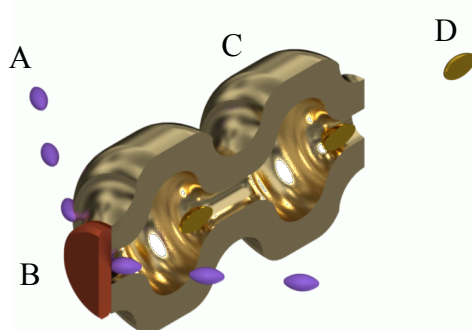


Figure 2.13: Schematic representation of an RF electron gun showing the drive ionisation laser pulse (A), the photocathode (B), the RF cavities (C), and the electron bunch (D).

2.3.2 Sample delivery

In principle, electron diffraction is capable of probing molecules in all states of matter. However, the technique is particularly well suited to the study of samples where a thin interaction region can be established, such as molecular beams and thin solids. Electron diffraction is often associated with the study of molecules in the gas phase, perhaps as a result of the poor performance of X-rays to determine gas-phase structures. In this section the most widely used nozzle designs in GED and TRED are described.

In traditional GED, gaseous samples are introduced into the electron beam path using an effusive nozzle. Typically mounted as close as possible to the electron beam, these nozzles allow molecules to enter the interaction region having experienced relatively few collisions. For this reason, effusive nozzles do not impact the temperature of the sample, which results in very broad Boltzmann distributions

of states. To increase the range of systems studied using GED, these nozzles are routinely fitted with heating elements, which allow samples with low vapour pressures to be delivered to the electron beam. Furthermore, heated nozzles allow otherwise inaccessible conformations to be studied using GED.¹⁶⁰

In TRED experiments the use of pulsed electron beams, and the need to keep background pressures low, favours the use of pulsed nozzle systems. Typically driven by solenoid or piezo actuators, these nozzles are triggered using the drive laser signal-delay-generator (SDG) to ensure synchronicity and temporal overlap between pump/probe and molecular beams. The pressure in the transport line backing the nozzle causes the molecular beam to undergo supersonic expansion. At the nozzle orifice, molecules are forced to collide with each other before entering the low-pressure environment of the diffraction chamber, homogenising the velocity distribution of molecules, and lowering their temperatures.¹⁶¹ Although rare, TRED experiments have been carried out using effusive nozzles, either as a result of the lack of commercially available high-repetition rate (> 1 kHz) pulsed nozzles or due to nozzle-drive stability difficulties.

2.3.3 Detector

Early GED experiments used photographic films or image plates to record diffraction patterns. However, the majority of electrons passing through the sample do not scatter, and the few that do have very small scattering angles, resulting in large radial intensity gradients in the diffraction patterns. Left uncorrected this intensity gradient results in oversaturated or washed-out diffraction patterns and the loss of structural information. To improve the dynamic range of the detector and prevent detector saturation, mechanical filters, known as rotating sectors,¹⁶² were used to partially block the detector and compensate for the intensity gradient in diffraction data. In the York GED apparatus this technology is still routinely used to acquire diffraction data, see Appendix B.

The advent of silicon-based photon detectors marks the start of a new era in electron detection technology. The painstaking developing of photographic films or scanning of image plates, is giving way to the online viewing of diffraction patterns, recorded using CCD detectors optically coupled to terbium-doped gadolinium oxysulfide (GdOS:Tb) scintillators. An apodising filter, placed between the scintillator and the CCD chip, acts as a virtual rotating sector, keeping diffraction intensities within the

operating range of the detector. In order to record diffraction data with quality comparable to that of photographic film, CCD detectors must achieve high dynamic ranges with low read-out noise.

Modern electron diffraction experiments have taken CCD detector technology one-step further, with the use of electron-multiplying CCD (EMCCD) chips. These high-efficiency detectors represent the state-of-the-art in optical imaging technology.¹⁶³ On the other hand, complementary metal-oxide semiconductor (CMOS) technology offers a more cost-effective alternative to CCD chips, albeit with lower image quality.¹⁶⁴ Built on CMOS technology, direct detection devices (DDD) have been shown to capture virtually noise-free diffraction patterns. Proven in the emerging field of cryo-electron microscopy, DDD detectors, also known as direct electron detectors (DEDs), are expected to revolutionise data collection in electron diffraction, achieving unprecedented signal-to-noise ratios.¹⁶⁵ A prototype DED is currently being tested on the UED apparatus at SLAC.¹⁶⁶

Chapter 3. Methods

The roadmap presented in Section 1.6, uses a combination of experimental, computational and software tools to explore the structural dynamics of molecules in the gas-phase. In this Chapter, the methods and instruments designs underlying the methodology proposed in the roadmap are introduced. Sections 3.1 to 3.3 introduce the instruments used to record the time-averaged and time-resolved structural information discussed in Chapters 4 and 5, and, where applicable, the results of instrument calibration and optimisation studies carried out as part of this project will be presented. In Section 3.4, the role of computational chemistry in the study of structure function relationships will be discussed. Special emphasis will be placed on how one might use the wealth of computational approaches available to overcome experimental limitations and complement electron diffraction studies. Moreover, Section 3.4 introduces the methods employed in the computational exploration of the case studies presented in this thesis, and discusses their suitability. Section 3.5 is dedicated to the presentation of the software tools developed throughout my PhD project to extract, visualise and interpreted the result of computational and experimental studies.

3.1 Gas-phase electron diffraction at York

The Wann group has two continuous-beam time-averaged GED instruments in York: the telefocus electron gun GED apparatus, brought from the University of Edinburgh in 2013, and the GED apparatus formerly housed at the University of Reading. The latter was brought to York in the autumn of 2015 and renamed the York GED apparatus. A significant part of my PhD was dedicated to the assembly, repair, and upgrade of the York GED apparatus. Diffraction data recorded during the York GED apparatus commissioning, discussed in Section 3.1.2, were used to train and test the data handling and extraction routines at the core of the data analysis packages presented in Section 3.5.

3.1.1 York GED apparatus overview

At the University of Reading, David Rice and Elizabeth Page used the then-Reading GED apparatus to determine the ground-state structures of a wide range of metal complexes and small organic molecules, publishing dozens of papers on GED-refined structures in the 1990s and 2000s.^{167–174} Following a thorough overhaul of its

vacuum system and modernisation of its electronics, the apparatus was brought back online in 2016, making it the only working GED apparatus in the UK. The apparatus is shown in Figure 3.1 and consists of three vertically stacked modular sections, referred to as the column, the chamber, and the detector modules, housing the electron gun, nozzle system, and detector assembly, respectively. A detailed description of these modules can be found in Appendix B.

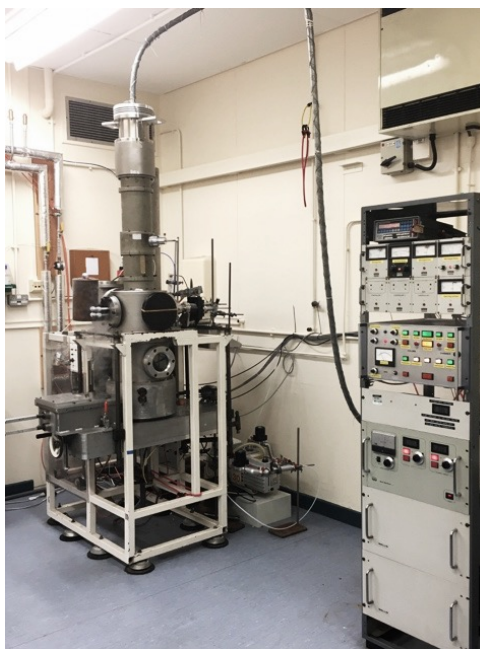


Figure 3.1: Photograph of the York GED apparatus.

3.1.2 Apparatus commissioning

In the spring of 2016, following the replacement of the tungsten filament and the realignment of the electron gun geometry, the apparatus produced its first electrons at York. With stable electron emission restored, the quality of the electron beam was optimised based on the qualitative assessment of its shape and brightness as viewed on a retractable scintillator, described in Appendix B. To confirm that data recorded using the York GED apparatus were of refinable quality, the structure of benzene, a common calibration sample in GED, was investigated.¹⁷⁵

Benzene was acquired from Sigma-Aldrich and delivered to the electron beam using an effusive nozzle (details on the nozzle assembly can be found in Appendix B). A voltage of approximately 42.2 kV was used to accelerate electrons, resulting in an electron wavelength of 5.85 pm. Data were recorded at nozzle-to-detector distances of 240.5 and 488.0 mm, referred to as short and long nozzle-to-detector distances,

respectively. A total of ten image plates were recorded, five for each nozzle-to-detector distance, and digitised using the Fuji BAS-1800 II flat-bed scanner. Figure 3.2 shows the diffraction patterns of benzene, recorded at the long and short nozzle-to-detector distances. Diffraction patterns were converted to scattering intensity curves using the purposely-developed extraction code *XTRACT* (see Section 3.5.1). These curves were corrected for the York GED apparatus rotating-sector and scaled to generate refinable MICs.

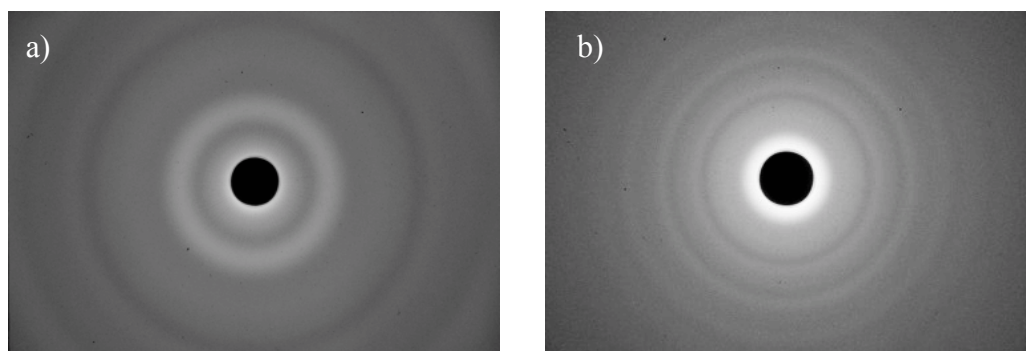


Figure 3.2: Scanned image plates showing the diffraction patterns of benzene at a) long, and b) short nozzle-to-detector distances.

GED data were analysed using the ED@ED v3.0¹⁴⁵ least-squares refinement program employing the electron scattering factors of Ross *et al.*¹⁷⁶ The structure of benzene was described using a D_{6h} -symmetric parameterised model based on the C–C and C–H bond lengths calculated at the CCSD(T) level employing correlation-consistent basis sets extrapolated to the complete basis set (CBS) limit. The suitability of these computational methods to GED refinements is discussed in Section 3.4.1 The parameterised model was refined to yield interatomic distances of the r_{hl} type (see Chapter 2). The refined geometric parameters and amplitudes of vibration for benzene are summarised in Tables 3.1 and 3.2. The success of the refinement, for which the R_G factor was 0.060, with an R_D factor (which ignores the off-diagonal elements of the weight matrix) of 0.052, can be gauged from the agreement between experimental and theoretical MICs and RDCs, shown in Figure 3.3. The least-squares correlation matrix and refined Cartesian coordinates for the GED-determined structure of benzene can be found in Appendix G.

Table 3.1: Refined (r_{hl}), theoretical^a (r_e), and literature^b geometric parameters and SARACEN restraints^b applied in the least-squares refinement of benzene. Distances are tabulated in picometers.

Parameter	r_{hl}	r_e	Lit. r_e
p_1 $r\text{C-C}$ (avg.)	139.60(3)	139.43	139.2
p_2 $r\text{C-H}$ (avg.)	108.7(2)	108.3	108.2

^a Obtained from an *ab initio* geometry optimisation at the CCSD(T)/CBS level; ^b Obtained from Reference 177.

Table 3.2: Selected interatomic distances (r_a), refined (u_{GED}), and theoretical^a (u_{hl}) amplitudes of vibration, and distance corrections (k_{hl}) for the GED refinement of benzene.

Atomic pair	r_a	u_{GED}	Restraint	k_{hl}	u_{hl}
u_1 C-H	108.6(2)	5.8(2)	7.5(8)	0.3	7.5
u_2 C-C	139.45(3)	5.6(1)	4.5(5)	0.1	4.5
u_3 C \cdots H <i>ortho</i>	215.3(1)	10.8(2)	9.8(10)	0.3	9.8
u_4 C \cdots C <i>meta</i>	241.68(5)	6.7(1)	5.5(6)	0.1	5.5
u_6 C \cdots C <i>para</i>	278.86(5)	8.6(2)	6.2(6)	-0.1	6.2
u_7 C \cdots H <i>meta</i>	339.9(2)	12.3(3)	9.4(9)	0.1	9.4
u_8 C \cdots H <i>para</i>	387.7(2)	10.1(4)	9.4(9)	0.1	9.4

^a Obtained from the SHRINK analysis of an *ab initio* vibrational frequency calculation at the CCSD(T)/cc-pVDZ.

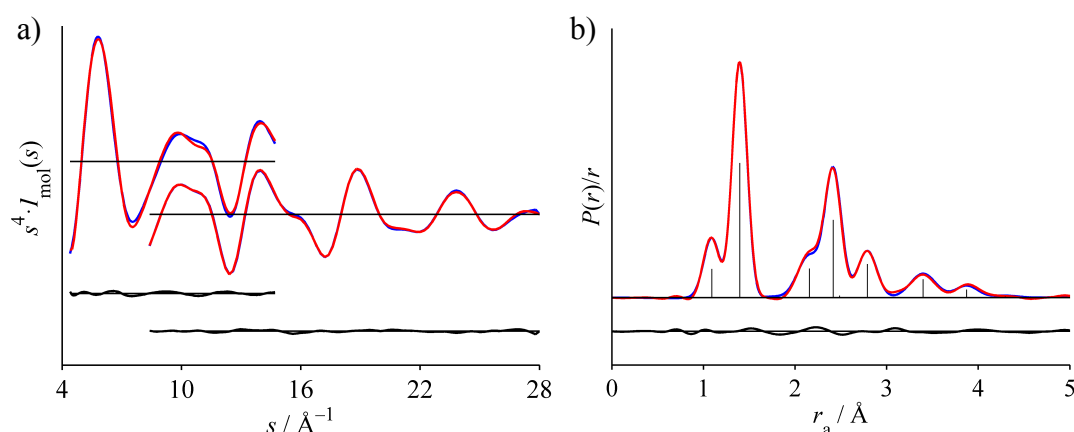


Figure 3.3: Experimental (red), theoretical (blue), and difference (experimental-minus-theoretical, black) a) MICs, and b) RDCs for benzene. The MICs for the long (top) and short (bottom) nozzle-to-detector datasets are offset. The overlap between the two datasets serves as an indicator of data quality. Experimental and theoretical MICs were multiplied by $s \cdot \exp(-2s^2 \cdot 10^{-5} / [(Z_{\text{C}} - f_{\text{C}})(Z_{\text{H}} - f_{\text{H}})])$ prior to Fourier inversion. f_{C} and f_{H} denote the atomic scattering factors for carbon and hydrogen taken from Reference 176.

The agreement between the interatomic distances of the experimental and theoretical equilibrium parameters testifies to the accuracy of the structural solution. The C–C and C–H interatomic bonded distances for benzene were determined to within 0.4 pm (0.3%) and 0.5 pm (0.5%) of the theoretical result, respectively.

The successful determination of the structure of benzene marked the end of the York GED apparatus commissioning, demonstrating that the apparatus is in perfect working condition and can be used to study more interesting systems.

3.1.3 The York GED apparatus scope

The York GED apparatus was given a new lease of life as a tool for the study of ground-state structures in the context of the roadmap proposed in Section 1.6. To further expand the scope of GED at York, and to ensure its contribution to future time-resolved studies, the York GED apparatus was fitted with an air-heated nozzle assembly designed to deliver samples with low volatilities, such as DMABN, to the gas phase. The GED study of DMABN, presented in Chapter 4, showcases the new experimental capabilities of the York GED apparatus.

In its current configuration, the York GED apparatus is a valuable tool for the determination of the ground-state structure of molecules in the gas phase, either as stand-alone time-averaged GED studies, or as support experiments for TRED studies at York and UED studies at SLAC.

3.2 Time-resolved electron diffraction at York

The Wann group time-resolved electron diffraction (TRED) apparatus, the first of its kind in the UK, was commissioned in 2014 at the York Centre for Laser Spectroscopy and Photochemistry. The TRED apparatus, described in detail elsewhere,^{37,178} was developed to address the needs of the photochemistry and dynamics community for time-resolved structural information. Furthermore, its modular construction allows operational parameters to be changed on the fly, facilitating instrument development and the exploration of new experimental methods. The apparatus is built around a 100 kV DC electron gun using the Department of Chemistry ultrafast laser system, the power and stability of which allows TRED experiments previously limited to large central facilities to be carried out using a university-based table-top apparatus. The versatility and cost effectiveness of the TRED apparatus, shown in Figure 3.4, has allowed the Wann

group to make advances in the field of TRED and develop experimental methods for TRED studies in the York and UED studies at SLAC.

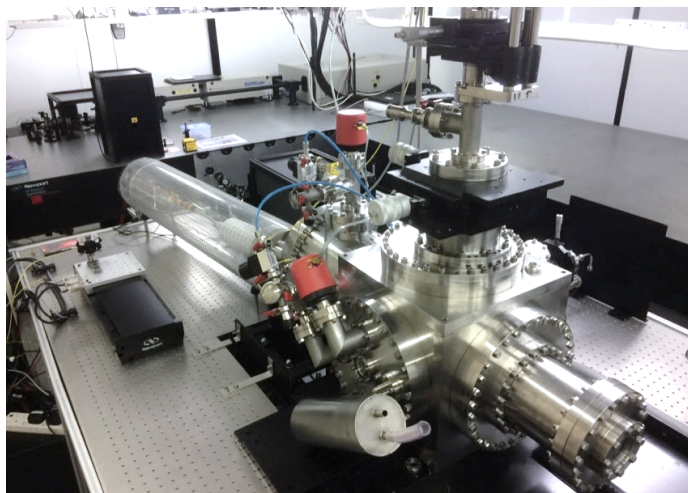


Figure 3.4: Photograph of the TRED apparatus at York.

The TRED apparatus consists of seven modules: the electron gun, the laser set-up, the electron beam optics, the sample delivery system, the detector module and the vacuum system, arranged according to the diagram shown in Figure 3.5. A detailed description of components and functionality of these modules can be found in Appendix C. In this Section apparatus calibrations, component optimisations, and design improvements, carried out as part of my PhD project, will be presented and discussed.

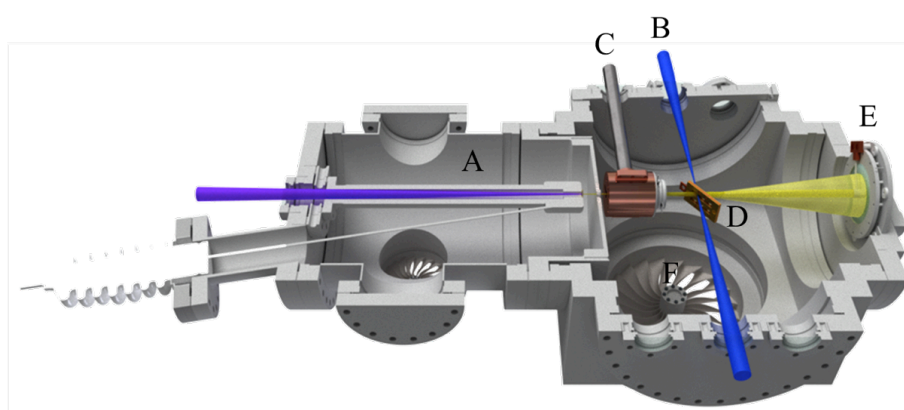


Figure 3.5: Diagrammatic illustration of the TRED apparatus showing the electron gun (A), the laser set-up (B), the electron beam optics (C), the sample delivery system (D), the detector module (E), and the vacuum system (F).

3.2.1 Electron beam characterisation

The charge and spatial profile of the electron beam greatly influence the quality of the diffraction data recorded. Therefore, a series of calibration experiments were carried out to ascertain the characteristics of the TRED apparatus electron beam. In this Section, the charge and full-width half-maximum (FWHM) of the electron beam are determined as a function of both drive-laser fluency and accelerating potential, using a Faraday cup (see appendix C), a Keithley picoammeter, and the translatable beam mask, shown in Figure 3.6. Moving the mask orthogonally to the axis of propagation of the electron beam allows different regions of the beam to be sampled, hence constructing an intensity profile of the electron beam, from which FWHM measurements can be obtained. Measurements of the full electron beam current are carried out without the mask.



Figure 3.6: Photograph of the TRED apparatus beam mask. The mask contains two orifices, 200 μm and 500 μm in diameter.

3.2.1.1 Charge vs drive UV

In photocathode-based electron guns, the charge of the electron bunch, *i.e.* number of electrons per pulse, is proportional to the laser fluency at the photocathode. In the TRED apparatus, the fluency of the drive laser can be modulated using the angle of the β -barium borate (BBO) crystals in the third-harmonic generator (THG) set-up (see Appendix C). Small changes in the angle of this crystal can result in considerable changes in the efficiency of the harmonic generation and, consequently, the laser fluency and the number of electrons per pulse. The interaction between the linear polarisation of the incident laser light and the BBO crystal lattice, produces a 180° periodicity in conversion efficiency as a function of BBO angle. The TRED apparatus beam current calibration curve, shown in Figure 3.7, allows the beam current to be inferred from the angle of the BBO crystal and, during experimental runs, can also be used to navigate between beam charge densities without the Faraday cup and picoammeter.

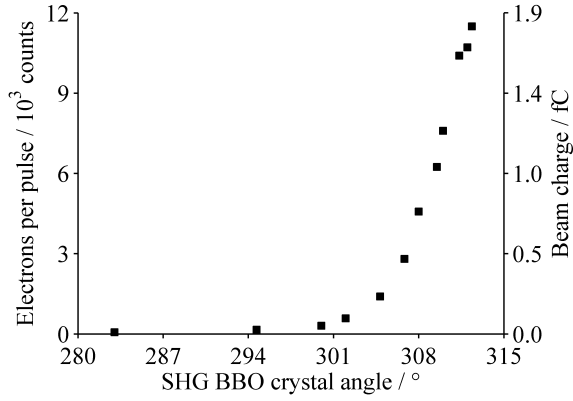


Figure 3.7: Calibration curve for the number of electrons per pulse and beam charge as a function of BBO crystal angle.

3.2.1.2 Charge vs full width half maximum

In a DC electron gun, the anode plug acts as the first collimator removing electrons with large angular distributions from the main electron beam. Collimators are routinely used to improve the energy distribution of electron beams, albeit at the cost of bunch charge. Electron beams with lower bunch charges are expected to be less affected by space-charge broadening and have smaller diameters. In the TRED apparatus, the relationship between beam charge and diameter was verified in a series of FWHM measurements carried out for different beam charges, shown in Figure 3.8. All measurements were carried out at an accelerating potential of 45 kV. The FWHM of an electron beam with a charge of 1.6 fC was found to be approximately 30% larger than that of a 0.8 fC electron beam.

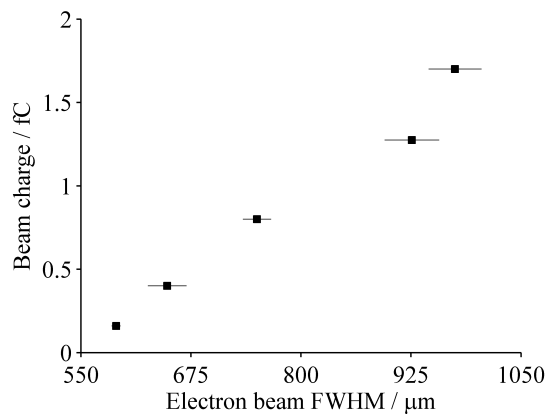


Figure 3.8: FWHM of an electron beam as a function of charge density.

3.2.1.3 Spatial profile

Particle tracer simulations, described elsewhere,^{37,178} have shown that electron beams containing 10^4 electrons per pulse, *i.e.* 1.6 fC, offer the best compromise between spatial resolution and signal-to-noise ratio. The shape of the electron beam at this optimum charge density was investigated through a series of beam-current measurements along the two axes orthogonal to the propagation axis of the electron beam. To minimise the effect of actuator backlash, grid scans were performed unidirectionally and, after each line, the beam mask was re-centred at the point with the highest beam current before moving to the next line. This two-dimensional profile of the electron beam can be used to diagnose problems and to calibrate the electron gun, but is also used as an experimental parameter in the generation of simulated datasets, a concept discussed further in Section 3.5. The two-dimensional profile of the TRED apparatus electron beam, shown in Figure 3.9a, confirms that, in photocathode-based electron sources, the spatial profile of the drive-laser beam is transferred onto the electron beam. The transverse profile of the TRED apparatus electron beam was found to be Gaussian in nature, matching that of the drive laser. Though bright and uniform, the electron beam, shown in Figure 3.9a, is not suitable for the acquisition of structural data, as its large FWHM would result in the blurring of diffraction features, leading to the loss of information.

A solenoid lens, described in Appendix C, allows the transverse profile of the TRED apparatus electron beam to be adjusted according to the experimental needs. The homogeneity of the magnetic field inside the solenoid lens ensures that the Gaussian profile is maintained despite the change in FWHM, shown in Figure 3.9b.

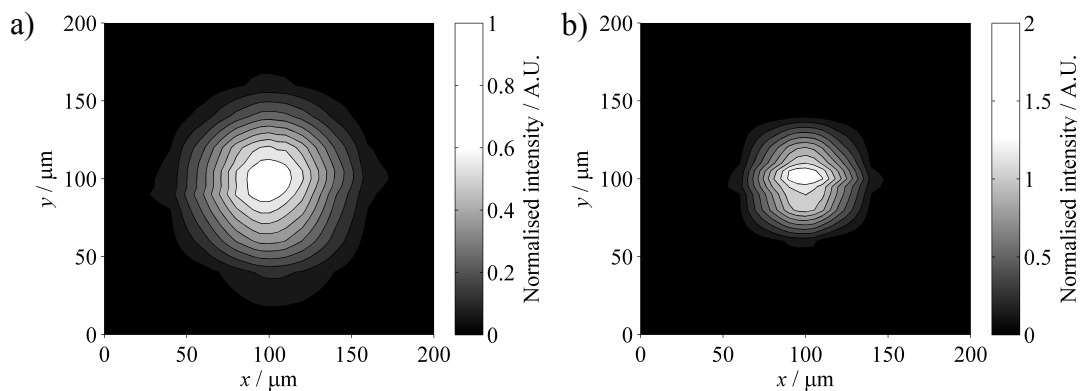


Figure 3.9: Two-dimensional profile of a) an unfocused, and b) a focused electron beam.

3.2.1.4 Beam FWHM vs accelerating potential

The timing stability, and spatial and temporal resolutions of electron beams generated using photocathode-based DC electron guns are dependent on the magnitude and stability of the accelerating potential. Furthermore, from the point of view of classical mechanics, electron bunches accelerated using a larger potential are expected to travel at higher speeds and hence be less susceptible to broadening effects. Therefore, one expects electron guns operating at higher voltages to produce sharper electron beams. The TRED apparatus electron beam transverse profile dependency on the accelerating potential was investigated through a series of FWHM measurements at various electron-gun voltages, shown in Figure 3.10. As expected, an inversely proportional relationship was found between the FWHM of the electron beam and the accelerating voltage. In the TRED apparatus, electron beams accelerated at 50 kV were found to have a 15% smaller FWHM than those accelerated at 32.5 kV. The calibration data presented in this section allow the user to tune the electron beam charge and transverse profile according to the experimental requirements, and to access the quality of the electron beam during preliminary diagnostic experiments.

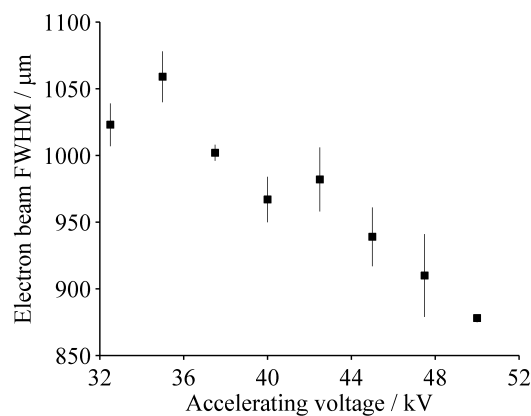


Figure 3.10: FWHM of an electron beam as a function of accelerating voltage. All measurements were recorded for a 1.6 fC electron beam.

3.2.2 Electron optics calibration

The focusing performance of the York solenoid lens (see Appendix C) was investigated in a series of calibration experiments, designed to quantify the effect of solenoid current in the transverse profile of the electron beam. The FWHM of a 1.6 fC electron beam accelerated using a potential of 45 kV was measured as a function

of solenoid current, producing the focal-response calibration curve shown in Figure 3.11. The performance of the York solenoid lens was benchmarked against focal-response data acquired for an older solenoid lens design, described elsewhere,¹⁷⁸ under identical conditions. Although both solenoid lenses were found to nearly halve the FWHM of the electron beam at 1.2 A, the York solenoid lens was found to have a smoother focal profile than its older counterpart. Furthermore, the new York solenoid lens, with its heat dissipative design and thicker wire gauge (see Appendix C.4), allowed for a more extensive calibration over a wider range of currents. At its maximum operating current of 1.6 A, 33% higher than the older design, the York solenoid lens was able to produce an electron beam of 400 μm FWHM, corresponding to an overall 40% decrease in the spot size of the original beam.

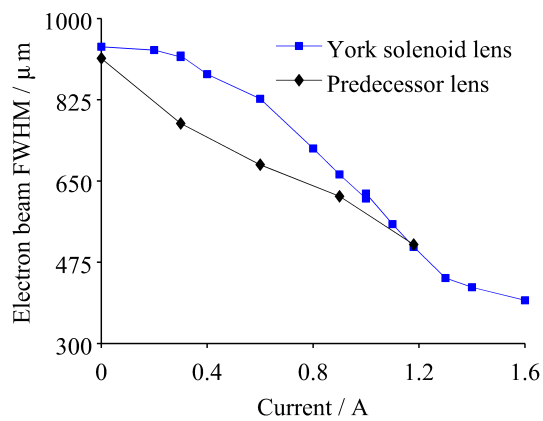


Figure 3.11: Evolution of the FWHM of an electron beam as a function of solenoid current for the York solenoid lens and its predecessor. All FWHM measurements were taken at the interaction region using the technique introduced in Section 3.2.1.

In solid-state electron diffraction experiments, access to high solenoid currents is paramount, as the FWHM of the electron beam at the sample is inversely proportional to the spatial resolution of the diffraction data. The sharpness of the two diffraction patterns recorded for polycrystalline platinum using an 800 and 400 μm electron beam, shown in Figure 3.12, illustrate this inversely proportional relationship. The improved focusing power of the York solenoid lens allowed previously undetectable diffraction features to be observed with sharp focus.

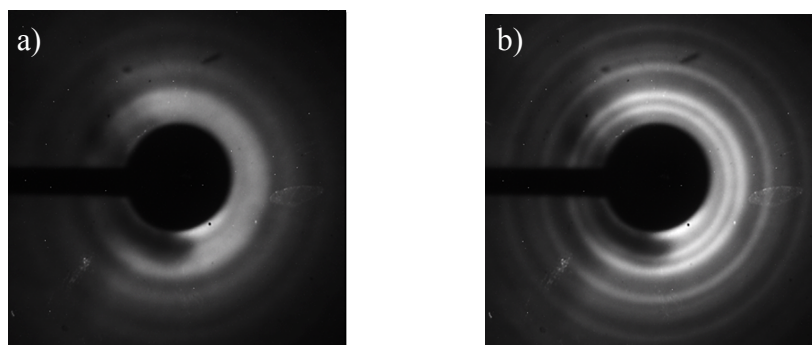


Figure 3.12: Diffraction of a polycrystalline platinum sample captured using an electron beam with a FWHM of a) 800 μm , and b) 400 μm .

The effect of the electron beam FWHM on the spatial resolution of diffraction data is far less pronounced in gas electron diffraction experiments. The lack of long-range interactions and low sample density results in inherently more diffuse diffraction features, the acquisition of which benefits from an electron beam focused at the detector. To better understand the performance of the York solenoid lens in GED experiments, the calibration curve in Figure 3.11 was extrapolated to the detector position, producing the focal-response calibration curve, shown in Figure 3.13. A solenoid current of 1.18 A was found to produce the optimum beam focus profile for a GED experiment. At solenoid currents higher than 1.18 A, the electron beam becomes over-focused with respect to the detector plane, resulting in a loss of spatial resolution.

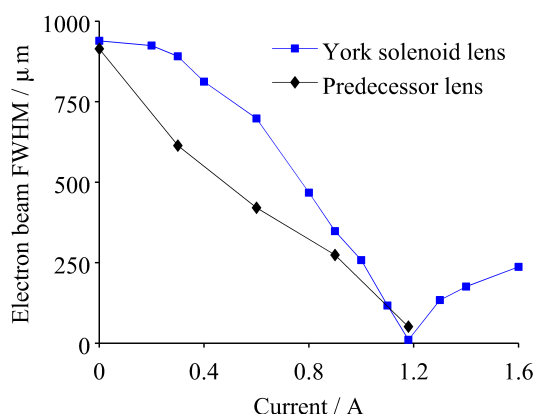


Figure 3.13: Evolution of the FWHM of an electron beam at the detector position as a function of solenoid current for the York solenoid lens and its predecessor. The FWHM measurements were extrapolated from the calibration curve in Figure 3.11, assuming a linearly divergent electron beam.

Solenoid lens calibration experiments have identified the optimum current settings for both solid-state and gas-phase experiments. Furthermore, these calibration curves demonstrate how the York solenoid lens can be used to tune the transverse profile of the TRED apparatus electron beam.

3.2.3 Deflector-plate calibration

The ability to adjust the flight path of the electron beam was investigated in a series of deflection calibration experiments, in which the position of the electron beam was monitored as a function of deflection voltage. The code used to extract the position of the electron beam centroid from recorded images can be found in Appendix E. All deflection calibration experiments were carried out using a 45 kV electron beam containing 10^4 electrons per pulse. Beam position measurements were taken for horizontal and vertical deflector plate potentials between 0 and 1 kV, in 100 V steps. The deflection potential was capped at 1 kV to prevent arc-discharge events, which could cause damage to the detector assembly. The outcome of the TRED apparatus beam deflector calibration experiments is summarised in Figure 3.14.

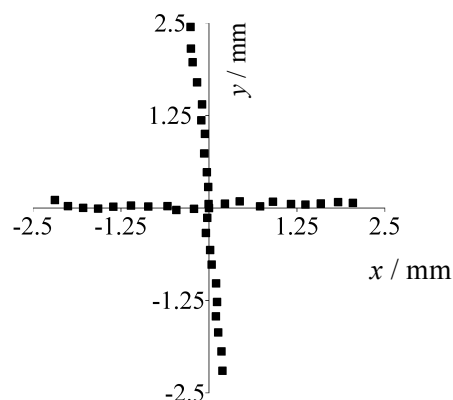


Figure 3.14: Plot of electron beam shift as a function of the voltage applied to the deflector plates along the x and y directions. Voltages varied between -1 kV and $+1$ kV in 100 V increments.

The linear relationship between the applied voltage and deflection magnitude allows the electron beam to be positioned accurately with respect to the detector and interaction region. This ability to steer the electron beam has resulted in a more accurate centring of the electron beam on the Faraday cup, better spatial overlap between electron and molecular beams, and the ability to search the interaction region for volumes of higher diffraction output.

3.2.4 MCP gain optimisation

Though widely used in imaging, spectroscopy, and mass spectrometry as a signal amplifier, MCP technology is far less common in electron diffraction apparatus. The TRED apparatus MCP consists of two layers of angled honeycomb channels, 15 μm in diameter, and arranged in chevron configuration. When an incident electron hits the walls of one of these channels, a cascade of secondary electrons is emitted. The potential between the first layer (A), held at ground, and the second layer (B), typically held at a positive voltage (MCP voltage), accelerates the cascade of electrons away from the first layer. The potential between the MCP assembly and the scintillator (C), held at an even larger voltage (scintillator voltage), accelerates the secondary electrons away from the back of the MCP and towards the scintillator screen. A schematic representation of an MCP is shown in Figure 3.15. In an MCP-based detector, gain is measured as the ratio between incident and emitted electron, which is proportional to the number of MCP layers and the accelerating potential across the detector. On the other hand, the spatial resolution of an MCP-based electron detector is inversely proportional to its gain, as information regarding the position and angle of the incident electron is lost with every electron cascade event inside the MCP channels. The effects of MCP gain on the quality of diffraction data quality were investigated for the TRED apparatus detector.

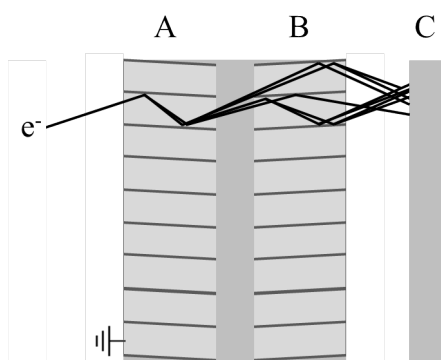


Figure 3.15: Diagram of a typical MCP, showing the first MCP layer (A), the second MCP layer (B), and the scintillator screen (C).

Firstly, the effect of scintillator voltage on the brightness and sharpness of diffraction data was investigated, as shown in Figure 3.16. At a scintillator voltage of 4.0 kV the detector gain was found to be nearly one order of magnitude higher than at 3.6 kV. Although experiments carried out using scintillator voltages above 4.0 kV showed an

increase in signal intensity, the improvement was deemed too small to justify the added risk of arc-discharge. Therefore, these data points were not included in the calibration plot shown in Figure 3.16a. An identical investigation was carried out to determine the effect of MCP voltage on the intensity and sharpness of the TRED apparatus diffraction signal, as shown in Figure 3.16b. Diffraction data recorded using MCP voltages above 1.7 kV were found to be less sharp than data recorded at lower voltages. The optimum compromise between signal intensity and spatial resolution for the TRED apparatus was found for a scintillator voltage of 4.0 kV, and a MCP voltage of 1.6 kV.

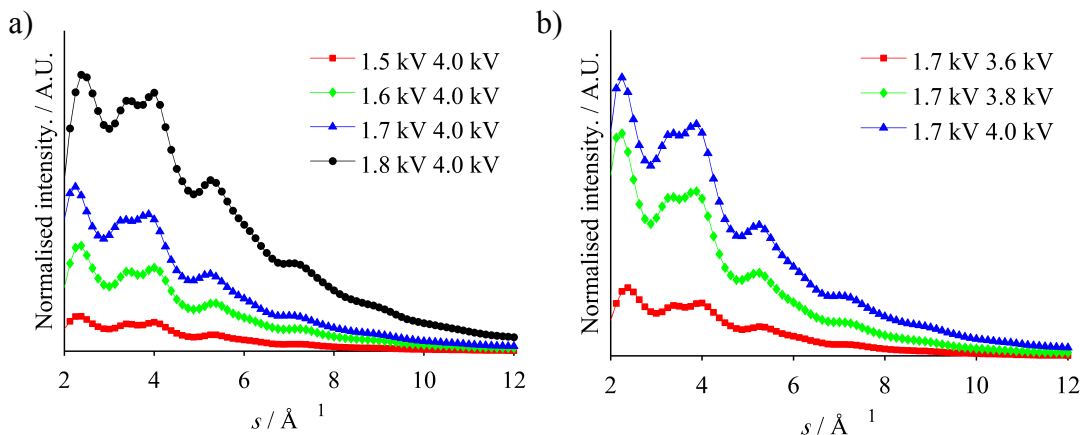


Figure 3.16: Diffraction curves recorded for a sample of polycrystalline platinum using a) three different difference scintillator voltages, and b) four different MCP voltages.

3.2.5 Detector geometry optimisation

The spatial resolution of MCP-based detectors is strongly dependent on the distance between the MCP and the scintillator screen, as well the accelerating potential across the detector and the diameter of the MCP channels; the latter of which is limited by the design specifications of the MCP. Following the MCP gain optimisation, discussed in Section 3.2.4, a series of calibration experiments were carried out to investigate the effect of detector geometry on the spatial resolution of the TRED apparatus. In these experiments, diffraction pattern sharpness was found to be inversely proportional to the distance between the MCP and the scintillator. This phenomenon was attributed to the inherently divergent nature of secondary electrons, depicted schematically in Figure 3.17. The gap between the MCP and scintillator screen ensures that these two plates remain electrically isolated, and prevents the occurrence of potentially damaging arc-discharge effects. In the TRED apparatus, an

MCP-to-detector distance of 5 mm, was found to offer the best compromise between spatial resolution and the risk of arc-discharge.

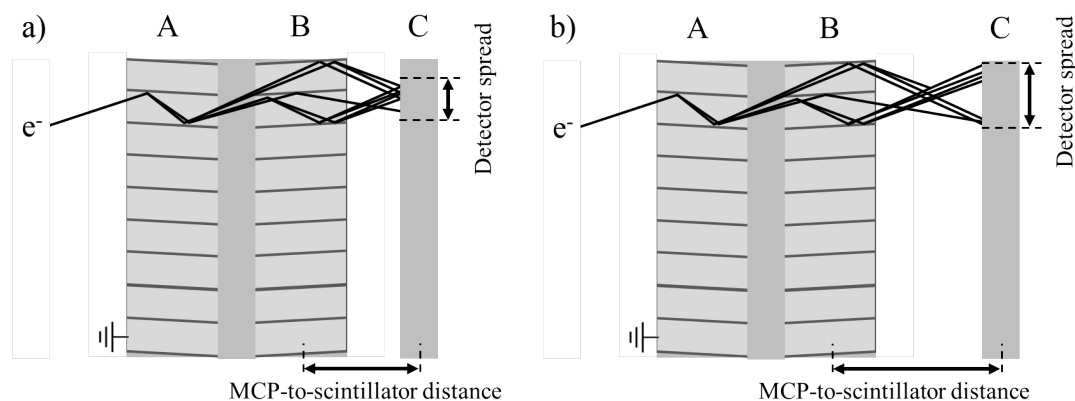


Figure 3.17: Schematic illustration of the spatial resolution of an MCP-based detector with a) a short, and b) a long MCP-to-scintillator distance.

In the TRED apparatus, diffraction patterns projected on the back of the scintillator screen are recorded as image frames using a CCD camera (Stingray F-146 B). The intensity and sharpness of these images is strongly dependent on the sensitivity of the CCD chip, the quality of the lens, the focus, and the active pixel area. To maximise the collection efficiency of the 17 mm Schneider lens, the original CCD camera was positioned at its near-field position, mounted on a linear stage, and focused on to the scintillator plane using a back-focus chart, also known as Siemens star.

In summary, the optimisation of MCP gain and detector geometry, have improved the SNR and spatial resolution of diffraction patterns recorded using the TRED apparatus, as demonstrated by the before and after comparison shown in Figure 3.18.

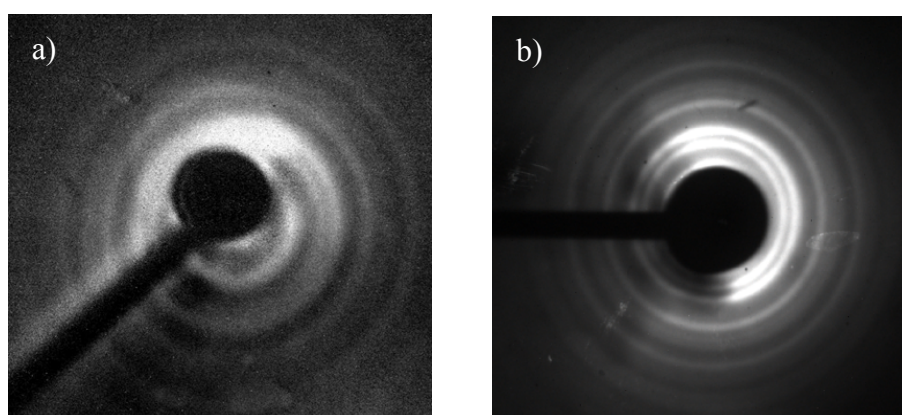


Figure 3.18: Diffraction pattern of a polycrystalline platinum standard acquired using a) the original, and b) the optimised detector configuration.

3.2.6 Magnetic distortion corrections

Improvements in the spatial resolution of the diffraction data recorded using the TRED apparatus allowed the Bragg peaks of polycrystalline platinum to be resolved with unprecedented resolution. However, upon closer inspection of the spacing between Bragg peaks, these were found to be distorted anisotropically with respect to the centre of the pattern. To better understand the source of this distortion, average Bragg peak positions were extracted along 40 discrete azimuthal angles and compared against simulated peak positions, as shown in Figure 3.19. The positions of the Bragg peaks were found to be distorted particularly for the lower portions of the pattern and especially in the fourth quadrant.

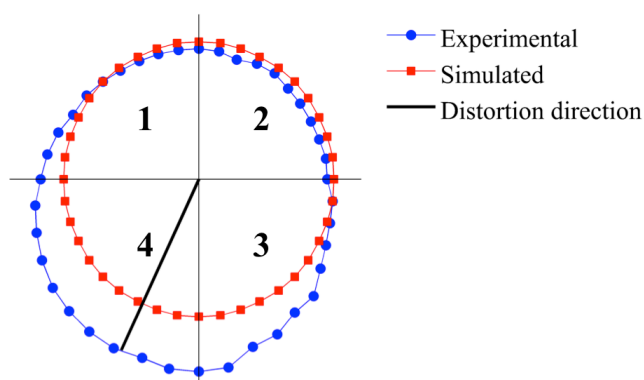


Figure 3.19: Plot of the simulated (circles) and measured (squares) Bragg peak positions for diffraction from polycrystalline platinum, showing the direction of distortion. Data points are spread over four quadrants identified as 1 to 4.

Generally, these discrete perturbations of the electron flight path are attributed to highly directional magnetic fields, such as those produced by the TRED apparatus magnetically levitated turbo molecular pumps, or the superconducting magnets in the NMR Centre of Excellence adjacent to the laboratory. The analysis of the magnetic-field emission measurements carried out by Edwards on the STPA2203 pump, and the study of the apparatus orientation with respect to the NMR Centre revealed neither of these sources to be responsible for the magnitude of the distortion observed. However, careful inspection of the schematics for the laboratory, showed that the TRED apparatus is angled 51.4° with respect to the geographic north. Therefore, the magnitude and orientation of the Earth's magnetic field with respect to the flight path of the electron beam was calculated using the geometric coordinates of the laboratory and average annual estimate for the Earth's magnetic

field from the National Oceanic and Atmospheric Administration world magnetic model.¹⁷⁹ The Earth's magnetic field was found to cross the electron propagation axis at an angle of 51° northeast, and a decline of 68.4° , as shown in Figure 3.20a. The projected magnetic field vector onto the propagation axis of the electron beam was found to be in very good agreement with the direction of the Bragg peak distortion, as shown in Figure 3.20b. The Earth's magnetic field was identified as the primary source diffraction pattern distortion in the TRED apparatus. Therefore, at the start of every TRED experiment, the diffraction pattern of a polycrystalline platinum standard is recorded, allowing the magnetic distortion in the data to be corrected in post-processing.

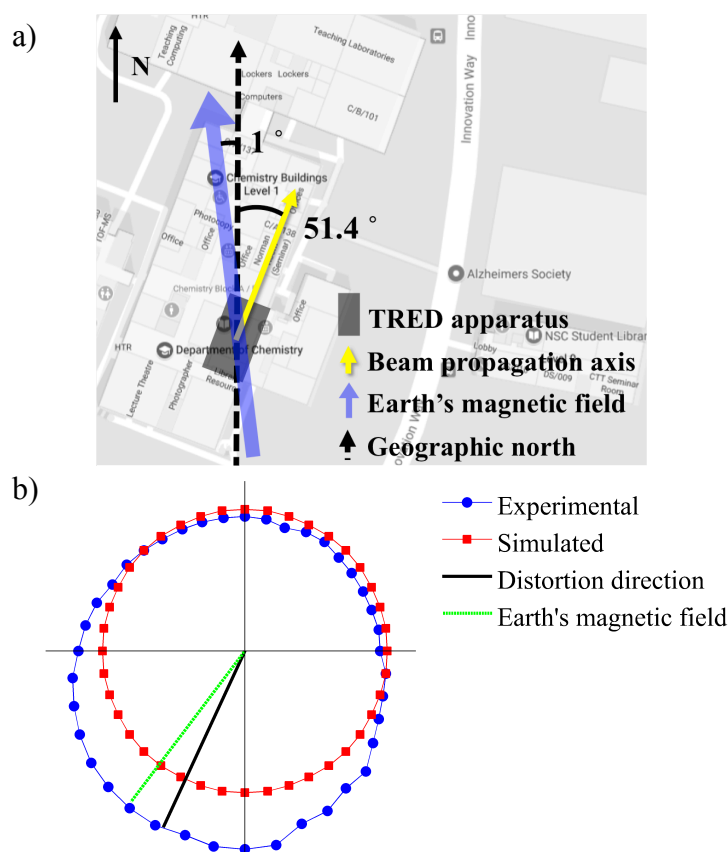


Figure 3.20: Illustration of a) the orientation of the Earth's magnetic field with respect to the orientation of the TRED apparatus and the geographic north, and b) the projection of the Earth's magnetic field on the Bragg peak distortion plot.

3.2.7 Determining time zero

The delay setting corresponding to optical pump and electron probe arriving at the sample simultaneously, is called time zero, and, in the TRED apparatus, is determined using the photoionisation-induced lensing (PIL) method. Developed by

Zewail *et al.* in 1997,^{180,181} the PIL method uses the transient electric field in the wake of a plasma to distort the electron beam. Plasma formation is typically achieved through multiphoton ionisation of the sample. The delay position at which the electron distortion is maximised signifies time zero.

The TRED apparatus time zero was determined using a version of the PIL method developed by Miller *et al.*,¹⁸² in which a fine copper mesh replaces a gas target as the plasma source. A time-zero finder device, depicted schematically in Figure 3.21, was installed in the TRED apparatus solid-state and gas-phase delivery system and used to investigate the apparatus time zero under different experimental conditions. The delay between the arrival of the electron beam and plasma formation is controlled using a motorised delay stage and the pump power is kept below 70 μJ to prevent the ablation of the copper mesh. The beam deflector steers the beam towards the scintillator, allowing the entire electron beam to be imaged using the CCD camera.

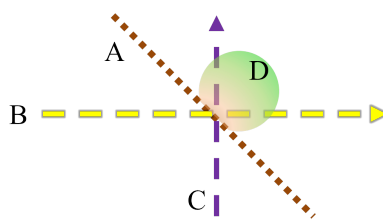


Figure 3.21: Schematic representation of time-zero finder device used in the PIL experiment, showing a fine copper mesh (A), the electron and laser beams (B and C, respectively), and the copper plasma (D).

Poor temporal overlap between the electron beam and the plasma allows the electron beam to pass through the copper mesh unperturbed producing the beam pattern shown in Figure 3.22a. However, as the pump delay approaches the time-zero position, the temporal overlap between the electron beam and the plasma causes electrons at the centre of the beam to be displaced, producing the distortion pattern shown in Figure 3.22b.



Figure 3.22: Image frame recorded during PIL time-zero determination experiments with a) poor, and b) optimum temporal overlap.

The distortion onset is recorded as a series of image frames captured as a function of the pump-probe delay, shown in Figure 3.23, and used to determine the position of maximum distortion, *i.e.* time zero. To the experimentally found time-zero position, a plasma on-set delay must be added to account for the time it takes the plasma to form, which for a copper mesh is typically 10 picoseconds.

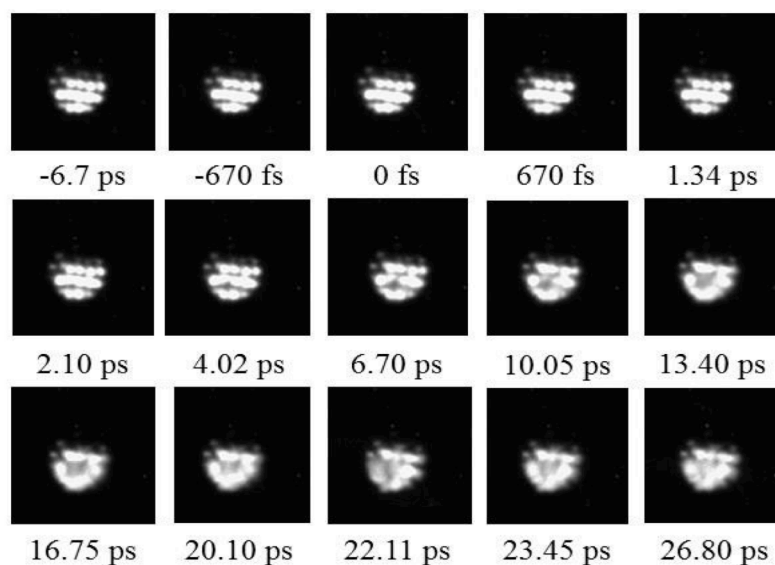


Figure 3.23: Series of frames showing the evolution in electron beam distortion as a function of time delay.

3.2.8 Sample delivery system

The TRED apparatus was designed to carry out experiments in both the solid and gas phases. Therefore, a considerable portion of my PhD project was spent designing and developing sample delivery solutions for the TRED apparatus, which would allow solid-state and gas-phase experiments to be carried out in the same diffraction chamber. The sample holder, shown in Figure 3.24, was developed to deliver an array of 6 samples to electron beam. For ease of transportation, samples are deposited onto thin copper grids (TEM grids). At the centre of the sample holder, a set of perpendicular holes, intersecting at the sample plane, allow the experimental time zero to be determined *in situ*, using the plasma lensing technique discussed in Section 3.2.7. Moreover, these holes can be used as a spatial overlap alignment tool during sample holder installation. One of the positions in the sample holder is reserved for an internal standard, typically a film of polycrystalline platinum.



Figure 3.24: Photograph of the TRED apparatus sample holder, showing the polycrystalline platinum internal standard at position 1. The diffraction signal from the internal standard is routinely used to optimise the solenoid lens focusing.

In the TRED apparatus, gas-phase samples, which include neat gases and vapours suspended in carrier gases, are delivered to the electron beam using a modular gas-handling system coupled to either an effusive or pulsed nozzle, shown in Figure 3.25a and 3.25b respectively. A details description of these sample delivery systems can be found in Appendix C.



Figure 3.25: Photograph of the TRED apparatus a) effusive and b) pulsed nozzle.

Similarly to the solid sample holder, the pulse nozzle is fitted with a spatial and temporal overlap piece consisting of two perpendicular holes, intersecting at the sample plane. This purpose-built brass time-zero finder, shown in detail in Figure 3.26, allows the experimental time zero to be determined using the plasma lensing method (see Section 3.2.7). CAD drawings for the nozzle head and time-zero finder can be found in Appendix H.

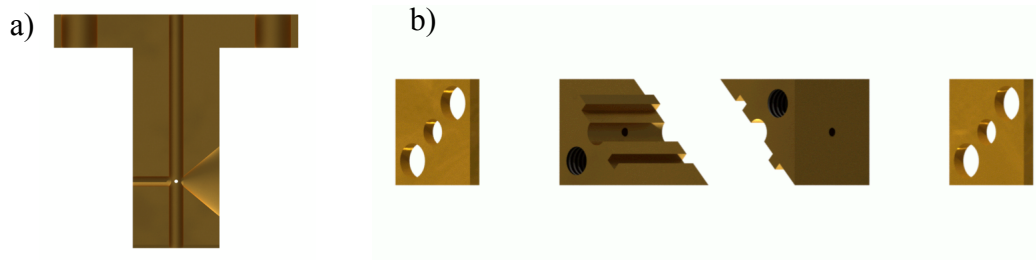


Figure 3.26: Drawings showing the cross-section of a) the nozzle head, and b) an exploded view of the time-zero finder.

3.2.9 Design improvements to the high-voltage coupling

Towards the later stages of my PhD, silent arc-discharges between the high-voltage connector and the Faraday cage surrounding the high-voltage feedthrough limited the TRED apparatus accelerating voltage to 35 kV. Moreover, multiple discharges had damaged the surface of the Perspex case, described elsewhere,¹⁷⁸ causing it to flake, and promoting further discharge events. To restore the TRED apparatus accelerating voltage range to its original specification, a new high-voltage enclosure was designed. Manufactured at the mechanical workshop, this enclosure, shown in Figure 3.27, consists of a 550 mm long stainless-steel cylinder mounted onto the high-voltage feedthrough flange using a custom-made polytetrafluoroethylene (PTFE) fitting. A stainless-steel end-plate cap ensures that the high-voltage connector is centred with respect to the cylinder, which is grounded to the electron gun chamber. To prevent future arc-discharges, the high-voltage connection between the high-voltage cable and the ceramic feedthrough is coated with a non-corrosive thixotropic dielectric silicone.

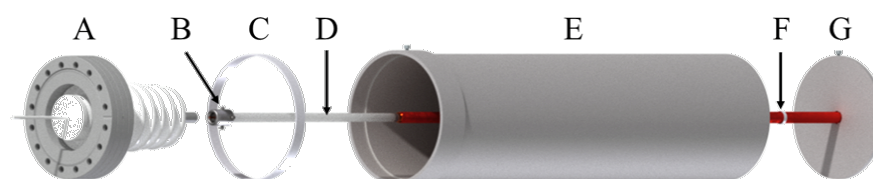


Figure 3.27: CAD drawing of the enclosure surrounding the high-voltage feedthrough in the TRED apparatus electron gun, showing the HV feedthrough (A), HV connector (B), the PTFE flange fitting (C), the HV cable (D), the steel cylinder enclosure (E), the PTFE cable fitting (F), and end plate (G).

3.3 Ultrafast electron diffraction at SLAC

Housed in the accelerator structure test area (ASTA) at SLAC, the MeV UED apparatus was commissioned in 2014 as part of the UED/UEM initiative launched by the US Department of Energy strategic plan for national facilities.⁹² The UED beam line, schematically shown in Figure 3.28, consists of four modules: the electron gun, the laser set-up, the sample delivery system, and the detector module. A detailed description of the UED apparatus can be found elsewhere.⁴¹ The design and commissioning of the UED apparatus gas-phase set-up was carried out by the UED group at SLAC in collaboration with the Centurion group¹⁸³ at Nebraska and Markus Gühr¹⁸⁴ at Potsdam.



Figure 3.28: Schematic illustration of the UED apparatus at SLAC showing the RF electron gun (A), the main solenoid (B), the beam diagnostic module (C), the diffraction chamber (D), the sample delivery system (E), the near detector (F), and the EMCCD far detector (G).

In the summer of 2016, a collaboration between Wann group and the UED group at SLAC was stabilised with the aim of expanding the scope of the apparatus towards the exploration of fundamental mechanisms in photochemistry, of which the ring-opening of 1,2-dithiane, discussed in Chapter 5, is an example. In the autumn of 2016, and thanks to the support of the Wild Overseas Scholar Fund, I was able to secure beam time at SLAC for the UED study of 1,2-dithiane. During my three-month visit to SLAC, I took part in an intensive operator-training programme, which resulted in my qualification as a test-stand operator and an independent data collector at the ASTA facility. A brief description of the experimental setup used during the 2016 gas-phase UED run can be found in Appendix D.

3.3.1 MeV UED experiment workflow

The experimental method used to record time-dependent diffraction data using the MeV UED apparatus consists of six stages, schematically depicted in Figure 3.29. This methodology was developed by the UED group at SLAC to maximise the

temporal resolution and signal-to-noise ratio of diffraction data recorded using the MeV UED apparatus, whilst minimising the detrimental impact of timing jitter.¹⁸⁵

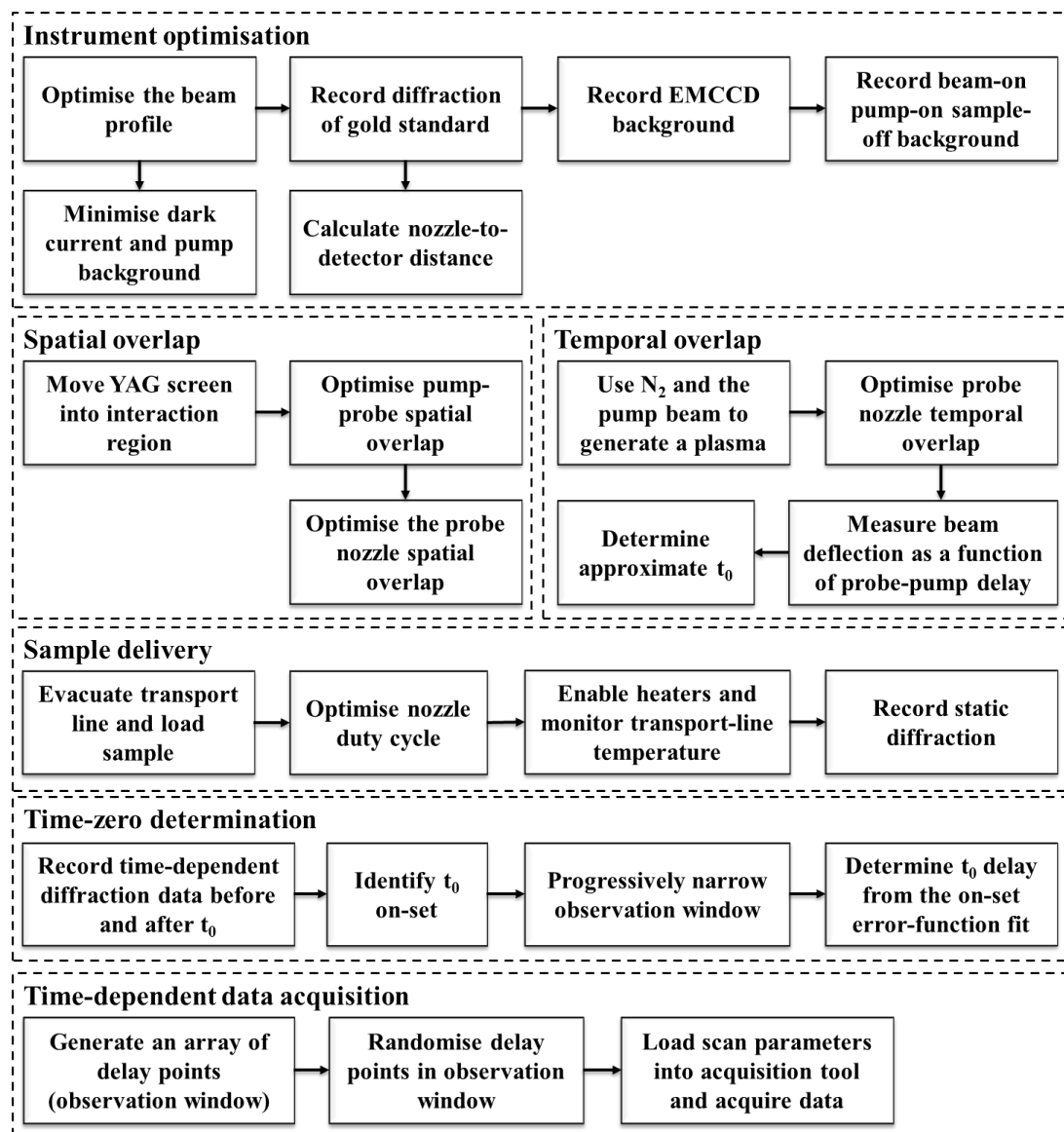


Figure 3.29: Schematic depiction of the experimental protocol developed by the UED group at SLAC and used to acquire UED data for 1,2-dithiane.

3.4 Computational chemistry

Computational chemistry is the branch of science responsible for the study of molecular structures and chemical reactions using theoretical methods translated into computer programs operating in a virtual environment. Through the use of physical models and quantum mechanisms, computational methods allow us to explore new time domains, discover new interactions, and predict the properties of novel materials. Developments in algorithm efficiency, the advent of parallel computing,

and Moore's law (predicting the transistor density in computer chips to double every two years), have allowed computational chemistry to study increasingly large and more complex molecules with ever improving accuracy.¹⁵³ Quantum chemical calculations deemed unfeasible a decade ago, can be routinely carried out using university-based workstations and high-performance computer (HPC) clusters. Moreover, recent developments in quantum-chemical packages have opened the field of quantum chemistry, previously limited to a small group of theoreticians, to a much wider and more diverse audience of experimental chemists, physics, and biologists. Due to this improved accessibility, the use of computational chemistry to assess the viability of research projects, and support experiments in a cost-effective manner has become common practice.

In the roadmap to molecular movies presented in Section 1.6, computational chemistry is placed alongside GED and TRED experiments as a tool for the study of structural dynamics.

In the context of time-averaged GED, electronic structure calculations can be used with the SARACEN¹³⁸ method to fill in the gaps of experimental data, improving the quality of structure refinements. In this approach, *ab initio* geometry optimisations are used to build and restrain the parameterised models used in structure refinement, while vibrational frequency calculations are used to generate the vibrational corrections required to account for "shrinkage effects" in GED structures (see Chapter 2). In this thesis parameterised models used in the GED refinement were constructed from geometries optimised using either a double-hybrid density functional theory (DFT)¹⁸⁶ function with an MP2-like perturbation correction, B2PLYP,¹⁸⁷ or the "gold-standard" method in quantum chemistry, Coupled Cluster single-double and perturbative triple, CCSD(T).^{188,189} The suitability of these methods to produce structurally accurate results has established in extensive benchmark studies by Werner and Grimme *et al.*^{187,190-192} All GED refinements were carried out using restraints obtained from geometries optimised using hybrid DFT (DFT) functionals. The cost effectiveness of these methods, of which B3LYP¹⁹³ is the most common example, make them ideal sources of GED restraints. In fact, one's ability to adequately restraint the refinement is directly related to the quality and variety of functionals used, and the number of calculations carried out. In vibrational frequencies calculations, correlation consistent basis sets were used preferentially, as

these are designed to converge systemically, allowing for the basis sets to be extrapolated to the complete basis set (CBS) limit.¹⁹⁴ A brief overview of these methods can be found in Appendix A.

In TRED and UED studies, computational exploration of molecular dynamics usually precedes experiments, allowing motion amplitude and timescale to be taken into account in the design of system-specific experiments. Typically, a combination of chemical intuition and computational exploration of the quantum chemical nature of the sample allow complex three-dimensional motions to be reduced to their key one-dimensional components, allowing TRED and UED experiments to take advantage of the sensitivity of electrons to the evolution of nuclear wavepackets. In fact, the success of the roadmap to “molecular movies” presented in Section 1.6 is equally dependent on the spatio-temporal resolution of the apparatus, and on the quality of the theoretical framework supporting the experiments.

In the computational studies presented in Chapter 6 and 7, future time-resolved experiments are supported by the computational exploration of conformational space and excited state topography, using Møller–Plesset perturbation theory functionals,¹⁹⁵ and linearly interpolated internal coordinate (LIIC) scans at the multi-configurational self-consistent-field (MCSCF) level of theory,^{196–198} respectively. Møller-Plesset functionals, such as MP2,^{199–201} use perturbation theory to account for the effects of electron correlation, yielding quantitatively accurately electronic energies, which can be used to calculate the conformer ratio of sample at a given experimental temperature. The use of MCSCF methods, such as complete active space self-consistent-field (CASSCF),^{202–206} allows for a qualitatively adequate description of regions where states are in close proximity, for example conical interceptions. Through the linear combination of configuration state functions (CSFs) selected according to the nature of the orbitals and number of electrons in a user defined active space, this approach can provide a more focused description of specific electronic structure features and dynamics. To validate the choice of active space, the shape of potential energy surfaces calculated using MCSCF methods are compare to those generated using dynamic correlation corrected multi-reference methods, such as multi-reference configuration interaction (MRCI).^{207–211} This computational description of the system can then be used to simulate the motion of nuclear wavepackets using surface-hopping molecular dynamics. Computational

studies in this thesis use the quantum chemical packages, such as Columbus^{212–214} and MOLCAS²¹⁵, interfaced molecular dynamics wrappers, such as Newton-X^{216–219} and SHARC,²²⁰ to propagate this MCSCF description in time and explore the structural implication of potential energy surface topography. A detailed description of these methods can be found in Appendix A.

3.5 Software tools

In the roadmap to molecular movies software-based data extraction, analysis, and interpretation tools are shown to be crucial to the success of modern time-averaged and time-resolved electron diffraction studies. The development of user-friendly software, capable of transforming thousands of diffraction images into plots showing the evolution of interatomic distances as a function of time, has made electron diffraction undoubtedly more appealing to the wider community. Furthermore, the automation of experimental procedures and data analysis routines has allowed electron diffraction to transcend the niche research field to occupy a more central role in the study of structural dynamics, as a research tool for chemistry and physics.

For many years, the lack of a universal data format and standard data analysis tools meant that one could not easily visualise or compare the results of electron diffraction experiments in a structurally relevant fashion. In the X-ray crystallographic community, this limitation was overcome in the 1960s with the development of the SHELXL suit of packages,²²¹ which allowed X-ray crystallography to become the go-to technique for structure determination in crystals. However, the development of such software tools in electron diffraction has lagged behind developments in electron sources and detector technologies. Therefore, a considerable amount of my PhD project was dedicated to the development universal data formats and extraction software.

The advent of high-performance computing and the development of robust computational methods for the study of excited-state molecular dynamics have revolutionised our ability to design and simulate UED experiments. Quantum chemical simulations of molecular motion can be used predictively, converting the output from trajectory simulations into theoretical time-dependent diffraction patterns, or reactively, helping to deconvolute the temporal blur in experimental diffraction patterns and facilitating the identification of the unique signature of

specific molecular motions in reciprocal space. Examples of these simulations and their use in the analysis of UED data can be found in Chapters 5. The interpretation of UED data is subject to the same challenges faced by traditional GED, in addition to those associated with the temporal blurring of structural information in time-dependent diffraction patterns. A suite of purpose-built software packages has been developed to extract structural information from diffraction data, using a combination of routines incorporating both tried-and-tested methods implemented in tradition GED and novel analysis methods.

Throughout my PhD project, a total of nine packages (Sections 3.5.1 to 3.5.9) have been developed to address the challenges associated with the extraction, visualisation and analysis of results from diffraction experiments and computational studies associated with the roadmap to molecular movies. These packages have been developed using MATLAB²²² and designed to be easily deployable, parallelisable, and cross-platform compatible. All wrapper scripts and functions can be found in Appendix E. In order to distinguish between previously existing software packages, and those developed as part of my PhD project, the latter will be shown in italics.

3.5.1 GED extraction package (*XTRACT*)

The GED extraction package, *XTRACT*, was developed to read image frames from a wide range of detectors and convert diffraction patterns into molecular intensity curves. The output of the *XTRACT* package, which comprises of a list of s value and corresponding scattering intensities in the extensible markup language (XML) format, can be read directly into the least-squares refinement software, ED@ED.¹⁴⁵ The variety of input formats compatible with the *XTRACT* package and the instrument-independent output format, which facilitates the transfer of data between routines are discussed in Sections 3.5.1.2 and 3.5.1.3, respectively. Moreover, benchmarking of the *XTRACT* package against the widely used data-extraction package, XPKG,¹⁴⁰ can be found in Section 3.5.1.4.

3.5.1.1 *XTRACT* workflow and subroutine description

XTRACT takes full advantage of the highly-optimised matrix-manipulation functions inbuilt into MATLAB, to azimuthally average diffraction patterns into simple strings of data. The data extraction routine consists of eight subroutines, called according to the scheme shown in Figure 3.30.

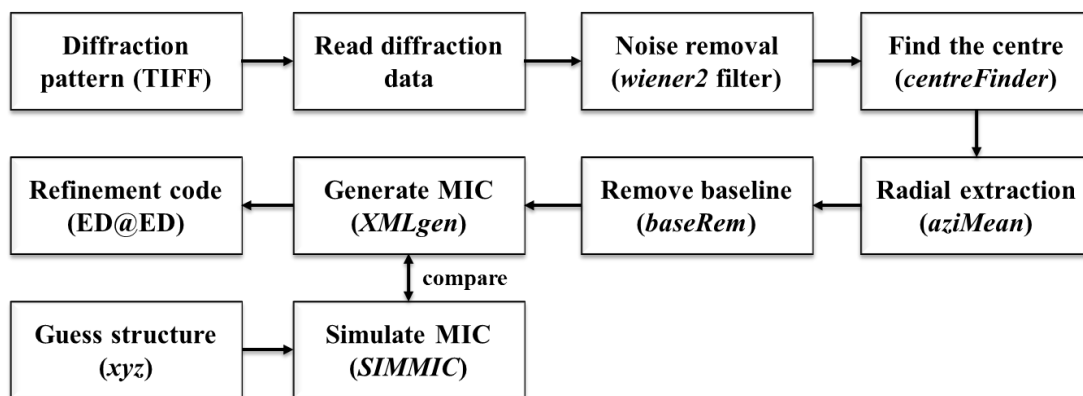


Figure 3.30: Flowchart representation of a typical data extraction using *XTRACT*.

At the beginning of the data-extraction routine, *XTRACT* calls the *SIMMIC* package, described in further detail in Section 3.5.2, to simulate MICs for a guess structure provided as an *xyz* file. Diffraction images, generally stored in tagged image file format (TIFF), are imported from a user-defined folder into the *XTRACT* environment and converted to double-precision floating point matrices. TIFF is the format of choice for raw diffraction data in the electron diffraction community, as it is widely used in flat-bed scanners and the publishing industry. A two-dimensional Wiener filter is then applied to the imported images, removing white noise and improving the SNR of the data, as shown in Figure 3.31. Wiener filters lower noise levels by minimising the mean-square error between the stationary signal and noise spectra, assuming that these are stochastic in nature and have distinct spectral properties.²²³ These filters are widely used in noise cancellation and signal identification in scientific and industrial applications.

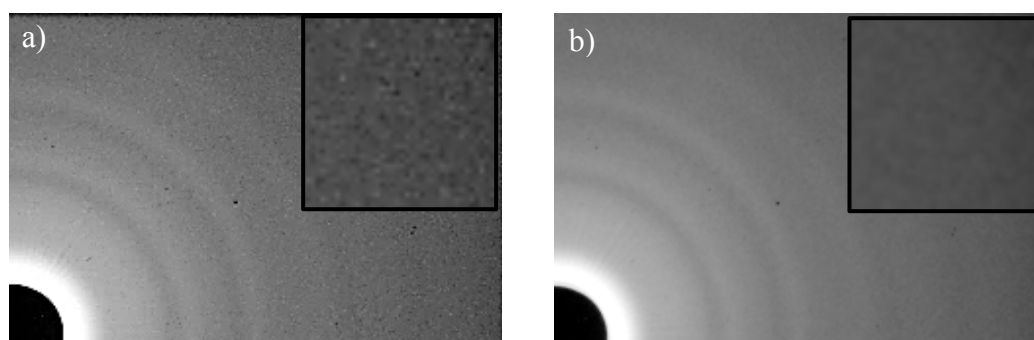


Figure 3.31: Diffraction pattern of benzene a) before, and b) after, the application of a Wiener filter. The zoomed section on the upper-right corner of each pattern illustrates the reduction in image graining before and after the Wiener filter.

Diffraction patterns are converted into MICs using the azimuthal average method, which requires the accurate determination of the centre of the diffraction pattern in order to prevent blurring. The *XTRACT* *centrefinder* subroutine uses a circle-fitting algorithm to determine the centre point of concentric isolines from a contour map of the diffraction pattern. Generally, the average centre point of five isolines is used as the centre of the diffraction pattern. A toggle switch in the main *XTRACT* wrapper code allows the *centrefinder* subroutine to be bypassed and a user-defined centre of the diffraction pattern to be provided instead. The azimuthal average subroutine, *azimean*, uses a polar-coordinate system to average the intensity of all pixels with the same radius value based on either the user-defined or the calculated centre of the diffraction pattern. The *azimean* code outputs a list of average pixel intensities at various distances from the centre of the detector, which are converted to scattering-vector values using the known nozzle-to-detector distance and electron beam wavelength. For diagnostic purposes, diffraction images are extracted in four separate 90° quadrants, shown in Figure 3.32a, and their outputs compared to assess the validity of the centre found and inspect the anisotropy of the data. Furthermore, artefacts caused by irregularities in the detector system can be removed through a careful selection of the angular constraints imposed during the azimuthal averaging. The azimuthal average of each quadrant (Figure 3.32b) comprises a mixture of molecular and atomic scattering, background scattering, and detector readout noise.

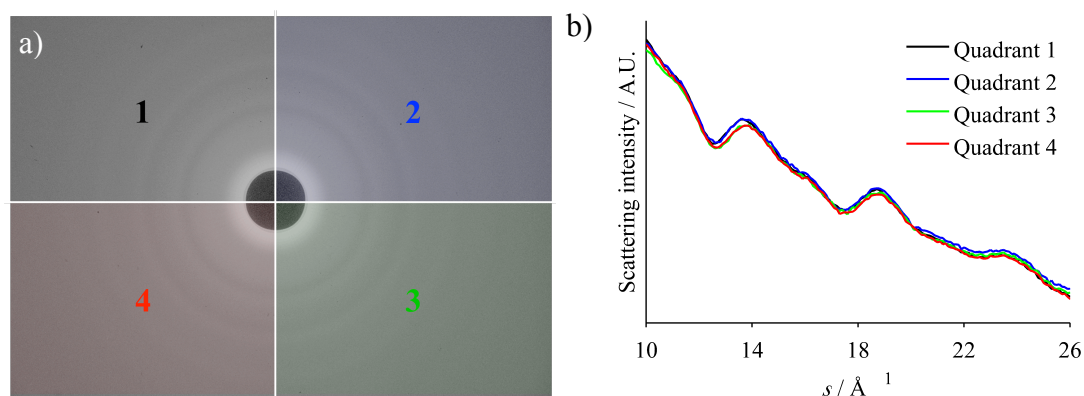


Figure 3.32: Examples of a) a diffraction pattern divided into quadrants, and b) the output of the *azimean* code, showing the overlap between quadrants. The similarity between all four detector quadrants is indicative of the adequate selection of the centre of the diffraction pattern.

To retrieve structural information from diffraction data, the molecular scattering terms must be extracted from the raw diffraction signal. Therefore, for the purposes of data extraction, all other terms and contributions are considered as background. In the *bkgrem* subroutine, the background signal, which is assumed to be inherently smooth and static, is fitted using a third-order polynomial and subtracted from the diffraction signal, producing a flat MIC. Outliers in the MIC are removed using a linear least-squares local regression in which data points beyond six mean deviations are assigned zero weight. The resulting molecular intensity curves are spline fitted over adequately spaced scattering-vector intervals, producing the smooth MICs shown in Figure 3.33a. Experimental MICs are normalised, scaled, and compared to the simulated MICs generated using *SIMMIG*, as shown in Figure 3.33b. The *mic2xml* subroutine converts the MICs into XML files compatible with the refinement package ED@ED. Routines used in *XTRACT* to find the centre and to convert the distances of pixels from the centre to scattering-vector values, and to azimuthally average diffraction patterns, are also employed in the extraction of UED data through the *UEDEXTRA* package, discussed in Section 3.5.5.

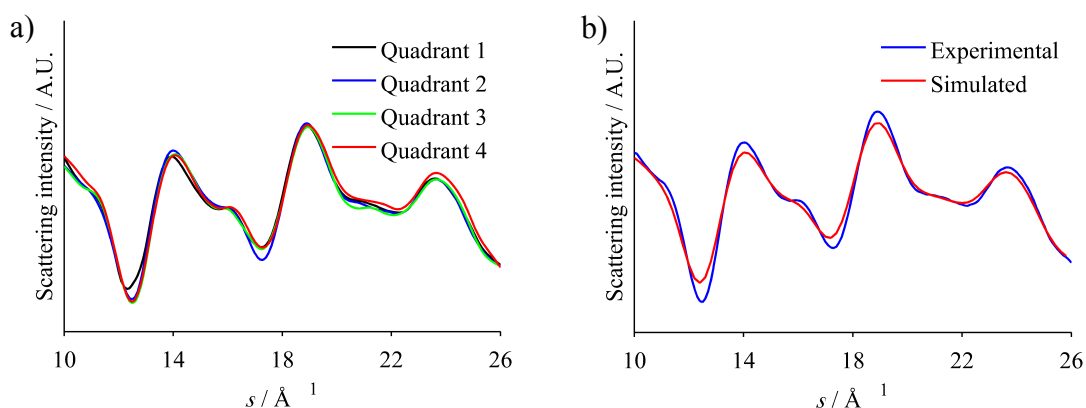


Figure 3.33: MICs before least-squares refinement for benzene shown a) separately for each quadrant, and b) spline fitted and compared against simulated data. Agreement between experimental and simulated MICs is indicative of data quality.

3.5.1.2 *XTRACT* input format

The *XTRACT* package was initially developed to extract diffraction data acquired using the image plates in the York GED apparatus; however, it has since been used to extract data from both photographic film and CCD-based detectors, recorded using the Edinburgh GED apparatus,²²⁴ and York telefocus GED apparatus,²²⁵

respectively. The lack of instrument-specific information in the input allows *XTRACT* to extract diffraction data regardless of the detector type, size, or age.

3.5.1.3 *XTRACT* output format

The MICs generated using the *XTRACT* package are independent of the instrument used to record the data, addressing the need for an universal file format for GED. These universal MICs consist of a list of scattering-vector intensities, normalised between 0 and 1, as a function of scattering value. Separate datasets are generated for short and long nozzle-to-detector distances, which are usually presented in 0.2 or 0.1 \AA^{-1} scattering value increments, respectively. Therefore, diffraction data recorded using the York GED apparatus can be compared directly with those recorded using photographic film for the Edinburgh GED apparatus, provided that both datasets are extracted using the *XTRACT* package and use the universal MIC format.

3.5.1.4 *XTRACT* benchmark against XPKG

The suitability of the azimuthal averaging method and the polar-coordinate system used in *XTRACT* as a tool for the extraction and dimensional reduction of diffraction data was investigated in a benchmark study against XPKG, a tried-and-tested extraction package developed in 2005 by Rankin *et al.*¹⁴⁰

XPKG uses a series of loops to visit every pixel in a diffraction image, retrieving pixel intensity and its distance from the centre of the diffraction pattern. A detailed description of the XPKG can be found elsewhere.¹⁴⁰ Though easy to understand, this approach is remarkably inefficient from a computational point of view, as it requires the repetitive calling of the same script in every loop, thus bottlenecking the size and number of images that can be extracted. Furthermore, it would be computationally unfeasible to extract the output of modern CCD cameras in real time using such a code. *XTRACT* on the other hand, uses a series of matrix operations and transformations to replace nested loops and thousands of repetitive calculations. Moreover, *XTRACT* makes use of parallel computing protocols to further speed up data extraction, in both the workstation and cluster environments. The validity of the azimuthal averaging method in *XTRACT* was tested against the traditional XPKG extraction routine using a diffraction pattern for benzene recorded using the Edinburgh apparatus as a test dataset. Diffraction curves obtained using the *XTRACT* package were found to be in excellent agreement with those generated using XPKG,

as shown in Figure 3.34. This proof-of-concept experiment demonstrates that *XTRACT* is suitable for extracting diffraction data in a robust fashion.

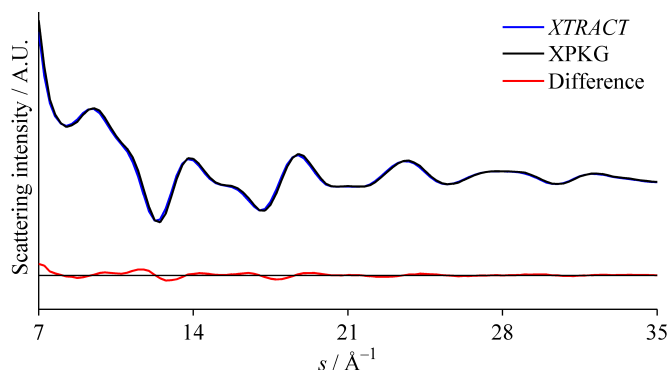


Figure 3.34: Comparison of MICs generated using *XTRACT* and *XPKG* for the diffraction patterns of benzene recorded using the Edinburgh GED apparatus.

3.5.2 Molecular intensity curve simulator (*SIMMIC*)

Simulated MICs are powerful tools in the design of new experiments and are routinely used to assess the quality of diffraction data. The MIC simulator package, *SIMMIC*, was developed to address the need for computationally inexpensive simulated MICs. *SIMMIC* was designed to be easily interfaced with data extraction and analysis packages, such as *XTRACT* and *UEDEXTRA*.

3.5.2.1 *SIMMIC* workflow and subroutine description

The *SIMMIC* package requires two inputs to simulate MICs: the *xyz* coordinate file containing an optimised or guess geometry, and the differential cross-sections of the elements in the molecule at the experimental electron wavelength. The latter is generated using the Dirac partial-wave calculation package, *ELSEPA*,²²⁶ discussed in Section 3.5.2.2. The *xyz* coordinate is converted into a list of atomic pairs, for which the atomic and molecular scattering curves are calculated using Equation 2.5. A typical *SIMMIC* run is illustrated in the flowchart shown in Figure 3.35.

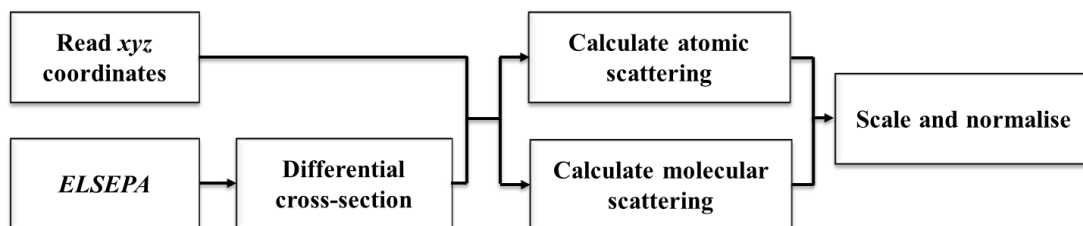


Figure 3.35: Flowchart representation of a typical MIC simulation using *SIMMIC*.

The differential cross-sections of all elements in the molecule are weighted and combined to generate a system-specific atomic-scattering function, shown in Figure 3.36, which can be used to remove the atomic scattering background from experimental data.

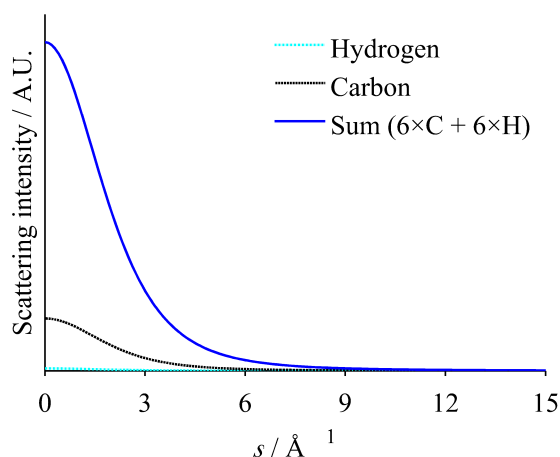


Figure 3.36: *SIMMIC* simulation of the atomic scattering of benzene, generated from the sum of the atomic scattering of six carbon and six hydrogen atoms.

A series of nested loops calculates the molecular scattering contribution of each pair of atoms to the overall diffraction signal. For simplicity purposes the effects of temperature and molecular vibrations are not taken into account in the calculation of theoretical diffraction patterns. MICs generated using *SIMMIC*, an example of which is shown in Figure 3.37, are cropped at a user-defined scattering range, normalised, and stored as a text string. The *SIMMIC* output is generated in a universal MIC format, which can be compared with data from any instrument.

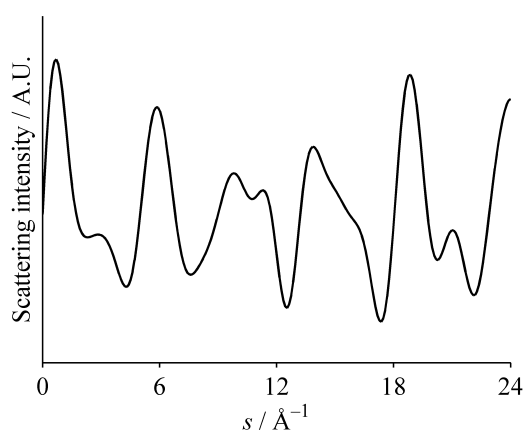


Figure 3.37: *SIMMIC* simulation of the MIC for benzene.

3.5.2.2 *SIMMIC* interface with ELSEPA

The elastic scattering of electrons and positrons by neutral atoms (ELSEPA) package, developed in 2004 by Salvat *et al.*,²²⁶ uses relativistic Dirac partial-wave analysis to compute the scattering amplitudes and differential cross-sections for elements between hydrogen and lawrencium based on their interactions with projectiles for kinetic energies between 10 eV and 1 GeV. ELSEPA is written in FORTRAN 77,²²⁷ which can be interfaced with the *SIMMIC* environment in MATLAB, to either run on request or as a stand-alone tool, which can be run at the beginning of a large batch of simulations. Electron diffraction apparatus are designed to operate over a narrow range of energies and, in most cases, beam energies are optimised for a given accelerating potential, which usually remains unchanged for the entire duration of the experiment. Therefore, *SIMMIC* features a repository of differential cross-sections for 103 elements calculated at the most widely-used electron-beam energies. The bash script used to run a batch of ELSEPA differential cross-section calculations can be found in Appendix E.

3.5.3 Time-dependent molecular intensity curve simulator (*TD-SIMMIC*)

The time-dependent molecular intensity curve simulator, *TD-SIMMIC*, employs the core subroutines developed for *SIMMIC* to simulate MICs with an additional temporal coordinate. *TD-SIMMIC* uses the output of molecular dynamics simulations, usually in the form of trajectory files, to generate time-dependent MICs similar to those obtained from UED studies.

3.5.3.1 *TD-SIMMIC* workflow and subroutine description

The *TD-SIMMIC* package requires two inputs to generate time-dependent MICs: an ensemble of trajectory files in a multi-xyz format, and the differential cross-sections of the elements in the molecule at the experimental electron wavelength. The ensemble of trajectory files are sorted by simulation time step and the individual xyz coordinates are separated into discrete geometry files and used with *SIMMIC* to generate MICs; these are then combined to generate a single time-step-specific MIC and added to a time-dependent MIC matrix. The conversion of trajectory files to a time-dependent MIC matrix is schematically depicted in Figure 3.38.

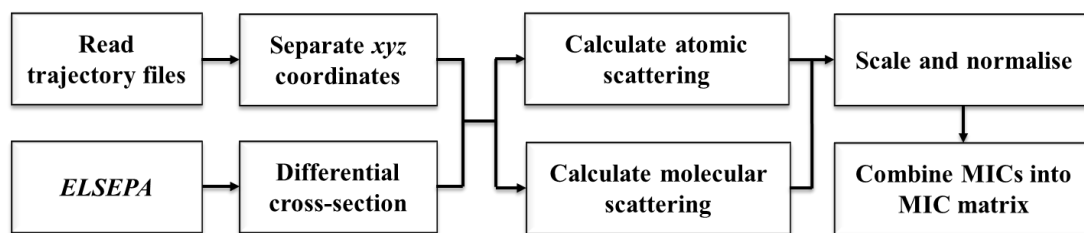


Figure 3.38: Schematic depiction of a typical time-dependent MIC simulation using *TD-SIMMIC*.

Although illustrative of the evolution of diffraction features as a function of simulation time, time-dependent MIC matrices cannot be compared with experimental data directly, as they assume an infinitesimally small temporal resolution for the instrument. Therefore, time-dependent MIC matrices are convoluted using an instrument-response function, which is usually based on the FWHM of the electron bunch at the sample, as determined during beam-profile studies, or taken from particle-tracer simulations. The use of these simulated datasets in the design of UED experiments and the analysis of UED data are further discussed in Chapter 5.

3.5.4 Molecular dynamics trajectory analysis package (*TRAVIS*)

The typical outputs of molecular dynamics simulations consist of a series of trajectory files containing information on the evolution of nuclei as a function of time. Most molecular dynamics simulation packages provide a suite of analytical tools to convert these multi-xyz files into structurally relevant parameters, which can be visualised, analysed, and compared to experimental data. However, these software tools are often limited to the analysis of internal coordinates and are difficult to customise.

The trajectory analysis and visualisation, *TRAVIS*, package was developed to address the need for a versatile visualisation tool for trajectory simulations. *TRAVIS* facilitates the study of the relationship between molecular and electronic structures, leading to a more complete understanding of PES topography and the wave-packet dynamics it induces.

3.5.4.1 Internal coordinate visualisation tool (*TRAVIS-ICV*)

The *TRAVIS* internal coordinate visualisation tool, *TRAVIS-ICV*, converts the output from internal coordinate analysis packages into trace plots. Data on the evolution of

internal coordinates are normalised and presented as a function of time. For clarity purposes, discontinuities in dihedral angles representing rotating groups are corrected to produce smooth curves. Alternatively, dihedral angles can be normalised between -180 and $+180^\circ$, which results in the loss of information regarding the direction of the rotation. Examples of internal coordinate evolution plots generated using *TRAVIS-ICV* can be found in Chapters 6 and 7.

3.5.4.2 Internal coordinate extraction tool (*TRAVIS-ICX*)

Internal coordinate analysis tools, such as the Newton-X statistical analysis routine,²¹⁶ are limited to the extraction of structural data concerning the distances and angles between discrete nuclei. Though sufficient to describe most conformation changes, such as isomerisations and dissociations, these parameters are not sufficient to describe the concerted motion of planes of atoms, observed in more complex mechanisms. This limitation is overcome with the *TRAVIS* internal coordinate extraction tool, *TRAVIS-ICX*, which uses vector analysis to calculate the geometric relationship between any two discrete points, axes, or planes in a molecule, and generates the internal coordinate evolution trace accordingly. The analysis of the ring-opening dynamics of asparagusic acid, presented in Chapter 6, showcases the capabilities of the *TRAVIS-ICX* tool.

3.5.4.3 Heat-map representation of phase space (*TRAVIS-HM*)

Structural dynamics are governed by the topography of the potential energy surface, and the initial conditions at excitation. Conceptually, one could use the path of a trajectory to map the shape of the hypersurface. However, the multi-dimensional nature of a hypersurface makes it impossible to plot and, therefore, hard to visualise. Alternatively, a hypersurface can be presented as a series of phase spaces, which can be plotted in two-dimensions, provided some assumptions and simplifications can be made. The *TRAVIS* heat-map tool, *TRAVIS-HM*, uses two internal-coordinate-analysis output files to generate a two-dimensional representation of the phase space visited. Normalised geometry abundances are transformed into a colour scale and displayed as a heat map. Potential reaction pathways can be identified easily in the two-dimensional projection of the hypersurface as discrete areas of high intensity between the reactant and the product. Examples of the phase-space heat-map representation generated using *TRAVIS-HM* can be found in Chapters 6 and 7.

3.5.4.4 Geometry overlay (*TRAVIS-GO*)

The visualisation of multiple geometric parameters in *TRAVIS-ICV* or *TRAVIS-HM* plots can become unfeasible as the system moves away from the Franck-Condon region and motions start to dephase. This issue was addressed with the development of the *TRAVIS* geometry overlay (*TRAVIS-GO*), which allows multiple geometries to be aligned along a user-defined internal coordinate and overlaid in a single image. Therefore, *TRAVIS-GO* allows the conformational space of the target molecules to be visually inspected at different instances during the simulation.

3.5.5 UED data-analysis package (*UEDEXTRA*)

UED experiments rely on software tools to transform noisy, temporally convolved diffraction patterns into structurally relevant time-dependent data, as discussed in Chapter 2. Despite the addition of a fourth dimension, time, the inherently lower SNR, and the vast increase in the number of diffraction images, UED data are analysed using similar methods to those implemented in traditional GED data analysis packages, such as *XTRACT*.

The UED extraction and analysis, *UEDEXTRA*, package was developed to address the need for robust methodologies for the analysis of time-dependent diffraction data. *UEDEXTRA* was designed for both parallel and serial operation in workstation or cluster environments, Moreover the low computational requirements of its core routines make it ideal as an on-the-fly data analysis tool for UED experiments. *UEDEXTRA* was originally developed as an analysis tool for the TRED apparatus in the summer of 2015 and later expanded to process data recorded using the SLAC UED apparatus, where its performance was benchmarked against similar packages developed by collaborators at SLAC.

3.5.5.1 *UEDEXTRA* workflow and subroutine description

UEDEXTRA transforms thousands of time-stamped diffraction patterns into a single time-dependent MIC matrix, showing the evolution of diffraction features as a function of time. During a typical run of *UEDEXTRA*, over ten subroutines are called to extract, transform, and plot data, as shown in Figure 3.39. At the start of the data extraction, diffraction patterns in a user-defined data repository are imported and assigned a unique ID number based on their acquisition time, scan identifier, and time delay.

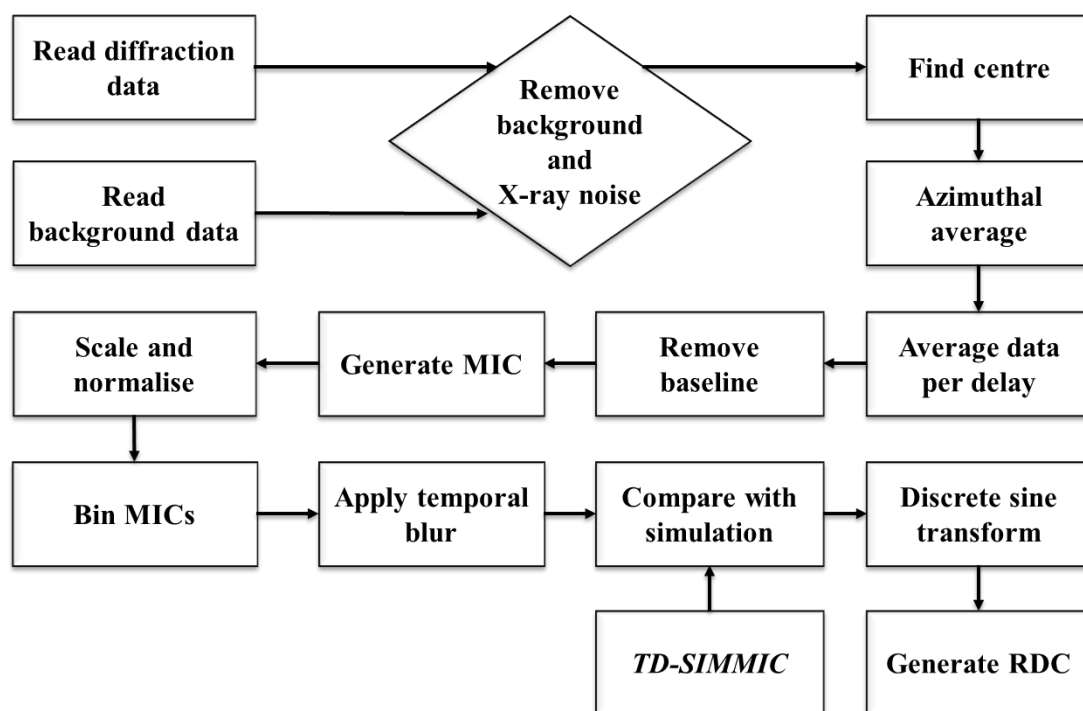


Figure 3.39: Flowchart showing a typical UED data extraction run using *UEDEXTRA*.

3.5.5.2 *UEDEXTRA* noise reduction

X-rays are amongst the main sources of noise in EMCCD detectors, such as the ANDOR iX888 Ultra²²⁸ at SLAC. These high-energy stray beams are generated when the electron beam hits an object, such as a collimator or the scintillator screen. Since CCD-chip technology is sensitive to both electrons and X-rays, diffraction images must be scanned meticulously for X-ray hits before data can be extracted. An X-ray hit results in a characteristic saturation of the pixel well as charge overflows into neighbouring pixels, producing a cluster of saturated pixels. These clusters are classified as sporadic or permanent, according to the X-ray hit removal algorithm show in Figure 3.40. X-ray hits classified as sporadic are replaced by the median of equivalent pixels from diffraction patterns recorded for the same time delay, while permanent hits are replaced by the median intensity of the radial polar coordinate elsewhere in the same image.

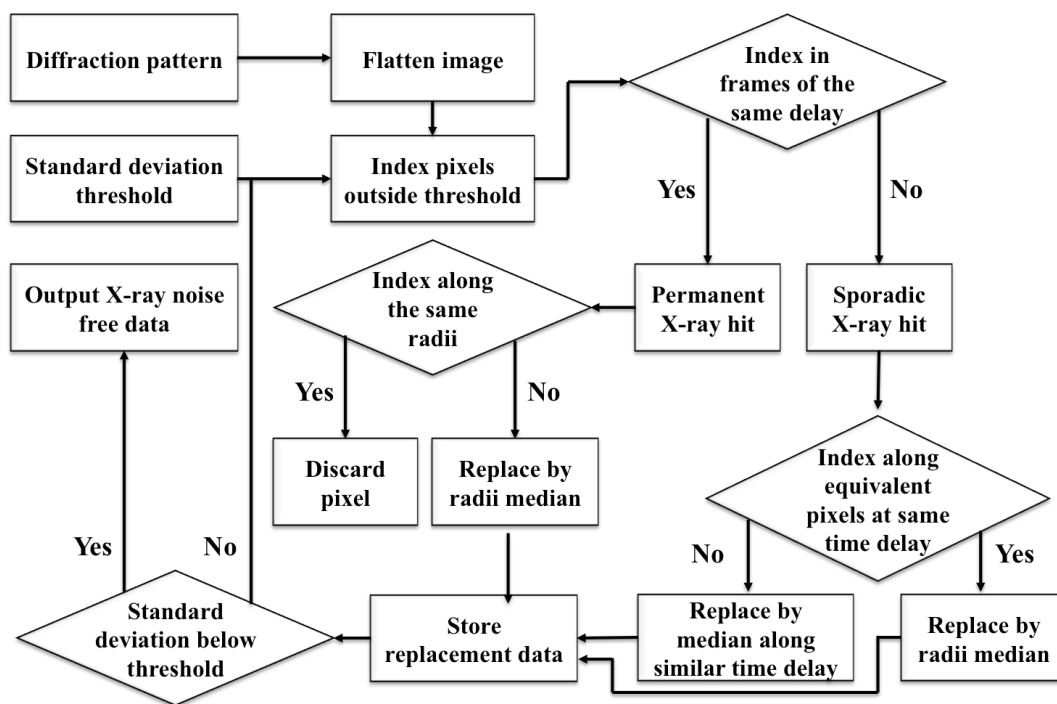


Figure 3.40: Flowchart showing the X-ray hit removal algorithm implemented in *UEDEXTRA*.

The X-ray removal cycle, shown in Figure 3.40, is interrupted when convergence is reached, and the standard deviated threshold is met. Failure to converge after 50 cycles causes the whole image frame to be removed from the dataset. The impact of X-ray removal on the SNR of a diffraction pattern is shown in Figure 3.41.

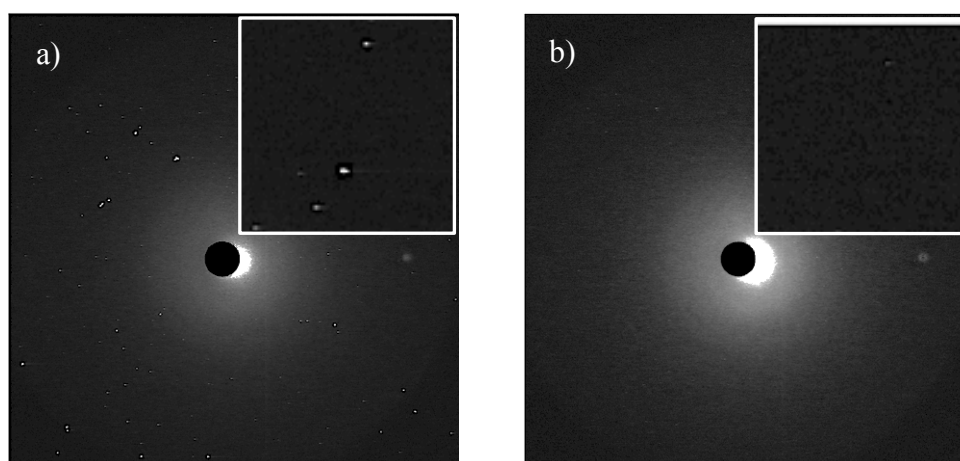


Figure 3.41: Diffraction pattern for 1,2-dithiane before time zero a) before, and b) after X-ray hit removal. The zoomed at the top-right corner of each pattern clearly illustrated the reduction in image noise achieved by the X-ray hit removal routine.

3.5.5.3 *UEDEXTRA* data extraction

Following the removal of X-rays, image frames are passed through a Wiener filter function and, using the *XTRACT* package (see Section 3.5.1), are azimuthally extracted into raw diffraction curves. The raw diffraction curves consist of a mixture of molecular scattering, atomic scattering, and background light from the optical pump. For signal post-processing purposes, atomic scattering and instrument-specific background are assumed to be smooth and remain constant during the exposure. Therefore, the smooth background signal is fitted with a logarithmic third-order polynomial and subtracted from the raw data, revealing the molecular scattering signal.

Temporally identical MICs are averaged to produce a single time-dependent MIC, which is then placed into 0.2 \AA^{-1} bins along the scattering vector dimension, to prevent data-point correlation, and added to a time-dependent MIC matrix. A convolution filter, obtained from beam-profile studies or from particle-tracer simulations, is used to smooth the MIC matrix along the temporal dimension, further improving its SNR, by removing high-frequency noise. The output of *TD-SIMMIC*, usually run ahead of UED experiments, is used to predict the quality of the time-dependent diffraction data.

A discrete sine transform (Fourier transform using the real matrices) is used with a Gaussian envelope function to convert time-dependent MICs into time-dependent RDCs, showing the evolution of discrete interatomic distances as a function of delay time. Examples of *UEDEXTRA*-generated time-dependent RDCs can be found in the UED study of 1,2-dithiane discussed in Chapter 5.

3.5.6 Future work and outlook

XTRACT, *SIMMIC*, *TRAVIS*, and *UEDEXTRA* were designed to address the needs of GED, UED, and computational studies, paving the way for the development of more robust methods and the expansion of functionality. Developments in detector technology, such as the commercial availability of direct-electron detectors, will require a complete redesign of the data extraction tools in order to cope with the considerably larger file sizes. Furthermore, technological improvement in high-performance computing technology, and the development of more robust molecular dynamics simulation packages, will undoubtedly lead to the simulation of larger and

more complex systems, for which analysis and visualisation will require ingenious software solutions. Therefore the upgrade of existing software packages and the development of new ones are unlikely to slow down in the foreseeable future.

Though crucial to the design of novel data-extraction and analysis methods, knowledge of GED and UED is not strictly necessary for the implementation of such methods in a software environment. Despite my efforts to optimise core scripts, minimise repetitive callbacks, and avoid redundancies, future versions of the packages described in this Section would undoubtedly benefit from the input of a trained programmer.

Chapter 4. GED study of DMABN

In Chapter 1 the photochemistry of DMABN is presented as a possible case study for UED. Therefore, ahead of future time-resolved experiments, a comprehensive study has been carried out on the ground-state structure of DMABN in the gas phase. The York GED apparatus was used to determine the structure of DMABN and also to ascertain the sample delivery parameters and experimental conditions required for future studies using the UED.

4.1.1 Aims and considerations

In 1994, Zachariasse *et al.* solved the crystal structure of DMABN using X-ray crystallography and reported an amino group pyramidalisation angle of $10.8(2)^\circ$.²²⁹ This pyramidalisation describes the angle between the plane of the aromatic ring and the plane made by the nitrogen and two methyl carbons. Microwave spectroscopy studies determined the amino-group in the gas-phase DMABN to be slightly more pyramidal at 15° .²³⁰ Although one could rationalise this difference as being a result of crystal packing, the fact remains that the ground-state structure of DMABN is still a topic of discussion. Furthermore, the pyramidalisation angle of DMABN determined from *ab initio* methods was found to be highly sensitive to the level of theory used and poorly predicted by most methods. For example, most DFT functionals, such as B3LYP and M06-2X,²³¹ failed to describe the pyramidalisation of DMABN, finding the benzene ring and the heavy atoms of the amino group to be coplanar. Therefore, the GED study presented in this Section aims to resolve the structure of DMABN unambiguously, including its pyramidalisation angle and, in the process, benchmark the computational methods.

4.1.2 GED experiment

GED data for DMABN were recorded on Fuji BAS-IP MP 2025²³² image plates at nozzle-to-detector distances of 234.5 and 487.0 mm. An accelerating potential of 42.22 keV was applied, producing electrons with an approximate wavelength of 5.85 pm. The low vapour pressure of DMABN (30 mTorr at 60°C)²³³ was overcome by the use of the heated nozzle assembly, described in Appendix B. The sample holder, transport lines and nozzle were held at 433 K, for both the longer and shorter nozzle-to-detector distances. The exposed image plates were scanned using a Fuji BAS-1800 II flat-bed scanner.²³⁴ Although five image plates were collected for each

nozzle-to-detector distance, only the three highest quality diffraction patterns were extracted using *XTRACT*. The experimental parameters used in the GED study of DMABN are summarised in Table 4.1.

Table 4.1: Summary of experimental parameters for the GED study of DMABN.

Nozzle-to-detector distance / mm	234.5	487.0
Electron wavelength / pm	5.85	5.85
T_{sample} / K	423	423
T_{nozzle} / K	433	433
Δs / Å	0.2	0.1
s_{min} / Å	8.4	4.4
s_{max} / Å	27.0	12.6
sw_1^a / Å	10.4	6.2
sw_2^a / Å	25.6	10.8
Scale factor (k)	0.0130(3)	0.0041(1)
Correlation parameter	0.476	0.498

^a Weighting points for the off-diagonal weight matrices

4.1.3 Theoretical methods

In the GED study of DMABN all *ab initio* quantum-chemical calculations were carried out using GAUSSIAN 09²³⁵ at the University of York Advanced Research Computing Cluster (YARCC).²³⁶ The highest-level geometry optimisations were carried out assuming C_s symmetry, at the B2PLYP/cc-pVQZ level, and extrapolated to the CBS limit. To establish the flexible restraints for use in the SARACEN-type GED refinement, a series of geometry optimisations were carried out at a lower level using different DFT functionals and employing correlation-consistent basis sets extrapolated to the CBS limit. A tabulated summary of these calculations can be found in Appendix G. The characters of all stationary points computed at this level were verified using vibrational frequency analysis and determined to correspond to minima on the ground-state potential-energy surface. Analytical force fields calculated at the B2PLYP/cc-pVDZ level were used with the SHRINK program to calculate accurate amplitudes of vibration (u_{h1}), and curvilinear correction (k_{h1}) needed to allow for the shrinkage effect in the GED experiment.

4.1.4 Geometric model

The geometric model of DMABN is based on C_s point-group symmetry and consists of 16 parameters, namely nine interatomic bonded distances (p_1 - p_9), five bond angles (p_{10} - p_{14}), and two dihedral angles (p_{15} - p_{16}), listed in Table 4.2. The numbering scheme used in the parameter description of DMABN is shown in Figure 4.1.

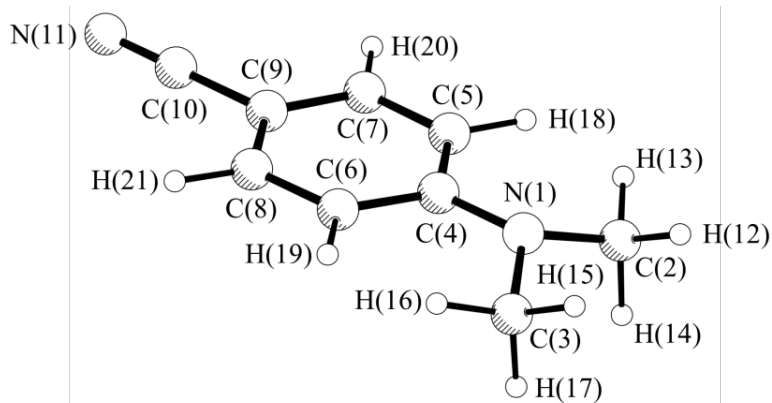


Figure 4.1: Structure of DMABN with atom numbering.

DMABN has six similar C–N and N–C bonded distances, which would fall under a single peak in the RDC and would be difficult to resolve separately. Therefore, refinement of these distances was carried out using a weighted average and corresponding difference parameters (p_1 - p_6). The cyano group carbon-to-nitrogen bonded distance is described using a separate parameter (p_7), while the methyl and benzyl carbon-to-hydrogen distances, are described as average parameters p_8 and p_9 , respectively. The aromatic ring interior angles are defined using parameters p_{10} and p_{11} and the benzyl and methyl hydrogen angles are defined with respect to the carbon backbone using the average parameters p_{12} and p_{13} , respectively. Parameters p_{14} and p_{15} define the amino group angle and pyramidalisation with respect to the aromatic ring. The last parameter, p_{16} , describes the dihedral angles between the methyl hydrogen and the benzyl-amino bond.

Table 4.2: List of parameters used the refine the structure of DMABN.^a

Parameter	Contributions
p_1 $rC-C, rC-N$ (Avg.)	$[C(9)-C(10) + 2 \times C(7)-C(9) + 2 \times C(5)-C(7) + 2 \times C(4)-C(5) + N(1)-C(4) + 2 \times N(1)-C(2)] / 10$
p_2 $rC-C, rC-N$ Diff. 1	$C(7)-C(9)/2 + C(4)-C(5)/2 - C(5)-C(7)$
p_3 $rC-C, rC-N$ Diff. 2	$C(4)-C(5) - C(7)-C(9)$
p_4 $rC-C, rC-N$ Diff. 3	$[C(9)-C(10)/4 + N(1)-C(4)/4 + N(1)-C(2)/2] - [C(7)-C(9)/3 + C(4)-C(5)/3 + C(5)-C(7)/3]$
p_5 $rC-C, rC-N$ Diff. 4	$[C(9)-C(10)/3 + 2 \times N(1)-C(2)/3] - N(1)-C(4)$
p_6 $rC-C, rC-N$ Diff. 5	$N(1)-C(2) - C(9)-C(10)$
p_7 $rC \equiv N$	$C(10)-N(11)$
p_8 $rC-H$ (Methyl) (Avg.)	$[C(2)-H(12) + C(2)-H(13) + C(2)-H(14)] / 3$
p_9 $rC-H$ (Benzyl) (Avg.)	$[C(5)-H(18) + C(7)-H(20)] / 2$
p_{10} $aC(5)C(4)C(6)$	$C(5)-C(4)-C(6)$
p_{11} $aC(7)C(9)C(8)$	$C(7)-C(9)-C(8)$
p_{12} $aCCH$ (Methyl) (Avg.)	$[C(4)-C(5)-H(18) + C(9)-C(7)-H(20)] / 2$
p_{13} $aCCH$ (Benzyl) (Avg.)	$[C(1)-C(2)-H(12) + C(1)-C(2)-H(13) + C(1)-C(2)-H(14)] / 3$
p_{14} $aC(2)N(1)C(4)$	$C(2)-N(1)-C(4)$
p_{15} $dC(5)C(4)N(1)C(2)$	$C(5)-C(4)-N(1)-C(2)$
p_{16} $dC(4)N(1)C(2)H(12)$	$C(4)-N(1)-C(2)-H(12)$

^a Refer to Figure 5.14 for the atom numbering scheme.

Refinable difference parameters can be combined with C-C and C-N average to represent discrete interatomic distances, as shown in Equations 4.1 to 4.6.

$$rC(9)-C(10) = p_1 + \frac{3p_4}{5} + \frac{p_5}{4} - \frac{2p_6}{3} \quad \text{Eq. 4.1}$$

$$rC(8)-C(9) \text{ and } rC(7)-C(9) = p_1 - \frac{p_4}{4} + \frac{p_2}{3} - \frac{4p_3}{5} \quad \text{Eq. 4.2}$$

$$rC(6)-C(8) \text{ and } rC(5)-C(7) = p_1 - \frac{p_4}{4} - \frac{2p_2}{3} - \frac{3p_3}{10} \quad \text{Eq. 4.3}$$

$$rC(4)-C(6) \text{ and } rC(4)-C(5) = p_1 - \frac{p_4}{4} + \frac{p_2}{3} - \frac{p_3}{5} \quad \text{Eq. 4.4}$$

$$rC(4)-N(1) = p_1 + \frac{3p_4}{5} - \frac{3p_5}{4} \quad \text{Eq. 4.5}$$

$$rN(1)-C(2) \text{ and } rN(1)-C(3) = p_1 + \frac{3p_4}{5} + \frac{p_5}{4} - \frac{p_6}{3} \quad \text{Eq. 4.6}$$

4.1.5 Structure refinement

GED data were analysed using the ED@ED v3.0¹⁴⁵ refinement program employing the electron scattering factors of Ross *et al.*¹⁷⁶ A total of 16 geometric parameters and 21 groups of amplitudes of vibration were refined during the least-squares refinement process. Flexible restraints were employed, using the SARACEN method, for 12 geometric parameters and 16 amplitudes of vibration. The remaining geometric parameters were allowed to refine freely. Amplitudes of vibration under the same peak in the RDC were tied to the amplitude with the greatest scattering intensity, which was then refined freely. Tied amplitudes were allowed to change according to their ratios with respect to the refining value. Amplitudes between hydrogen atoms were not tied or refined. The refined (r_{hl}) geometric parameters, selected interatomic distances (r_{a}), and amplitudes of vibration (u_{hl}) are listed in Tables 4.3 and 4.4, respectively. A complete list of the refined interatomic distances and amplitudes of vibration, and the least-squares correlation matrix can be found in Appendix G.

Table 4.3: Selected^a refined (r_{hl}) and theoretical^b (r_{e}) geometric parameters^c and SARACEN restraints^d applied in the refinement of DMABN.

Parameter	r_{hl} Value	r_{e} Value	Restraint
p_1 $r_{\text{C}-\text{C}}, r_{\text{C}-\text{N}}$ (Avg.)	141.74(5)	140.77	-
p_2 $r_{\text{C}-\text{C}}, r_{\text{C}-\text{N}}$ Diff. 1	2.3(1)	2.4	2.4(1)
p_3 $r_{\text{C}-\text{C}}, r_{\text{C}-\text{N}}$ Diff. 2	1.33(4)	1.33	1.33(3)
p_4 $r_{\text{C}-\text{C}}, r_{\text{C}-\text{N}}$ Diff. 3	3.3(2)	2.7	2.7(2)
p_5 $r_{\text{C}-\text{C}}, r_{\text{C}-\text{N}}$ Diff. 4	6.9(2)	6.9	6.9(1)
p_6 $r_{\text{C}-\text{C}}, r_{\text{C}-\text{N}}$ Diff. 5	2.3(4)	2.4	2.4(3)
p_7 $r_{\text{C}\equiv\text{N}}$	113.8(4)	116.0	-
p_{10} $a_{\text{C}(5)\text{C}(4)\text{C}(6)}$	117.40(9)	117.40	117.44(1)
p_{11} $a_{\text{C}(7)\text{C}(9)\text{C}(8)}$	118.52(8)	118.54	118.54(1)
p_{14} $a_{\text{C}(2)\text{N}(1)\text{C}(4)}$	119.3(4)	118.6	-

^a Angles to hydrogen atoms were not included for brevity. ^b B2PLYP/CBS.

^c Distances (r) are in pm, angles (a) and dihedrals (d) in degrees. ^d Derived from sequential DFT geometry optimisations using the B3LYP, B2PLYP, B3P86,²³⁷ B3PW91,²³⁸ HSEH1PBE,²³⁹⁻²⁴³ and PBEH1PBE^{244,245} functionals and the cc-pVDZ,²⁴⁶ cc-pVTZ,²⁴⁷ and cc-pVQZ²⁴⁸ basis sets; subsequently extrapolated to the CBS limit.

Table 4.4: Selected^{a,b} interatomic distances (r_a), refined (u_{GED}) and theoretical (u_{h1}) amplitudes of vibration and distance corrections (k_{h1}) for DMABN.

Atomic pair	r_a	u_{GED}	Restraint	k_{h1}	u_{h1}
u_{134} C(9)⋯N(11)	256.5(4)	7.0(3)	5.1(5)	-1.0	5.1
u_{77} C(5)⋯C(8)	278.6(2)	8.4(3)	6.5(7)	-0.1	6.5
u_7 N(1)⋯C(8)	369(2)	9.3(3)	6.4(6)	-2.1	6.4
u_8 N(1)⋯C(9)	420.3(2)	8.8(3)	6.8(7)	-2.4	6.8
u_{95} C(6)⋯N(11)	480.6(4)	10.7(5)	9(9)	-3.0	9.0
u_{64} C(4)⋯N(11)	538.4(4)	8.1(6)	7.3(7)	-3.6	7.3
u_9 N(1)⋯C(10)	563.1(3)	8.0(6)	7.3(7)	-3.6	7.3
u_{46} C(3)⋯C(10)	650.3(7)	12.4(8)	10.6(11)	-0.5	10.6
u_{10} N(1)⋯N(11)	674.5(4)	9.6(7)	7.8(8)	-6.0	7.8
u_{47} C(3)⋯N(11)	759.7(8)	13.7(8)	11.8(12)	-3.0	11.8

^a For clarity, amplitudes to hydrogen atoms were not included. ^b H⋯H amplitudes were not refined and remains fixed to the theoretical value (u_{h1}) determined from geometries calculated at the B2PLYP/cc-pVDZ level.

The good agreement between experimental and theoretical MICs and RDC, shown in Figures 4.2 and 4.3, respectively, testifies to the success of the refinement, for which $R_G = 0.062$ ($R_D = 0.041$). The structure of DMABN was determined with less than a tenth of a picometer of uncertainty on all distance parameters. Furthermore, interatomic distances, distance differences, angles, and dihedral angles were refined to within 1.5 pm (1.3%), 0.6 pm (0.6%), 0.8° (0.6%), and 0.03° (0.2%) of the theoretical values, respectively. Refined Cartesian coordinates for the GED-determined structure of DMABN can be found in Appendix G.

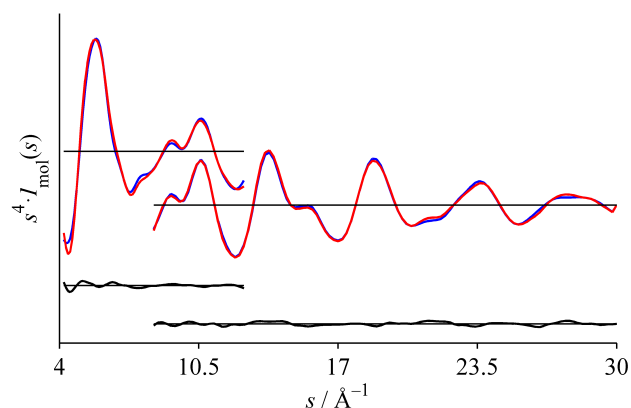


Figure 4.2: Experimental (red), theoretical (blue), and difference (experimental-minus-theoretical, black) MICs for DMABN.

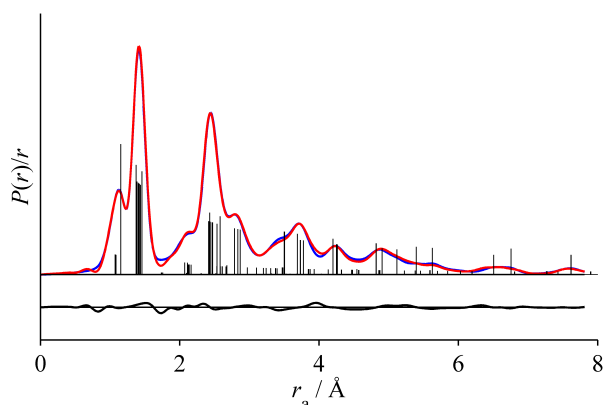


Figure 4.3: Experimental (red), theoretical (blue), and difference (experimental-minus-theoretical, black) RDCs for DMABN. Before Fourier inversion, experimental and theoretical MICs were multiplied by $s \cdot \exp(-2s^2 \cdot 10^{-5} / [(Z_N - f_N)(Z_C - f_C)])$ prior to Fourier inversion. f_N and f_C denote the atomic scattering factor for nitrogen and carbon taken from Reference 176.

The refinement of the dihedral angle $dC(5)C(4)N(1)C(2)$, which indirectly defines the pyramidalisation angle of the amino group, was found to have little impact in the overall R_G value. Therefore, the $C(5)C(4)N(1)C(2)$ dihedral angle was refined by stepping the value of parameter p_{15} and recording the R factor at every step to ascertain the best fit. Measurements were taken between 0° and 14° in 0.5° steps. The C_s symmetry of DMABN means that structures with negative $C(5)C(4)N(1)C(2)$ dihedral angles are mirror images of their positive counterparts. Therefore, the R factor for $dC(5)C(4)N(1)C(2)$ between 0 and -14° was inferred from the measured values between 0 and 14° . The evolution of R_G as a function of p_{15} value is shown in Figure 4.4. Three stationary points were identified within the 95% confidence limit: two local minima at 8° and -8° , the latter implied by symmetry, and one local maximum at 0° . The topography of the R_G evolution strongly resembles the double-well potential characteristic associated with the inversion of ammonia, hence suggesting similar behaviour in DMABN. The rapid interconversion between two local minima, *via* amino group inversion, would result in DMABN momentarily assuming a planar conformation, as the methyl groups cross the benzyl plane. The position of the 0° local maximum with respect to the 95% confidence limit (see Figure 4.4) corroborates the hypothesis of a constantly inverting DMABN, as it shows that a small fraction of the GED data could originate from a planar structure. Structures inside the two wells contribute the most to the diffraction signal and therefore produce the lowest R factor for the GED refinement. The R_G evolution data

in Figure 4.4 were fitted with a quadratic function and the minimum R_G value was found at a C(5)C(4)N(1)C(2) dihedral angle of 7.5° , which is equivalent to a pyramidalisation angle of 12.7° . Therefore, the pyramidalisation angle of DMABN was resolved within 2.3° (15%) and 1.9° (18%) of values determined by microwave spectroscopy and X-ray crystallography, respectively.

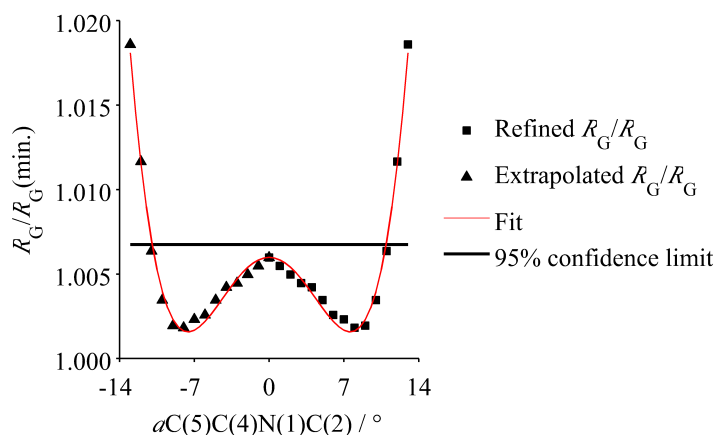


Figure 4.4: Variation in measured (squares) and symmetry inferred (triangles) $R_G/R_G(\text{min.})$ as a function of $dC(5)C(4)N(1)C(2)$. Data were fitted to a quadratic function (red line). The horizontal line denotes the 95% confidence limit.

The *ab initio* methods used in this study were benchmarked against the GED structure of DMABN. Table 4.5 shows the tabulated comparison between refined GED parameters and the geometric parameters determined from geometry optimisations carried out using different DFT functionals. The calculated geometry of DMABN at the B2PLYP/CBS level of theory was the closest to that determined from the GED experiment. In the case of DMABN, the use of higher level DFT methods is not only justified, but crucial to the accurate determination of molecular structure, as all other functionals fail to describe the pyramidalisation of DMABN.

Table 4.5: Refined GED and theoretical geometric parameters obtained from *ab initio* geometry optimisations of DMABN.

Parameter	GED	B2PLYP/ CBS	B3LYP/ CBS	B3P86/ CBS	PBEH1PBE/ CBS
$rC-C, rC-N$ (Avg.)	141.7(1)	140.8	140.8	140.3	140.3
$rC\equiv N$	114.5(4)	115.98	115.30	115.28	115.19
$aC(5)-C(4)-C(6)$	117.42(8)	117.44	117.34	117.54	117.55
$aC(2)-N(1)-C(4)$	119.3(36)	118.56	119.41	119.69	119.75
$dC(5)-C(4)-N(1)-C(2)$	8.49(1)	8.49	0.56	0.00	0.00

In summary, this Chapter reports the first complete GED structure refinement of DMABN, in which a pyramidalisation angle of 12.7° is revealed. Furthermore, this study has allowed for the benchmark of DFT functionals against the GED results, from which the double-hybrid DFT functional, B2PLYP, was identified as the best performing functional for DMABN. The GED study of DMABN is currently been prepared for publication.

Chapter 5. Experimental study of 1,2-dithiane

In this Chapter the photoinduced dynamics of 1,2-dithiane will be explored using time-averaged and time-resolved electron diffraction. These experimental studies will build upon previous observation by the Sølling group, and will be supported by computational studies carried out by the Wann group in 2016. All aspects of the roadmap to molecular movies proposed in Section 1.6 will be explored as diffraction is used to image the molecular motions of 1,2-dithiane following the absorption of mid-UV light.

5.1 Literature on 1,2-dithiane

In the 2015, Stephansen *et al.*, used a combination of time-resolved mass spectrometry (TRMS) and static quantum chemical calculations to explore the photoinduced dynamics of 1,2-dithiane, with the aim of understanding the role of S–S bridges in the photostability of folded structures protein structures.^{107,109} Stephansen’s potential energy surface scans along the S–S coordinate revealed a strongly dissociative S_1 state, accessible upon the absorption of mid-UV light.^{108,109} The steep topography of the potential energy surface between the Franck-Condon point and an S_1/S_0 minimum energy conical intersection (MECI), shown in Figure 5.1, was found to be consistent with the energetic cleavage of the disulfide bond.

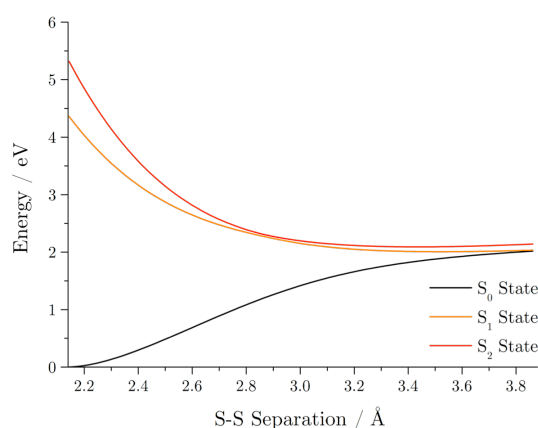


Figure 5.1: Diagrammatic representation of the potential energy surface of 1,2-dithiane along the S–S coordinates. Adapted from reference 108.

An elegant TRMS experiment by Stephansen *et al.* revealed an oscillating ion current with a ~ 400 fs period, which was assigned to the system rocking between the MECI and the S_1 min, shown in Figure 5.1.¹⁰⁹ Stephansen model for the ring-opening of 1,2-dithiane, suggested the wavepacket oscillates between the MECI and the S_1 minimum, leaking population to the S_0 state with every pass near the MECI,

whilst remaining confined to a maximum S···S separation (r_{S-S}) of 3.9 Å. This subtle “rocking” motion was found to be inconsistent with the topography of the dissociative state, which suggests the S-termini to move away from each other with considerable momentum. Moreover, a maximum r_{S-S} of less than 4 Å was believed to be unreasonably short considering the flexibility of the carbon-chain and the magnitude of the dissociative forces acting on the S-termini. The questions raised by Stephansen’s interpretation of the TRMS data drove the Wann group to computationally study the internal conversion dynamics of 1,2-dithiane.

In 2016, Rankine *et al.*, reported a more classically intuitive ring-opening motion for 1,2-dithiane.²⁴⁹ Non-adiabatic multi-reference molecular dynamics (NAMMD) simulations carried out at the SA3-CASSCF(10,8)/def2-SV(P) level using the NEWTON-X v1.4²¹⁶ and COLUMBUS v7.0,²¹³ revealed an oscillating elongation and contraction of the r_{S-S} coordinate, with a periodicity of ~350 fs and maximum r_{S-S} of 5 Å, as shown in Figure 5.2. More importantly, transient species straight-chain species were found between these oscillations. A detailed description of the methodology used to record these simulations can be found in reference 249.

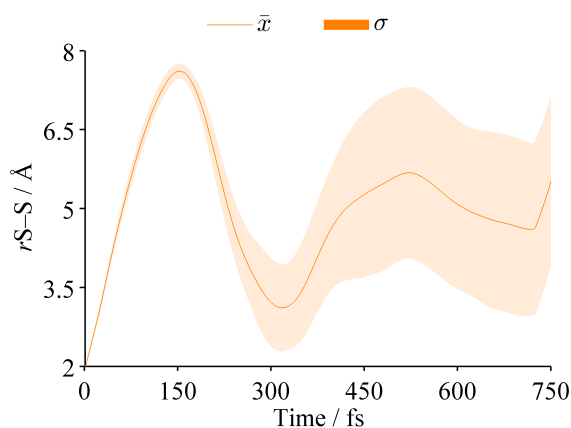


Figure 5.2: Evolution of r_{S-S} internal coordinate as a function of simulation time. Adapted from Reference 249.

The carbon backbone was found to force the S-termini, initially moving at ~3 pm per fs, into a curved trajectory around the carbon backbone, promoting the collision of the S-termini and ring closing opposite to the original bond. Furthermore, the motion associated with these oscillatory S-termini collisions was found to diphas quickly. Following the initial collision, the flexibility of the carbon backbone fails to confine the S-termini to pathways leading to further collisions and disulfide recombination.

Despite the discrepancies in predicted S⋯S separation, the motion proposed by Rankine *et al.*, does not dispute the experimental observation of Stephansen *et al.*, but rather proposes an alternative, more classically intuitive interpretation to the data. In fact, both models predict the same periodicity for $rS-S$ oscillation.

5.2 Aims and motivation

The study of 1,2-dithiane using diffraction aims to settle the dispute surrounding the motion 1,2-dithiane following mid-UV absorption. The more classically intuitive motion proposed by Rankine *et al.* will be referred to as the “molecular clackers model”, as the trajectory of the S-termini resembles that of the spheres in the clackers toy, shown in Figure 5.3; and the motion reported by Stephansen *et al.*, will be referred to as the “rocking model”.

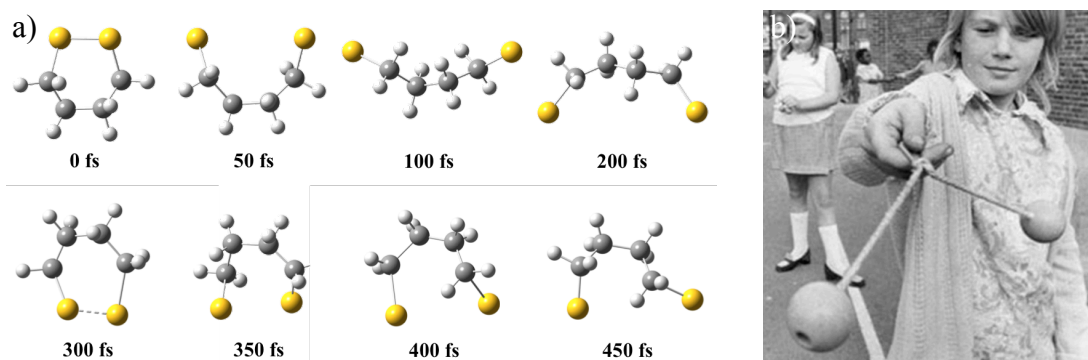


Figure 5.3: a) series of snapshots from a single trajectory simulation depicting the “molecular clackers” motion, and b) photograph of the clackers toy.²⁵⁰

The complex motions described by the “rocking” and “molecular clackers” models can be reduced to the evolution of the $rS-S$ internal coordinate, allowing the validity of the models to be assessed using a single parameter, *i.e.* whether or not the S⋯S separation exceeded 4 Å. The ability of electron diffraction to follow the evolution of interatomic distances with Ångström resolution make it ideally suited to the investigation of the 1,2-dithiane ring-opening dynamics, and possible validation of either the “rocking” or “molecular clackers” models. However, the sub-200 fs timescale suggested by both models, meant that this experimental investigation could not be carried out using the TRED apparatus at York, which temporal resolution is limited to 1 ps. Therefore, the time-resolved study of 1,2-dithiane was carried out using the UED apparatus at SLAC, described in Appendix D.

5.3 GED study of 1,2-dithiane

The accurate description of ground-state structures is at the foundation of any time-resolved structural study. In the case of 1,2-dithiane, the first step in the imaging of excited state dynamics involved the determination of its ground-state structure in the gas-phase using time-averaged GED.

5.3.1 Synthesis and characterisation

1,2-dithiane was synthesised at the University of York, using the method proposed by Whiteside *et al.*²⁵¹ A concentrated solution of HCl (0.7 mL of a 37 wt% aqueous solution, 8.6 mmol) was added to a solution of 1,4-butanedithiol (1.0 mL, 21.5 mmol) in DMSO (17 mL) and the reaction mixture was stirred at room temperature for two days. To prevent the propagation of undesired odours – characteristic to sulphur-containing compounds – the reaction vessel was fitted with a bleach trap vent. The mixture was then poured into iced water and extracted using dichloromethane (DCM). The organic layer was washed with water and dried with sodium carbonate. The extracted layer was concentrated at reduced pressure to yield a colourless liquid, consisting of a mixture of monomers and oligomers. 1,2-dithiane was separated by vacuum distillation (30-60 °C at 1 Torr) and collected in a dry ice-acetone trap, in the form of colourless needle-shaped crystals. Product purity was confirmed using ¹H NMR(CDCl₃): δ 2.83 (s, 4H) and δ 1.97 (s, 4H) [lit.²⁵¹ 2.85 (s, 4H) and 1.97 (s, 4H)]. ¹H and ¹³C NMR spectra were recorded using a 500 MHz Bruker spectrometer (AVIIIHD500) at the York Centre of Excellence for NMR. Furthermore, the crystal structure of 1,2-dithiane was determined using single-crystal X-ray diffraction, using an Oxford Diffraction SuperNova diffractometer at the experimental conditions listed in Table 5.1. The unit-cell dimensions and packing of 1,2-dithiane are presented in Table 5.2 and Figure 5.4, respectively. ¹H and ¹³C NMR spectra, X-ray crystallographic files, and crystal-structure refinement parameters for 1,2-dithiane can be found in Appendix G.

Table 5.1: X-ray crystallography experimental parameters for 1,2-dithiane.

Temperature / K	Crystal size / mm	Wavelength / Å	Goodness-of-fit
110.05(10)	0.275 × 0.113 × 0.049	CuKα (λ = 1.54184)	1.098

Table 5.2: Unit cell dimension for 1,2-dithiane.

Crystal system	Space group	a / pm	b / pm	c / pm
Orthorhombic ^a	Pnm2	531.77(3)	777.66(4)	675.47(4)

^a $\alpha = \beta = \gamma = 90^\circ$

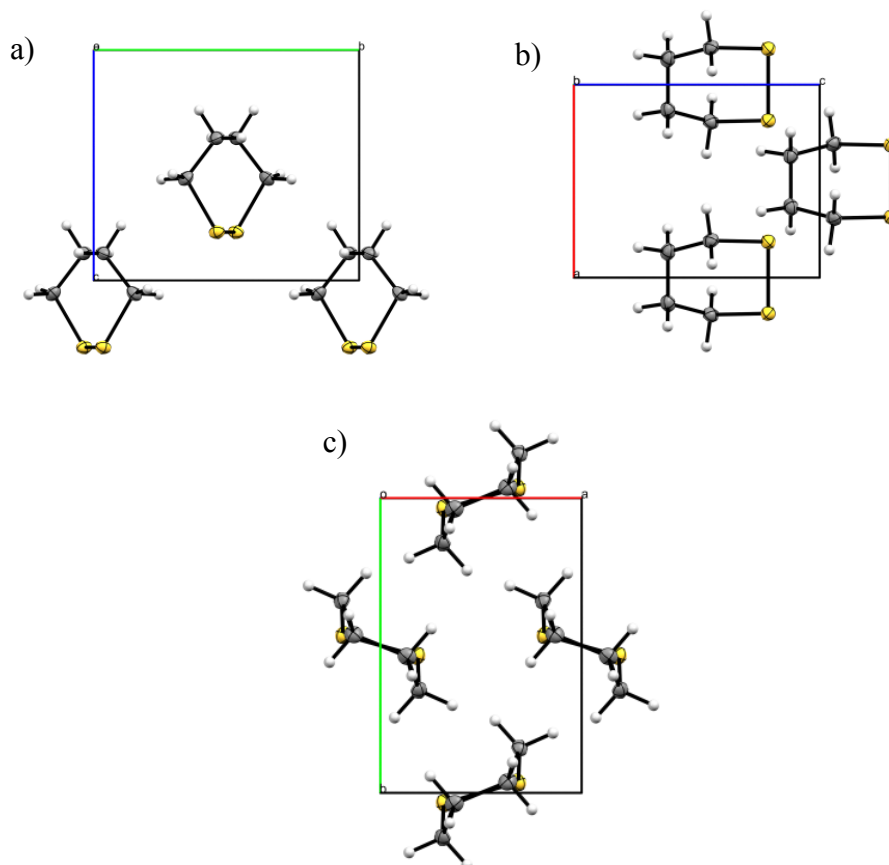


Figure 5.4: Crystal packing of 1,2-dithiane viewed along the a) a , b) b and c) c axes of the unit cell.

5.3.2 GED experiment

GED data for 1,2-dithiane were acquired using the York GED apparatus. An accelerating potential of 42.22 keV was applied, producing electrons with an approximate wavelength of 5.85 pm. The scattering intensities were recorded on Fuji BAS-IP MP 2025 image plates at nozzle-to-detector distances of 244.0 and 489.1 mm. 1,2-dithiane was delivered at room temperature to the path of the electron beam using an effusive nozzle (see Appendix B). The exposed image plates were scanned using a Fuji BAS-1800 II flat-bed scanner. Diffraction patterns were processed and extracted using the *XTRACT* software, described in Chapter 3. Although five image

plates were collected for each nozzle-to-detector distance, only the four highest quality diffraction patterns were converted to MICs and combined to produce the dataset used in the least-squares refinement. The experimental parameters used in the GED study of 1,2-dithiane are summarised in Table 5.3.

Table 5.3: Summary of experimental parameters for the GED data collection and refinement of 1,2-dithiane.

Nozzle-to-detector distance / mm	244.0	489.1
Electron wavelength / pm	5.85	5.85
T_{sample} / K	295	295
T_{nozzle} / K	293	293
Δs / Å	0.2	0.1
s_{min} / Å	8.4	4.8
s_{max} / Å	23.8	12.0
sw_1^a / Å	10.4	6.4
sw_2^a / Å	20.4	11.1
Scale factor (k)	0.203(4)	0.143(4)
Correlation parameter	0.485	0.495

^a Weighting points for the off-diagonal weight matrices

5.3.3 Theoretical methods

In the GED study of 1,2-dithiane all *ab initio* quantum-chemical calculations were carried out using the GAUSSIAN 09 software suite on YARCC. The highest-level geometry optimisations for 1,2-dithiane were performed in the C_2 -symmetric point group at the CCSD(T) level, employing the cc-pVTZ basis sets. The characters of all stationary points computed at this level were verified using vibrational frequency analysis and determined to correspond to minima on the ground-state potential-energy surface. To establish the flexible restraints for use in the SARACEN-type GED refinement, a series of geometry optimisations was also carried out using different DFT methods and employing correlation-consistent basis sets extrapolated to the complete basis set limit. A tabulated summary of these calculations can be found in Appendix G. Analytical force fields calculated at the B3LYP/cc-pVQZ level were used with the SHRINK program to determine the amplitudes of vibration (u_{h1}) and curvilinear corrections (k_{h1}) needed to account for the shrinkage effect in the GED experiment.

5.3.4 Geometric model

The geometric model for 1,2-dithiane comprises four interatomic bonded distances (p_1 - p_4), six bond angles (p_5 - p_{10}), and two dihedral angles (p_{11} - p_{12}), listed in Table 5.4 and represented as r , a and d , respectively. Figure 5.5 shows the atom numbering scheme used in the model.

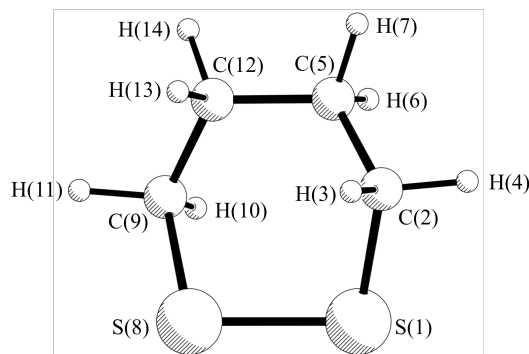


Figure 5.5: Structure of 1,2-dithiane with atom numbering.

Table 5.4: List of parameters used to refine the structure of 1,2-dithiane.

Parameter	Contributions
p_1 r_{S-S}	S(1)–S(8)
p_2 r_{S-C} (avg.)	[S(1)–C(2) + S(8)–C(9)] / 2
p_3 r_{C-C} (avg.)	[C(2)–C(5) + C(12)–C(9)] / 2
p_4 r_{C-H} (avg.)	[C(2)–H(3) + C(2)–H(4) + C(5)–H(6) + C(5)–H(7) + C(9)–H(10) + C(9)–H(11) + C(12)–H(13) + C(12)–H(14)] / 8
p_5 a_{SSC} (avg.)	[S(1)S(8)C(9) + S(8)S(1)C(2)] / 2
p_6 $a_{SCH_{eq}}$ (avg.)	[S(1)C(2)H(4) + S(8)C(9)H(11)] / 2
p_7 $a_{SCH_{ax}}$ (avg.)	[S(1)C(2)H(3) + S(8)C(9)H(10)] / 2
p_8 a_{SCC} (avg.)	[S(1)C(2)C(5) + S(8)C(9)C(12)] / 2
p_9 $a_{CCH_{eq}}$ (avg.)	[C(2)C(5)C(7) + C(9)C(12)C(14)] / 2
p_{10} $a_{CCH_{ax}}$ (avg.)	[C(2)C(5)C(6) + C(9)C(12)C(13)] / 2
p_{11} dX^a_{SSC}	XS(8)S(1)C(2)
p_{12} $dSSCC$ (avg.)	[S(8)S(1)C(2)C(5) + S(1)S(8)C(9)C(12)] / 2

^a Dummy atom 1 Å away from the centroid of the S(1)–S(8) bond along the S(1)S(8)C(12) plane.

5.3.5 Structure refinement

GED data were analysed using the ED@ED v3.0¹⁴⁵ refinement program employing the electron scattering factors of Ross *et al.*¹⁷⁶ Flexible restraints were applied using the SARACEN method for seven geometric parameters and 12 amplitude of vibration. The remaining geometric parameters were allowed to refine freely. Amplitudes of vibration under the same peak in the RDC were grouped together, with only the one with the greatest scattering intensity allowed to refine and all other amplitudes allowed to change according to their ratios to the refining values. Amplitudes of vibration between hydrogen atoms were not refined, instead being fixed to theoretical values. The refined (r_{hl}) geometric parameters, and interatomic distances (r_{a}) and amplitudes of vibration (u_{hl}), are listed in Tables 5.5 and 5.6, respectively. For brevity purposes, angles and amplitudes to hydrogen were removed from Tables 5.5 and 5.6. A complete list of the refined interatomic distances and amplitudes of vibration and the least-squares refinement correlation matrix can be found in Appendix G. The comparisons between experimental and theoretical MICs and RDCs, shown in Figures 5.6 and 5.7, respectively, illustrate the successful refinement of 1,2-dithiane, for which $R_{\text{G}} = 0.082$ ($R_{\text{D}} = 0.050$).

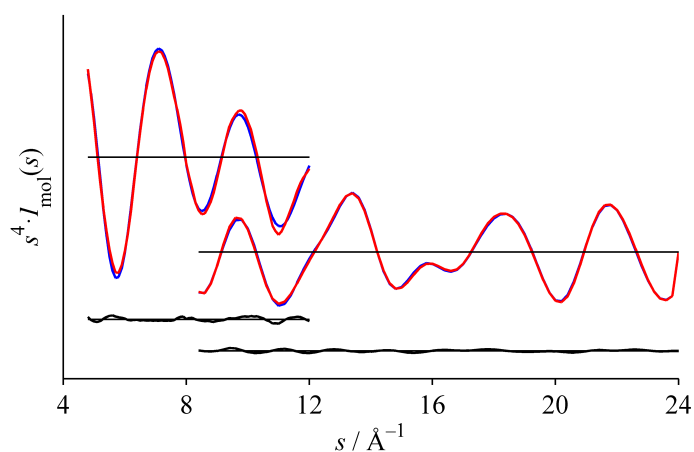


Figure 5.6: Experimental (red), theoretical (blue), and difference (experimental-minus-theoretical, black) MICs for 1,2-dithiane.

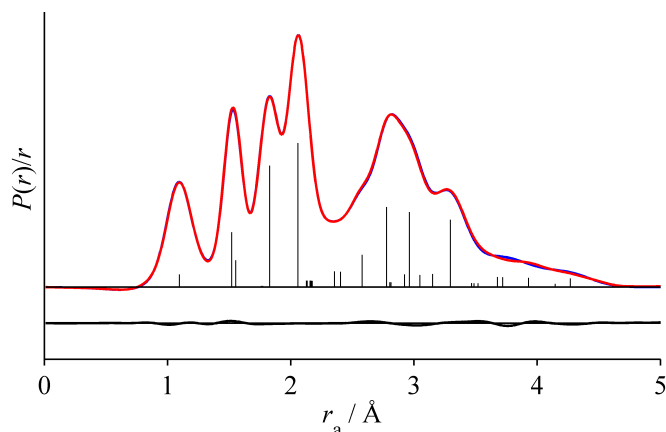


Figure 5.7: Experimental (red), theoretical (blue), and difference (experimental-minus-theoretical, black) RDCs for 1,2-dithiane. Experimental and theoretical MICs were multiplied by $s \cdot \exp(-2s^2 \cdot 10^{-5} / [(Z_S - f_S)(Z_C - f_C)])$ prior to Fourier inversion. f_S and f_C denote the atomic scattering factors for sulfur and carbon taken from Reference 176.

Table 5.5: Refined (r_{h1}) and theoretical^a (r_e) geometric parameters^b and SARACEN restraints^c applied in the refinement of 1,2-dithiane.

Parameter	r_{h1} Value	r_e Value	Restraint
<i>Independent</i>			
p_1 $rS-S$	205.7(2)	206.9	-
p_2 $rS-C$ (avg.)	183.0(2)	182.6	-
p_3 $rC-C$ (avg.)	152.1(5)	152.8	-
p_4 $rC-H$ (avg.)	109.4(2)	109.1	109.1(6)
p_5 $aSSC$ (avg.)	99.4(2)	99.1	-
p_6 $aSCH_{eq}$ (avg.)	104.9(2)	104.8	104.8(2)
p_7 $aSCH_{eq}$ (avg.)	108.43(8)	108.43	108.43(7)
p_8 $aSCC$ (avg.)	111.9(3)	112.7	-
p_9 $aCCH_{eq}$ (avg.)	108.17(9)	108.18	108.18(8)
p_{10} $aCCH_{ax}$ (avg.)	108.76(4)	108.76	108.76(4)
p_{11} $dXSSC$	28.4(2)	28.2	28.2(3)
p_{12} $dSSCC$ (avg.)	-62.3(5)	-61.8	-61.8(5)
<i>Dependent</i>			
d_1 $rC-C$ (opposite $rS-S$)	155.2(9)	153.5	-
d_2 $dSCCC$ (avg.)	64.5(9)	64.8	-
d_3 $dCCCC$ (avg.)	63.0(12)	61.4	-

^a B3LYP/CBS. ^b Distances (r) are in pm, angles (a), and dihedral angles (d) in degrees. ^c Derived from geometry optimisations using B3LYP, B2PLYP, B3P86, B3PW91, HSEH1PBE and PBEH1PBE at the CBS limit.

Table 5.6: Selected^{a,b} interatomic distances (r_a), refined (u_{GED}) and theoretical (u_{h1}) amplitudes of vibration and distance corrections (k_{h1}) for 1,2-dithiane.

Atomic pair	r_a	u_{GED}	Restraint	k_{h1}	u_{h1}
u_{43} C(5)–C(12)	155.4(9)	3.1(4)	5.2(5)	0.2	5.2
u_1 S(1)–C(2)	182.9(2)	4.9(4)	-	0.1	5.4
u_7 S(1)–S(8)	205.7(2)	5(3)	-	0.1	5.1
u_{22} C(2)⋯C(12)	258(7)	6.6(7)	7.1(7)	−0.2	7.1
u_4 S(1)⋯C(5)	277.8(4)	6.8(5)	-	−0.2	6.9
u_8 S(1)⋯C(9)	296.3(4)	8.4(4)	-	−0.2	8.1
u_{11} S(1)⋯C(12)	329.6(4)	10.7(2)	7.7(8)	−0.4	7.7

^a Amplitudes to hydrogen atoms were not included for brevity. ^b H⋯H amplitudes were not refined and remained fixed to the theoretical value (u_{h1}) determined from geometries calculated at the B3LYP/CBS level.^{193,211}

All interatomic distances, angles, and dihedrals angles were refined to within 1.1 pm (0.5%), 0.8° (0.5%), and 0.5° (0.8%) of the theoretical values, respectively. The agreement between the experimental and theoretical equilibrium-structure parameters testifies to quality of the data and the success of the refinement. Cartesian coordinates for the GED-determined structure of 1,2-dithiane can be found in Appendix G. Table 5.7 compares the values for geometric parameters obtained using CCSD(T) and DFT methods with those from GED and X-ray structures.

Table 5.7: Refined GED and X-ray^a and theoretical geometric parameters *ab initio* geometry optimisations of 1,2-dithiane.

Parameter	GED	X-ray	CCSD(T) /cc-pVTZ	B2PLYP /CBS	B3LYP /CBS
$r_{\text{S-S}}$	205.8(2)	205.3(1)	207.6	205.5	206.9
$r_{\text{S-C}}$ (avg.)	182.9(2)	181.9(4)	182.7	181.7	182.6
$r_{\text{C-C}}$ (avg.)	151.9(5)	151.1(6)	153.0	152.6	152.8
$r_{\text{C-H}}$ (avg.)	109.5(3)	-	109.4	109.0	109.1
a_{SSC} (avg.)	99.3(2)	98.78(11)	98.2	98.9	99.1
a_{SCC} (avg.)	111.9(3)	112.2(3)	112.2	112.5	112.7
d_{XSSC}	28.4(2)	-	29.2	28.7	28.2
d_{SSCC} (avg.)	−62.3(5)	−62.9(3)	−63.71	−62.6	−61.8

^a Recorded during the characterisation of 1,2-dithiane (see Section 5.3.1).

The bonded S–S interatomic distance is overestimated by more than 2 pm at CCSD(T)/cc-pVTZ level and 1 pm at the B3LYP/CBS level compared to the GED structure. The calculated geometry of 1,2-dithiane at the B2PLYP/CBS level was closest to that obtained from both GED and X-ray crystallography experiments. For this particular cyclic disulfide, the perturbation-corrected double-hybrid DFT functional, B2PLYP, was found to out-perform other hybrid DFT and CC methods. Furthermore, the distances, angles, and dihedral angles refined from GED data were found to be within 1 pm (0.5%), 0.5° (0.5%), and 0.6° (0.6%) of those from X-ray crystallography. Little difference was found between the structures of 1,2-dithiane the gas phase and the crystal. Therefore, the structure of 1,2-dithiane appears to be reasonably impervious to distorting lattice effects. This observation is further corroborated by the lack of evidence for intramolecular bonding in the unit cell of 1,2-dithiane, shown in Figure 5.4.

In summary, this Section reports on first gas-phase structure of 1,2-dithiane, which was used as a starting point for the UED study presented in Section 5.4.

5.4 UED simulation of 1,2-dithiane

Following the methodology proposed in the roadmap to molecular movies, the results of computational studies by Rankine *et al.*²⁴⁹ were used to simulate UED data, allowing for a more informed accessed of experimental feasibility. The *TD-SIMMIG* package, presented in Section 3.5.3, was used to generate time-dependent molecular intensity curves and simulate the signature of the ring-opening motion of 1,2-dithiane in the reciprocal space.

Assuming the “molecular clackers” model, the UED signal of 1,2-dithiane, shown in Figure 5.8a, was simulated for the s values between 1 and 8 Å⁻¹, which is the typical scattering range of UED apparatus.⁴¹ To simulate the detrimental effects of limited temporal resolution in the quality of UED data, a Gaussian shaped instrument-response blur function was applied to the simulated UED signal, as shown in Figure 5.8b.

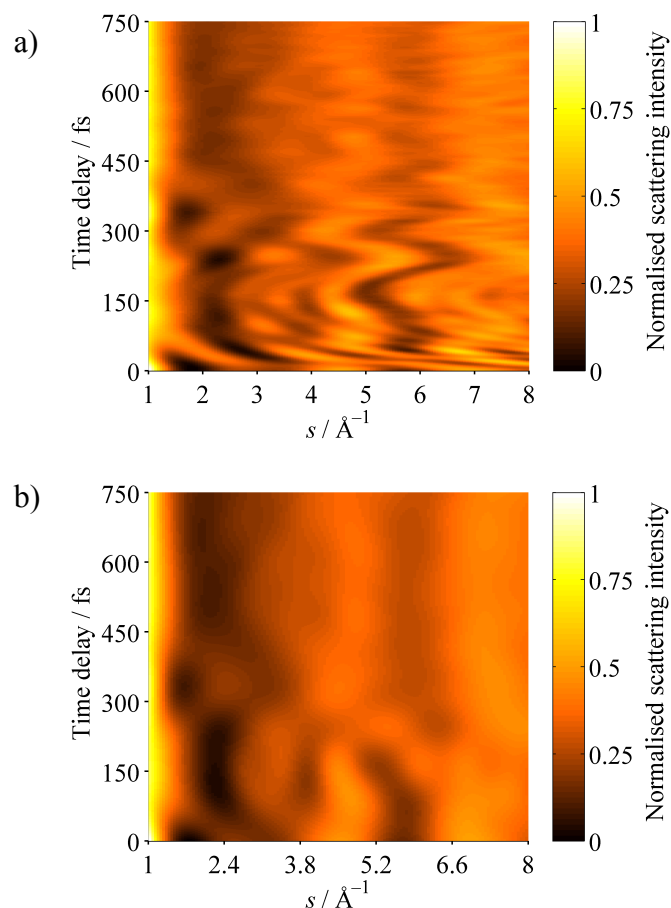


Figure 5.8: Simulated time-dependent MIC matrix for 1,2-dithiane a) before, and b) after convolution with a 200 fs instrument-response function.

The UED simulation for 1,2-dithiane predicted the time-dependent signal to be confined to an s range of 1 to 5 \AA^{-1} , as shown in Figure 5.8b. In most UED apparatus, including the MeV apparatus at SLAC, the geometry and size of the detector prevents the detection of electrons between 1 and 2.5 \AA^{-1} , which in the case of 1,2-dithiane would have resulted in a considerable loss of structural information. Therefore, these results were used pre-emptively to optimise the geometry of the SLAC UED detector prior the UED study of 1,2-dithiane. Moreover, the signature of the ring opening of 1,2-dithiane in reciprocal space was identified as a subtle oscillation in diffraction features between 1 and 4 \AA^{-1} with a periodicity of approximately 350 fs. The discrete sine transform of simulated MICs revealed the real-space signature of the “molecular clackers” motion, which was identified as the periodic increase in interatomic distances between 4 and 6 \AA , shown in Figure 5.9.

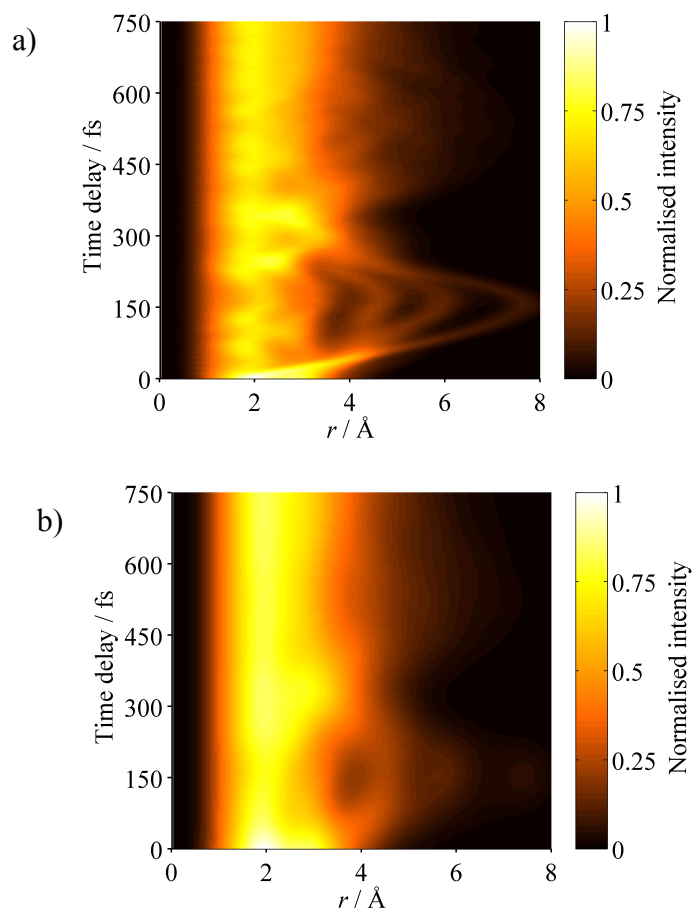


Figure 5.9: Simulated time-dependent RDC matrix for 1,2-dithiane a) before and b) after convolution with a 200 fs instrument-response function.

5.5 UED study of 1,2-dithiane

The study of the photoinduced dynamics of 1,2-dithiane was carried out using the UED apparatus at SLAC.⁴¹ UED experiments presented in this Section were purposely designed to follow the r S–S coordinate in 1,2-dithiane, and unambiguously report on the nature of its ring-opening motion.

5.5.1 Synthesis and characterisation

The thermal polymerisation of cyclic disulfides, such as 1,2-dithiane, is well described in the literature.²⁵² Murata *et al.* reported a polymerisation yield of $\sim 27\%$ for a solution of 1,2-dithiane at 313 K.²⁵³ Therefore, the shipping of 1,2-dithiane to SLAC could compromise the purity of the sample and, consequently, the quality of the UED data. To prevent sample contamination, 1,2-dithiane was synthesised at the PULSE Institute, located inside the SLAC complex, according to the route described in Section 5.3.1, and stored at $-5\text{ }^{\circ}\text{C}$. The melting point of 1,2-dithiane was measured

at 32 °C (literature: 31-32 °C),²⁵⁴ confirming the purity of the sample. Furthermore, the gas-phase UV absorption spectrum of 1,2-dithiane was recorded using a modified UV-vis PerkinElmer spectrophotometer, which was found to be in very good agreement with simulated spectra, albeit with a blue shift of 10 nm, as shown in Figure 5.10. The UV absorption spectrum of 1,2-dithiane was calculated using the nuclear ensemble approach²⁵⁵ implemented in NEWTON-X v2.0 at the TD-PBEH1PBE/6-311+G* level. In this approach, absorption bands are computed from the transition energies and the transition moments of a Wigner-distributed ensemble of structures, which are then convoluted and phenomenologically smoothed to produce experimentally representative spectral intensities and widths.

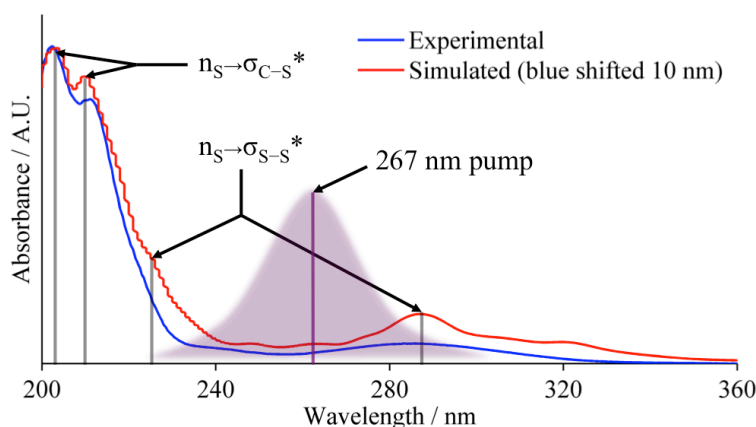


Figure 5.10: Simulated and recorded UV absorption spectra of 1,2-dithiane, showing four absorption bands centred at approximately 202, 211, 238, and 286 nm, corresponding to two $n_S \rightarrow \sigma_{C-S}^*$ and two $n_S \rightarrow \sigma_{S-S}^*$ transitions, respectively.

The UED study of 1,2-dithiane focused on the dynamics initiated following the absorption of 267 nm light, which lies between the two broad absorption bands centred at ~ 238 and ~ 286 nm, corresponding to a transition from the n orbital on the S atom to the C-S σ^* orbital.

5.5.2 Experimental parameters

In the UED study of 1,2-dithiane, the MeV UED apparatus electron gun was operated at 40° phase, 4.4 MeV, and with a repetition rate of 180 Hz, producing electrons with an approximate wavelength of 0.3 pm. A series of solenoid lenses and collimators were used to optimise the brightness and transverse profile of the electron beam at the interaction region, and minimise the dark current at the detector.

The UED simulations carried out ahead of experiments (see Section 5.4), predicted the diffraction features associated with the ring opening of 1,2-dithiane to fall within the low angle scattering components of the diffraction, *i.e.* below 2 \AA^{-1} . To prevent the hole in the centre of the scintillator from cropping these structurally rich diffraction features, the electron beam was deflected towards the edge of the detector aperture (see Appendix D for details on the detector geometry). Although suitable for capturing the ring-opening motion of 1,2-dithiane in reciprocal space, this configuration is much more prone to saturation of the detector, as small deflections in the path of the beam could cause unscattered electrons to hit the edge of the hole, producing a cascade of high-energy X-rays. The detector response to scattered electrons, dark current and pump laser background, was optimised using the diffraction pattern of crystalline gold, shown in Figure 5.11.

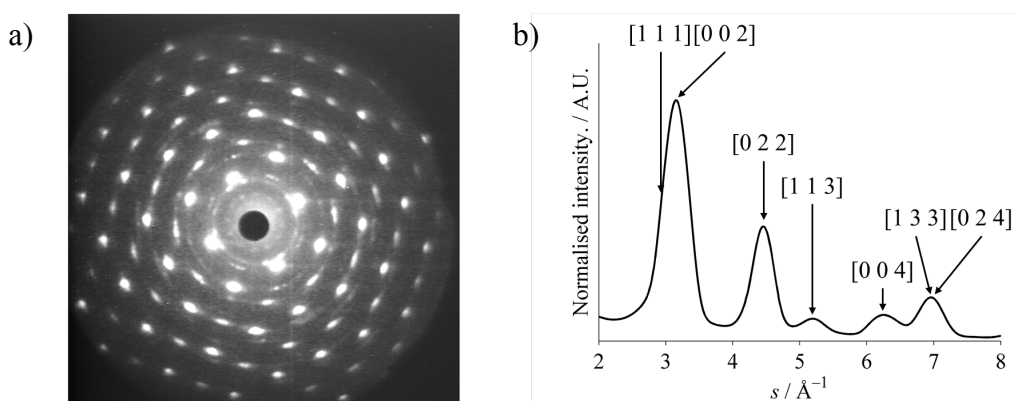


Figure 5.11: a) Diffraction pattern and b) Bragg peak assignment for crystalline gold.

5.5.3 Sample delivery

1,2-dithiane was carried into the gas-phase using a flow of helium (300 mbar) carrier gas and delivered to the electron beam using a Parker pulsed nozzle. However, the rate of volatilisation of 1,2-dithiane was found to be insufficient to maintain a stable sample delivery at the optimum pulsed nozzle duty cycle of 180 Hz with an opening time of 200 μs . To increase the volume of sample available, 1,2-dithiane was allowed to evaporate overnight inside the sample holder, which, once saturated, was able to deliver a constant sample density for over five hours. During the overnight evaporation and for the duration of the UED experiment, the sample holder was kept slightly below room temperature, and the nozzle and transport line heaters were disabled to prevent the polymerisation of 1,2-dithiane.

Diffraction data recorded before time zero were found to be in very good agreement with the GED data recorded for ground-state 1,2-dithiane (see Section 5.3), as shown in Figure 5.12. The static diffraction of 1,2-dithiane was used to fine-tune the spatial overlap between the nozzle and the electron beam and to confirm the purity of the sample.

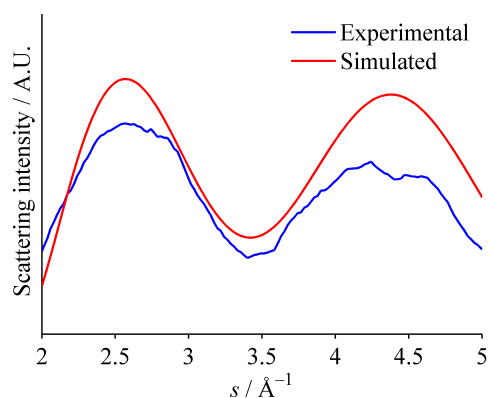


Figure 5.12: Comparison between the experimental and simulated MICs for 1,2-dithiane recorded before time zero, and simulated for a ground-state structure.

5.5.4 Time-zero determination

The time-zero of the UED study of 1,2-dithiane was determined using the photoionisation-induced lensing method described in Section 3.2.7. Despite its reliability, this method is only accurate to within 100 fs of the true experimental time-zero. To improve the accuracy of the time-zero, UED simulations (see Section 3.5.3) were used to identify the dynamics of the most dominant time-dependent features in reciprocal space, which in the case of 1,2-dithiane are the increase in scattering intensities between 4 and 5 \AA^{-1} , $I(4-5)$, and the simultaneous depletion of the intensities between 3.5 and 4 \AA^{-1} , $I(3.5-4)$. By monitoring the evolution of the $I(4-5)/I(3.5-4)$ ratio over a series of two-point scans carried out at increasingly narrowed temporal window, the onset of the 1,2-dithiane ring-opening was mapped with 50 fs resolution. The evolution of $I(4-5)/I(3.5-4)$ was fitted with a Gaussian cumulative distribution function, shown in Figure 5.13, allowing the time zero, *i.e.* delay of half maximum intensity, to be determined accurately.

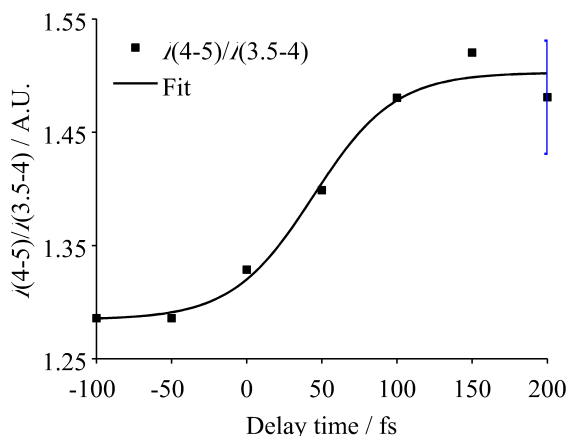


Figure 5.13: Evolution of the $I(4-5)/I(3.5-4)$ as a function of delay time, showing the onset of the ring-opening motion. Representative error bars are included in the 200 fs datapoint.

5.5.5 Time-dependent diffraction data acquisition

Time-dependent diffraction data were acquired in three UED experiments, comprising 90 individual scans, each containing 18 delay points. The diffraction pattern at each time delay was acquired over a single 20 s exposure using an EMCCD detector (see Appendix D for details). The range of the observation window used in UED experiments was chosen to encompass two periods of the ~ 350 fs S–S oscillations reported by both models in the literature (see Section 5.1). This observation window consisted of 18 time delays equidistantly spaced between -50 and 750 fs in 50 fs steps, and a delay at -1 ps and 5 ps for normalisation purposes. Before each scan the observation window was randomised, eliminating the effects of instrument-specific drifts and instabilities on the time-dependent data. Data were time stamped and stored according to the scan number and position in the delay stage.

5.5.6 Reduction, extraction and manipulation of UED data

The conversion of UED data into easily interpretable molecular movies, requires a few substantial transformations to the data, as thousands of diffraction patterns must be converted to simple representations of the evolution of interatomic distances as a function of delay time. This process is facilitated by the purpose-built *UEDEXTRA* package described in great detail in Section 3.5.5.

The first step in the processing of the UED data for 1,2-dithiane involved the subtraction of the background produced by EMCCD detector, using background images recorded at the beginning of each experiments. Following the removal of the detector background, the image post-processing tool implemented in the *UEDEXTRA* package was used to identify and remove read-out noise and noise caused by X-ray hits, improving the SNR of the UED data by over 50%. The efficacy of the background subtraction and X-ray removal algorithm in the reduction of the noise levels is demonstrated in Figure 5.14 for the before-time-zero diffraction of 1,2-dithiane.

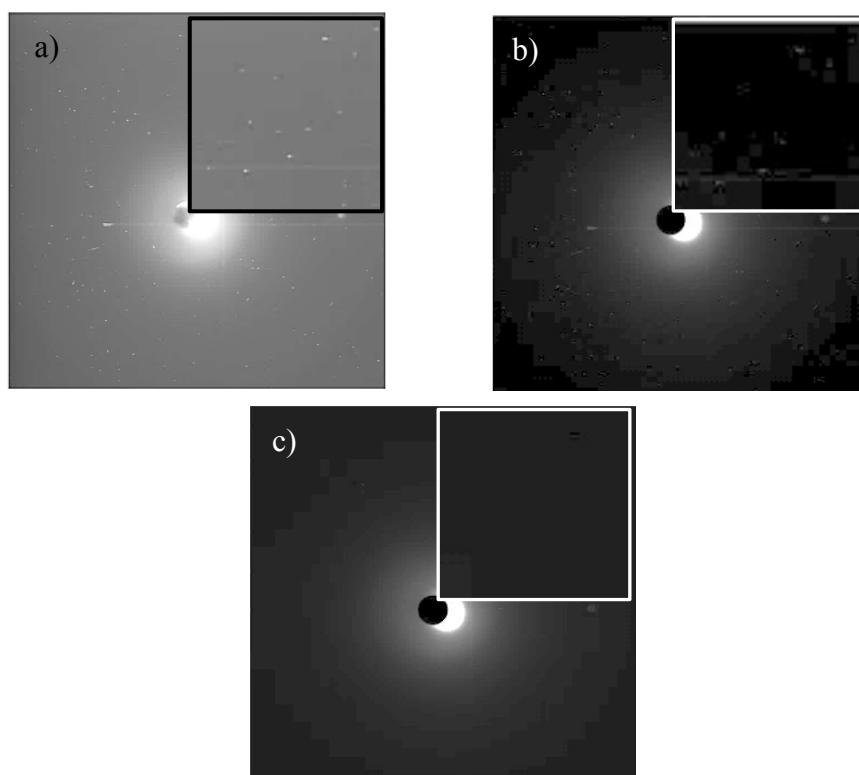


Figure 5.14: Time-dependent diffraction patterns of 1,2-dithiane a) before the subtraction of the EMCCD background, and b) before and c) after the removal of X-ray noise. Zoomed areas at the top-right corner of each frame, clearly show the reduction in noise.

These X-ray hit free diffraction patterns were extracted using the azimuthal averaging routine implemented in *UEDEXTRA*, producing the ensemble of scattering intensity curves and time-dependent MICs, shown in Figure 5.15.

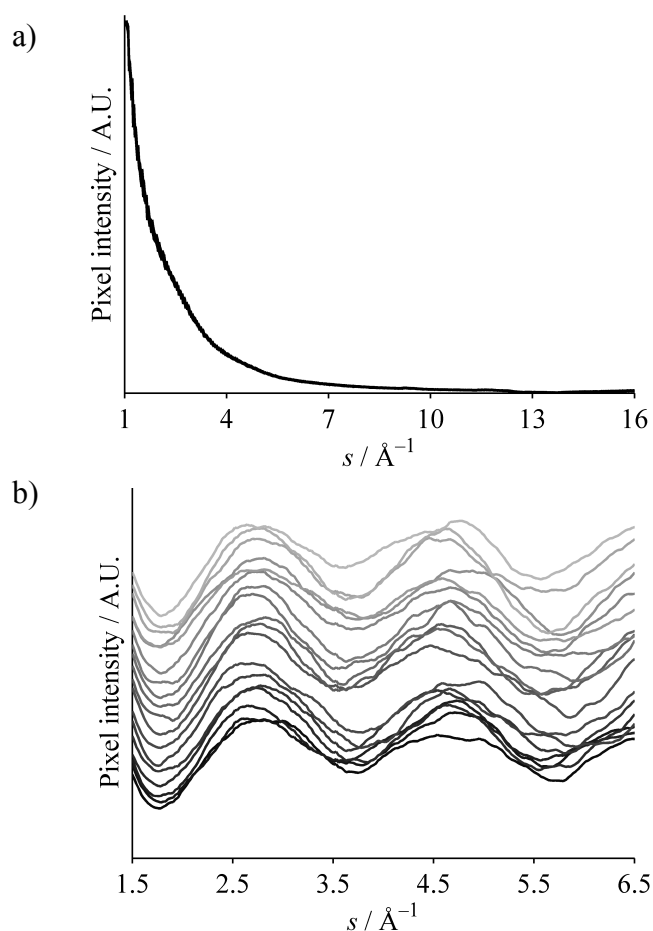


Figure 5.15: Time-dependent a) scattering intensity curves, and b) MICs for 1,2-dithiane.

Time-dependent MICs were sorted according to time delay, averaged, and compiled as a single time-dependent MIC matrix, showing the evolution of diffraction features as a function of time. The averaged time-dependent MICs were binned in 0.2 \AA^{-1} intervals, producing the MIC matrix shown in Figure 5.16a. The size of the “bin” was selected based on the GED study of 1,2-dithiane, which showed that a 0.2 \AA^{-1} separation between data points reduced the overall correlation of the data. The binned MIC matrix was convoluted with a Gaussian envelope, with a shape identical to the temporal profile of the electron beam, producing the MIC matrix shown in Figure 5.16b.

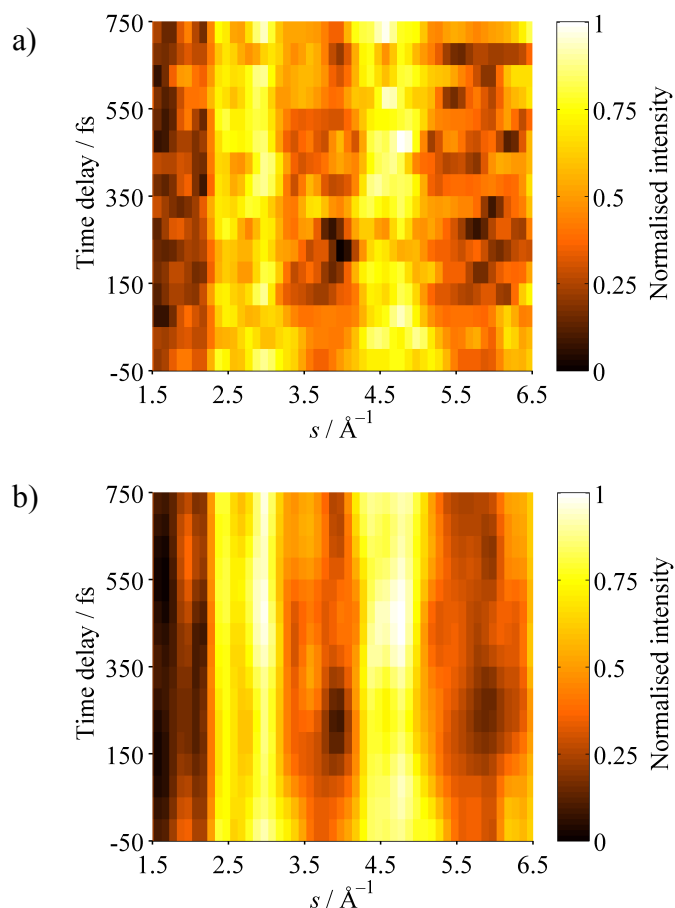


Figure 5.16: Time dependent MIC matrix for 1,2-dithiane a) before and b) after the Gaussian envelope convolution.

The time-dependent MIC matrix for 1,2-dithiane, showing the ring-opening of 1,2-dithiane in reciprocal space, was transformed into a real-space representation of the evolution of discrete interatomic distances, expressed as a time-dependent RDC. The discrete sine transform used to generate the time-dependent RDC, shown in Figure 5.17, was supported by the Gaussian envelope function, G , in Equation 5.1:

$$G(s) = \exp(-0.05s^2), \quad \text{Eq. 5.1}$$

where s is the scattering vector. This support function was determined empirically during the development of the *UEDEXTRA* package using the static diffraction data for nitrogen. To minimise the number of artefacts induced by the discrete sine transform of a finite dataset, the time-dependent MIC matrix was padded with zeros.

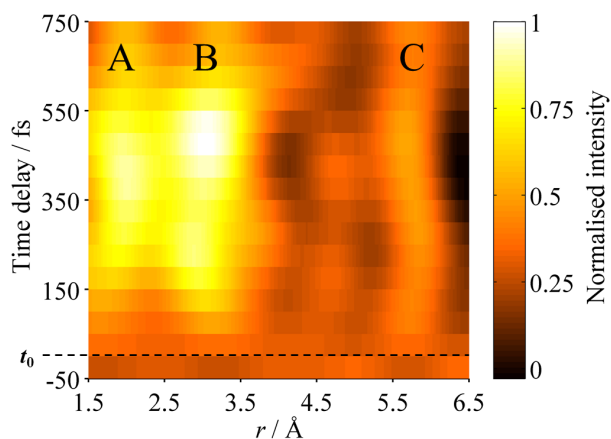


Figure 5.17: Time-dependent RDC matrix for 1,2-dithiane, showing the evolution of interatomic distances between 1.5 and 2.5, 2.5 and 3.5, and 4.0 and 6.5 Å, labelled A, B and C, respectively.

The intensity of the diffraction signal associated with interatomic distances between 1.5 and 2.5 Å, was found to increase approximately 100 fs after the elongation of interatomic distances between 2.5 and 3.5 Å. These sets of interatomic distances, corresponding to the r_{S-S} , $r_{S-C\alpha}$, $r_{C\alpha-C\beta}$, $r_{C\beta-C\beta}$ and $r_{C\alpha\cdots C\beta}$, and the $r_{S\cdots C\beta}$, $r_{S\cdots C\alpha}$ and $r_{C\alpha\cdots C\alpha}$ internal coordinates, (labelled features A and B in Figure 5.17), respectively, are depicted schematically in Figure 5.18.

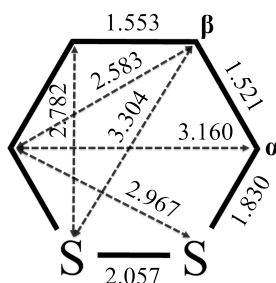


Figure 5.18: Molecular structure of 1,2-dithiane with labelled interatomic distances. Interatomic distances are shown in Å, and for clarity purposes distances to hydrogens atoms are not included.

The interatomic distances between 4 and 6.5 Å, grouped under feature C, were found to undulate with an amplitude of approximately 1 Å and a period of ~ 400 fs. Despite being in agreement with the oscillation reported by Stephansen *et al.* for the S \cdots S separation,^{107,109} the observation of structural features with interatomic distances between 4 and 6.5 Å disproved Stephansen’s “rocking” motion, which predicted a

maximum S··S separation of 3.83 Å. A detailed analysis of the time-dependent RDCs of 1,2-dithiane can be found in Section 5.5.7.

5.5.7 Molecular movie of 1,2-dithiane

The time-dependent RDC matrix of 1,2-dithiane, more specifically the evolution of interatomic distances between 4 and 6.5 Å, suggests that the internal conversion of 1,2-dithiane occurs *via* the periodic opening and closing of the disulfide ring intermediated by straight chain species. Interatomic distances between 3.5 and 4 Å and 5.25 and 6.25 Å were attributed to S··C separations in the ring and the S··S separation, respectively. In this Section, all structural information is interpreted from the shifts in the interatomic distances, rather than from their nominal intensities, as these are strongly dependent on the extraction method employed. For simplicity purposes, interatomic distances to hydrogen atoms were excluded from this analysis.

The time-dependent RDC matrix, shown in Figure 5.19, revealed the onset of long S··S interatomic distances (5.2 to 6 Å) ~50 fs after excitation, which is consistent with energetic cleavage of the disulfide bond and elongation of the S··S separation. Interatomic distances corresponding to the S··C α and S··C β internal coordinates, measured in the ring-closed ground-state structure of 1,2-dithiane at 2.9 and 3.3 Å (see Figure 5.19), were also found to increase, albeit with a ~50 fs delay with respect to the onset of *r*S··S elongation. After reaching a maximum S··S separation at 200 fs, the S-termini were found to move towards each other, forcing the ring to close, resulting in a decrease in interatomic distances above 3.5 Å. The S··S and S··C separations are shortest at 450 fs, suggesting a near-closed ring and possible recombination of the disulfide bond. As predicted by NAMMD simulations, disulfide bond recombination was shortly followed by a second ring-opening event, expressed as the rapid increase in S··C and S··S separations (3.5 to 4.5 Å, and 5.8 to 6.2 Å, respectively). The periodicity of the *r*S··S oscillation, measured to be ~400 fs, is in good agreement with the 411 fs period reported by Stephansen *et al.*^{107,109} The delayed onset of the ring-opening motion with respect to the disulfide cleavage, the periodic oscillation of the inter-ring distances, and periodic elongation of the *r*S··S to an almost straight-chain configuration, strongly corroborate the “molecular clackers” motion predicted by Rankine *et al.*²⁴⁹

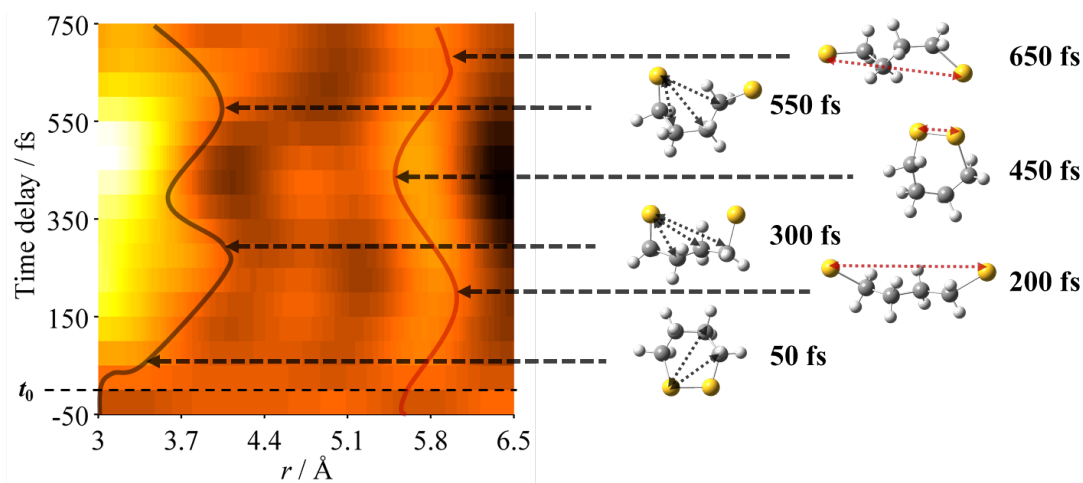


Figure 5.19: Diagram showing the time-dependent RDC matrix of 1,2-dithiane with a schematic representation of the “molecular clackers” motion.

In summary, the UED measured amplitude and periodicity of $rS\cdots S$ was found to support the “molecular clackers” model, settling the argument presented in Section 5.1. Moreover, the UED study of 1,2-dithiane produced the first molecular movie for a cyclic disulfide, capturing previously unseen ring-opening motions of this class of molecules.

5.5.8 Publication of the UED study of 1,2-dithiane

The findings reported in this Chapter, are currently being prepared for publication. The UED study of 1,2-dithiane is an ideal chase study to showcase the synergistic relationship between NAMMD simulations and UED experiments, and how these can be used to reveal previously unseen structural dynamics. Crucial to this relationship is the ability to compare experimental results with simulation, and *vice versa*. Therefore, a new set of NAMMD simulations has been requested to better reproduce the experimental conditions of the UED study. In these simulations, geometries in the Wigner-ensemble will be selected based on the overlap between the calculated vertical excitation energy and the measured profile of the pump laser at SLAC, and geometries with vertical excitations outside the bandwidth of the laser will be rejected. These simulations will be carried out using the new NEWTON-X 2.0 package,²¹⁷ where much improved speed will allow a two-fold increase in the number of trajectories that can be calculated. The quality of experimental data will also be improved with the development of new software tools for handling and re-sorting data.

Chapter 6. Computational study of asparagusic acid

The UED study of the internal conversion dynamics of 1,2-dithiane paved the way and motivated the study of more complex and biologically relevant systems, such as 1,2-dithiolane-4-carboxylic acid, commonly known as asparagusic acid. Unlike 1,2-dithiane, where the flexibility of the carbon backbone allows the ring-opening motion to explore a vast region of the hypersurface, asparagusic acid is expected to remain confined to a more discrete region of phase space, as the freely rotating carboxylic acid group sterically hinders the motion of the S-termini. The computational study in this Chapter aims to explore the excited-state dynamics of asparagusic acid, particularly the effect of the carboxylic acid group on the photostability of the disulfide bond, constituting the body of work supporting future UED studies.

The study of photoinduced dynamics of asparagusic acid was carried out using a combination of static electronic structure calculations and molecular dynamics simulations, presented in Section 6.1 and 6.2, respectively. In Section 6.4, the excited-state dynamics of asparagusic acid are contrasted with those of 1,2-dithiane, elucidating the role of functional groups and steric hindrance in the photostability of cyclic disulfides.

6.1 Static electronic structure calculations for asparagusic acid

Static electronic structure calculations were used to explore the conformational space of asparagusic acid in the ground state, and to validate the selection of active space used to describe the disulfide bond breaking and subsequent ring-opening dynamics. The numbering scheme used in these calculations is shown in Figure 6.1. These calculations constitute the theoretical body of work supporting the molecular dynamics simulations presented in Section 6.2.

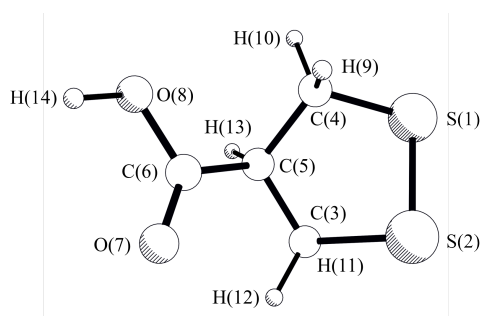


Figure 6.1: Numbering scheme used in the computational study of asparagusic acid.

6.1.1 Conformational space search

The conformational space of asparagusic acid was explored using a series of potential energy surface scans of the dihedral angle between the ring and the carboxylic acid group, $dC(4)C(5)C(6)O(7)$. Relaxed potential energy surface scans carried out at the MN12SX/def2svp^{256,257} level using GAUSSIAN 09, revealed three unique conformers, shown in Figure 6.2.

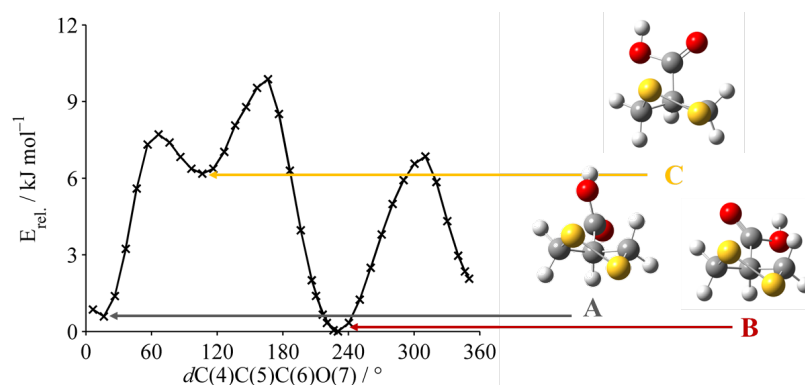


Figure 6.2: Relaxed potential energy surface scan of asparagusic acid along the $dC(4)C(5)C(6)O(7)$ internal coordinate.

The three conformers were optimised at the MP2/cc-pVTZ level, and validated as local minima using vibrational frequency calculations. The optimised structures of the three conformers of asparagusic acid can be found in Appendix F. Conformers A and B consist of a twisted heterocycle with an equatorial carboxylic acid group rotated $\sim 90^\circ$ and $\sim 120^\circ$ with respect to the plane of the ring, respectively. On the other hand, conformer C consists of an envelope heterocycle with an axial carboxylic acid group rotated $\sim 10^\circ$ with respect to the plane of the ring. The conformer search revealed a shallow PES, with energy barriers between conformers of less than 10 kJ mol^{-1} , implying that, at room temperature, asparagusic acid exists as a distribution of conformers. Therefore, the Boltzmann distribution expression shown in Equation 2.13 was used to calculate the conformer ratios of asparagusic acid at common sample delivery temperatures, presented in Table 6.1.

Table 6.1: Conformer ratios for asparagusic acid at room temperature (293 K), melting point (350 K), and in a supersonic molecular beam ($<100 \text{ K}$).

Sample delivery	Temperature / K	A/B/C conformer ratio / %
Supersonic	<100	0/100/0
Effusive (25 °C)	293	8/57/35
Effusive (melt)	350	11/53/36

Asparagusic acid has an estimated vapour pressure at room temperature of 5.1×10^{-5} Torr, making its delivery to the gas phase challenging. Therefore, future UED studies are likely to be carried out at higher temperatures using molten asparagusic acid. For this reason, all computational studies in this section were carried out assuming an A/B/C conformer ratio of 11/53/36%.

6.1.2 Active-space selection

A series of rigid scans at the TD-B3LYP/6-311G* level^{258,259} revealed that, although energetically separated at the Franck-Condon point, the four lowest singlet states (S_0 , S_1 , S_2 , S_3) in asparagusic acid come into close proximity at large $rS-S$ separation. Therefore, further computational investigations were carried out using CASSCF averaged over four states. The choice of active space for these CASSCF calculations consisted of five doubly occupied orbitals: two σ_{S-C} (HOMO-4 and HOMO-3), one σ_{S-S} (HOMO-2), two sets of sulfur lone-pairs (HOMO-1 and HOMO), and three virtual orbitals: one σ^*_{S-S} (LUMO) and, two σ^*_{S-C} (LUMO-1 and LUMO -2) orbitals. For simplicity purposes, only the active space of the most abundant conformer at the predicted experimental temperature of 350 K is shown in Figure 6.3. The molecular orbital representation of the selected active space in the three conformers can be found in Appendix F.

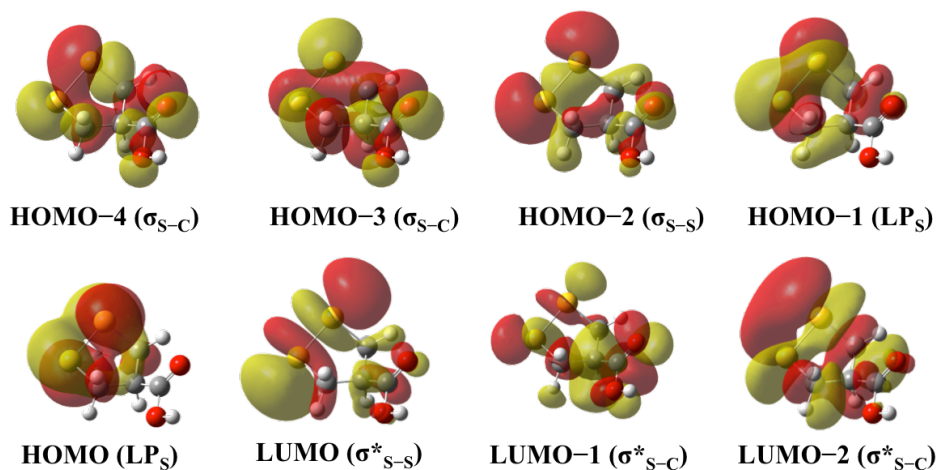


Figure 6.3: Choice of active space for asparagusic acid (conformer B).

The S_0 and S_1 minima geometries of asparagusic acid were optimised using the geometry direct inversion in the iterative subspace (GDIIS) algorithm²⁶⁰ implemented in COLUMBUS v7.0 at the SA4-CASSCF(10,8)/6-31G* level and

validated using SA4-CASPT2/cc-pVDZ in MOLCAS v8.0. In the SA4-CASPT2 calculations an imaginary shift of 0.3 was imposed to overcome the detrimental effects induced by weakly coupled intruder states. The Cartesian coordinates of the S_0 and S_1 minima of three conformer of asparagusic acid can be found in Appendix F. The vertical excitation energy between the S_0 minima and the S_1 Franck-Condon point was computed at ~ 3.5 eV, which corresponds to light with a wavelength of ~ 354 nm. Although, estimated and based on a “static” model, knowledge of the wavelength required to trigger a conformational change is a key aspect in the design of UED experiments.

6.1.3 Interpolated internal coordinate potential energy surface scans

The S_1 Franck-Condon point and S_0 and S_1 minima were used as waypoints in a series of LIIC scans, designed to map the topography of the dissociative potential energy surface. These scans, calculated at the SA4-CASSCF(10,8)/cc-pVDZ level and validated at the SA4-CASPT2/cc-pVDZ level using MOLCAS v8.0, revealed a steep topography between the S_1 Franck-Condon point and the S_1 minima resembling that of 1,2-dithiane (see Section 5.1). The agreement between LIICs computed using CASSCF and CASPT2, shown in Figure 6.4, validates the choice of active space and the use of SA4-CASSCF(10,8) in the calculation of oscillator strengths, vertical excitation energies, and non-adiabatic coupling constants in the NAMMD simulations, presented in Section 6.2.

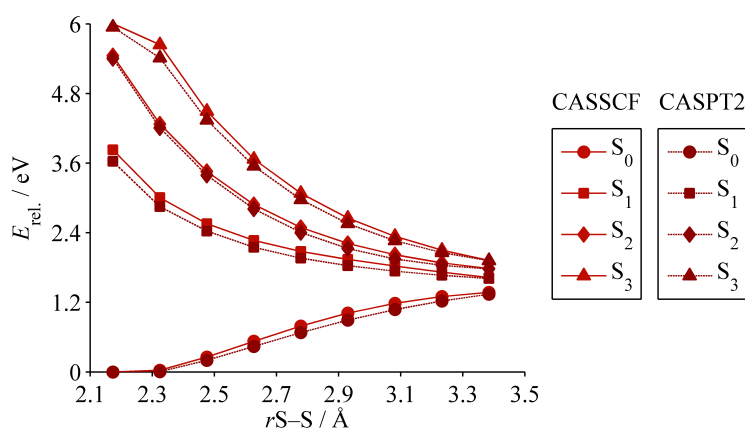


Figure 6.4: Linearly interpolated internal coordinate (LIIC) scans at the SA4-CASSCF(10,8)/cc-pVDZ and SA4-CASPT2/cc-pVDZ levels for asparagusic acid (conformer B). Identical plots for conformers A and C can be found in Appendix F.

6.2 Molecular dynamics simulations

The ring-opening dynamics of asparagusic acid were explored using NAMMD simulations carried out at the SA4-CASSCF(10,8)/6-31G* level using the interface between COLUMBUS v7.0 and the molecular dynamics package NEWTON-X v1.4. A Wigner-distributed ensemble containing 50 structures per conformer was vertically excited to the S_1 state and independently propagated in 0.5 fs time steps for 1500 fs. All simulations were carried out using the YARCC high-performance computer in the spring of 2017.

6.3 Trajectory analysis

Completed trajectory simulations were visually inspected and analysed using the *TRAVIS* package (see Section 3.5.4) and internal coordinate analysis routine in NEWTON-X v1.4.¹⁸³ The ring-opening motions of asparagusic acid can be deconstructed into the three key motions: the elongation of $rS-S$, and the rotations of $dS(1)C(4)C(5)C(3)$ and $dS(2)C(3)C(5)C(4)$, schematically depicted in Figure 6.5.

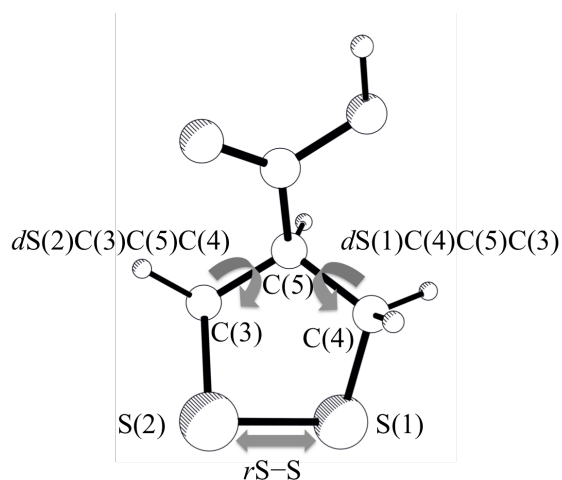


Figure 6.5: Schematic depiction of the elongation of the $rS-S$ internal coordinate, and the rotation of the two dihedral angles along the ring carbon backbone, $dS(1)C(4)C(5)C(3)$ and $dS(2)C(3)C(5)C(4)$.

The evolution of the $S\cdots S$ separation as a function of simulation time, shown in Figure 6.6a, revealed the rapid elongation of the $S-S$ bond, leading to the cleavage of the disulfide bond at 150 fs. Shortly after the initial elongation, the $S\cdots S$ separation was found to recoil momentarily, only to extend past the initial elongation in the following 100 fs. This two-stage elongation of the $rS-S$ coordinate is consistent across all conformers.

The evolution of the two d SCCC internal coordinates, shown in Figure 6.6b–c, revealed that during the first 125 fs the two S-termini, S(1) and S(2), rotate away from each other in order to accommodate the rapid r S–S elongation, coming into close proximity with the oxygen atoms in the carboxylic acid group. Steric effects between the two groups force the S-termini to slow down and the C(4)–C(5) and C(3)–C(5) bonds to rotate. Therefore, the carboxylic acid group is responsible for moderating the ring-opening motion, controlling the trajectory and velocity of the S-termini. Force vector velocity analysis revealed that before the steric interaction the S-termini travel at $4.4 \times 10^{-2} \text{ \AA fs}^{-1}$, with respect to each other. However, this velocity is nearly halved following the steric interaction, to $2.5 \times 10^{-2} \text{ \AA fs}^{-1}$, indicating that the carboxylic acid acts as a sink for the momentum of the S-termini. The implications of the functional group moderation in the ring-opening dynamics of asparagusic acid are discussed further in Section 6.3.

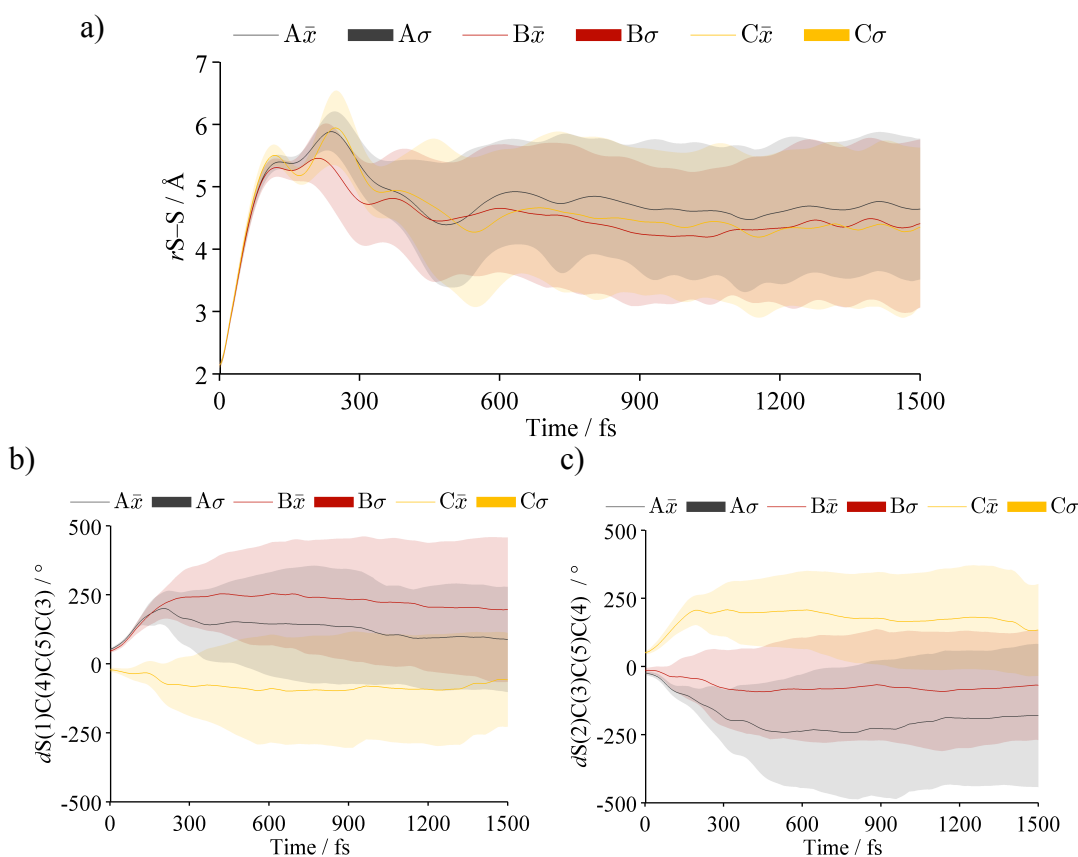


Figure 6.6: Plot of the evolution of a) the r S–S, b) the d S(1)C(4)C(5)C(3), and c) the d S(2)C(3)C(5)C(4) internal coordinates as a function of time for conformer A (grey), B (red) and C (yellow). The mean value and standard deviation of the internal coordinates are denoted as \bar{x} and σ , respectively.

The steric effects between the S-termini and the carboxylic acid are illustrated in Figure 6.7 with the help of the van der Waals radii.

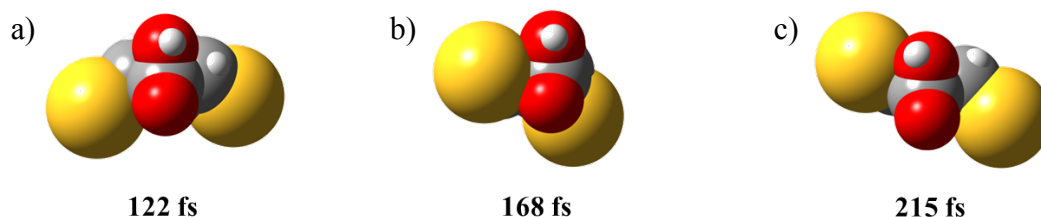


Figure 6.7: Schematic representation of the van der Waals radii of asparagusic acid at a) 122, b) 168, and c) 215 fs, corresponding to S···S separations of 5.49, 5.46 and 5.87 Å, respectively.

During the first 250 fs, the S-termini were found to follow a disrotatory motion, indicated by the signs of the two d SCCC internal coordinates. Changes in the direction of rotation, expressed as a change in sign in Figure 4.10b–c, have been found to, in some cases, indicate collisions between S-termini. Depending on the momentum and orientation of the S-termini, these can either lead to the recombination of the disulfide bond, or drive further ring-opening events. However rare, stable S-termini recombination events were found to occur under very specific conditions. The S-termini collision and disulfide bond recombination ratios for each conformer of asparagusic acid are presented in Table 6.2.

Table 6.2: Conformer specific S-termini collision and disulfide bond recombination ratios for asparagusic acid.

Conformer	Collision ratio / 50	Recombination ratio / 50
A	8	4
B	9	8
C	10	6

Differences in the rates of disulfide bond recombination have been attributed to structural differences between conformers, more specifically ring conformation and carboxylic acid orientation. Therefore, the two types of ring conformation in asparagusic acid, *i.e.* twisted and envelope, are expected to generate slightly different ring dynamics, expressed as changes in internal coordinates r S–S and d S(1)C(4)C(3)S(2), referred to as d SCCS. A plot showing the evolution of the d SCCS internal coordinate as a function of time can be found in Appendix F. Though coherent during the first 200 fs, the evolution of r S–S and d SCCS was found

to dephase quickly, leading to the exploration of a large region of hypersurface. The *TRAVIS* package was used to explore the ring dynamics using two-dimensional heat-map representations of the hypersurface. Though dimensionally simplified, these heat maps demonstrate the motion of the wavepacket along the PES of asparagusic acid, from the Franck-Condon region to the photoproducts. In the first 100 fs, the wavepacket moves away from the Franck-Condon region towards larger $rS-S$ with a small change in $dSCCS$ (see Figure 6.8a). When the $rS-S$ reaches a local maximum, the $dSCCS$ rotates as one, or both, S-termini move pass the van der Waals radii of the oxygen atoms in the carboxylic acid (see Figure 6.8b). At 200 fs the carbon backbone starts to flex (see Figure 6.8c), causing the wavepacket to visit a vast region of the phase space. Disulfide bond recombinations and ring-closing events are characterised by a rapid decrease in $rS-S$ coupled with a narrowing of the distribution of $dSCCS$ angles. The channelling of the wavepacket towards ring-closed structures can be observed in Figure 6.8d.

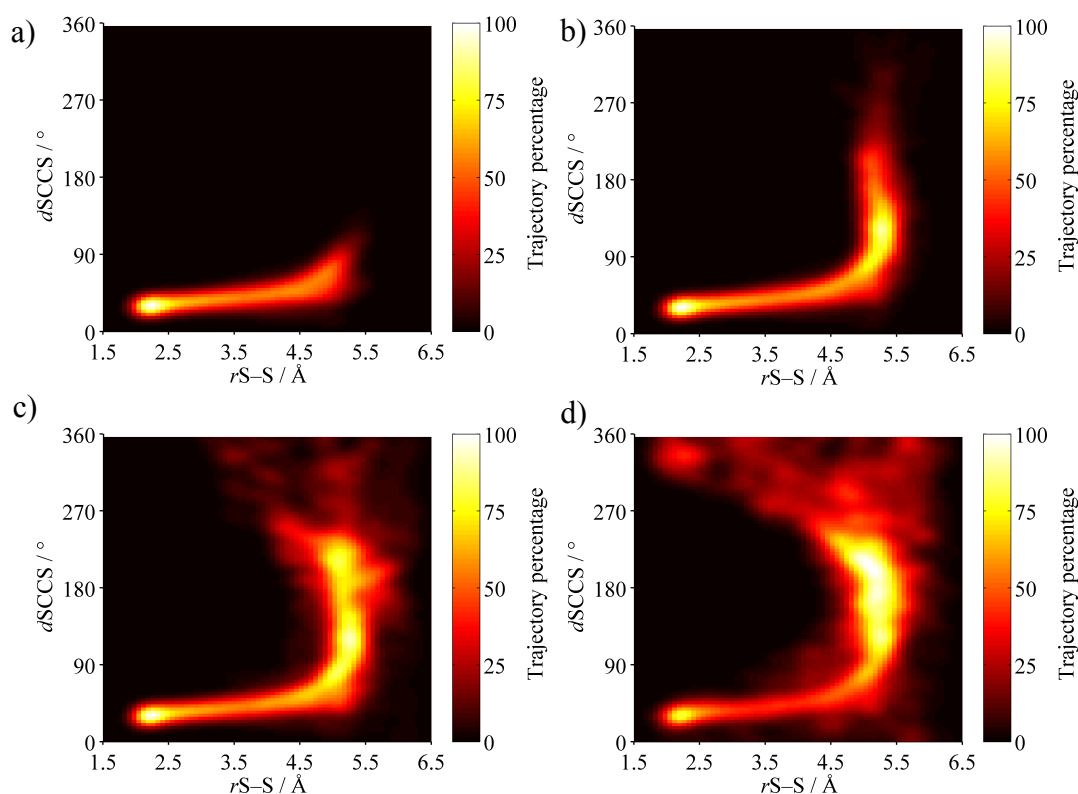


Figure 6.8: Heat-map representation of the $rS-S/dSCCS$ phase space for conformer B, at a) 100, b) 200, c) 400, and d) 1500 fs. For clarity purposes $dS(1)C(4)C(3)S(2)$ is expressed in terms of relative dihedral angle normalised between 0 and 360° .

The $rS-S/dSCCS$ phase-space heat map of conformers A and C, shown in Figure 6.9, revealed different ring dynamics for twisted *vs.* envelope rings. Conformer C, which features an envelope ring in the ground state, was found to explore a smaller portion of the phase space and yield a less varied range of ring-open photoproducts, than its twisted-ring counterpart, conformer A.

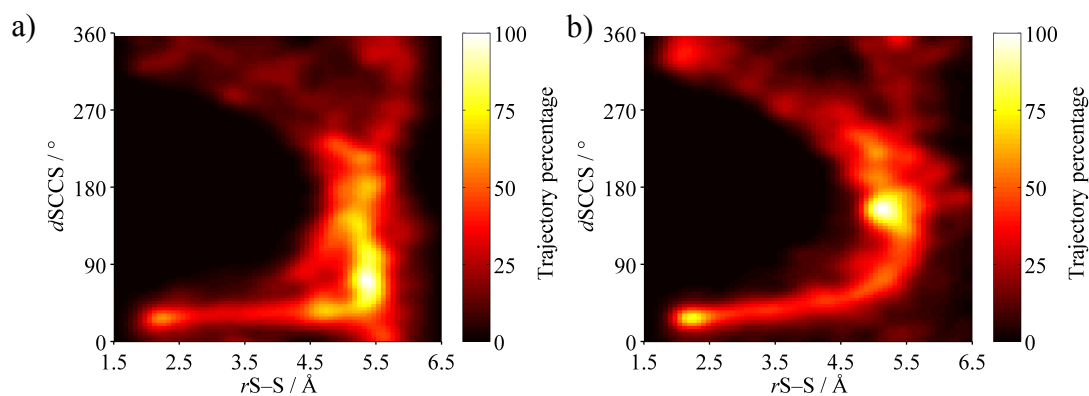


Figure 6.9: Heat-map representation of the $rS-S/dSCCS$ phase space for conformers a) A, and b) C.

The conformational space of ring-opened photoproducts for asparagusic acid was explored using the universal conformer generation and analysis (UCONGA) package.²⁶¹ Five unique photoproducts were found and optimised at the CASSCF(10,8)/cc-pVDZ level, the Cartesian coordinates of which can be found in Appendix F.

To understand the mechanisms that cause different asparagusic acid conformers to undergo slightly different ring-opening motions and produce different photoproducts, one must first study the dynamics of the carboxylic acid group. The orientation of the carboxylic acid group with respect to the ring was defined as the angle between the C(3)C(5)C(4) plane in the ring (pCCC), and the O(7)C(6)O(8) plane in the carboxylic acid (pOCO), referred to as $apCCCpOCO$ and schematically depicted in Figure 6.10.

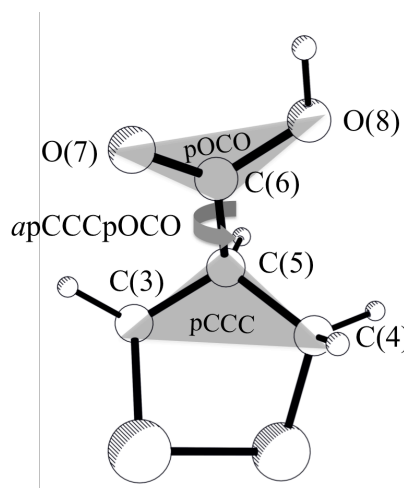


Figure 6.10: Schematic depiction of the elongation of the $rS-S$ internal coordinate, and the rotation of the two dihedral angles along the ring carbon backbone, $dS(1)C(4)C(5)C(3)$ and $dS(2)C(3)C(5)C(4)$.

The evolution of the $apCCCpOCO$ angle as a function of simulation time was calculated from the Cartesian coordinates in the 150 trajectory files using the vector operations in Equation 6.1 and 6.2:

$$\theta = \text{atan2}\left(\left|\vec{u} \times \vec{v}\right|, \vec{u} \cdot \vec{v}\right) \text{sgn}\left(\left(\vec{u} \times \vec{v}\right) \cdot \vec{n}\right), \quad \text{Eq. 6.1}$$

$$\text{atan2}(\vec{u}, \vec{v}) = \tan^{-1}\left(\frac{\vec{v}}{\sqrt{\vec{u}^2 + \vec{v}^2} + \vec{u}}\right), \quad \text{Eq. 6.2}$$

where u and v are normal vectors for planes $pCCC$ and $pOCO$, respectively, and n the normal vector for a third reference plane. The second term of Equation 6.3 describes the directionality of the rotation with respect to the reference plane and is calculated using Equation 6.3:

$$\text{sgn}(\vec{u}) = \frac{d}{d\vec{u}} |\vec{u}| \quad \text{Eq. 6.3}$$

The normal vector of the $pOCO$ plane at time zero was chosen as the reference plane, producing a positive $apCCCpOCO$ when the carboxylic acid group rotates anticlockwise. The time-dependent evolution of the $apCCCpOCO$ angle, shown in Figure 6.11, revealed a preferentially anticlockwise rotation of the carboxylic acid group in all conformers. To preserve directional information, and better illustrate the trends in carboxylic acid orientation, angles are presented in the non-normalised, cumulative format.

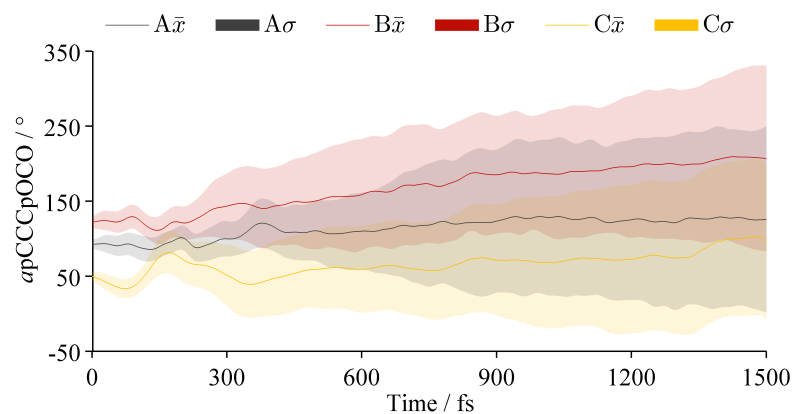


Figure 6.11: Average evolution of the $apCCCpOCO$ angle for asparagic acid.

Though preferentially anticlockwise, the carboxylic acid group was found to rotate clockwise during the first ~ 150 fs, before sharply changing direction at 200 fs. Particularly pronounced in conformer C, the change in the direction and speed of rotation of $apCCCpOCO$ is consistent with the transfer of momentum between the S-termini and the carboxylic acid, proposed in the sterically mediated ring-opening model. To explore the effects of carboxylic acid orientation on the ring dynamics, the heat-map representation of the $rS-S/apCCCpOCO$ phase space was computed using *TRAVIS*, as shown in Figure 6.12.

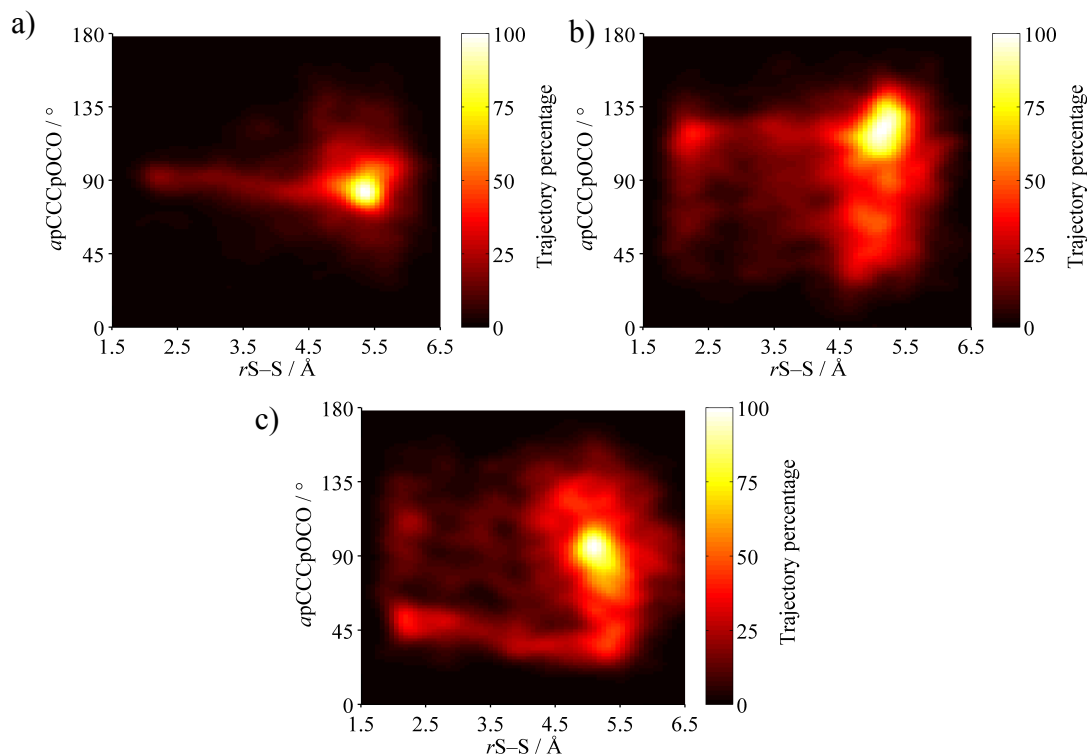


Figure 6.12: Heat-map representation of the $rS-S/apCCCpOCO$ phase space for conformers a) A, b) B, and c) C. Angles were normalised between 0 and 180° .

The $rS-S/apCCCpOCO$ heat maps revealed three distinct pathways for ring opening, illustrating the impact of initial structure on the outcome of the dynamics. Conformers A and B exhibited very similar behaviours, generating photoproducts with the same $apCCCpOCO$ angle as the initial structure. However, conformer C showed no preference for the $apCCCpOCO$ angle of the initial structure, settling instead for the seemingly more favourable 80 to 120° angle adopted by conformers A and B. Moreover, conformer C explored the largest portion of the $rS-S/apCCCpOCO$ phase space. These disparities in behaviour are consistent with the differences in functional group position and ring conformation between conformer C and conformers A and B. Unlike conformers A and B, where the carboxylic acid group is at the equatorial position in a twisted ring, conformer C features an envelope ring with the carboxylic acid group in the axial position.

A difference in the behaviour of conformers seems to suggest that variations in the initial structure dictate the outcome of the excited-state dynamics and the distribution of photoproducts. The conformation of the ring and the orientation of the carboxylic acid were found to influence the geometry at which the oxygen atoms in the carboxylic acid group sterically interact with the S-termini, modifying the ring dynamics twice during every oscillation of the $rS-S$ internal coordinate. Although dimensionally simplified, these observations illustrate the impact of structure in the stability and function of molecules in nature.

6.4 Comparative analysis: asparagusic acid vs. 1,2-dithiane

The effect of functional group sterics on the ring-opening dynamics of cyclic disulfides was investigated in a comparative study between the photoinduced dynamics of asparagusic acid and 1,2-dithiane. For the purposes of this analysis, differences in ring size will not be taken into account, as asparagusic acid and 1,2-dithiane were found to have identical ring strain, illustrated by the similar average $rS-S$ elongation velocities, shown in Table 6.3.

Table 6.3: Average $rS-S$ elongation velocities for 1,2-dithiane and asparagusic acid.

Molecule	Conformer	$rS-S$ elongation velocity / $10^{-2} \text{ \AA fs}^{-1}$
1,2-dithiane	-	4.78
Asparagusic acid	A	4.39
	B	4.51
	C	4.74

Given the similarities in the active space and the velocity of the S-termini, one might think of asparagusic acid, as 1,2-dithiane with an added functional group. However, this approximation breaks down when the long-term photostability of the disulfide bond, shown in Table 6.4, is taken into account.

Table 6.4: Comparison table showing the percentage of collision and recombination events for 1,2-dithiane and asparagusic acid.

Molecule	Conformer	Collision / %	Recombination per collision / %	Recombination total / %
1,2-dithiane	-	58	26	10
Asparagusic acid	A	16	50	8
	B	18	88	16
	C	20	60	12

Though more prone to collisions between S-termini, 1,2-dithiane was found to have fewer disulfide recombinations per collision than any of the conformers of asparagusic acid. The sterically unhindered backbone in 1,2-dithiane allows it to explore a larger portion of the $rS-S/dSCCS$ phase space than its functionalised counterpart, as shown in Figure 6.13. However, the more time a trajectory spends away from a region prone to collisions, the greater the likelihood of accessing a conformation incompatible with disulfide recombination. Furthermore, the absence of interactions that could dissipate energy, such as those between S-termini and the oxygen atoms in asparagusic acid, allows the S-termini in 1,2-dithiane to collide with greater momenta, promoting secondary disulfide-fission events. In asparagusic acid, the functional group acts as a kinetic-energy sink, dissipating the S-termini momenta, resulting in a greater probability of disulfide recombination per collision.

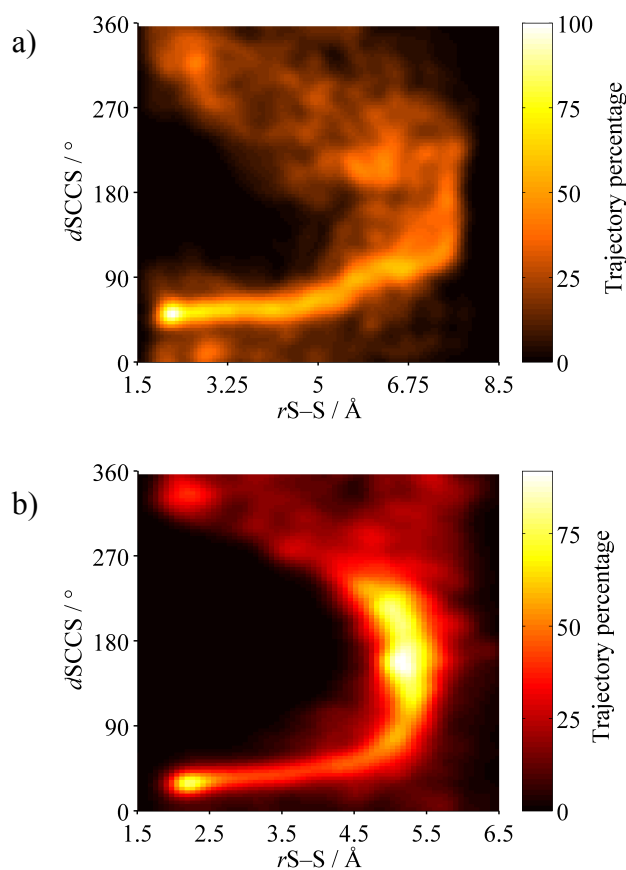


Figure 6.13: Heat-map representation of the $rS-S/dSCC\beta$ phase space for a) 1,2-dithiane, and b) asparagusic acid.

The presence and motion of a carboxylic acid functional group were found to modify the topography of the hypersurface, moderating the ring-opening dynamics of cyclic disulfides, and ultimately affecting their apparent photostability. The comparative study of 1,2-dithiane and asparagusic acid illustrates how proteins might use functional groups to create carefully tailored environments to control the photostability of their disulfide cross-links.

6.5 UED simulations

The trajectory data from the NAMMD simulations were used with the *TD-SIMMIC* package to compute time-dependent molecular intensity curves, simulating future UED experiments. The UED signal of asparagusic acid, shown in Figure 6.14a, was simulated for the s range of 1 to 8 \AA^{-1} at the predicted experimental A/B/C conformer ratio of 11/53/36%. A Gaussian-shaped instrument response blur function, 200 fs in FWHM, was applied to the simulated UED signal, generating the experimentally representative MIC matrix shown in Figure 6.14b. Although

NAMMD simulations were run for 1500 fs, only the first 500 fs were used to simulate the UED signal, as the rapid dephasing of the rS - S oscillation yields a featureless time-dependent MIC after 500 fs.

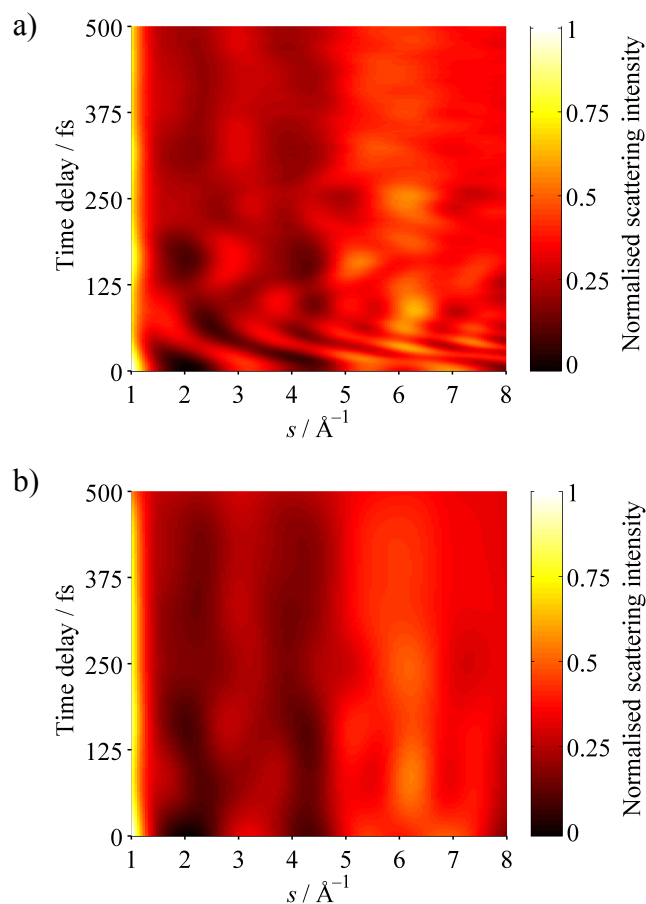


Figure 6.14: Simulated time-dependent MIC matrix for asparagusic acid a) before, and b) after the convolution with a 200 fs instrument-response function.

The position and intensity of the simulated UED signal between the s values of 1 and 5 \AA^{-1} was found to undulate, in a pattern similar to that found in the UED data of 1,2-dithiane. In real space, the signature of the asparagusic acid ring dynamics was identified as the subtle oscillation in interatomic distances between 2 and 7.5 \AA with a periodicity of approximately $\sim 175 \text{ fs}$, shown in Figure 6.15.

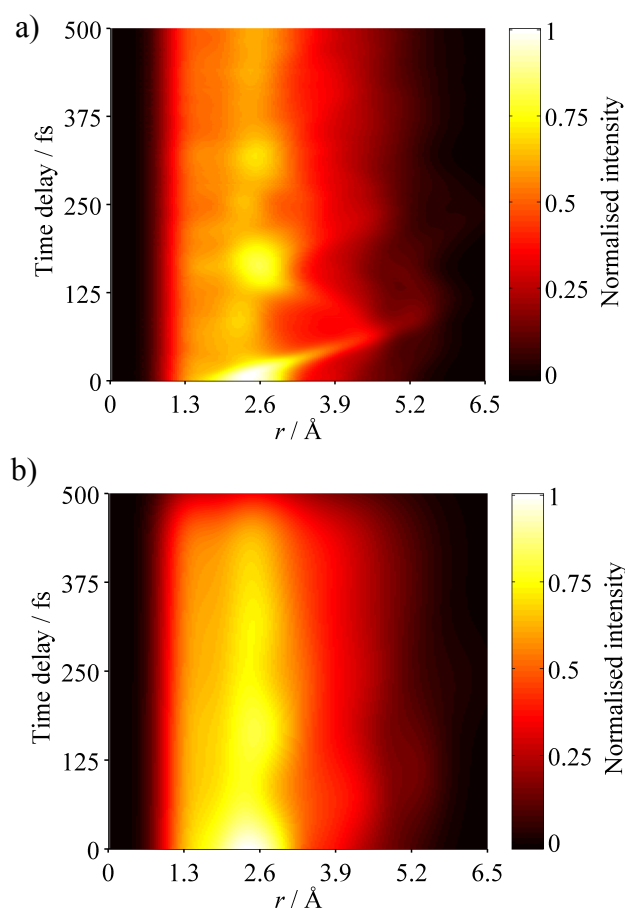


Figure 6.15: Simulated time-dependent RDC matrix for asparagusic acid a) before and b) after the convolution with a 200 fs instrument-response function, assuming the A/B/C conformer ratio of 11/53/36%.

In summary, the computational study asparagusic acid presented in this Chapter, which to my knowledge is the first of its kind, has been able to map the topography of the hypersurface controlling the ring-opening dynamics of asparagusic acid, and identify the structural features regulating its apparent photostability. Moreover, this study reports the first simulated molecular movie of asparagusic acid generated using the results of NAMMD simulations. These simulations were used to design future UED experiments, and secure beam time for the study of asparagusic acid during the 2018 gas-phase UED run at SLAC.

Chapter 7. Computational study of Halon-2402

The computational study of the photodissociation dynamics of Halon-2402, aims to explore the structure, lifetime, and mechanism leading to the formation of transient mono-halogenated radical species. The result of these investigations is expected to support future UED studies contrasting the photodissociation dynamics of Halon-2402 with its halogenated analogue, 1,2-diiodotetrafluoroethane.

7.1 Static electronic structure calculations for Halon-2402

Static electronic structure calculations were used to explore the conformational space of Halon-2402 in the ground state, and to confirm the selection of active space used to describe the C–Br bond cleavage. Furthermore, the results of these calculations were used to assess the validity of the computational methods used to simulate the excited-state dynamics of Halon-2402, presented in Section 7.2. The numbering scheme used in these studies is shown in Figure 7.1.

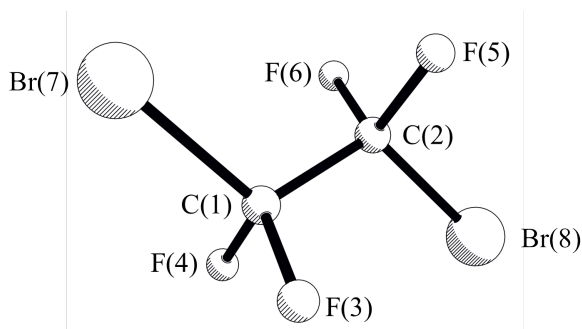


Figure 7.1: Numbering scheme used in the computational study of Halon-2402.

7.1.1 Conformational space search

The conformational space of Halon-2402 was explored using a relaxed PES scan along the Br(7)C(1)C(2)Br(8) dihedral angle, $d\text{BrCCBr}$, shown in Figure 7.2. Carried out at the MP2/aug-cc-pVDZ level using GAUSSIAN 09 at YARCC, this scan revealed two unique conformers: the *anti* and the *gauche* Halon-2402. The optimised structures of the *anti* and *gauche* conformers can be found in Appendix F.

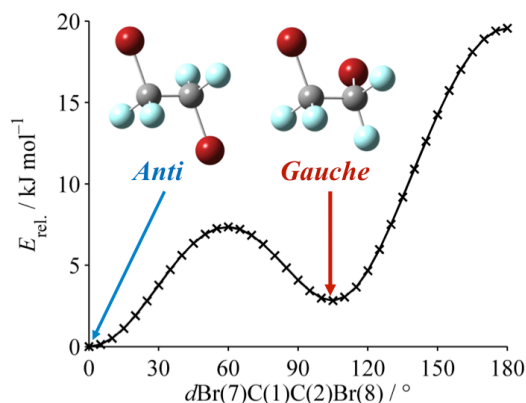


Figure 7.2: Relaxed potential energy surface scan of Halon-2402 along the $d\text{BrCCBr}$ internal coordinate.

The relaxed PES scan revealed an energy barrier between the *anti* and *gauche* conformers of less than 10 kJ mol^{-1} , and a maximum barrier to rotation of 20 kJ mol^{-1} . This means that, at room temperature, Halon-2402 is expected to interconvert freely between conformers. The *anti*-to-*gauche* conformer ratio for Halon-2402 was calculated under supersonic expansion and effusive nozzle conditions, shown in Table 7.1, using the Boltzmann distribution expression (see Equation 2.13).

Table 7.1: Conformer ratios for Halon-2402 under effusive nozzle (293 K) and supersonic expansion ($<100 \text{ K}$) conditions.

Sample delivery	Temperature / K	<i>Anti/gauche</i> conformer ratio / %
Supersonic	<100	96/4
Effusive (25 °C)	293	75/25

Halon-2402 has an estimated vapour pressure at room temperature of 285 Torr, allowing its delivery using both supersonic and effusive nozzle systems, without the need for heating. However, all computational studies in this section were carried out assuming an *anti/gauche* conformer ratio of 75/25% (effusive nozzle at room temperature), since most UED apparatus are pursuing repetition rates outside the working range of pulsed nozzles.

7.1.2 Active-space selection

Preliminary rigid potential energy surface scans along the dissociative $r\text{C-Br}$ internal coordinate, at the TD-B3LYP/6-31G+* level, revealed the coming together of 9 states, five singlet states (S_0, S_1, S_2, S_3, S_4) and four triplet states (T_1, T_2, T_3, T_4). Therefore, the quantum-chemical description of the photodissociation of Halon-2402

was carried out using CASSCF averaged over 5 singlet states and 4 triplet states, allowing spin-orbit coupling to be recovered through the RASSI routine in MOLCAS v8.0. The choice of active space for these calculations consisted of six doubly occupied orbitals [two $\sigma_{\text{C-Br}}$ (HOMO-5 and HOMO-4) and four sets of bromine lone-pairs (HOMO-3, HOMO-2, HOMO-1, HOMO)] and two virtual orbitals [$\sigma^*_{\text{C-Br}}$ (LUMO and LUMO-1)]. For clarity purposes, only the active space for the most abundant conformer is shown in Figure 7.3. The molecular orbitals representing the active space for the *gauche* conformer can be found in Appendix F.

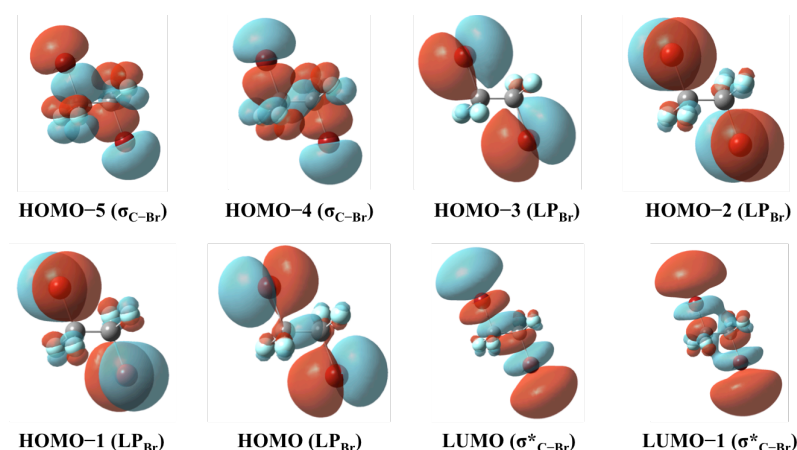


Figure 7.3: Choice of active space for the *anti* conformer in Halon-2402.

The choice of active space was validated at the CASPT2 level, using a basis set of Stoll and co-workers for the valence electrons and the corresponding pseudo-potentials for the inner electrons.^{262,263} Additional polarisation functions were added in the form of d orbitals for carbon and fluorine. The Cartesian coordinates for the ground-state structures of the *anti* and *gauche* conformers of Halon-2402, optimised at the CASSCF and CASPT2 levels, can be found in Appendix F. The vertical excitation energy between the S_0 minima and the S_1 Franck-Condon point was calculated at 5.9 eV, which is equivalent to the absorption of a 209 nm photon.

7.1.3 Interpolate internal coordinate potential energy surface scans

The dissociative nature of the excited states of Halon-2402 was explored using a series of LIIC scans along the $r_{\text{C-Br}}$ internal coordinate. Concerted elongation of both C-Br bonds was assumed for the purpose of these scans. LIIC scans carried out at both the CASSCF and CASPT2 levels, revealed a steep topography between the Franck-Condon region and high $r_{\text{C-Br}}$, shown in Figure 7.4.

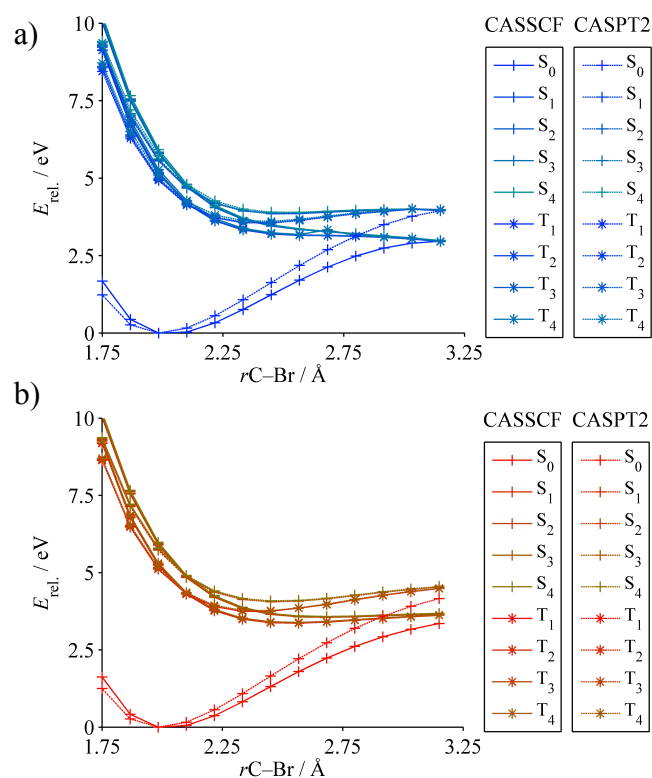


Figure 7.4: Linearly interpolated internal coordinate scans at the CASSCF and CASPT2 levels for the a) *anti* and b) *gauche* conformers of Halon-2402.

The one-dimensional approximation of the topography of the $r\text{C-Br}$ internal coordinate provides the theoretical support necessary to explore the effects of PES topography in the dynamics of other internal coordinates and the distribution of photoproducts.

7.2 Molecular dynamics simulations

The photodissociation mechanism of Halon-2402 was explored using on-the-fly adiabatic molecular dynamics, carried out using a modified version of SHARC v1.0, where the surface-hopping algorithm has been disabled. The interface with MOLCAS v8.0 allowed spin-orbit coupling to be taken into account during gradient evaluation. The RASSI routine was used to compute the spin-orbit coupling at every step, from the interaction matrix elements of two CASSCF/(Stoll-ECP+P) calculations: a SA5-CASSCF(12,8) and SA4-CASSCF(12,8) describing the singlet and triplet states, respectively. A Wigner-distributed ensemble of 200 structures (100 from each conformer) was vertically excited to the brightest states and propagated in 0.25 fs steps for 250 fs.

7.3 Trajectory analysis

Trajectory data were analysed using the *TRAVIS* package. The change in C \cdots Br separation as a function of simulation time, shown in Figure 7.5, revealed the rapid elongation of around half of the r C–Br internal coordinates and fission of at least one of the C–Br bonds within the first 50 fs. These results corroborate the photofragment translation spectroscopy (PTS) studies by Zou *et al.*, in which a near-immediate cleavage of one of the C–Br bonds is reported.¹⁰⁹

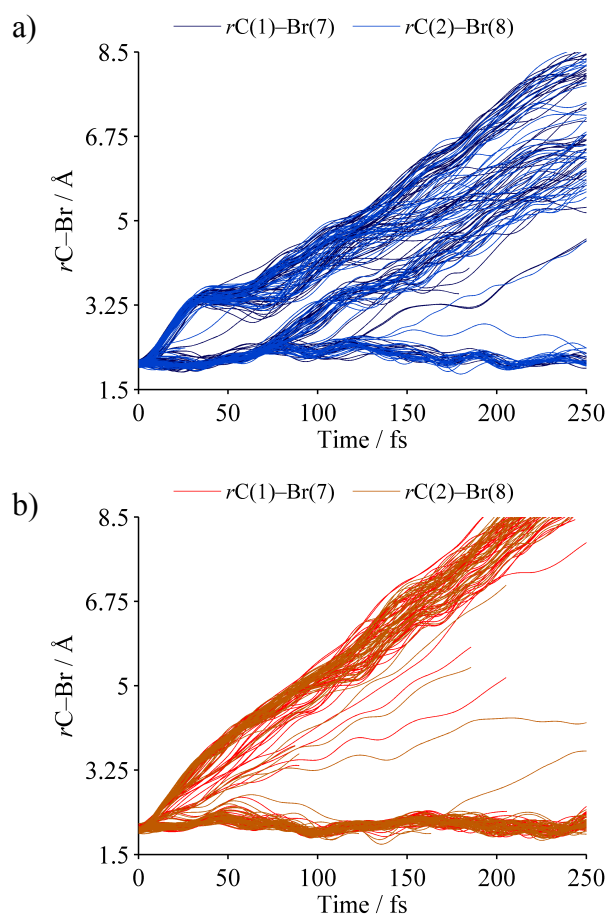


Figure 7.5: Plot of the evolution of the r C–Br internal coordinate as a function of time for the a) *anti*, and b) *gauche* conformers. For clarity purposes, the two r C–Br internal coordinates are labelled r C(1)–Br(7) and r C(2)–Br(8).

In the *gauche* conformer, half of the r C–Br internal coordinates were found to increase continuously, leading to the cleavage of one C–Br bond per molecule and the formation of a bromine radical and a bromotetrafluoroethane radical intermediate. Forces generated during the C–Br bond fission event are dissipated vibrationally, expressed as the oscillation of the bonded r C–Br internal coordinates,

shown in Figure 7.5b. Quantum-chemical calculations have shown two possible structures for this class of transient species:⁷⁵ the classically intuitive “non-bridging” structure with a bromine associated with one of the two $-\text{CF}_2$ moieties, shown in Figure 7.6a, and the symmetrically “bridged” structure with a bromine shared between two $-\text{CF}_2$ moieties, shown in Figure 7.6b. The latter, locks the fluorine atoms in their initial position, as it prevents rotation about the C–C bond.

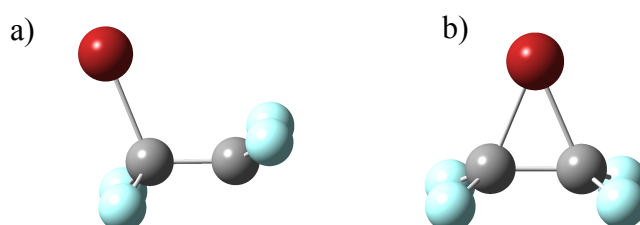


Figure 7.6: Structure of a) a non-bridging and b) bridged bromotetrafluoroethane radical intermediate.

Molecular dynamic simulations showed no evidence of “bridged” bromotetrafluoroethane radical intermediates for the *gauche* conformer of Halon-2402. These findings are in good agreement with the TRED study of 1,2-diodotetrafluoroethane ($\text{C}_2\text{F}_4\text{I}_2$), by Zewail and co-workers, which found the inclusion of bridged- $\text{C}_2\text{F}_4\text{I}$ in the parameterised model of iodotetrafluoroethane to have a detrimental effect on the goodness-of-fit for the refinement.⁷⁵

The rate of $\text{C}\cdots\text{Br}$ elongation for this internal coordinate in the *anti* conformer was found to decrease shortly after the cleavage of one of the C–Br bonds. Once again, the simulations showed no evidence of a bridging radical species, with all bromotetrafluoroethane intermediates adopting a “classical” non-bridged geometry. The sudden increase in $\text{C}\cdots\text{Br}$ separation for bonded $r\text{C}\text{--Br}$ internal coordinates, 100 fs after the first C–Br bond cleavage, is consistent with a secondary photodissociation event and consequently the formation of the doubly dissociated species, reported by Zou *et al.*¹¹⁷ In over 80% of the trajectories, the *anti* conformer of Halon-2402 was found to undergo a stepwise photodissociation yielding a neutral tetrafluoroethane photoproduct. However, in around 10% of the trajectories initiated to the S_4 state, concerted fission of both C–Br bonds was observed. Excitation to a higher-energy state, emphasised the structural implications of hypersurface topography on the momentum of the wavepacket and ultimately on the photostability of the Halon-2402 system.

7.4 UED simulations

Trajectories recorded during the molecular dynamic simulations described in Section 7.2 were used with the *TD-SIMM* package to simulate the outcome of future UED experiments. The time-dependent MIC matrix of Halon-2402, shown in Figure 7.7a, was simulated for an s range of 1 to 8 \AA^{-1} at the assumed *anti/gauche* conformer ratio of 75/25%. Individual time-dependent MIC matrices for each conformer can be found in Appendix F. To better account for the effect of limited temporal resolution in the UED data, and produce experimentally representative simulations, the MIC matrix in Figure 7.7a was convoluted with a Gaussian function, 200 fs in FWHM, producing the UED dataset shown in Figure 7.8b. The size and shape of the temporal convolution and the s range used in the UED simulation are consistent with the instrument-response function and detector range at the UED apparatus at SLAC (see Appendix D).

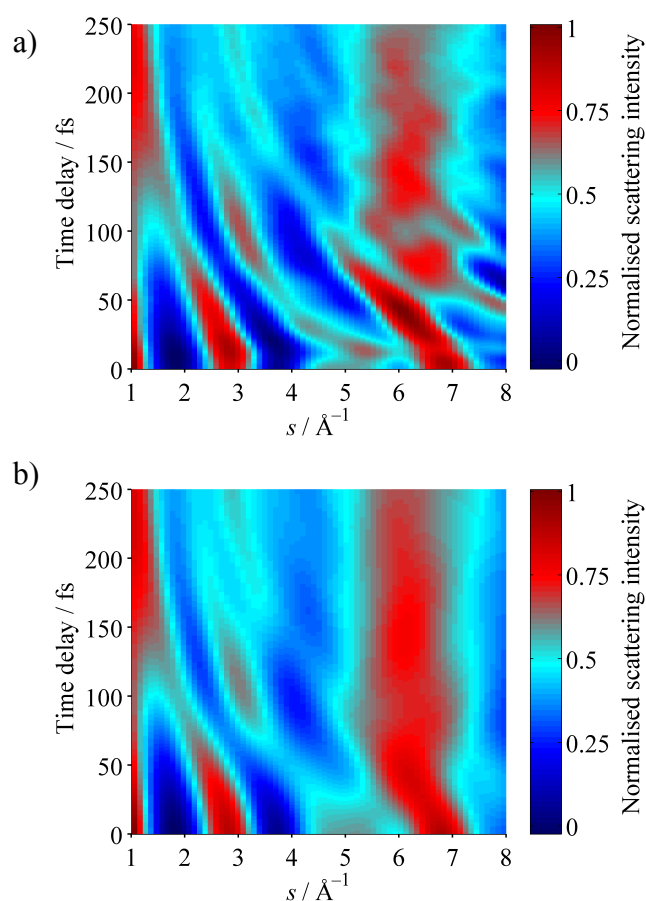


Figure 7.7: Simulated time-dependent MIC matrix for an *anti/gauche* conformer ratio of 75/25% of Halon-2402 a) before and, b) after the convolution with a 200 fs instrument-response function.

The bleaching and shifting of diffraction features between 2 and 8 \AA^{-1} , were identified as the reciprocal-space signature for the photodissociation of Halon-2402. Furthermore, the portion of molecules undergoing a secondary fission event, *i.e.* photoproduct of the *anti* conformer, was found to be proportional to the scattering intensity observed between the s values of 2.5 and 3.5 \AA^{-1} , and 5 and 7 \AA^{-1} . A discrete sine transform was applied to the simulated MIC matrix, revealing the real-space representation of the photodissociation of Halon-2402, shown in Figure 7.8.

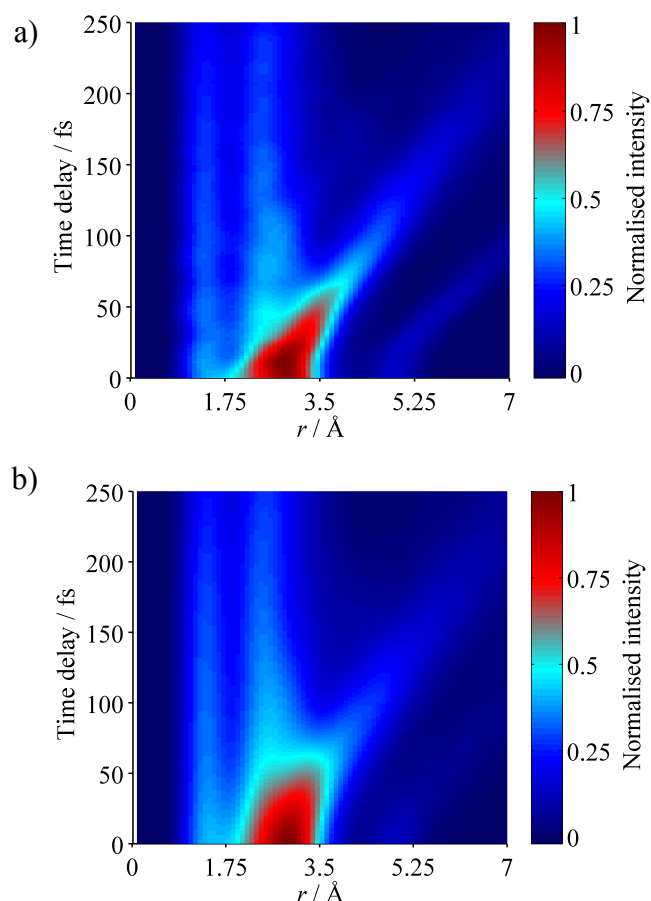


Figure 7.8: Simulated time-dependent RDC matrix for Halon-2402 a) before, and b) after the convolution with a 200 fs instrument-response function.

The primary photodissociation event causes interatomic distances between 1.75 and 3.5 \AA to shift to higher values, at an approximate speed of 2 \AA per 100 fs, as the bromine atoms move away from the bromotetrafluoroethane radical fragment. However, such a pronounced shift in interatomic distances is not repeated for the secondary C–Br fission, observed in the RDC matrix as a subtle bleaching of interatomic distances between 1.5 and 3.5 \AA . The dissipation of excess energy by the vibrationally hot photoproducts of the *gauche* conformer results in the oscillation of

interatomic distances between 2 and 3.5 Å, with an approximate periodicity of 100 fs. These simulated datasets will be used in the design and analysis of future UED experiments at SLAC, discussed in Chapter 8.

In summary, this Chapter reports on a first computational exploration of the photodissociation mechanism of Halon-2402 using molecular dynamics, complemented by thorough simulation of the UED signal expected in future experimental studies.

Chapter 8. Conclusion and future work

In this Chapter, the most relevant findings of this thesis are summarised, and new avenues of research unveiled as a result my PhD project are discussed in Sections 8.1 to 8.3. In Section 8.4 of this concluding Chapter, I will give a personal perspective on the future of UED as tool for the study of molecular dynamics, and its role in the roadmap to four-dimensional UEM proposed by Zewail.

8.1 Achievements prompt by the roadmap to molecular movies

This thesis has demonstrated the viability of the roadmap to molecular movies, through the study of the internal conversion dynamics of 1,2-dithiane, in which achievements in software development, data analysis and instrument design led to the successful recording of the first molecular movie for this class of cyclic disulfide. The motion revealed by the experimentally generated molecular movies settled the argument in literature, of either 1,2-dithiane follows a “molecular clackers” or “rocking” motion when illuminated with mid-UV light. Moreover, the inclusion of traditional GED structure determination in the methodology proposed by the roadmap to molecular movies, gave GED a new lease of life, as showcase by the GED study of DMABN. The experimental studies of the ground state structure of DMABN and the structural dynamics of 1,2-dithiane are currently being prepared for publication. Furthermore, computational studies carried out during my PhD have led to the identification of asparagusic acid and Halon-2402 as suitable case studies for future UED experiments. Molecular dynamic simulations for asparagusic acid and Halon-2402 were used to demonstrate the feasibility of such UED experiments, allowing the Wann group to secure beam time at the SLAC UED apparatus.

8.2 Challenges and future work

The development and exploration of the roadmap to molecular movies has led to identification of challenges in time-averaged and time-resolved electron diffraction. In this Section, these challenges are discussed in the scope of future instrument developments and experimental studies.

8.2.1 Challenges and future work in GED

As GED becomes more involved in the support of time-resolved studies and cements its role in benchmarking modern computational methods, the demand for accurate structure information is expected to increase. Therefore, it is important to ensure that the York GED apparatus remains operational and up-to-date with the latest technology. In this Section, the challenges and limitations associated with the current York GED apparatus configuration are discussed briefly, and plans are presented to expand its scope and improve the existing workflows.

A typical GED experiment at the York GED apparatus starts with the optimisation of the electron beam parameters, which, due to the lack of beam current measuring devices, is based exclusively on the qualitative assessment of the beam brightness as it hits the retractable scintillator screen. This method relies on operator perception and judgment to produce the highest quality electron beam, which could result in poor experimental reproducibility as a result of operator bias. In the absence of beam current or diffraction intensity metrics, exposure times are determined using a combination of experimental iteration and intuition. Depending on the sample and the experience of the operator, the determination of the optimum exposure time can take between one and three experimental runs. In fact, the determination of experimental conditions is by far the most time-consuming step of the GED experimental workflow. To overcome the limitations associated with the visual assessment of electron beam brightness and the potential lack of experimental reproducibility it entails, a new beam diagnostic tool, shown in Figure 8.1, has been designed around the existing retractable scintillator.

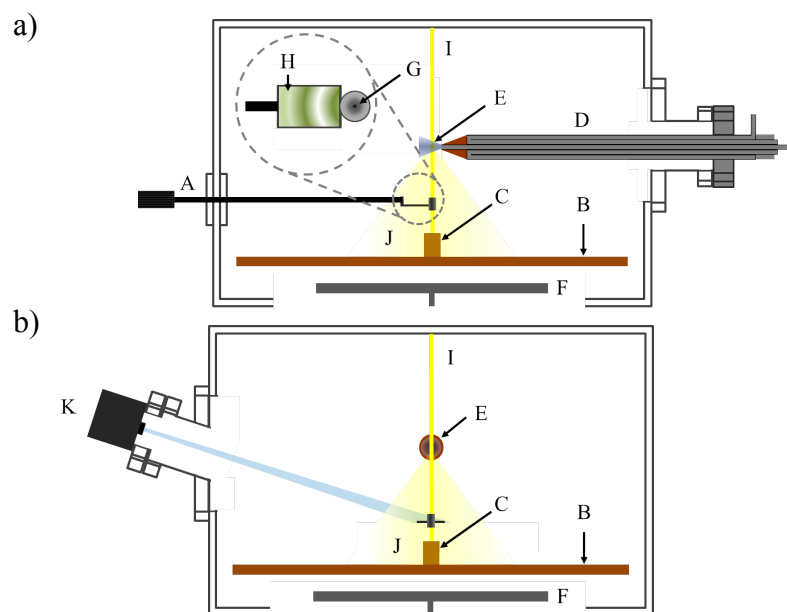


Figure 8.1: A schematic representation of the proposed beam diagnostic tool view from the a) the front and b) side showing: the retractable rod (A), the rotating sector (B), the beam stop (C), the nozzle (D), the interaction region between the electron beam and the sample (E), the image plate holder (F), the Faraday cup (G), the $\text{Gd}_2\text{O}_2\text{S}$ imaging screen (H), the electron beam (I), electrons scattered from the sample (J), and CCD camera (K).

A Faraday cup (G) mounted at the end of the retractable rod (A) would allow the electron beam (I) current to be measured accurately. Scattered electrons that are not collected by the Faraday cup hit the $\text{Gd}_2\text{O}_2\text{S}$ screen (H), producing a “preview” of the diffraction pattern. A flange mounted CCD camera (K) observing the screen, captures this “preview”, allowing diffraction signal intensity to be assessed on the fly. Following a series of calibration experiments, this beam diagnostic tool would allow beam quality to be accurately reproduced and exposure time to be determined without the need to expose, scan, or extract image plates.

The York GED apparatus must not rely exclusively on heated nozzle technology to deliver samples to the gas phase, as some of the less volatile samples, such as 1,2-dithiane, may decompose upon heating. In these cases, the target sample needs to be carried into the gas phase using a carrier gas such as helium. Plans to fit a bubbler onto the existing effusive nozzle have been passed on to the group, and will likely lead to the development of new sample delivery system for the York GED apparatus.

8.2.2 Challenges and future work in TRED

In this section, the challenges and limitations associated with the TRED apparatus are briefly discussed, and plans to expand the scope of TRED experiments at York are presented. The discussion will be focused around the temporal resolution, read-out noise of the CCD detector, and transverse coherence of the electron source; these topics were identified as potentially scope limiting.

8.2.2.1 Temporal resolution

The photocathode-based DC electron gun used in the TRED apparatus limits the temporal resolution of experiments to a few picoseconds. In its current configuration, the TRED apparatus is therefore suited to the study of relatively slow molecular motions, such as the isomerisation of system containing bulky groups or heavy atoms. The use of the TRED apparatus to study the ultrafast molecular dynamics of sub-picosecond processes would likely result in temporally blurred information regarding the initial and final structures. However, these studies would still allow the identification of fast molecular motions and the determination of observation windows ahead of UED studies with better time resolution. Therefore, in addition to its role as a “test bed” for the development of novel diffraction techniques, the TRED apparatus can also be used to acquire preliminary datasets and to determine experimental parameters. To improve the time resolution of the TRED apparatus, the electron gun could be further developed through the installation of a bunch compressor. The Centurion group has recently demonstrated the potential of RF bunch compressed DC electron guns, in the capture of molecular motions with sub-400 fs temporal resolution.⁹⁶

8.2.2.2 Detector performance

The detector upgrades and optimisations, presented in Section 3.2, resulted in a net improvement in the SNR of diffraction data of 62%, relative to the original data. In solid-state experiments, the improved spatial resolution allowed the Bragg peaks of platinum to be resolved accurately and the effect of the Earth’s magnetic field on diffraction patterns to be quantified. Furthermore, in solid-state experiments, higher detection efficiency allowed data-acquisition times of several minutes to be reduced to only a few seconds. However, issues with the MCP performance in the presence of gaseous samples meant that such improvements in data-acquisition time could not

be achieved for gas-phase experiments. Sample gas left in the wake of the supersonic molecular beam was found to undergo field ionisation inside the MCP channels, causing the MCP to become saturated. In addition to a decrease in SNR caused by operating the electron gun at only 10% of its duty cycle, signal intensity was further reduced by the removal of the MCP from the detector assembly. Increasing data-acquisition times compensated this deficit in signal intensity. Therefore, time-averaged GED experiments require several hours of data acquisition to raise the SNR above the Rose criterion,¹⁴⁹ leaving the apparatus more susceptible to the detrimental effects of thermal drifts of the laser. Possible solutions to this issue involve using a CCD camera with a higher detection efficiency or increasing the distance between the MCP and the molecular beam. Plans for a flange-mounted EMCCD camera coupled to an elongated detector module are shown in Figure 8.2.

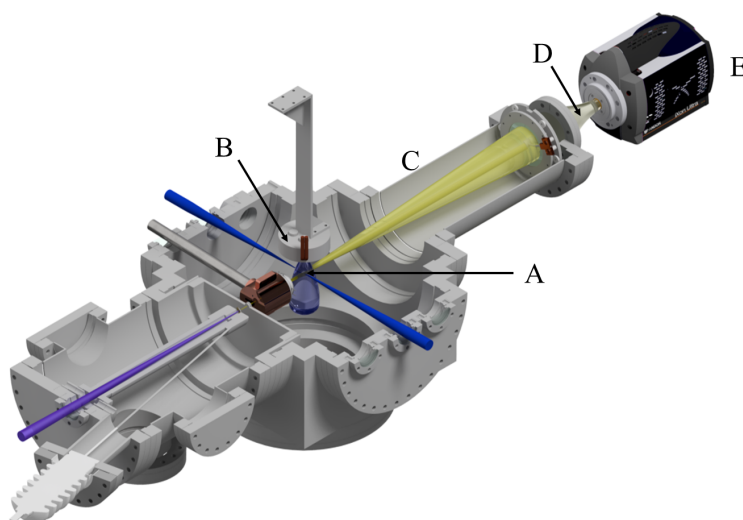


Figure 8.2: CAD drawing of the TRED apparatus future detector modules, showing the interaction region (A), the 1 kHz pulsed nozzle (B), the elongated detector module (C), the flange-mounted optical taper (D), and the EMCCD camera (E).

8.2.2.3 Transverse coherence of the electron beam

The transverse coherence of electrons from photocathode DC electron guns, such as that used with the TRED apparatus, is limited by the large size of the area from which electrons are emitted and their energy spread. Regardless of the quality of the photocathode and the focus of the drive laser, a highly coherent electron beam cannot be achieved in this type of electron gun. Therefore, in its current configuration the TRED apparatus is limited to the study of relatively small molecules. However, in a project spearheaded by Conor Rankine, the Wann group is

developing its own nanotip electron gun, based on the work by the Ropers group,^{98–100} briefly discussed in Chapter 1. The ultrafast point-projection microscopy apparatus, currently under construction at York, will serve as a test bed for the development of nanotip sources for imaging and diffraction applications. In the future these point sources might be installed in the TRED apparatus.

8.2.3 Future UED studies

The photodissociation dynamics of Halon-2402, the ring-opening dynamics of asparagusic acid, presented in Chapter 6 and 7, and the isomerisation dynamics of *E*-cinnamionitrile have been identified as potential candidates for future UED studies. Preliminary GED studies and NAMMD simulations on these systems have allowed the Wann group to secure beam time at the SLAC UED apparatus. Moreover, my collaboration with the UED group at SLAC will extend far beyond the scope of these case studies, as I plan to continue to develop robust methodologies for the study of molecular dynamics using electron diffraction, of which the roadmap presented in this thesis is an example.

8.2.3.1 Ring opening dynamics of asparagusic acid

The UED study of the light-driven dynamics of asparagusic acid aims to explore the effect of cyclic disulfide functionalisation on the photostability of the disulfide bond. These UED experiments will focus on the evolution of the S···S separation as a function of carboxylic acid orientation, capturing the dynamics of two internal coordinates simultaneously. Given the large number of possible ring-opening pathways, these UED studies will rely on statistical analysis to uncover the dominant pathways from which trends can be rationalised. The need for statistically relevant data is likely to lead to prolonged data acquisition periods, making the quality of the UED data directly proportional to the stability of the laser power, RF power, and timing systems driving electron emission. Furthermore, the multi-conformer nature of asparagusic acid will require the development of novel data-analysis routines, as the UED signal for each conformer must be deconvoluted from the overall UED data, in order to investigate the role of initial structures on the internal conversion pathway and photostability of the system. Therefore, the success of the UED study of asparagusic acid is dependent on the timely implementation of upcoming developments in instrument and software design. Over the past year, the UED group

at SLAC has been committed to improving the time jitter and long-term timing stability of the apparatus, while at York, the results of NAMMD simulations were used to develop conformer deconvolution routines to be implemented in the existing data analysis package. In collaboration with the UED group at SLAC, we aim to develop a universal data-analysis methodology, making UED more accessible to the wider structural dynamics community.

8.2.3.2 Photodissociation of Halon-2402

The study of Halon-2402 aims to uncover trends in the photostability and atmospheric dynamics of this class of haloalkanes by contrasting the findings from UED signal and computational results for Halon-2402 with those of its iodinated analogue, $C_2F_4I_2$. The UED study of Halon-2402 should allow us to compare the UED data from both systems and investigate the effect of the halogen substituent on the photodissociation dynamics of haloalkanes. This comparative study will be aided by simulated data sets generated from the results of molecular dynamics simulations carried out for $C_2F_4I_2$ and Halon-2402, shown in Figure 8.3.

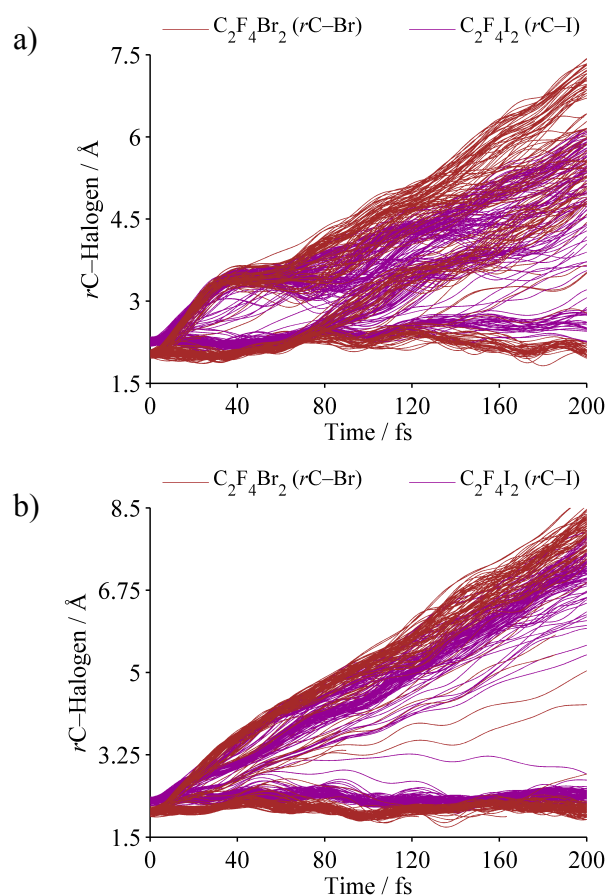


Figure 8.3: Plot of the evolution in carbon halogen separation as a function of time for a) the *anti*, and b) the *gauche* conformers of Halon-2402 and $C_2F_4I_2$.

8.2.3.3 *E/Z* isomerisation of *E*-Cinnamitrile

The light-driven formation of the polyaromatic N-heterocycle quinoline from *E*-cinnamitrile is believed to involve an *E/Z* isomerisation step, the mechanism of which is a topic of debate in the community.²⁶⁴ Despite the extensive experimental and theoretical studies carried out in model systems, such as stilbene,²⁶⁵ styrene,²⁰⁵ and ethene,²⁶⁶ consensus has not yet been reached on the formation dynamics of polyaromatic N-heterocycles from quinoline. In 2010, mass spectrometric data recorded during the CASSINI probe fly-by of Titan, the largest moon of Saturn, revealed the presence of polyaromatic heterocycles.²⁶⁷ Understanding the mechanism behind the light-driven formation of these systems is likely to reveal the evolutionary pathway which led to their ubiquity on Earth.

The light-driven formation of polyaromatic N-heterocycle quinoline from *E*-cinnamitrile will be investigated using a combination of computational, spectroscopic, and structural methods. Preliminary computational studies, carried out by Conor Rankine, have revealed a complex hypersurface with a multitude of conical intersections, internal conversion, and isomerisation pathways, schematically depicted in Figure 8.4. The nature of these conical intersections will be explored using fluorescence measurements carried out using the laser-induced fluorescence apparatus, described in Section 8.3.1.

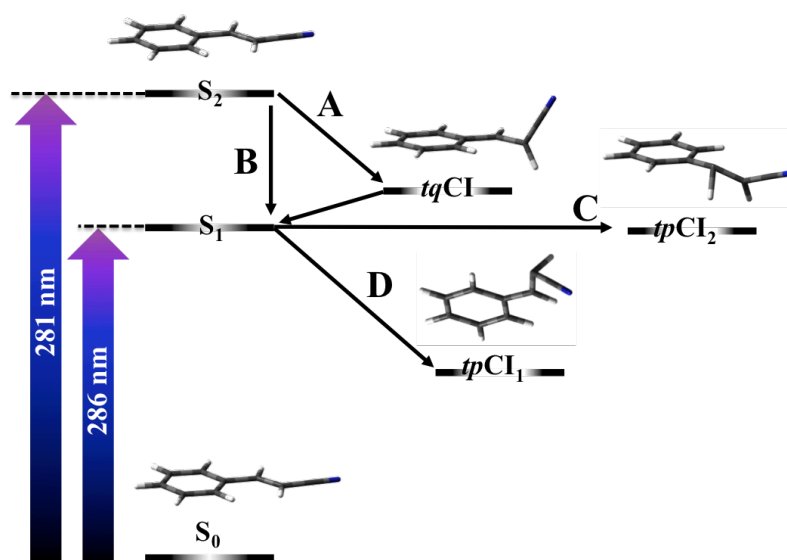


Figure 8.4: Schematic depiction of the main internal conversion pathways, A and B, and isomerisation pathways, C and D, for *E*-cinnamitrile.

Pathway A, the generally accepted pathway for the S_2/S_1 internal conversion in *E*-cinnamionitrile, suggests that internal conversion occurs *via* a twisted conical intersection (CI) (labelled *tg*CI).²⁶⁴ However, our calculations suggest that S_2/S_1 internal conversion occurs *via* pathway B, before the twisted CI geometry can be reached. UED experiments will allow us to determine unambiguously the dominant internal conversion pathways, by searching for evidence of twisting in the first 100 fs following photoexcitation. The photoisomerisation of *E*-cinnamionitrile is mediated by two CIs (*tp*CI₂ and *tp*CI₁), accessible via pathways C and D, respectively. Depending on the nature of previous internal-conversion events, the internal energy of the system and the pathway taken, the timescale for the photoisomerisation of *E*-cinnamionitrile can vary between the 200 fs and 100 ps. The effect of excitation wavelength on the timescale of the photoisomerisation dynamics will be investigated using the UED apparatus optical parametric amplifier.

8.3 Complementary projects

In the latter stages of my PhD, I became involved in two projects complementary to electron diffraction, namely the design of an ultrafast point projection microscopy apparatus, and the development of a laser-induced fluorescence (LIF) apparatus, in collaboration with the Department of Physics and Electronics, and the Cockett group, respectively. The impact of these projects to the future of TRED at York is discussed in Sections 8.3.1 and 8.3.2.

8.3.1 Laser Induced Fluorescence of supersonic molecular beams

The collaboration between the Cockett and Wann groups has resulted in the development of an apparatus for the study of laser-induced fluorescence (LIF) in the gas phase. In LIF spectra, bands arising from 0-0 transitions (purely electronic transitions between $v=0$ levels appearing in both absorption and fluorescence spectra) will be used to map the relative energies of optically accessible excited states, investigate the relative population of excited state minima and benchmark the computational methods employed in molecular dynamics simulations.^{268,269} Moreover, the broadening of LIF spectra will be used to investigate the temperature distribution inside the molecular beams used in UED experiments.^{270,271} My involvement in this collaboration was limited to the

installation and commissioning of the main chamber and vacuum system for the laser-induced fluorescence apparatus, shown in Figure 8.5.

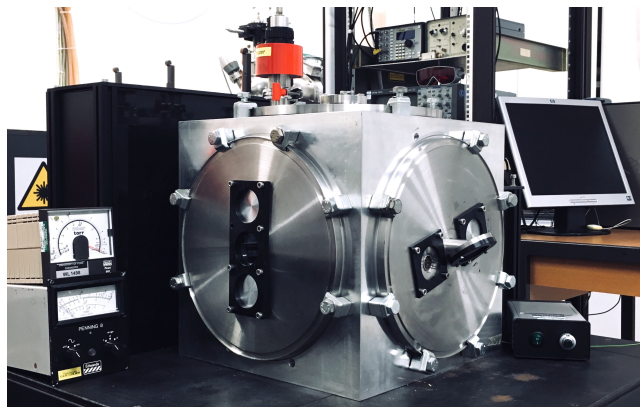


Figure 8.5: Photograph of the York laser-induced fluorescence apparatus.

8.3.2 High transverse coherence electron source

The work of Ropers *et al.*^{98–100 91–93} has inspired the Wann group to collaborate with Jun Yuan, Andrew Pratt, and Steve Tear to develop an apparatus for the study of highly coherent photoelectron emission from nanotips. The York ultrafast point-projection microscopy apparatus, shown in Figure 8.6, consists of a single vacuum chamber housing an atomically sharp nanotip, a flange-mounted sample holder, and a detector assembly. The nanotip is mounted on an in-vacuum two-axis translator stage, allowing the position of the resulting electron beam to be adjusted with respect to the sample. The magnification can be adjusted by changing the distance between the electron source and the sample. The detector assembly consists of an MCP and scintillator screen inside the vacuum, and a CCD camera outside the vacuum. To achieve the electron fluency required for imaging, the York UPPM nanotip electron gun uses the output of the 42 MHz Mai-Tai oscillator from the YULS to drive electron emission. My involvement in the development of the UPPM apparatus included the revision of the designs for the detector assembly and nanotip holder, the commissioning of the vacuum system, and the design of the laser layout.



Figure 8.6: Photograph of the York ultrafast point-projection microscopy apparatus.

Proof-of-concept experiments will include the point-projection imaging of two-dimensional material such as graphene and boron nitride, and the time-resolved imaging of phase transitions in gold nanowires, the success of which will lead to the design of a nanotip-based electron gun for the TRED apparatus.

8.4 Outlook in UED: beyond molecular movies

Recent developments in UED have allowed molecular movies to transcend conceptual reality, and become a highly demanded tool for the study of molecular motions. However, molecular movies must use a combination of scattering and spectroscopic methods to explore the nuclear and electronic terms of the wavepacket, respectively. Therefore, the future of UED resides on its ability to become part of a wider toolbox for the study of molecular motions and on its ability to resolve discrete molecular motions unambiguously. Molecular movies will no longer rely on a single technique, but rather on the cooperative efforts of several experimental and computational methods. Furthermore, bringing together different techniques under a single methodology, will promote the dialogue between different communities in physical chemistry, instigating interdisciplinary collaborations.

8.4.1 Towards 4D-UEM

Our understanding of chemical and biological functions is limited by the spatial and temporal resolutions of the imaging tools available. Ahmed Zewail believed four-dimensional (x, y, z, t) UEM (4D-UEM) to be the ultimate imaging tool for the study of complex systems in nature, offering a balanced combination of temporal and spatial resolution.²⁷²

In the article entitled “4D ultrafast electron microscopy evolutions and revolutions”,²⁷³ Zewail presented 4D-UEM as the result of the convergent evolution of UED, UEM, and Ultrafast Electron Crystallography (UEC). By unifying these three fields under a single technique, 4D-UEM allows the exploration of structural dynamics in both the reciprocal and real spaces. To better illustrate the experimental implications of such technique, a hypothetical study of self-assembled monolayers using 4D-UEM was devised. In this study, UEC could be used to determine the structure of the substrate and the monomers with atomic resolution, allowing UED to focus on the dynamics of the interaction between the substrate and the monomer with sub-picosecond temporal resolution. Ultrafast electron microscopy could then be used to explore the nature of microscopic motions induced by molecular structures and vibrations. The possibility to switch between UEC, UED, and UEM would result in an unprecedented insight into the structure, binding, and order of systems at both the molecular and microscopic levels, narrowing the knowledge gap between these two domains. Developments in 4D-UEM are expected to revolutionise our understanding of structure-function relationships in nature.

Appendix A. Overview on computational chemistry

A.1. Introduction to quantum mechanics

In mathematical terms, a molecular system can be described using a wavefunction, and according to Schrödinger, Equation A.1 can be used to calculate the eigenvalue, E , for a particular eigenstate using a description of the molecular wavefunction, Ψ , and a Hamiltonian operator, \hat{H} :²⁷⁴

$$\hat{H}\Psi = E\Psi. \quad \text{Eq. A.1}$$

In Equation A.2, the Hamiltonian operator is shown as the sum of kinetic and potential terms. The first term describes the kinetic energy of electrons and nuclei and the second, more complex term, describes the potential energy associated with nuclear-nuclear, electron-electron, and electron-nuclear Coulombic interactions:

$$\hat{H} = -\frac{\hbar}{2m_e}\nabla^2 - \frac{\hbar}{2m_n}\nabla^2 + \sum_{i,j(i\neq j)} \frac{Z^2e^2}{4\pi\epsilon_0|R_i - R_j|} + \sum_{i,j} \frac{Ze^2}{4\pi\epsilon_0|r_i - R_j|} + \sum_{i,j(i\neq j)} \frac{e^2}{4\pi\epsilon_0|r_i - r_j|}. \quad \text{Eq. A.2}$$

In Equation A.2, \hbar is the reduced Planck's constant, Z is the charge of the nucleus, e is the electronic charge, ϵ_0 is the free space permittivity, R_i is the position of nucleus i , r_i is the position of electron i , and m_e and m_n are the masses of electrons and nuclei, respectively.

Though theoretically possible, solving the Schrödinger equation for systems containing more than one electron becomes unfeasible. Therefore, Equation A.2 can only be used to calculate the exact energy of species such as H, He⁺ and H₂⁺. In order to apply Schrödinger's equation to larger systems assumptions and approximations must be made.²⁷⁵ In 1927, Max Born and J. Robert Oppenheimer proposed that, because the mass of the nuclei in a system is much greater than that of the electrons, the velocity difference between nuclei and electrons is large enough for the two timescales of motion to be treated separately.²⁷⁶ Known as the Born-Oppenheimer approximation, it states that nuclei can be assumed to be stationary on the timescale of electronic motion. Therefore, the nuclear kinetic energy term in Equation A.3 can be set to 0 and the nuclear-nuclear potential energy set to be constant. The

Schrödinger equation can therefore be modified by the Born-Oppenheimer approximation to produce Equation A.3:

$$\hat{H} = -\frac{\hbar}{2m_e} \nabla^2 + \sum_{i,j} \frac{Ze^2}{4\pi\epsilon_0|r_i - R_j|} + \sum_{i,j(i \neq j)} \frac{e^2}{4\pi\epsilon_0|r_i - r_j|}. \quad \text{Eq. A.3}$$

In order to describe multi-electron systems, the wavefunction in Equation A.1 can be built from a linear combination of single-electron wavefunctions, assuming that electrons are indistinguishable and move independently of each other. This assumption, mathematically expressed in Equation A.4, allows the energy of a multi-electron system to be calculated from the solution of the Schrödinger equation for a single electron in the system:

$$\Psi(r_1, r_2, \dots, r_N) = \psi_1(r_1)\psi_2(r_2)\dots\psi_N(r_N) = \prod_{i=1}^N \psi_N(r_i). \quad \text{Eq. A.4}$$

This assumption, however useful, can be very inaccurate, as electrons are known to interact with each other. For this reason, many methods have been developed to account for electronic interactions and improve the outcome of quantum chemical calculations.

A.2. Hartree-Fock theory

In the late 1920s Hartree proposed a method to calculate approximate wavefunctions and energies for atoms. The Hartree method assumes that electrons move through the electron density generated by surrounding electrons, according to the modified electronic wavefunction shown in Equation A.5:²⁷⁷

$$n(r) = \sum_i |\psi_i(r_i)|^2. \quad \text{Eq. A.5}$$

Incorporating this expression into the Hamiltonian operator yields Equation A.6:

$$\hat{H} = -\frac{\hbar}{2m_e} \nabla^2 + \sum_{i,j} \frac{Ze^2}{4\pi\epsilon_0|r_i - R_j|} + \sum_i \int_0^\infty \frac{e^2 n(r')}{4\pi\epsilon_0|r_i - r'|} dr'. \quad \text{Eq. A.6}$$

One of the drawbacks of Hartree's theory was that it allowed for electrons to exist in very close proximity, ignoring the Coulombic forces between electrons. This resulted in an overestimation of the energy of the system, in what is known as the "Coulomb correlation problem". One of the assumptions made by Born, Oppenheimer, and

Hartree was that electrons are indistinguishable. However, if one were to swap the position of two electrons, the sign of the wavefunction would have to be inverted in order to obey Pauli's exclusion principle. To account for electron spin asymmetry and the resulting "exchange principle", Fock proposed that the electron wavefunction should be written as Slater determinants, known as Fock operators.

Hartree-Fock (HF) theory combines Hartree's modified Hamiltonian with Fock's exchange-principle-corrected wavefunctions.²⁷⁸ Despite not accounting for the electron correlation energy resulting from the "Coulomb correlation problem", HF methods are amongst the most commonly used computational methods.²⁷⁹

A typical HF energy calculation starts by producing an initial guess wavefunction for the system, followed by an energy determination using the HF method. The guess wavefunction is then modified and the energy recalculated. The energy change at each wavefunction modification cycle is monitored, until the energy stops changing. At this point the wavefunction is assumed to have converged and the final energy for the system is reported. The iterative convergence of electronic energies is known as self-consistent-field (SCF) theory and conceptually underlies most quantum chemical methods.²⁸⁰

A.3. Møller-Plesset perturbation theory

Built on the core concepts of HF, Møller-Plesset (MP) perturbation theory uses a perturbation to the HF energy to account for the missing correlation energy.^{195,277} Known as a post-HF method, proposed by Møller and Plesset in 1934, MP theory perturbs the Hamiltonian according to Equation A.7:

$$\hat{H}(\lambda) = \hat{H}_0 + \lambda \hat{H}' , \quad \text{Eq. A.7}$$

where \hat{H}_0 is the unperturbed Hamiltonian, usually an HF-type Hamiltonian, and \hat{H}' is the perturbing potential. The linear combination of unperturbed Hamiltonian and perturbing potential produces the perturbed Hamiltonian $\hat{H}(\lambda)$, expressed as a function of perturbation order λ . The larger the perturbation used, the more accurate the outcome of the calculation, although often at a significant computational expense. In most cases the optimum balance between accuracy and computational cost is found for the second-order perturbation MP, known as MP2.¹⁹⁹ Larger

perturbation orders, such as MP3 and MP4,^{281,282} are usually reserved for small molecular systems.

A.4. Coupled-cluster methods

Coupled-cluster (CC) methods use an exponential cluster operator to describe the electron correlation in multi-electron wavefunctions generated from basic HF calculations.²⁸³ This post-Hartree-Fock numerical method provides incredibly accurate calculations for small systems. However, the study of larger systems using CC methods quickly becomes unfeasible, due to scaling computation costs.²⁸⁴

A.5. Density functional theory

Density function theory (DFT) takes an entirely different approach to the problem of calculating the electronic energy of a multi-electron system, by assuming that the electronic energy of a system is only dependent on its electron density.¹⁹³ Known as the Hohenberg-Kohn theorem, this method proposed that a unique functional can be used to describe the properties of a system without knowing the precise location of its electrons.¹⁸⁶ The implementation of the effective potential functional in DFT, $[U_{\text{DFT}}(r_i)]$, in the Hamiltonian is shown in Equation A.8:

$$\hat{H} = -\frac{\hbar}{2m_e}\nabla^2 + \sum_{i,j} \frac{Ze^2}{4\pi\epsilon_0|r_i - R_j|} + \sum_r \int_0^\infty \frac{e^2 n(r')}{4\pi\epsilon_0|r_i - r'|} dr + \sum_r U_{\text{DFT}}(r_i). \quad \text{Eq. A.8}$$

For small systems, the density described by $U_{\text{DFT}}(r_i)$ is assumed to be the same as that of an electron moving in a homogeneous electron gas, according to the local density approximation (LDA) method. LDA is known to have a tendency to over-estimate the exchange-correlation energy, as it assumes the electron density to be the same throughout the system. This tendency is routinely corrected using the generalised gradient approximation (GGA), which accounts for the non-homogeneity of the true electron density using expanded charge gradient terms.²⁷⁷ An example of this type of DFT exchange-correlation function is the screened-exchange (SX) Minnesota functional, MN12-SX.²⁵⁶ Despite producing very accurate ground-state energies for a wide range of systems, this functional is known to calculate the exchange part of the energy inaccurately. This drawback in DFT can be overcome with the use of hybrid methods. The DFT hybrid B3LYP,¹⁹³ unquestionably the most widely used DFT functional, employs Becke's third functional (adapted HF method

used to calculate the exchange energy) and an LYP functional to account for electron correlation.^{285–287} To improve the accuracy of these methods for systems featuring large electron-electron and electron-nuclei distances, long-range corrections can be applied to counteract the steep drop-off in the non-Coulombic part of exchange functionals. An example of these long-range corrected functionals is CAM-B3LYP.²⁸⁸

A.6. Time-dependent density functional theory

An extension of the DFT method described in Section A.4, known as time-dependent density functional theory (TD-DFT), can calculate the energies of molecules in their excited states.²⁵⁸ In TD-DFT, the system is initially calculated in its ground state and then adiabatically excited, inducing changes in its electron density. The analysis of these changes is then used to determine the total energy of the system.

A.7. Multireference configuration interaction theory

Multireference configuration interaction (MRCI) theory uses an expansion of the electronic Hamiltonian eigenstate, in a set of Slater determinants for the ground and excited electronic states, to calculate the energy of a system.²⁰⁷ The Slater determinants involved in excitation are known as reference determinants. Provided that an adequate set of reference determinants are selected, MRCI calculations generate very accurate correlation-balanced energies for ground and excited states alike.^{208,211}

A.8. Multi-configurational self-consistent-field theory

Multi-configurational self-consistent-field (MCSCF) theory can be described as a combination between configuration interaction (CI) and Hartree-Fock methods, where SCF routines are applied to a CI subset of orbitals known as the active space.^{289–291} In MCSCF the coefficients of a linear combination of configuration state functions, used to describe the electronic wavefunction, are varied until energy convergence is achieved. These wavefunctions are often used as reference states for MRCI (see Section A.6) or multireference perturbation (see Section A.8) calculations. Capable of handling complex systems, MCSCF methods produce very satisfactory results in both ground- and excited-state calculations. In MCSCF's most widely used approach, complete active space SCF (CASSCF), a linear combination

of fully-optimised reaction space SCFs is used to describe the electronic configuration of a user-defined set of active orbitals.²⁹² Setting all other orbitals as inactive allows CASSCF to focus on a specific electronic configuration. Active spaces are usually selected using spectroscopic studies from the literature or previous computational studies as a guide. CASSCF calculations are denoted as CASSCF(m,n), where m is the number of electrons and n the number of orbitals in the active space. To improve the performance of MCSCF calculations, determinants calculated using HF or SCF methods are used as initial guesses.

A.9. Molecular dynamics simulations

Molecular dynamics simulation packages allow the quantum chemical methods described in Section A.5 to A.7, to be dynamically propagated in time, thus describing how the nuclear and electronic configurations change as the system moves along energy surfaces. NEWTON-X^{218,219} and SHARC²²⁰ are examples of such molecular dynamics simulation packages. In these general-purpose packages the energy gradients and non-adiabatic coupling constant calculations, necessary for the propagation of molecules in time, are outsourced from quantum mechanical packages, such as MOLPRO,^{293,294} MOLCAS, and COLUMBUS. The flowchart in Figure A.1 outlines how MD packages use a combination of quantum and classical approaches to simulate molecular motions.

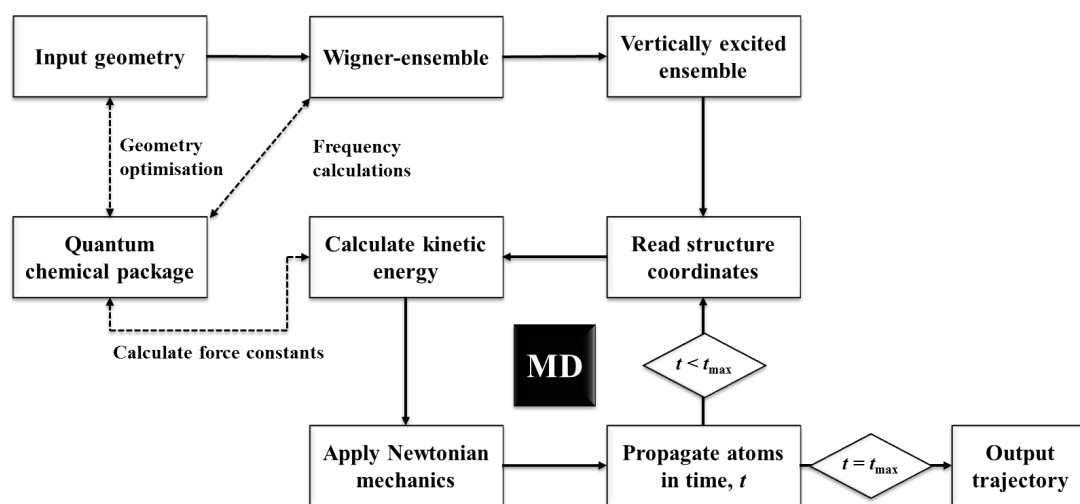


Figure A.1: Flowchart illustration of a typical molecular dynamics simulation in NEWTON-X.

The use of MD to simulate molecular motion usually starts with an optimised geometry in the ground state, from which N (user defined) structures are generated and vertically promoted to the excited state of choice, according to transition moments computed by the quantum chemical package. To initiate the MD simulation cycle, the force constants associated with each atom in the molecule are calculated using the quantum chemical package of choice and converted into kinetic energies using classical Newtonian mechanics equations. The kinetic energy of each atom is then expressed as a translation in atom position. At this point the new coordinates are stored and the structure enters the next iteration of the MD cycle. The system will continue to be propagated in time until the simulation time has elapsed. During the force-constant calculation step, the MD package uses non-adiabatic statistics and a stochastic algorithm to assess in which state the molecule is most likely to be. When a system changes state, known as a “hop”, the kinetic energies of the atoms are scaled so that overall energy is conserved. At the end of the simulation, the positions visited by each atom in the system are compiled as time-stamped trajectory files. The energy of the system for each step, populations of states, and state-hopping times and geometries are also outputted. To generate a truly representative average molecular motion, multiple independent trajectories are calculated simultaneously for any given system.

A.10. Basis sets

In quantum chemistry the set of parameters used to describe a wavefunction is known as the basis set. Generally centred on an atom, these functions attempt to describe the probability of finding electrons. To a certain extent basis sets approximate the shapes of atomic orbitals, and for this reason can be combined using the linear combination of atomic orbitals (LCAOs) approach to describe molecular orbitals. Basis sets that use a single function to describe an orbital are denoted as single- ζ basis sets. In increasing accuracy are basis sets using two, three, or four functions known as double- ζ , triple- ζ , and quadruple- ζ , respectively.²⁷⁷ The two main types of basis sets implemented in quantum chemistry packages and widely used by the computational chemistry community are the Pople-style and correlation-consistent basis sets.

Pople-style basis sets use Gaussian functions to describe the atomic orbitals.²⁹⁵ This type of basis sets is denoted by the format $k-nlmG$, where k is the number of

functions used to describe the core electrons and n and l the number of functions used to describe inner and outer valence electron, respectively. A classic example of a Pople-style basis set is 6-31G.^{296,297} For heavy atoms, the term m is used to add an extra valence shell function (6-311G).²⁹⁸ Adding a “+” after the nlm terms calls for diffuse functions to be included in s- or p-type orbitals. In the basis set 6-31++G, the second “+” calls for diffuse functions to be included for the hydrogen s orbitals. Polarisation terms can be added to the basis set using letter suffixes. For example, the basis set denoted 6-31G(d) includes an additional polarisation function in the d orbital. In some packages 6-31G(d) can be presented as 6-31G*. Additional letter suffixes can be included to better describe the system. In the basis set 6-311++G(2df,2pd), two extra d orbitals and one extra f orbital are requested for all heavy atoms, and two extra p orbitals and one d orbital are requested to better describe the hydrogen atoms.

Correlation-consistent basis sets are built by grouping together orbital types with similar correlation terms.²⁷⁷ This type of basis sets is denoted by the form cc-pVnZ, where n represents the number functions used. For example, keywords cc-pVDZ,²⁴⁶ cc-pVTZ,²⁴⁷ cc-pVQZ,²⁴⁸ call for correlation-consistent basis sets including polarisation valence double, triple, quadruple, and quintuple zeta, respectively. Adding the prefix “aug” before the cc term calls for diffuse functions to be used. One useful feature of correlation-consistent basis sets is the ability to extrapolate to the basis-set limit.

In systems containing heavy atoms, the core electrons of such atoms can be described using a single function, known as an effective core potential (ECP), significantly reducing the computational cost of the calculation.

An adequate choice of basis set is crucial to the success of any computation study. For this reason, extensive basis-set benchmark studies are usually carried out using a range of methods and functions ahead of any high-level calculations.

Appendix B. York GED apparatus

B.1. Electron gun

The York GED apparatus electron source, mounted at the top of the column module, consists of a tungsten hairpin filament (Agar A050), shown in Figure B.1a, a tantalum Wehnelt cap, and a stainless steel anode. The relative height of the Wehnelt cap with respect to the filament can be adjusted using the Wehnelt cylinder, which is electrically insulated from the rest of the gun. This enables the size and focal plane of the electron beam to be varied, without changing the relative positions of the anode and cathode (filament). Typically, electrons are accelerated across a 42.2 kV potential, generated using a Start Spellman high-voltage power supply. A high-voltage cable connects the power supply to the electron gun's high-voltage feedthrough.

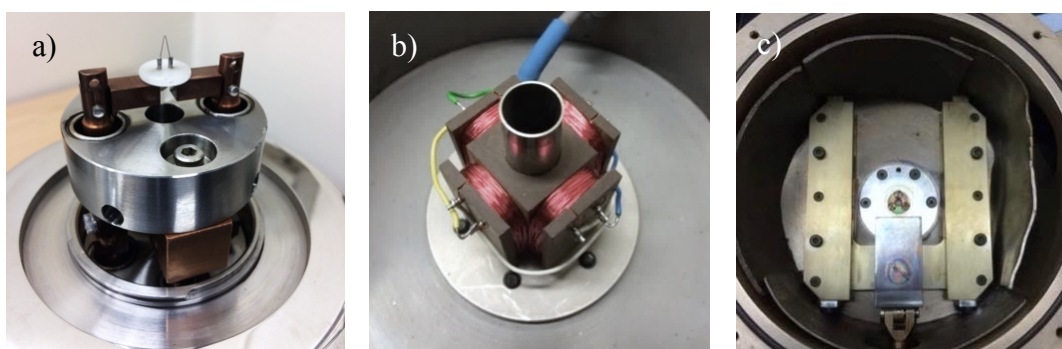


Figure B.1: Photographs of the York GED apparatus: a) the filament, b) a solenoid deflector, and c) the shutter mechanism. The shutter mechanism includes a lead beam dump and lead shielding.

Inside the column, two sets of solenoid deflectors, shown in Figure B.1b, guide the electron beam through a platinum aperture in the shutter mechanism, shown in Figure B.1c, positioning the beam at the centre of the detector assembly. Inside the bottom half of the column module, a solenoid lens focuses the electrons at the detector plane, ensuring that the sharpest diffraction pattern is recorded.

B.2. Sample delivery

Inside the chamber module an effusive nozzle, shown in Figure B.2a, delivers the target sample to the electron beam. The nozzle is coupled to a three-axis flange-mounted translator, which allows the nozzle position to be adjusted relative to the

electron beam. Under normal conditions the nozzle orifice is positioned 250 to 500 μm away from the electron beam. Two clean-up apertures, secured onto the nozzle body, ensure the best possible beam quality is achieved at the interaction region. A 15 mm aperture, positioned a few centimetres above the interaction region, prevents stray electron projections from reaching the detector, hence avoiding detector saturation and loss of diffraction data through high background. A 1 mm aperture placed a few millimetres upstream of the interaction region removes imperfections in the shape of the beam, producing a sharp collimated electron beam. Both apertures can be seen in Figure B.2b. The electron beam can be viewed through a lead-glass viewport using a retractable scintillator, as shown in Figure B.2c. Electron beam brightness, focus, and alignment are inspected visually and qualitatively assessed ahead of every GED experiment.

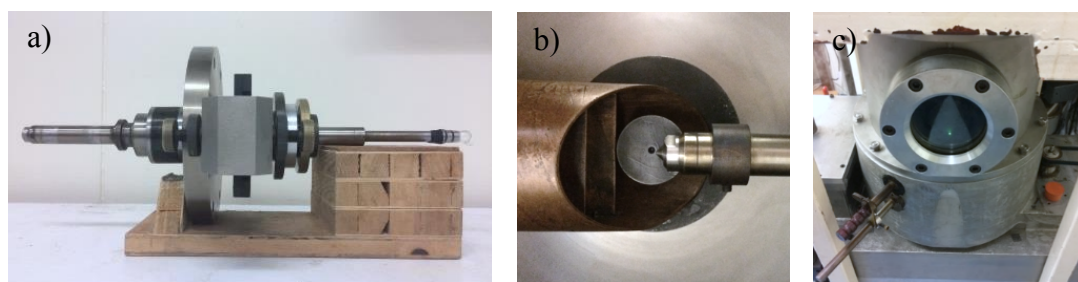


Figure B.2: Photographs of the York GED apparatus: a) the effusive nozzle, b) the nozzle and cold trap, and c) the electron beam viewed through the lead-glass viewport.

To reduce the background noise associated with high gas loads and multiple-scattering events, a liquid nitrogen cold trap is placed opposite the nozzle, condensing the sample shortly after diffraction. This considerably reduces background pressure in the chamber and detector modules, improving the overall quality of the diffraction data. At the end of every experiment the cold trap is warmed up to room temperature and degassed. The geometry of the York GED apparatus nozzle and cold trap are shown in Figure B.2b.

To deliver low volatility compounds to the gas phase, a heated nozzle originally designed for the telefocus electron gun GED apparatus, shown in Figure B.3, was adapted to the York GED apparatus using a custom ASA-to-CF reducer flange. The York mechanical workshop machined a $2\frac{3}{4}$ " bored CF flange onto an original York

GED apparatus blank flange, allowing the heated nozzle to be coupled to the York GED apparatus, as shown in Figure B.4.

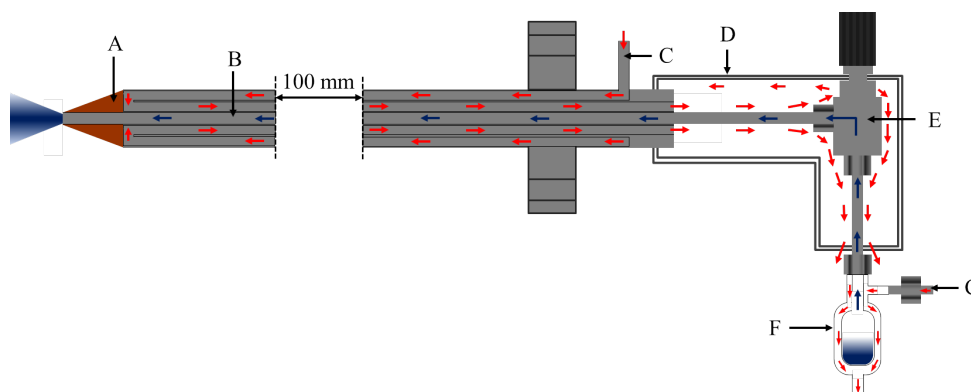


Figure B.3: Schematic depiction of the heated nozzle. The main components in the nozzle are: the copper tip (A), the sample tube (B), the compressed air inlets (C), the valve casing (D), the valve (E), and the sample holder (F). Red and blue arrows indicate the direction of the hot compressed air and sample flow, respectively.

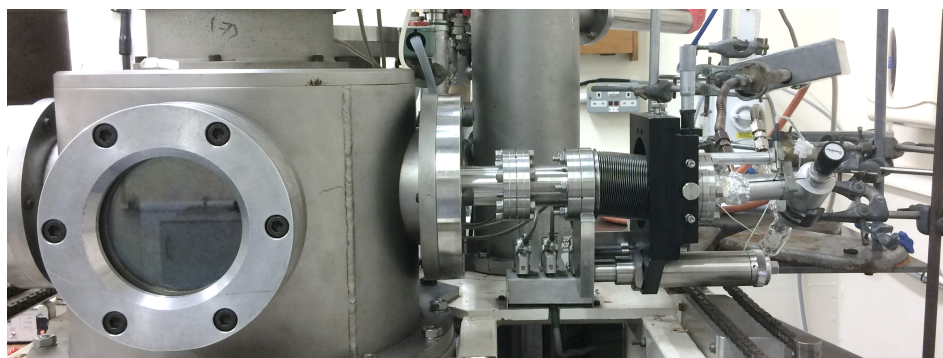


Figure B.4: Photograph of the heated nozzle adapted for the York GED apparatus.

The nozzle uses hot compressed air to heat the sample up to 675 K. The nozzle tip is kept 5 to 10 K warmer than the reservoir to prevent the sample from condensing inside the nozzle lines and blocking the flow of gas. The sample holder and nozzle tip are heated independently using two inline-cartridge-heaters connected to two proportional-integral-derivative (PID) controllers. The sample holder, manufactured in the York Chemistry glass-blowing workshop, uses a “reverse condenser design” to ensure even heating of the sample. A detailed description of the heated nozzle can be found in Stuart Young’s PhD thesis.²²⁵

B.3. Detector

In the York GED apparatus scattered electrons are detected using high-vacuum-compatible, reusable image plates (Fuji BAS-IP MP 2025). These consist of thin polyester films coated with barium fluorobromide grains doped with trace amounts of europium. When exposed to an energetic particle, such as a scattered electron, the Eu^{2+} ions are photo-oxidised, losing an electron to the barium fluorobromide lattice. In this way, position information on every electron hit is encoded in the oxidation-state distribution of the europium centres. Illuminating the plate with visible light, photoreduces the Eu^{3+} sites back to Eu^{2+} , triggering the emission of 400 nm photons, which are collected using a photomultiplier tube (PMT) and converted to a digital pixel intensity map. Routinely used in medical applications, this technology is commercially available in IP-Scanners. The direct proportionality between the number of electron hits, the number of photons emitted, and pixel intensity allows digitised image plates to be used quantitatively in GED experiments. Once scanned, image plates can be “erased” using UV light, which resets all Eu^{3+} sites back to their Eu^{2+} oxidation state. Therefore, image plates can be reused thousands of times, as long as they are not exposed to excessive radiation and are kept contaminant free. Furthermore, these europium-doped plates are less sensitive to light than other electron detectors, allowing very-high-temperature nozzles, *i.e.* incandescent nozzles, to be used in the GED study of short-lived species produced *via in situ* flash vacuum pyrolysis.²⁹⁹

At the beginning of each experiment, five image plates are mounted onto metal holders and loaded into the plate box attached to the top of the cast aluminium detector module. During the experiment the rods, levers and cranks, shown in Figure B.5a, are used to move the image plates from the plate box to the inside of the detector module, where a pneumatic actuator lifts them into the detector plane, situated immediately below the rotating sector shown in Figure B.5b. The plates are rotated sequentially between the plate box and the detector plane. At the end of the experiment, the image plates are removed from the plate box and scanned using the Fuji BAS-1800II flat-bed scanner, shown in Figure B.5c.



Figure B.5: Photographs of the York GED apparatus: a) the plate box, b) the rotating sector, and c) the flat-bed scanner. In the centre of the rotating sector, a beam stop collects unscattered electron, preventing detector damage. The edges of the beam-stop are coated with a thin layer of ZnS-based scintillator to facilitate the visual alignment of the electron beam.

The York GED apparatus detector module can be translated along the electron beam propagation axis, allowing diffraction data to be recorded at two nozzle-to-detector distances. In its long nozzle-to-detector distance configuration a removable chamber section is used to close the gap between the chamber and detector modules.

B.4. Vacuum system

To reduce the noise generated by background scattering events, GED experiments are carried out in high-vacuum environments. This ensures that the diffraction patterns recorded are a result of the electron beam scattering off the sample and not the background molecules. Furthermore, high-vacuum environments help prevent potentially damaging high-voltage discharge events, hence improving electron source longevity.

The York GED apparatus vacuum system consists of two diffusion pumps coupled to the chamber and column modules *via* two steel manifolds. A single Edwards belt-drive rotary pump is used to rough-pump the column and chamber modules, as well as back-pump the two diffusion pumps. The two pumping regimes, rough-pumping and backing, are controlled using a set of pneumatic solenoid and butterfly valves in the column and chamber manifolds. For this reason, adequate pneumatic pressure must be maintained at all times to ensure safe apparatus operation. Under normal operating conditions the column and chamber modules are pumped differentially and kept below 10^{-6} mbar. The shutter mechanism acts as a gate valve, which, when closed, allows the chamber to be vented and the image plates scanned without having

to switch off the electron gun. Following a partial vent, a second pump (Edwards 30 dual-stage rotary vane pump) is used to rough-pump the chamber module back to the operating pressure of diffusion pumps. This feature minimises the downtime associated with the breaking of vacuum and the scanning of image plates. During an experiment the pumping capability of the apparatus is temporarily enhanced using two cold traps: the chamber cold trap described in Section B.2, and the column cold trap. The latter is positioned above the column diffusion pump, preventing any oil from reaching the shutter mechanism and electron gun.

B.5. Controls and electronics

Most subsystems in the York GED apparatus, from the solenoid valves in the backing lines to the rotating-sector motor, are remotely operated using the control panel shown in Figure B.6. A robust set of interlocks and fail-safes prevents unsafe use, while a redundant supply of pneumatic pressure allows the apparatus to be run safely with minimal supervision.

During the commissioning of the York GED apparatus, the York Chemistry electronics workshop thoroughly inspected the apparatus wiring and electronic components. An industrial grade commando plug and master power switch was fitted to replace the original power cords and plugs, bringing the apparatus in line with the current safety standards and regulations. Furthermore, the beam deflection and focusing dials were replaced by modern Vernier potentiometers, vastly improving the precision and reproducibility of electron beam deflection.



Figure B.6: Photograph of the York GED apparatus control panel.

Appendix C. York TRED apparatus

C.1. Apparatus assembly and history

In 2013, the TRED apparatus was moved from the School of Chemistry at the University of Edinburgh, to the York Centre for Laser Spectroscopy and Photochemistry at the University of York. The TRED apparatus vacuum components were manufactured by Allectra GmbH³⁰⁰ and the optical elements and the vacuum pumps were purchased from ThorLabs³⁰¹ and Edwards,³⁰² respectively. The design of the TRED apparatus benefited greatly from the support of the Miller group at the Centre for Free-Electron Laser Science (CFEL) in Hamburg and at the University of Toronto, who were happy to share design ideas and critique some of our plans.³⁰³ In 2014, the sample delivery system, beam optics, and detector system of the TRED apparatus were commissioned using the UFL2³⁰⁴ laser loan pool laser. Following the termination of the EPSRC laser loan pool, in the summer of 2015, the Department of Chemistry acquired its own ultrafast laser system, allowing for the further development of the TRED apparatus.

During my PhD project, all modules of the TRED apparatus, with the exception of the electron gun, have undergone multiple development cycles. A detailed description of the apparatus configuration at the start of my PhD can be found elsewhere.¹⁷⁸

C.2. Electron gun

The TRED apparatus electron source consists of a photocathode-based DC compact electron gun, housed inside a differentially pumped electron gun chamber module. Its compact design reduces the distance between source and sample, thus minimising the effects of space-charge repulsion on the temporal profile of electron bunches. A cross-section of the electron gun chamber is shown in Figure C.1.

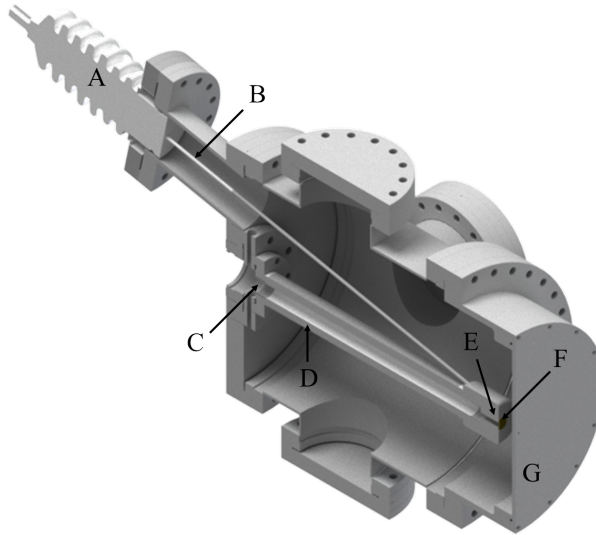


Figure C.1: CAD drawing of the TRED apparatus electron gun showing the high-voltage connector rod (B), connecting the high-voltage feedthrough (A) to the steel electrode (E), which is supported by a MACOR ceramic tube (D). The viewport (C) allows a laser to illuminate the photocathode (F), which together, with the anode plate (G) establishes the effective accelerating structure for the electrons.

In the TRED apparatus, electrons are generated by the ionisation of a thin-film gold photocathode using 267 nm laser light. The photocathode is secured onto a steel electrode (E) connected to the high-voltage feedthrough (A) *via* a steel rod (B) and held at a voltage of up to -100 kV. A MACOR³⁰⁵ ceramic tube (D) electrically isolates the steel electrode from the rest of the chamber. The back of the photocathode is optically accessible through a viewport (C) mounted opposite the end of the MACOR tube. A UV drive beam is focused on the back of the photocathode, producing a bunch of electrons with the same spatial and temporal profile as the laser beam. To minimise the energy distribution of the initial electron bunch, the thickness of the photocathode is tuned so that, using 267 nm laser light, only electrons close to the Fermi level are photo-emitted. In other words, the work function, *i.e.* the minimum energy needed to remove an electron from the gold photocathode, must match the energy deposited by the incident laser beam. In the TRED apparatus, this is achieved with a 20-45 nm film of gold, the work function of which, at 4.6 eV, matches the energy of a 267 nm photon.¹⁸⁰ The laser set-up used to produce the mid-UV light required to drive the electron gun can be found in Section C.3. The TRED apparatus photocathode, shown in Figure C.2, consists of a sapphire disc, coated with a 20-45 nm layer of 99.95% gold on the surface and approximately 100 nm of chromium around the edges. The gold and chromium coatings were

applied using thermal evaporation deposition. The sapphire-glass substrate was specially chosen for its surface flatness, high thermal conductivity, and UV transmission. Detailed descriptions of the photocathode manufacturing process and exact dimensions can be found elsewhere.¹⁷⁸

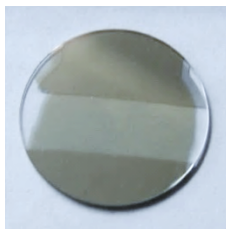


Figure C.2: Photograph of the York TRED photocathode.

The electrostatic potential between the photocathode and the grounded anode plug, 17 mm away, accelerates the electrons away from the surface of the gold, towards the diffraction chamber, with energies up to 100 keV. Under typical experimental conditions, the TRED apparatus electron gun produces an electron beam 1 mm in diameter, with 10^4 electrons per pulse, equating to a bunch charge of 1.6 fC, and a repetition rate of 1 kHz. The drive laser, described in Section C.3.1, controls the repetition rate, charge, and initial spatial and temporal profiles of the electron beam. The voltage output stability (it varies by as little as 0.001%) of the high-voltage power supply (Heinzinger PNC 100000), allows the TRED apparatus to generate a remarkably stable electron beam.

C.3. Laser set-up

The TRED apparatus laser set-up is responsible for driving the electron gun (see Section C.2), controlling the timing of the sample delivery system (see Section C.5), and optically pumping the sample in pump-probe-type experiments. For explanatory purposes the TRED apparatus laser set-up will be divided into two parts: the light source, and the optics set-up.

C.3.1. Light sources

During the course of my PhD project, two laser systems were interfaced with the TRED apparatus: the UFL2 EPSRC laser loan pool laser, and the departmentally acquired York ultrafast laser source (YULS).

The UFL2 EPSRC laser loan pool laser consisted of a Coherent Libra Ti:Sapphire amplifier fitted with an Evolution pump laser and Vitesse oscillator. This rugged one-box laser system produced horizontally polarised 800 nm light (15 nm bandwidth) with a pulse duration of 150 fs and an average energy of 1 mJ per pulse (total power of 1 W) at 1 kHz. This UFL2 was used during the commissioning stages of the apparatus in the spring of 2015.

Following the termination of the Loan Pool, the Department of Chemistry acquired the YULS, which consists of a Spectra-Physics Solstice Ace Ti:Sapphire one-box integrated amplifier. The seed laser to the regenerative amplifier is provided by a Spectra-Physics Mai-Tai oscillator tuned to a central wavelength of 802 nm with a bandwidth of 14 nm. The amplifier is pumped using a Spectra-Physics Empower Q-switched Nd:YLF laser. The YULS produces horizontally polarised light with a pulse duration of 80 fs and an average power of 6.2 W at 1 kHz. A beam splitter, coupled to the output port of the Solstice Ace, directs 80% of the output to a Spectra-Physics TOPAS-Prime optical parametric amplifier (OPA) and NirUVis mixing stage, which allows the YULS to produce ultrashort pulses of light at any wavelength between 410 and 2700 nm. The YULS was installed in the autumn of 2015 and was used to carry out the apparatus calibration and component optimisation experiments presented in Section 3.2.

C.3.2. Layout

The optics set-up includes all optical components used to direct or manipulate the output from the Ti:Sapphire laser system to the various sub-systems in the TRED apparatus. Since two distinct laser systems were used with the TRED apparatus, two optical set-ups will be described. Referred to as the Libra optics set-up and the Solstice optics set-up, these systems were designed using optical components purchased from Thorlabs and non-linear optical crystals from EKSMA optics.

The TRED apparatus optical set-up consists of two main beam paths: the electron generation path, and pump path, described in Section C.3.3 and C.3.4, respectively. These two paths are split from the main Ti:Sapphire output beam using a 70:30 beam splitter. For simplicity purposes no distinction will be made between the Libra and Solstice optics when describing the optical components and the functionality of the electron generation and pump path. The unique capabilities, advantages, and

disadvantages of the Libra and Solstice optics set-up are discussed in Sections C.3.5 and C.3.6, respectively.

C.3.3. Electron generation path

In the electron generation path, 30% of the Ti:Sapphire laser 800 nm output is sent to the third-harmonic generation (THG) set-up, frequency tripled to 267 nm, and directed towards the electron gun, where it is used to drive electron emission from the photocathode. To minimise the loss of fluency caused by attenuation in air, the THG set-up is positioned as close as possible to the electron gun. In the THG set-up, 800 nm light is directed towards a BBO second-harmonic generation (SHG) crystal, which combines 800 nm photons to produce 400 nm light of polarisation perpendicular to that of the incident IR photon. The conversion efficiency of the BBO crystal is strongly dependent on the crystal-lattice orientation with respect to the polarisation of the incident light. Therefore, small adjustments in the angle of the BBO crystal result in considerable changes in the fluency of 400 nm light. The output of the SHG crystal, which contains a mixture of 800 and 400 nm, is passed through a group velocity delay (GVD) calcite crystal, lengthening the pathway of the 800 nm photons, and temporally overlapping the two colours. The polarisation of the 800 nm light is then rotated to match that of the 400 nm light, using a $\lambda/2@800\text{ nm} / \lambda@400\text{ nm}$ wave plate. A second BBO crystal combines these co-propagating 800 and 400 nm photons to produce 266 nm light. The output of the second BBO crystal passes through a 267 nm bandpass filter, where the remaining 400 and 800 nm photons are removed. The beam is then directed towards the electron-gun viewport and focused on to the back of the photocathode using a 50 mm plano-convex lens. The spot size and position of the 267 nm beam illuminating the photocathode is optimised on the basis of electron beam current. The overall efficiency of the THG, expressed as the fluency of the 267 nm beam, is regulated using the angular orientation of the first BBO crystal. The effect of the BBO crystal angle on the charge and transverse profile of the electron beam is discussed in Section 3.2.1.1.

C.3.4. Pump path

In the pump path, 70% of the Ti:Sapphire output is directed towards the diffraction chamber and focused at the interaction region using a 75 mm plano-convex lens. The polarisation of the pump beam can be adjusted using a $\lambda/2$ wave plate and confirmed

using a polarising filter. A delay stage (300 mm Newport IMS-LS linear stage) allows the time of arrival of the pump pulses at the interaction region to be adjusted over a range of 20 ps in 350 fs steps. The fluency of the pump beam is adjusted using a set of attenuating neutral density filters secured onto flip mounts. Although currently set up to photo-excite the sample using 800 nm light, the pump path can be modified to deliver the output of a second THG set-up, or an OPA, with minimal changes to the optical layout.

C.3.5. Libra optics layout

The Libra optics set-up, shown in Figure C.3, was used between the summer of 2014 and the spring of 2015 in the commissioning of the TRED apparatus at York. The main design feature of the Libra optics set-up was its ability to deliver two counter-propagating overlapping pump beams to the interaction region. The grating-enhanced ponderomotive force generated by these spatially and temporally overlapped counter-propagating beams induces a deformation in the electron beam, the extent of which can be used to map the temporal profile of the electron beam. Though experimentally versatile, the Libra optics set-up, containing over 30 optical components, was particularly susceptible to vibrations and thermal drifts, which generally resulted in instabilities in the position and charge of the electron beam. Furthermore, the layout of the Libra optics set-up did not allow the output from the Ti:Sapphire laser source to be shared with other apparatus.

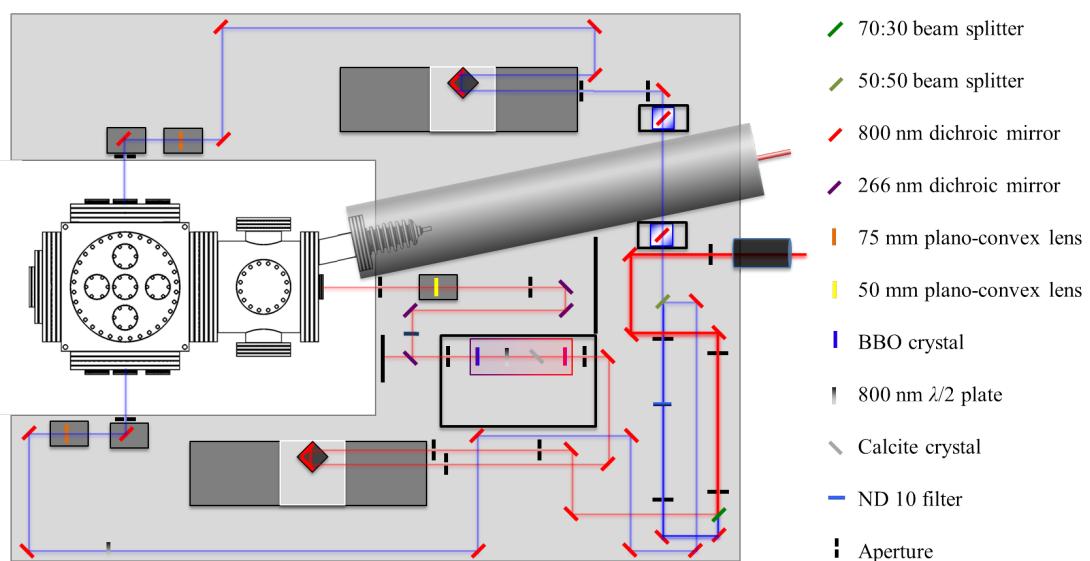


Figure C.3: Diagram of the Libra optics set-up, showing the layout of the electron generation and pump paths in red and blue, respectively.

C.3.6. Solstice optics layout

The Solstice optics set-up was designed and assembled by myself in the summer of 2015, following the commissioning of the YULS. Designed to address the experimental limitations of Libra optics set-up, the Solstice optics set-up, shown in Figure C.4, uses far fewer mirrors and shorter pathways to generate the same beam path and reach the same viewports as its older counterpart. This results in a more robust set-up, less susceptible to the detrimental effects of thermal drifts and vibrations, and consequently a more stable electron beam. User accessibility to the Ti:Sapphire laser is much improved, as only a small fraction, 18%, of the much more powerful YULS output is directed to the TRED apparatus. An even smaller portion of the YULS output, approximately 2% is used to drive the Wann group ultrafast point projection microscopy (UPPM) apparatus (see Section 8.3.2). A He:Ne alignment laser, co-propagational to the Ti:Sapphire beam, and a set of strategically placed apertures allow users to carry out delicate alignment tasks in a safe environment, without the need for IR viewers or laser cards. Furthermore, a two-layer interlock system allows for the YULS output to be interrupted by disabling the high-voltage power supply to the Solstice Ace Pockels cells, and closing the output shutter to the TRED apparatus. The interlock can be triggered using the emergency button outside the laser guard panels, or by pulling on the safety cord above the TRED apparatus control rack.

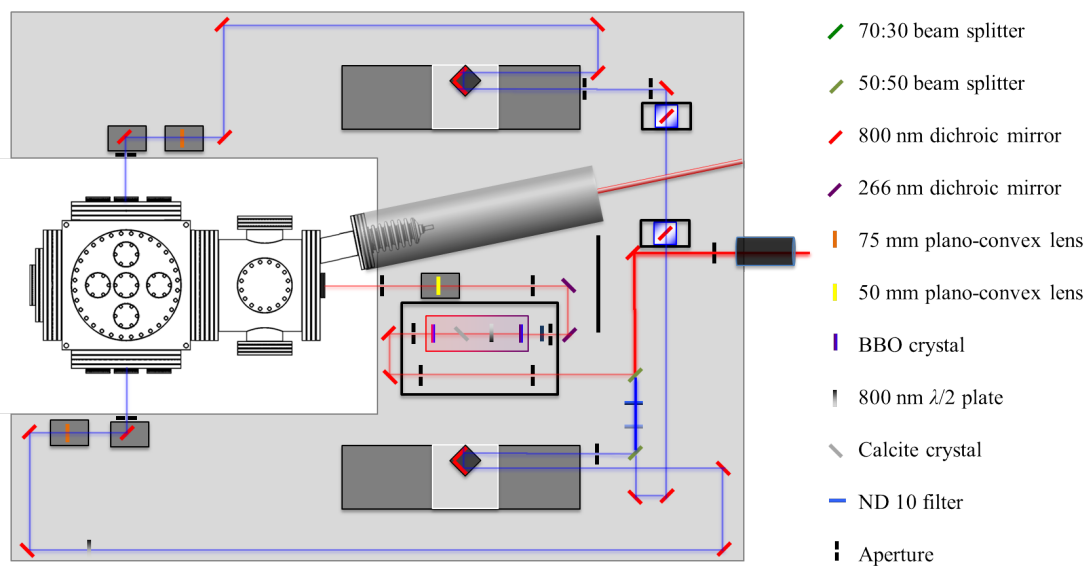


Figure C.4: Diagram of the Solstice optics set-up, showing the layout of the electron generation and pump paths in red and blue, respectively.

C.4. Electron optics

The TRED apparatus uses two sets of electron optics to control the transverse profile and flight path of its electron beam: a solenoid lens, and a beam deflector. A solenoid lens, placed immediately after the electron-gun output aperture, uses a combination of electric and magnetic forces, known as Lorentz forces, to focus the inherently divergent electron beam at the detector. The magnitude of the Lorentz forces acting on the electron beam is proportional to the number of turns of wire and current flowing through the solenoid. The focal point of the electron beam can be adjusted by varying the current supplied to the solenoid lens. Under experimental conditions, the solenoid lens remains energised for long periods of time, generating considerable amounts of heat, which, due to the absence of convective heat exchange in vacuum, can result in insulator damage and short-circuiting of the solenoid. Previous versions of a TRED apparatus solenoid lens, described elsewhere,¹⁷⁸ had been limited to 20 minutes of operation, due to poor heat dissipation, resulting in unwieldy experimental routines and excessive apparatus downtime. The novel solenoid lens design, presented in this Section and referred to as York solenoid lens, was developed in the autumn of 2014 to address the heat dissipation and usability shortcomings of its predecessor systems. The York solenoid lens, shown in Figure C.5, consists of 1000 turns of Kapton wire, wound around a bored iron core and encased in copper. The outer case was manufactured from a solid block of copper, to ensure the best possible thermal conductivity between the wires and an air-cooled mounting rod. Dry compressed air, cooled in copper tubing submerged in liquid nitrogen, is forced through the inside of the mounting rod, moving heat away from the lens. This design allows the York solenoid lens to operate at higher currents and for longer periods of time than it would otherwise. The heat dissipation efficiency of the York solenoid lens allows for continuous operation at 1 A. The operational time of the York Solenoid lens, at its maximum operating current of 1.6 A, is 20 times longer than a previous solenoid lens, which was also limited to a focusing current of 1.2 A. Calibration curves for the focusing performance of the York solenoid lens at various currents can be found in Section 3.2.2.

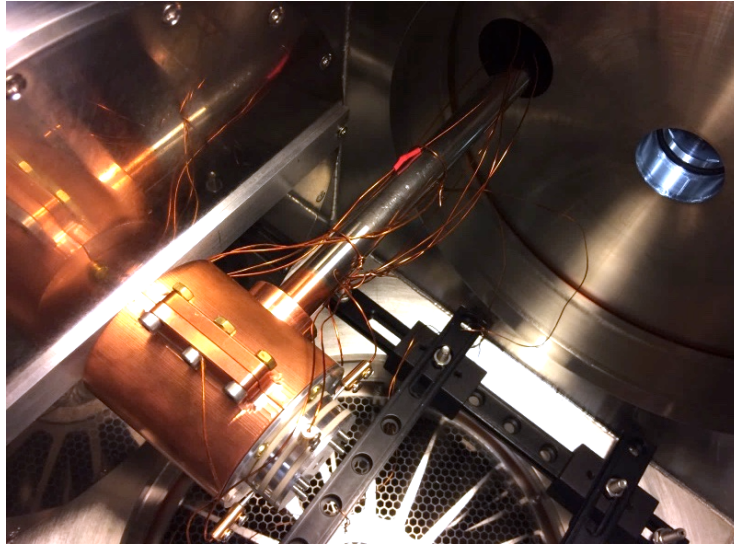


Figure C.5: Photograph of the York Solenoid lens inside the TRED apparatus diffraction chamber.

A beam deflector, coupled to the front of the York solenoid lens, allows the electron beam to be placed anywhere within a 2×2 mm area of the detector plane. The beam deflector, shown in Figure C.6, consists of four electrically isolated steel plates, grouped in two pairs of parallel plates, orthogonal to one another. Four high-voltage power supplies maintain a potential across each pair of plates, generating an electrostatic potential capable of deflecting electrons passing between the plates. Extensive calibration experiments, presented in Section 3.2.3, were carried out to determine how combinations of horizontal and vertical deflections could be used to steer the beam in a reproducible manner.

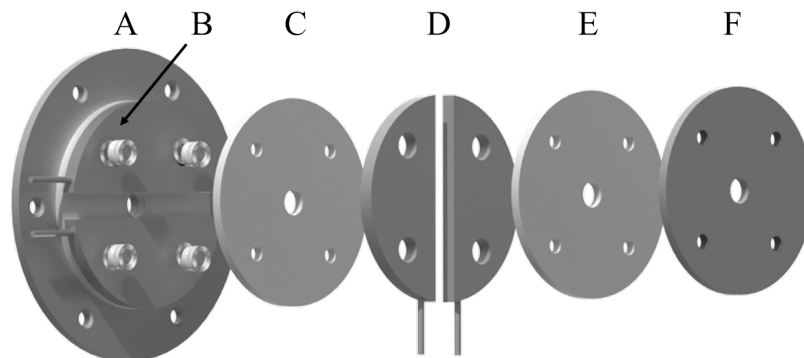


Figure C.6: CAD drawing of the TRED apparatus beam deflector, showing the mounting plates (A and F), the deflector plate pairs (B and D), and the MACOR spacers (C and E).

C.5. Sample delivery

The TRED apparatus sample holder, shown in Figure C.7, consists of three metal plates held together by six bolts and secured onto a flange-mounted *xyz*-translator stage. CAD drawings for the sample holder can be found in Appendix H. Solid-state samples are placed inside the wells (E) of the base plate (A) and secured in position by the copper frame (B), and the outer plate (C). The sample holder is placed at a 45° angle with respect to the axis of propagation of the electron beam, allowing an unobstructed line of sight through the sample for both the probe electron beam and the pump laser beams. The copper frame dissipates the heat generated by the optical pumping, thus improving the lifetime of the sample.

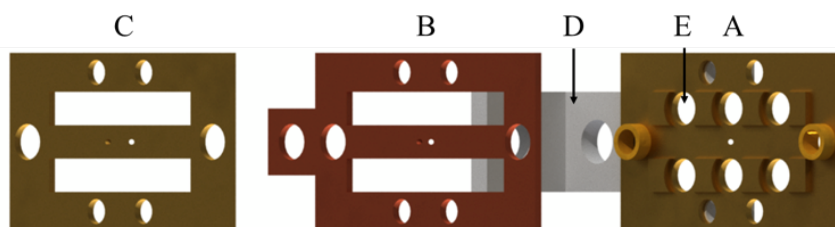


Figure C.7: CAD drawing of the TRED apparatus sample holder, showing the brass plate (A), the copper frame (B), the brass outer plate (C), the translator mount (D), and internal standard position (E).

The TRED apparatus effusive nozzle consists of a stainless steel needle, with an orifice of 0.25 mm, mounted onto a three-axis translator stage. The nozzle output is regulated using a needle valve.

The TRED apparatus pulsed nozzle uses a Parker Series 99 solenoid valve to generate a supersonic molecular beam. The repetition rate of the pulsed nozzle system is limited to 100 Hz, an order of magnitude smaller than the electron gun. To minimise the background noise associated with unscattered electrons, the repetition rate of the laser system and, consequently, the electron gun, is lowered to match that of the pulsed nozzle. A General Valve IOTA ONE pulse drive, externally triggered by the Ti:Sapphire laser signal-delay generator (SDG), is used to control the duty cycle of the solenoid valve. Temporal overlap between the electron beam and the pulsed molecular beam is achieved by changing the delay between the laser trigger and the IOTA ONE drive using a second SDG. At the beginning of each experiment this delay is optimised for maximum diffraction intensity.

When carrying out GED studies on samples with low vapour pressures, a gentle flow of helium is used to carry the sample into the chamber. Helium is the carrier gas of choice in GED and TRED experiments, due to its small scattering cross section. The TRED apparatus sample reservoir, shown in Figure C.8, allows the carrier gas to be bubbled through a liquid, delivering a gas-phase sample to the diffraction zone.

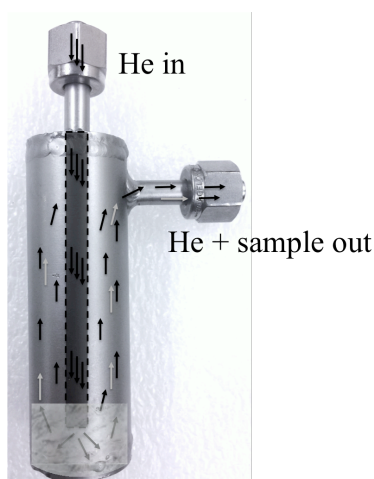


Figure C.8: TRED apparatus sample reservoir, showing the inlet of helium and the outlet of a mixture of helium and sample gas.

C.6. Detector

In the TRED apparatus, scattered electrons are recorded using a scintillator and CCD camera assembly, shown in Figure C.9. The scintillator screen consists of a 50 μm layer of ZnS:Cu (P22 green) deposited onto a float glass disk 155 mm in diameter and coated with a conductive layer of aluminium, approximately 50 nm thick. The grounded aluminium coating prevents charge from building up at the surface of the scintillator. In front of the scintillator screen a microchannel plate (MCP) multiplies the number of scattered electron, improving the signal-to-noise ratio of diffraction data. Outside the vacuum, a Stingray F146-B camera coupled to a Schneider 17 mm lens images the back of the scintillator screen, recording the position and brightness of the emitted photons as pixel intensity matrices. Diffraction data are relayed to the TRED apparatus data acquisition software and stored in a remote shared drive.

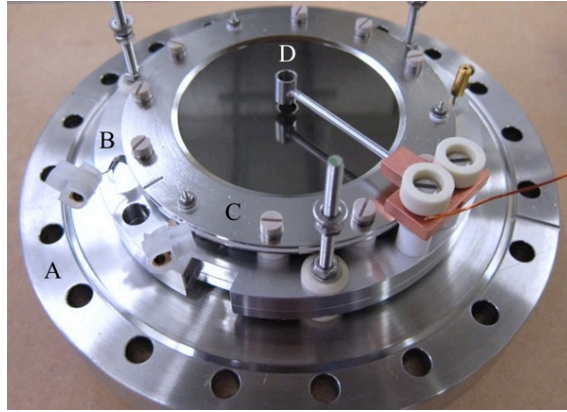


Figure C.9: Photograph of the TRED apparatus electron detector, showing the detector flange (A), scintillator mount (B), MCP (C), and beam stop (D).

The beam stop (D), collects unscattered electrons, prevents detector saturation or damage, and acts as a Faraday cup, allowing the electron beam current to be measured. The extension cone for the beam stop, shown in Figure C.10, was designed to improve the accuracy of beam-current measurement, and allow the transverse profile of the electron beam to be mapped. The beam stop and extension cone are electrically isolated from the rest of the detector and from each other through custom-designed MACOR ceramic spacers. A 500 μm hole at the bottom of the cone allows a small portion of the electron beam to reach the beam stop. A set of Kapton wires and feedthroughs connects the cone and beam stop to a switchboard outside the vacuum, allowing currents collected at the cone and beam stop to be measured independently. By maximising the current of the electron beam passing through the 200 μm^2 aperture in the cone one can optimise the alignment of the electron beam with respect to the centre of the beam stop, which helps minimise the background noise from unscattered electrons. Designs for the cone and MACOR spacers can be found in Appendix H.



Figure C.10: Photograph of the TRED apparatus Faraday cup and beam stop assembly viewed from a) the side, and b) the top.

The performance of the TRED apparatus detector was investigated extensively using the time-averaged diffraction signal from a polycrystalline platinum standard. Carried out during the first year of my PhD, the detector response optimisation experiments presented in Section 3.2.3 to 3.2.6 aimed to improve the overall SNR and spatial resolution of diffraction data without the addition of new components.

C.7. Vacuum system

The TRED apparatus consists of two chambers that are differentially pumped using two maglev turbo molecular pumps. The smaller of the two (Edwards STP-301C) is coupled to the gun chamber and used to maintain the pressure at the electron gun below 5×10^{-8} mbar. Both turbo molecular pumps are backed using oil-free scroll pumps (nXDS10i and XDS35i). Under normal operating conditions the diffraction chamber is maintained at 10^{-7} mbar using a larger turbo molecular pump (STP-A2203C). During gas-phase experiments the diffraction chamber pressure is kept below 10^{-4} mbar, in order to protect the photocathode and electron detector from becoming contaminated and to keep background noise levels to a minimum. Furthermore, two cryogenically cooled copper plates, and a conical-shaped cold trap, allow the pumping capacity of the TRED apparatus to be improved temporarily, further protecting the electron gun and detector assembly against contamination.

C.8. Apparatus accessibility

The TRED apparatus modular design, allows all components, with the exception of the electron gun, to be removed, or swapped without the need for prolonged shutdowns. Although modular, the original TRED apparatus compact design can limit component accessibility, which results in complex maintenance operations and a decrease in apparatus versatility. Accessibility issues have been partially addressed during my PhD with the design of new top and side flanges, referred to as second-generation flanges.

The original diffraction chamber layout, described elsewhere,²²⁹ consisted of two 12" side flanges with three 2¾" inch ports on each, one 12" top flange with five 2¾" inch ports, and one 12" back flange with one 6" port. This meant that in order to access a component inside the diffraction chamber, such as the cold trap, one had to remove a 12" top flange and all components connected to it. The second-generation flange, shown in Figure C.11a, eliminates the need for such labour-intensive

procedures, granting chamber access through an 8" offset bore. A two-axis translation stage attached to the 8" port allows a variety of nozzles and sample mounts to be coupled and a wider nozzle-to-detector range to be achieved without reconfiguring the detector assembly.

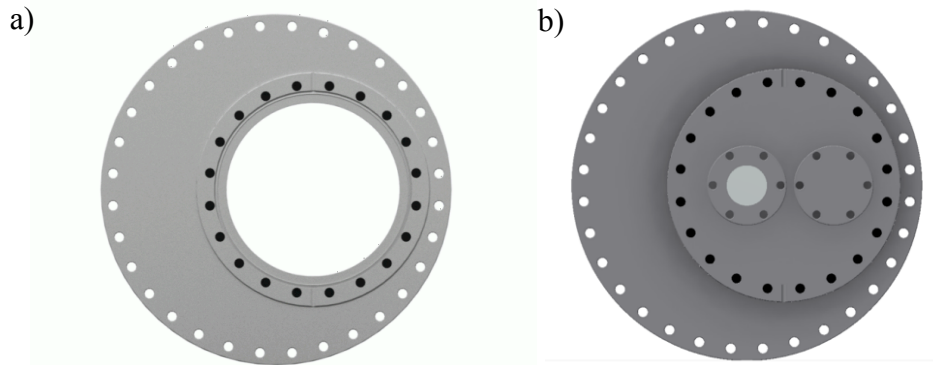


Figure C.11: CAD drawing of the second-generation TRED apparatus showing a) the top, and b) the side flanges. Both flanges consist of a zero-length 12" to 8" reducer with opposing knife edges and an offset centre, coupled to either a) an 8" spacer, or b) an 8" to two 2³/₄" zero-length reducer.

The York solenoid lens, described in Section C.4, was originally mounted onto one of the 2³/₄" ports in the side flange, which meant that it could not be removed as a single unit from the diffraction chamber. This resulted in unnecessarily complex maintenance routines, as the lens had to be disassembled inside the diffraction chamber. The second-generation side flange, shown in Figure C.11b, was built to streamline solenoid lens maintenance, allowing the solenoid lens to be removed from the apparatus as a single unit. The original TRED apparatus top and side flanges were repurposed and installed in the York Ultrafast Point Projection Microscopy apparatus (see Section 8.3.2).

C.9. Data acquisition workflow

The *TRED.run* data acquisition software was written to control all data acquisition in the TRED apparatus. A series of software-based interlocks prevents inappropriate operation, ensuring that the operator and apparatus remain safe. The TRED apparatus solenoid lens, laser shutter, and CCD camera are interfaced under a MATLAB environment. An inbuilt image acquisition package is used to bypass the CCD detector's own software, giving MATLAB and *TRED.run* full control over the acquisition parameters. Control over the solenoid lens and laser-shutter status is

achieved through the general-purpose input/output pins of a Raspberry Pi single-board computer, in which low-voltage logic is used to read the status of sensors and drive the relevant relays. Furthermore, the *TRED.run* software and fail-safe electronics allows the TRED apparatus to be run remotely from any computer in the office adjacent to the laboratory. An example of the data-acquisition routines employed in a typical experiment is illustrated schematically in Figure C.12.

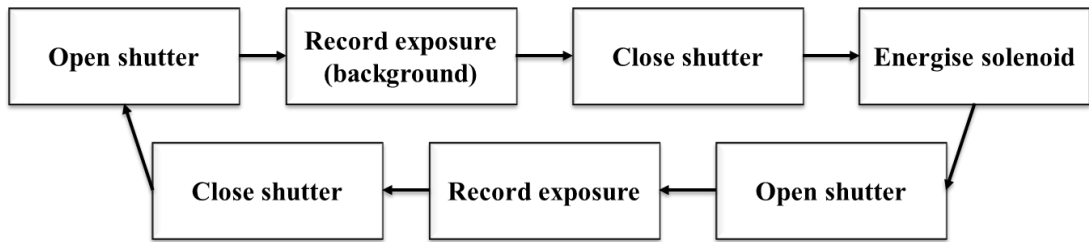


Figure C.12: Diagram of a data-acquisition routine implemented in the *TRED.run* software package.

Appendix D. SLAC UED apparatus

D.1. Electron gun

In the UED apparatus electrons are generated using a side-illuminated (70° incidence) photocathode RF electron gun, identical to the photoelectron gun used in the linear coherent light source (LCLS) injector.⁴¹ The RF electron gun is powered using a 50 MW S-band klystron and produces an electron beam containing 6×10^4 electrons per pulse at a repetition rate of 180 Hz. The energy of the electron beam can be adjusted between 2 and 5 MeV, with normal operation at 4.4 MeV. Housed inside a small cube half a metre in front of the electron gun, an yttrium aluminium garnet (YAG) screen and Faraday cup are used to image and measure the transverse profile and charge of the electron beam. Electron-steering magnets guide the electron beam through a series of collimators, which help to shape the electron beam and block the dark-current beam. The electron beam is focused using a solenoid lens, tuned to deliver the sharpest diffraction at the detector. A detailed description of the electron beam parameters can be found elsewhere.⁴¹

Inside the diffraction chamber, a YAG screen mounted on a retractable sample holder, is used to characterise the beam at the interaction region and to confirm the spatial overlap between the laser beam and the electron beam. A gold sample, mounted on the same holder, is used to calibrate the nozzle-to-detector distance and to assess the overall quality of the diffraction data.

D.2. Laser layout

The UED apparatus uses a 1 kHz, 5 mJ Ti:Sapphire laser system to generate the electrons and optically pump the gas target.⁴¹ About 10% of the 800 nm beam is frequency tripled in a THG set-up to generate the UV light used to trigger electron emission in the copper photocathode of the RF gun. The rest of the beam is directed to a 30 cm translation stage, which is used to adjust the delay between the pump and probe pulses. A second THG set-up and an optical parametric amplifier are used to adjust the pump wavelength. Two bored mirrors (holey mirrors) guide the focused pump beam through the interaction region and out of the diffraction chamber, as shown in Figure D.1. A detailed description of the UED apparatus laser layout can be found elsewhere.¹⁸⁵

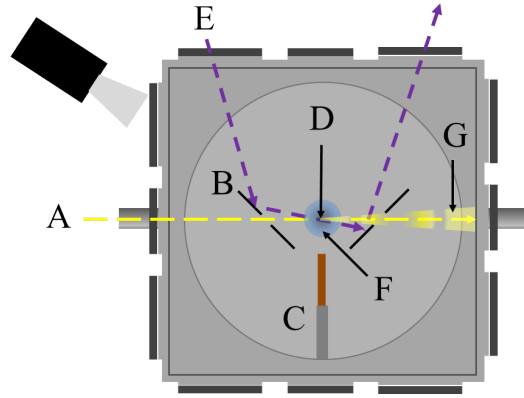


Figure D.1: Schematic representation of the layout of the MeV UED apparatus, showing the MeV electron beam (A), the two bored mirrors (B), the solid-state sample holder (C), the CCD camera imaging the interaction region (D), the incident pump beam (E), the molecular beam (F), and the scattered electron beam (G).

D.3. Sample delivery

The UED apparatus sample delivery system, schematically illustrated in Figure D.2, consists of a pulsed nozzle (in vacuum), a series of heaters (in vacuum and outside the vacuum), and a sample reservoir (outside the vacuum).

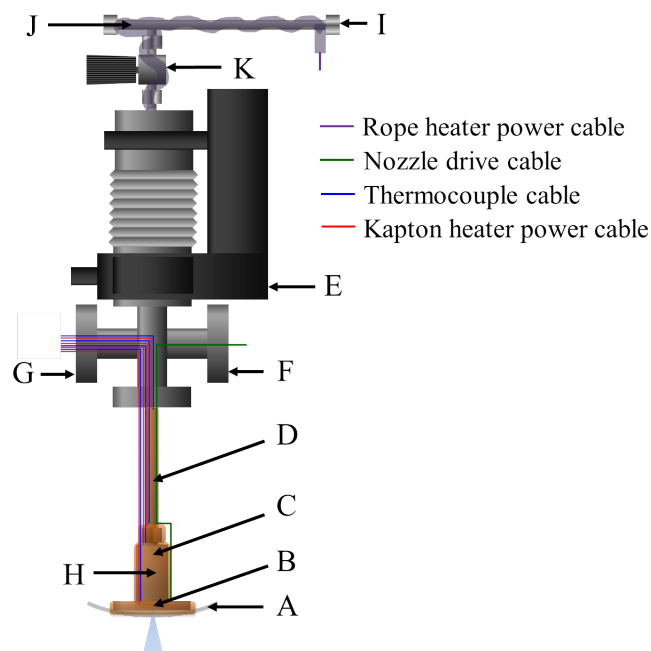


Figure D.2: Schematic representation of the MeV UED apparatus sample delivery system, showing the μ -metal shield (A), nozzle head (B), nozzle solenoid (C), in-vacuum transport line (D), three-axis manipulator (E), feedthrough for the nozzle drive (F), feedthrough for the in-vacuum heaters (G), Kapton in-vacuum heaters (H), out-of-vacuum transport line (I), out-of-vacuum rope heaters (J), and valve (K).

The UED apparatus pulsed nozzle system is identical to the one installed in the TRED apparatus. In fact, both apparatus share the same solenoid valve (Parker Series 9),³⁰⁶ the same solenoid drive (IOTA ONE), and the same nozzle geometry. The position of the nozzle with respect to the electron beam is controlled using a three-axis manipulator (E). A piece of μ -metal (A), attached to the front of the nozzle head (B), shields the magnetic field generated by the solenoid valve (C), preventing the deflection of the electron beam. Details on the duty cycle of the nozzle and the dimensions and efficacy of the μ -metal shield can be found elsewhere.¹⁸⁵

A series of in-vacuum Kapton heaters (H) and out-of-vacuum rope heaters (J) is used to maintain a positive temperature gradient between the sample reservoir (L) and the nozzle head (B), preventing the condensation of sample inside the nozzle and/or transport lines (D and I). The temperature of the heating element is monitored using K-type thermocouples and resistance temperature detectors (RTDs), and controlled using adjustable power supplies in current-limiting mode.

The transport line (I) can be connected to either a gas cylinder or, in UED experiments using liquid or solid samples, connected to a stainless steel bubbler or solid-sample holder, respectively. The bubbler allows liquid samples to be delivered to the gas phase using a backing pressure of helium as a carrier gas. The solid-state sample holder, shown in Figure D.3, was developed to allow solid-state samples with low volatility to be dispersed over a large volume and carried into the gas phase using a gentle flow of helium.

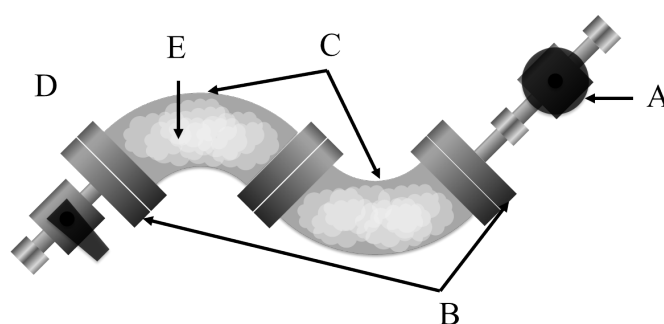


Figure D.3: Schematic representation of the solid-state holder developed during the 2016 gas-phase run, showing the intake needle valve (A), the Swagelok-to-conflat flange (CF) adaptors (B), 1/3" CF elbow fittings (C), quarter-turn valve (D), and glass-wool plug (E).

D.4. Detector

The MeV UED apparatus detector consists of a $\text{Gd}_2\text{O}_2\text{S:Tb}$ (P43-red) scintillator (A), a 45° mirror (B), and an EMCCD camera (ANDOR iX888 Ultra) (C) coupled to an $f/0.85$ collection lens (D). A set of holes through the scintillator and 45° mirror allow the unscattered electron beam to pass through the detector assembly, preventing damage to the scintillator and saturation of the EMCCD camera. The layout of the detector is shown schematically in Figure D.4.

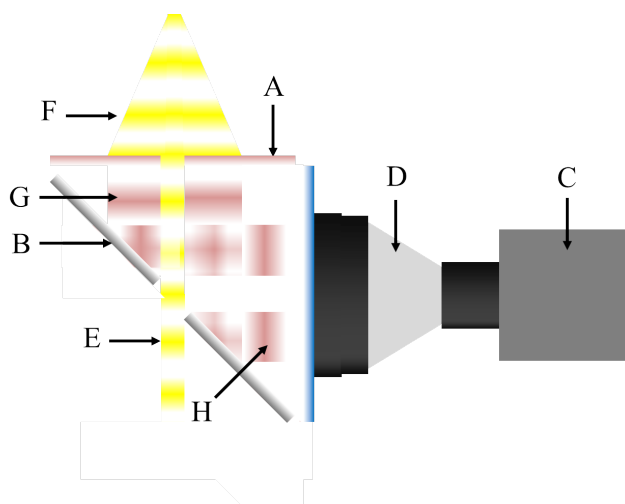


Figure D.4: Schematic representation of the MeV UED apparatus detector, showing the scintillator (A), 45° mirror (B), EMCCD camera (C), $f/0.85$ collection lens (D), unscattered electron beam (E), scattered electron beam (F), fluorescence from the scintillator (G), and reflected fluorescence (H).

Abbreviations

ASTA	accelerator structure test area
BBO	β -barium borate
CASPT2	complete active space perturbation theory
CASSCF	complete active space self-consistent-field
CBS	complete basis set
CC	coupled-cluster
CCD	charge-coupled device
CFEL	Center for Free-Electron Laser Science
CI	configuration interaction
CMOS	complementary metal-oxide semiconductor
CRT	cathode-ray tube
CSF	configuration state function
DC	direct current
DDD	direct detection device
DCM	dichloromethane
DED	direct electron detectors
DESY	Deutsches Elektronen-Synchrotron
DOE	Department of Energy
DFT	density function theory
DST	Discrete Sine Transform
DMABN	4-(<i>N,N</i> -dimethylamino)benzonitrile
ELSEPA	Elastic Scattering of Electrons and Positrons by neutral Atoms
EMCCD	electron multiplying charge-coupled device
FEL	free-electron laser
FWHM	full-width-half-maximum
GED	gas electron diffraction
GGA	generalised gradient approximation
GVD	group velocity delay
HF	Hartree-Fock
HPC	high-performance computer
ICT	intramolecular charge transfer
LCAO	linear combination of atomic orbitals

LCLS	linear coherent light source
LDA	local density approximation
LE	locally-excited
LIF	Laser-induced fluorescence
LIIC	linearly interpolated internal coordinate
MCP	microchannel plate
MCSCF	multi-configurational self-consistent-field
MD	molecular dynamics
MECI	minimal-energy conical intersection
MIC	molecular intensity curves
MOCED	molecular orbital constrained electron diffraction
MP	Møller-Plesset
MRCI	multireference configuration interaction
NAMMD	non-adiabatic multi-reference molecular dynamics
NMR	nuclear magnetic resonance
OPA	optical parametric amplifier
PES	potential energy surface
PID	proportional-integral-derivative
PMT	photomultiplier tube
PPM	point projection microscopy
PTFE	polytetrafluoroethylene
RDC	radial distribution curves
RF	radio frequency
RTD	resistance temperature detector
SCF	self-consistent-field
SDG	signal-delay-generator
SE	screened-exchange
SHG	second harmonic generation
SLAC	Stanford Linear Accelerator Centre
SNR	signal-to-noise ration
SPP	surface plasmon polaritons
SX	screened-exchange
TD-DFT	time-dependent density functional theory

THG	third harmonic generator
TIFF	tagged image file format
TOF-MS	time-of-flight mass spectrometric
TRED	time-resolved electron diffraction
TRMS	time-resolved mass spectrometric
TRXD	time-resolved X-ray diffraction
TTX	Tsinghua Thomson scattering X-ray
UCLA	University of California Los Angeles
UCONGA	universal conformer generation and analysis
UEC	ultrafast electron crystallography
UED	ultrafast electron diffraction
UEM	ultrafast electron microscopy
UPPM	ultrafast point projection microscopy
VELA	versatile electron linear accelerator
XML	extensible markup language
YAG	yttrium aluminium garnet
YARCC	York advanced research computing cluster
YULS	York ultrafast laser source

References

- 1 H. Jean-Ruel, M. Gao, M. a Kochman, C. Lu, L. C. Liu, R. R. Cooney, C. a Morrison and R. J. D. Miller, *J. Phys. Chem. B*, 2013, **117**, 15894–902.
- 2 V. R. Morrison, R. P. Chatelain, C. Godbout and B. J. Siwick, *Opt. Express*, 2013, **21**, 21–9.
- 3 C. J. Hensley, J. Yang and M. Centurion, *Phys. Rev. Lett.*, 2012, **109**, 1–5.
- 4 M. Eichberger, N. Erasmus, K. Haupt, G. Kassier, a. von Flotow, J. Demsar and H. Schwöerer, *Appl. Phys. Lett.*, 2013, **102**, 121106.
- 5 B. J. Siwick, J. R. Dwyer, R. E. Jordan and R. J. D. Miller, *Science*, 2003, **302**, 1382–1386.
- 6 R. J. D. Miller, R. Ernstorfer, M. Harb, M. Gao, C. T. Hebeisen, H. Jean-Ruel, C. Lu, G. Moriena and G. Sciaini, *Acta Crystallogr. Sect. A Found. Crystallogr.*, 2010, **66**, 137–156.
- 7 N. Hall, *Chem. Commun.*, 2002, **394**, 2185–2187.
- 8 C. Ruan, V. A. Lobastov, R. Srinivasan, B. M. Goodson, H. Ihee and A. H. Zewail, *Proc. Natl. Acad. Sci. U. S. A.*, 2001, **98**, 7117–7122.
- 9 B. Clegg, *The Man Who Stopped Time: the illuminating story of Eadweard Muybridge, pioneer photographer, father of the motion picture, murderer*, Joseph Henry Press, 2007.
- 10 The National Post, <http://nationalpost.com/news/eadweard-j-muybridge>, (accessed 1 September 2017).
- 11 O. D. Munn and A. E. Beach, *Sci. Am.*, 1878, **39**, 241.
- 12 Library congress, <http://hdl.loc.gov/loc.pnp/cph.3a45870>, (accessed 1 August 2017).
- 13 D. Polli, P. Altoè, O. Weingart, K. M. Spillane, C. Manzoni, D. Brida, G. Tomasello, G. Orlandi, P. Kukura, R. A. Mathies, M. Garavelli and G. Cerullo, *Nature*, 2010, **467**, 440–443.
- 14 O. Smitienko, V. Nadtochenko, T. Feldman, M. Balatskaya, I. Shelaev, F. Gostev, O. Sarkisov and M. Ostrovsky, *Molecules*, 2014, **19**, 18351–18366.

- 15 B. Guchhait, Y. Liu, T. Siebert and T. Elsaesser, *Struct. Dyn.*, 2016, **3**, 43202–43217.
- 16 T. Siebert, B. Guchhait, Y. Liu, R. Costard and T. Elsaesser, *J. Phys. Chem. B*, 2015, **119**, 9670–9677.
- 17 R. Neutze and J. Hadjdu, *Proc. Natl. Acad. Sci. U. S. A.*, 1997, **94**, 5651–5655.
- 18 V. A. Lobastov, J. Weissenrieder, J. Tang and A. H. Zewail, *Nano Lett.*, 2007, **7**, 2552–2558.
- 19 P. Baum, D. Yang, A. H. Zewail and H. Zewail, *Science*, 2007, **318**, 788–792.
- 20 R. Berera, R. van Grondelle and J. T. M. Kennis, *Photosynth. Res.*, 2009, **101**, 105–118.
- 21 E. T. J. Nibbering, H. Fidder and E. Pines, *Annu. Rev. Phys. Chem.*, 2005, **56**, 337–367.
- 22 A. Stolow, A. E. Bragg and D. M. Neumark, *Chem. Rev.*, 2004, **105**, 1719–1757.
- 23 M. J. J. Vrakking, D. M. Villeneuve and A. Stolow, *Phys. Rev. A - At. Mol. Opt. Phys.*, 1996, **54**, R37–R40.
- 24 M. Schmitt, S. Lochbrunner, J. P. Shaffer, J. J. Larsen, M. Z. Zgierski and A. Stolow, *J. Chem. Phys.*, 2001, **114**, 1206–1213.
- 25 G. Wu, P. Hockett and A. Stolow, *Phys. Chem. Chem. Phys.*, 2011, **13**, 18447.
- 26 V. Blanchet, A. Stolow and A. Stolow, *J. Chem. Phys.*, 2015, **108**, 4371–4374.
- 27 S. Lochbrunner, J. J. Larsen, J. P. Shaffer, M. Schmitt, T. Schultz, J. G. Underwood and A. Stolow, *J. Electron Spectros. Relat. Phenomena*, 2000, **112**, 183–198.
- 28 T. Schultz, J. Quenneville, B. Levine, A. Toniolo, T. J. Martínez, S. Lochbrunner, M. Schmitt, J. P. Shaffer, M. Z. Zgierski and A. Stolow, *J. Am. Chem. Soc.*, 2003, **125**, 8098–8099.

- 29 A. Stolow and J. G. Underwood, *Time-resolved photoelectron spectroscopy of nonadiabatic dynamics in polyatomic molecules*, Hoboken, NJ, USA, 2008, vol. 139.
- 30 V. Blanchet, M. Z. Zgierski, T. Seideman and A. Stolow, *Nature*, 1999, **401**, 52–54.
- 31 S. Ullrich, T. Schultz, M. Z. Zgierski and A. Stolow, *Phys. Chem. Chem. Phys.*, 2004, **6**, 2796.
- 32 H. R. Hudock, B. G. Levine, A. L. Thompson, H. Satzger, D. Townsend, N. Gador, S. Ullrich, A. Stolow and T. J. Martínez, *J. Phys. Chem. A*, 2007, **111**, 8500–8508.
- 33 I. Fischer, D. M. Villeneuve, M. J. J. Vrakking and A. Stolow, *J. Chem. Phys.*, 1995, **102**, 5566–5569.
- 34 M. Centurion, *J. Phys. B At. Mol. Opt. Phys.*, 2016, **49**, 62002–62017.
- 35 J. Chen and P. M. Rentzepis, *J. Phys. Chem. Lett.*, 2014, **5**, 225–232.
- 36 M. R. Armstrong, K. Boyden, N. D. Browning, G. H. Campbell, D. Colvin, W. J. Dehope, A. M. Frank, D. J. Gibson, F. Hartemann, S. Kim, W. E. King, T. B. Lagrange, B. J. Pyke, B. W. Reed, M. Shuttlesworth, B. C. Stuart and B. R. Torralva, *Ultramicroscopy*, 2007, **107**, 356–367.
- 37 M. S. Robinson, P. D. Lane and D. A. Wann, *Rev. Sci. Instrum.*, 2016, **86**, 13109.
- 38 G. Storeck, S. Vogelgesang, M. Siviš, S. Schäfer and C. Ropers, *Struct. Dyn.*, 2017, **4**, 44024.
- 39 E. A. Nanni, W. R. Huang, K. Hong, K. Ravi, A. Fallahi, G. Moriena, R. J. D. Miller and F. X. Ka, *Nat. Commun.*, 2015, **6**, 1–8.
- 40 S. Manz, A. Casandruc, D. Zhang, Y. Zhong, R. A. Loch, A. Marx, T. Hasegawa, M. Ho, M. Felber, M. Hachmann, F. Mayet, J. Hirscht, S. Keskin, M. Hada and S. W. Epp, *Faraday Discuss.*, 2015, **117**, 467–491.

- 41 S. P. Weathersby, G. Brown, M. Centurion, T. F. Chase, R. Coffee, J. Corbett, J. P. Eichner, J. C. Frisch, R. Fry, M. Gühr, N. Hartmann, C. Hast, R. Hettel, R. K. Jobe, E. N. Jongewaard, J. R. Lewandowski, R. K. Li, A. M. Lindenberg, I. Makasyuk, J. E. May, D. McCormick, M. N. Nguyen, A. H. Reid, X. Shen, T. Vecchione, S. L. Vetter, J. Wu, J. Yang, H. A. Dürr, X. J. Wang, S. P. Weathersby, G. Brown, M. Centurion, T. F. Chase, R. Coffee and J. Corbett, *Rev. Sci. Instrum.*, 2015, **86**, 73702–73707.
- 42 P. Baum, *Chem. Phys.*, 2013, **423**, 55–61.
- 43 A. Rodriguez, J. C. Hanson, J. Kim, G. Liu, A. Iglesias-juez and M. Ferna, *J. Phys. Chem. B*, 2003, **107**, 3535–3543.
- 44 K. Tashiro, Y. Ueno, A. Yoshioka and M. Kobayashi, *Macromolecules*, 2001, **34**, 310–315.
- 45 J. Kern, R. Alonso-Mori, R. Tran, J. Hattne, R. J. Gildea, N. Echols, C. Glöckner, J. Hellmich, H. Laksmono, R. G. Sierra, B. Lassalle-Kaiser, S. Koroidov, A. Lampe, G. H. Han and J. Yano, *Science*, 2013, **340**, 491–496.
- 46 C. G. Shull and E. O. Wollan, *Science*, 1948, **108**, 69–75.
- 47 J. C. H. Spence, *Struct. Dyn.*, 2017, **4**, 44027.
- 48 R. F. Egerton, *Adv. Struct. Chem. Imaging*, 2015, **1:5**, 1–11.
- 49 R. Henderson, *Q. Rev. Biophys.*, 1995, **28**, 171–193.
- 50 T. Elsaesser and M. Woerner, *Acta Crystallogr. Sect. A*, 2010, **A66**, 168–178.
- 51 Nevit Dilmen photography,
<https://commons.wikimedia.org/wiki/File:Windflower-05237-nevit.JPG#>,
(accessed 1 September 2017).
- 52 V. Srajer, T. Teng, T. Ursby, C. Pradervand, Z. Ren, S. Adachi, W. Schildkamp, D. Bourgeois, M. Wulff and K. Moffat, *Science*, 1996, **274**, 1726–1729.
- 53 G. Taubes, *Science*, 1994, **266**, 364–365.
- 54 M. Peplow, *Nature*, 2017, **544**, 408–410.

- 55 M. Gao, C. Lu, H. Jean-Ruel, L. C. Liu, A. Marx, K. Onda, S. Koshihara, Y. Nakano, X. Shao, T. Hiramatsu, G. Saito, H. Yamochi, R. R. Cooney, G. Moriena, G. Sciaini and R. J. D. Miller, *Nature*, 2013, **496**, 343–346.
- 56 J. J. Thomson, *Philos. Mag.*, 1897, **44**, 293–316.
- 57 W. C. Röntgen, *Science*, 1896, **3**, 227–231.
- 58 W. L. Bragg, *Proc. R. Soc. London*, 1913, **89**, 249–277.
- 59 T. Young, *Philos. Trans. R. Soc. London*, 1802, **92**, 12–48.
- 60 L. de Broglie, *Philos. Mag.*, 1924, **86**, 411–423.
- 61 D. Davisson and L. Germer, *Nature*, 1924, **119**, 558–560.
- 62 G. P. Thomson, *Nature*, 1927, **120**, 802.
- 63 W. H. Bragg, *Philos. Mag.*, 1920, **40**, 169–189.
- 64 P. Debye, *Ann. Phys.*, 1915, **351**, 809–823.
- 65 H. Mark and R. Wierl, *Naturwissenschaften*, 1928, **18**, 778–786.
- 66 A. A. Ischenko, V. V. Golubkov, V. P. Spiridonov, A. V. Zgurskii, A. S. Akhmanov, M. G. Vabischevich and V. N. Bagratashvili, *Appl. Phys. B*, 1983, **32**, 161–163.
- 67 G. Mourou and S. Williamson, *Appl. Phys. Lett.*, 1982, **41**, 44–45.
- 68 S. Williamson, G. Mourou and J. C. M. Li, *Phys. Rev. Lett.*, 1984, **52**, 2364–2367.
- 69 J. D. Ewbank, L. Schäfer, D. W. Paul, O. J. Benston and J. C. Lennox, *Rev. Sci. Instrum.*, 1984, **55**, 1598.
- 70 J. D. Ewbank, W. L. Faust, J. Y. Luo, J. T. English, D. L. Monts, D. W. Paul, Q. Dou and L. Schäfer, *Rev. Sci. Instrum.*, 1992, **63**, 3352.
- 71 T. S. Rose, M. J. Rosker and A. H. Zewail, *J. Chem. Phys.*, 1988, **88**, 6672–6673.
- 72 A. H. Zewail, *J Phys Chem A*, 2000, **104**, 5660–5694.
- 73 J. C. Williamson and A. H. Zewail, *Chem. Phys. Lett.*, 1993, **209**, 10–16.
- 74 B. J. Siwick, PhD Thesis, University of Toronto, 2004.

- 75 H. Ihee, V. A. Lobastov, U. M. Gomez, B. M. Goodson, R. Srinivasan, C. Ruan and A. H. Zewail, *Science*, 2001, **291**, 458–463.
- 76 B. J. Siwick, J. R. Dwyer, R. E. Jordan, R. J. D. Miller, R. S. Dwyer, R. E. Jordan and R. J. D. Miller, *Science*, 2003, **458**, 56.
- 77 H. Ihee, B. M. Goodson, R. Srinivasan, V. A. Lobastov and A. H. Zewail, *J Phys Chem A*, 2002, **106**, 4087–4103.
- 78 R. Srinivasan, V. a. Lobastov, C.-Y. Ruan and A. H. Zewail, *Helv. Chim. Acta*, 2003, **86**, 1761–1799.
- 79 T. Van Oudheusden, E. F. De Jong, S. B. Van Der Geer, W. P. E. M. Op 'T Root, O. J. Luiten and B. J. Siwick, *J. Appl. Phys.*, 2007, **102**, 93501.
- 80 J. B. Hastings, F. M. Rudakov, D. H. Dowell, J. F. Schmerge, J. D. Cardoza, J. M. Castro, S. M. Gierman, H. Loos and P. M. Weber, *Appl. Phys. Lett.*, 2006, **89**, 184109.
- 81 H. Jean-Ruel, M. Gao, M. A. Kochman, C. Lu, L. C. Liu, R. R. Cooney, C. A. Morrison and R. J. Dwayne Miller, *J. Phys. Chem. B*, 2013, **117**, 15894–15902.
- 82 U. J. Lorenz and A. H. Zewail, *Proc. Natl. Acad. Sci. U. S. A.*, 2013, **110**, 2822–2827.
- 83 R. M. Van Der Veen, O. Kwon, A. Tissot, A. Hauser and A. H. Zewail, *Nat. Chem.*, 2013, **5**, 395–402.
- 84 B. J. Siwick, J. R. Dwyer, R. E. Jordan and R. J. D. Miller, *J. Appl. Phys.*, 2002, **92**, 1643.
- 85 V. R. Morrison, R. P. Chatelain, K. L. Tiwari, A. Hendaoui, A. Bruhács, M. Chaker and B. J. Siwick, *Science*, 2014, **346**, 445–448.
- 86 P. Musumeci, J. T. Moody, C. M. Scoby, M. S. Gutierrez, M. Westfall, P. Musumeci, J. T. Moody, C. M. Scoby, M. S. Gutierrez and M. Westfall, *Appl. Phys. Lett.*, 2010, **63502**, 1–3.
- 87 R. Li, W. Huang, Y. Du, L. Yan, Q. Du, J. Shi, J. Hua, H. Chen, T. Du, H. Xu and C. Tang, *Rev. Sci. Instrum.*, 2010, **81**, 36110–36113.

- 88 G. H. Kassier, K. Haupt, N. Erasmus, E. G. Rohwer, H. M. Von Bergmann, H. Schwoerer, S. M. M. Coelho and F. D. Auret, *Rev. Sci. Instrum.*, 2010, **81**, 3–8.
- 89 G. H. Kassier, K. Haupt, N. Erasmus, E. G. Rohwer and H. Schwoerer, *J. Appl. Phys.*, 2009, **105**, 1–10.
- 90 P. M. Weber, S. D. Carpenter and T. Lucza, *SPIE*, 1995, **2521**, 23–30.
- 91 L. K. Rudge, S. Mathisen, P. Aden, R. J. Cash, J. A. Clarke, D. M. P. Holland, J. W. Mckenzie, M. D. Roper, T. C. Q. Noakes, J. Jones, A. Kalinin, B. L. Milityn, B. D. Muratori, D. Scott, F. Jackson, P. Williams, Y. Saveliev, M. Surman, S. Astec, D. A. Wann, P. D. Lane and J. G. Underwood, *Proc. 6th Int. Part. Accel. Conf.*, 2015, 2278–2281.
- 92 SLAC Strategic plan, https://www6.slac.stanford.edu/files/Strategic_Plan_2014.pdf, (accessed 1 August 2017).
- 93 J. Yang, V. Makhija, V. Kumarappan and M. Centurion, *Struct. Dyn.*, 2014, **1**, 44101.
- 94 J. Yang, J. Beck, C. J. Uiterwaal and M. Centurion, *Nat. Commun.*, 2015, **6**, 1–9.
- 95 J. Yang, M. Guehr, X. Shen, R. Li, T. Vecchione, R. Coffee, J. Corbett, A. Fry, N. Hartmann, C. Hast, K. Hegazy, K. Jobe, I. Makasyuk, J. Robinson, M. S. Robinson, S. Vetter, S. Weathersby, C. Yoneda, X. Wang and M. Centurion, *Phys. Rev. Lett.*, 2016, **117**, 1–6.
- 96 O. Zandi, K. J. Wilkin, Y. Xiong and M. Centurion, *Struct. Dyn.*, 2017, **4**, 0–10.
- 97 N. L. M. Müller, S. Trippel, K. Długolecki and J. Küpper, *J. Phys. B At. Mol. Opt. Phys.*, 2015, **48**, 244001–244007.
- 98 C. Ropers, D. R. Solli, C. P. Schulz, C. Lienau and T. Elsaesser, *Phys. Rev. Lett.*, 2007, **98**, 1–4.
- 99 C. Ropers, C. C. Neacsu, T. Elsaesser, M. Albrechty, M. B. Raschke and C. Lienau, *Nano Lett.*, 2007, **7**, 2784–2788.

- 100 J. Vogelsang, J. Robin, B. J. Nagy, P. Dombi, D. Rosenkranz, M. Schiek, P. Groß and C. Lienau, *Nano Lett.*, 2015, **15**, 4685–4691.
- 101 E. Lippert, W. Lüder, F. Moll, W. Nägele, H. Boos, H. Prigge and I. Seibold-Blankenstein, *Angew. Chemie*, 1961, **73**, 695–706.
- 102 Z. R. Grabowski, K. Rotkiewicz and W. Rettig, *Chem. Rev.*, 2003, **103**, 3899–4031.
- 103 B. F. E. Curchod, A. Sisto and T. J. Martínez, *J. Phys. Chem. A*, 2017, **121**, 265–276.
- 104 C. Reed, J.C., Lewis, H. Trejo, E., Winston, V. and Evilia, *Archaea*, 2013, **2013**, 1–14.
- 105 G. Cacciapuoti, F. Fuccio, L. Petraccone, P. Del Vecchio and M. Porcelli, *Biochim. Biophys. Acta - Proteins Proteomics*, 2012, **1824**, 1136–1143.
- 106 T. R. Ioerger, C. Du and D. S. Linthicum, *Mol. Immunol.*, 1999, **36**, 373–386.
- 107 A. B. Stephansen, M. A. B. Larsen, L. B. Klein and T. I. Sølling, *Chem. Phys.*, 2014, **442**, 77–80.
- 108 T. I. Sølling, T. S. Kuhlman, A. B. Stephansen, L. B. Klein and K. B. Møller, *ChemPhysChem*, 2014, **15**, 249–259.
- 109 A. B. Stephansen, R. Y. Brogaard, T. S. Kuhlman, L. B. Klein, J. B. Christensen and T. I. Sølling, *J. Am. Chem. Soc.*, 2012, **134**, 20279–20281.
- 110 O. Foss, A. Hordvik and J. Sletten, *Acta Chem. Scand.*, 1966, **20**, 1169–1171.
- 111 O. Foss and O. Tjomsland, *Acta Chem. Scand.*, 1958, **12**, 1810–1818.
- 112 S. C. Mitchell and R. H. Waring, *Phytochemistry*, 2014, **97**, 5–10.
- 113 N. Sakai and S. Matile, *Beilstein J. Org. Chem.*, 2012, **8**, 897–904.
- 114 H. Yanagawa, T. Kato, Y. Kitahara and N. Takahashi, *Plant Cell Physiol.*, 2018, **14**, 791–795.
- 115 S. Solomon, M. Mills, L. E. Heidt, W. H. Pollock and A. F. Tuck, *J. Geophys. Res.*, 1992, **97**, 25.

- 116 J. B. Burkholder, R. R. Wilson, T. Gierczak, E. Talukdar, S. A. McKeen, J. J. Orlando, G. L. Vaghjiani and A. R. Ravishankara, *J. Geophys. Res.*, 1992, **96**, 5025.
- 117 P. Zou, W. S. McGivern, O. Sorkhabi, A. G. Suits and S. W. North, *J. Chem. Phys.*, 2000, **113**, 7149.
- 118 A. Kalume, L. George, P. Z. El-Khoury, A. N. Tarnovsky and S. A. Reid, *J. Phys. Chem. A*, 2010, **114**, 9919–9926.
- 119 L. de Broglie, *C. R. Acad. Sci.*, 1923, **177**, 507–510.
- 120 D. W. H. Rankin, N. Mitzel and C. Morrison, *Structural Methods in Molecular Inorganic Chemistry*, Wiley, 2013.
- 121 N. I. Giricheva, M. S. Fedorov, S. N. Ivanov and G. V. Girichev, *J. Mol. Struct.*, 2015, **1085**, 191–197.
- 122 I. Hargittai and M. Hargittai, *Stereochemical Applications of Gas-Phase Electron Diffraction*, VCH Publishers Inc., New York, 1988.
- 123 Young's double slit, https://en.wikipedia.org/wiki/Double-slit_experiment#/media/File:Doubleslit3Dspectrum.gif, (accessed 1 September 2017).
- 124 O. Bastiansen and M. Trætteberg, *Acta Crystallogr.*, 1960, **13**, 1108.
- 125 V. A. Sipachev, *J. Mol. Struct. THEOCHEM*, 1985, **121**, 143–151.
- 126 Y. V. Vishnevskiy and Y. A. Zhabanov, *J. Phys. Conf. Ser.*, 2015, **633**, 3–7.
- 127 L. Hedberg and I. M. Mills, *J. Mol. Spectrosc.*, 1993, **160**, 117–142.
- 128 B. M. Cossairt, C. C. Cummins, A. R. Head, D. L. Lichtenberger, R. J. F. Berger, S. A. Hayes, N. W. Mitzel and G. Wu, *J. Am. Chem. Soc.*, 2010, **132**, 8459–8465.
- 129 A. V Zakharov, Y. V Vishnevskiy, N. Allefeld, J. Bader, B. Kurscheid, S. Steinhauer, B. Hoge, B. Neumann, H. Stammeler, R. J. F. Berger and N. W. Mitzel, *Eur. J. Inorg. Chem.*, 2013, **19**, 3392–3404.

- 130 B. Waerder, S. Steinhauer, J. Bader, B. Neumann, H. Stammeler, Y. V Vishnevskiy, B. Hoge and N. W. Mitzel, *Dalt. Trans.*, 2015, **44**, 13347–13358.
- 131 Y. V Vishnevskiy and D. Tikhonov, *Theor. Chem. Acc.*, 2016, **135**, 1–11.
- 132 D. A. Wann, A. V Zakharov, A. M. Reilly, P. D. McCaffrey and D. W. H. Rankin, *J. Phys. Chem. A*, 2009, **113**, 9511.
- 133 R. Blom, S. Cradock, S. L. Davidson and D. W. H. Rankin, *J. Mol. Struct.*, 1991, **245**, 369–377.
- 134 D. J. Romenesko, T. C. Wong and L. Bartell, in *Molecular Structure by Diffraction Methods*, eds. G. A. Sim and L. E. Sutton, The Chemical Society, 1975, pp. 72–80.
- 135 P. B. Liescheski and D. W. H. Rankin, *J. Mol. Struct.*, 1989, **196**, 1–19.
- 136 M. J. Davis, D. W. H. Rankin and S. Cradock, *J. Mol. Struct.*, 1990, **238**, 273–287.
- 137 V. J. Klimkowski, J. D. Ewbank, C. Van Alsenoy, J. N. Scarsdale and L. Schäfer, *J. Am. Chem. Soc.*, 1982, **104**, 1476–1480.
- 138 A. J. Blake, P. T. Brain, H. McNab, J. Miller, C. A. Morrison, S. Parsons, D. W. H. Rankin, H. E. Robertson and B. A. Smart, *J. Phys. Chem.*, 1996, **100**, 12280–12287.
- 139 P. W. Atkins, *Physical Chemistry*, Freeman, New York, 8th edn., 2006.
- 140 H. Fleischer, D. A. Wann, S. L. Hinchley, K. B. Borisenko, J. R. Lewis, R. J. Mawhorter, E. Robertson and D. W. H. Rankin, *Dalt. Trans.*, 2005, 3221–3228.
- 141 Y. V. Vishnevskiy, *J. Mol. Struct.*, 2007, **833**, 30–41.
- 142 S. L. Masters, S. J. Atkinson, M. Hölbling and K. Hassler, *Struct. Chem.*, 2013, **24**, 1201–1206.
- 143 A. V. Zakharov, G. A. Zhurko and G. V. Girichev, *Seriya Khimiya i Khimicheskaya Tekhnologiya*, 2013, **56**, 71–74.
- 144 UNEX, Y. V. Vishnevskiy, 2007.

- 145 B. Andersen, H. M. Seip, T. G. Strand and R. Stolevnik, *ACTA Chem. Scand.*, 1969, **23**, 3224–3234.
- 146 Spectra-Physics, www.spectra-physics.com/assets/client_files/files/documents/datasheets/TOPAS Prime.pdf, (accessed 1 September 2017).
- 147 J. Yang, *Personal Communication*, 2016.
- 148 P. Baum, *Chem. Phys.*, 2013, **423**, 55–61.
- 149 A. Rose, *Vision - Human and electronic*, Plenum Press, New York-London, 1973.
- 150 B. J. Siwick, A. a. Green, C. T. Hebeisen and R. J. D. Miller, *Opt. Lett.*, 2005, **30**, 1057.
- 151 W. Sibbett, H. Niu and M. R. Baggs, *Rev. Sci. Instrum.*, 1982, **53**, 758–761.
- 152 R. Guo, S. Mukamel and D. R. Klug, *Phys. Chem. Chem. Phys.*, 2012, **14**, 14023–14033.
- 153 P. Baum and A. H. Zewail, *Proc. Natl. Acad. Sci. U. S. A.*, 2006, **103**, 16105–10.
- 154 P. Zhang, J. Yang and M. Centurion, *New J. Phys.*, 2014, **16**, 83008.
- 155 M. Harmand, R. Coffee, M. R. Bionta, M. Chollet, D. French, D. Zhu, D. M. Fritz, H. T. Lemke, N. Medvedev, B. Ziaja, S. Toleikis and M. Cammarata, *Nat. Photonics*, 2013, **7**, 215–218.
- 156 Z. Zhang, Y. Du, L. Yan, Q. Du, J. Hua, J. Shi, J. Yang, D. Wang, W. Huang, H. Chen and C. Tang, *Phys. Rev. Spec. Top. - Accel. Beams*, 2014, **17**, 1–9.
- 157 REGAE: Time-resolved diffraction with relativistic electrons, <http://regae.desy.de>, (accessed 1 July 2017).
- 158 G. H. Kassier, N. Erasmus, K. Haupt, I. Boshoff, R. Siegmund, S. M. M. Coelho and H. Schworer, *Appl. Phys. B Lasers Opt.*, 2012, **109**, 249–257.
- 159 R. A. Bonham and M. Fink, *High Energy Electron Scattering*, Van Nostrand Reinhold, New York, USA, 1974.
- 160 K. Kveseth, R. Seip and D. A. Kohl, *Acta Chem. Scand. A*, 1980, **34**, 31–42.

- 161 R. Campargue, *J. Phys. Chem.*, 1984, **88**, 4466–4474.
- 162 S. A. Hayes, PhD Thesis, University of Edinburgh, 2008.
- 163 D. J. Denvir and E. Conroy, *Proc. SPIE*, 2002, **4796**, 165.
- 164 P. Magnan, *Nucl. Instruments Methods Phys. Res. Sect. A Accel. Spectrometers, Detect. Assoc. Equip.*, 2003, **504**, 199–212.
- 165 Gatan, <http://www.gatan.com/products/tem-imaging-spectroscopy/k2-direct-detection-cameras>, (accessed 1 September 2017).
- 166 T. Vecchione, P. Denes, R. K. Jobe, I. J. Johnson, J. M. Joseph, R. K. Li, A. Perazzo, X. Shen, X. J. Wang, S. P. Weathersby, J. Yang and D. Zhang, *Rev. Sci. Instrum.*, 2017, **88**, 33702–33711.
- 167 K. Aarset, E. M. Page and D. A. Rice, *J. Phys. Chem. A*, 1999, **103**, 5574–5580.
- 168 K. Aarset, E. M. Page and D. A. Rice, *J. Phys. Chem. A*, 2013, **117**, 3034–3040.
- 169 K. Aarset, E. M. Page and D. a Rice, *J. Phys. Chem. A*, 2006, **110**, 9014–9.
- 170 K. Aarset, E. M. Page and D. a Rice, *J. Phys. Chem. A*, 2010, **114**, 7187–90.
- 171 K. Aarset, E. M. Page and D. A. Rice, *J. Phys. Chem. A*, 2005, **109**, 4961–4965.
- 172 K. Aarset and E. M. Page, *J. Phys. Chem. A*, 2004, **108**, 5474–5478.
- 173 E. Johnsen, A. J. Downs, T. M. Greene, P. F. Souter, K. Aarset, E. M. Page, D. A. Rice, A. N. Richardson, P. T. Brain, D. W. H. Rankin and C. R. Pulham, *Inorg. Chem.*, 2000, **39**, 719–727.
- 174 E. M. Page, D. A. Rice, K. Hagen, L. Hedberg and K. Hedberg, *Inorg. Chem.*, 1991, **30**, 4758–4761.
- 175 R. J. F. Berger, M. Hoffmann, S. A. Hayes and N. W. Mitzel, *Zeitschrift für Naturforsch. - Sect. B J. Chem. Sci.*, 2009, **64**, 1259–1268.
- 176 A. W. Ross, M. Fink and R. Hilderbrandt, *International Tables for Crystallography*, Kluwer Academic Publishers, Dordrecht, Netherlands, 1992.

- 177 S. Gundersen, S. Samdal, T. G. Strand and H. V. Volden, *J. Mol. Struct.*, 2007, **832**, 164–171.
- 178 M. S. Robinson, PhD Thesis University of York, 2015.
- 179 NOAA, <https://www.ngdc.noaa.gov/geomag-web/#igrfwmm>, (accessed 1 October 2017).
- 180 M. Dantus, S. B. Kim, J. C. Williamson and A. H. Zewail, *J. Phys. Chem.*, 1994, **98**, 2782–2796.
- 181 J. C. Williamson, California Institute of Technology, 1998.
- 182 J. R. Dwyer, C. T. Hebeisen, R. Ernstorfer, M. Harb, V. B. Deyirmenjian, R. E. Jordan and R. J. D. Miller, *Philos. Trans. A. Math. Phys. Eng. Sci.*, 2006, **364**, 741–778.
- 183 Centurion group, <https://www.unl.edu/physics/centurion/ultrafast-dynamics-research>, (accessed 1 October 2017).
- 184 Gühr group, <http://exp-quantum.org>, (accessed 1 October 2017).
- 185 J. Yang, PhD Thesis, University of Nebraska, 2016.
- 186 W. Kohn and L. J. Sham, *Phys. Rev.*, 1965, **140**, 1133–1138.
- 187 S. Grimme, *J. Chem. Phys.*, 2006, **124**, 34108–34116.
- 188 G. D. Purvis and R. J. Bartlett, *J. Chem. Phys.*, 1982, **76**, 1910–1918.
- 189 J. A. Pople, M. Head-Gordon and K. Raghavachari, *J. Chem. Phys.*, 1987, **87**, 5968–5975.
- 190 G. Knizia, T. B. Adler and H. J. Werner, *J. Chem. Phys.*, 2009, **130**, 54104–54120.
- 191 L. Goerigk and S. Grimme, *Phys. Chem. Chem. Phys.*, 2011, **13**, 6670.
- 192 M. Korth and S. Grimme, *J. Chem. Theory Comput.*, 2009, **5**, 993–1003.
- 193 P. J. Stephens, F. J. Devlin, C. F. Chabalowski and M. J. Frisch, *J. Phys. Chem.*, 1994, **98**, 11623–11627.
- 194 T. H. Dunning, *J. Chem. Phys.*, 1989, **90**, 1007–1023.
- 195 C. Møller and M. S. Plesset, *Phys. Rev.*, 1934, **46**, 618–622.

- 196 T. D. Poulsen, J. Kongsted, A. Osted, P. R. Ogilby and K. V. Mikkelsen, *J. Chem. Phys.*, 2001, **115**, 2393–2400.
- 197 T. D. Poulsen, P. R. Ogilby and K. V. Mikkelsen, *J. Chem. Phys.*, 2002, **116**, 3730–3738.
- 198 T. D. Poulsen, P. R. Ogilby and K. V. Mikkelsen, *J. Chem. Phys.*, 2001, **115**, 7843–7851.
- 199 M. Head-Gordon, J. A. Pople and M. J. Frisch, *Chem. Phys. Lett.*, 1988, **153**, 503–506.
- 200 M. J. Frisch, M. Head-Gordon and J. A. Pople, *Chem. Phys. Lett.*, 1990, **166**, 281–289.
- 201 M. J. Frisch, M. Head-Gordon and J. A. Pople, *Chem. Phys. Lett.*, 1990, **166**, 275–280.
- 202 D. Hegarty and M. A. Robb, *Mol. Phys.*, 1979, **38**, 1795–1812.
- 203 R. H. A. Eade and M. A. Robb, *Chem. Phys. Lett.*, 1981, **83**, 362–368.
- 204 F. Bernardi, A. Bottoni, J. J. W. McDouall, M. A. Robb and H. B. Schlegel, *Faraday Symp. Chem. Soc.*, 1984, **19**, 137.
- 205 M. J. Bearpark, S. Wilsey, M. A. Robb, M. Olivucci and F. Bernardi, *J. Am. Chem. Soc.*, 1995, **117**, 6944–6953.
- 206 P. E. M. Siegbahn, *Chem. Phys. Lett.*, 1984, **109**, 417–423.
- 207 A. Berning, M. Schweizer, H. Werner, P. J. Knowles and P. Palmieri, *Mol. Phys.*, 2000, **98**, 1823–1833.
- 208 D. E. Woon and T. H. Dunning, *J. Chem. Phys.*, 1993, **99**, 1914–1929.
- 209 K. A. Peterson, D. E. Woon and T. H. Dunning, *J. Chem. Phys.*, 1994, **100**, 7410–7415.
- 210 K. A. Peterson, R. A. Kendall and T. H. Dunning, *J. Chem. Phys.*, 1993, **99**, 9790–9805.
- 211 K. A. Peterson, R. A. Kendall and T. H. Dunning, *J. Chem. Phys.*, 1993, **99**, 1930–1944.

- 212 H. Lischka, R. Shepard, R. M. Pitzer, I. Shavitt, M. Dallos, T. Müller, P. G. Szalay, M. Seth, G. S. Kedziora, Z. Zhang and S. Yabushita, *Phys. Chem. Chem. Phys.*, 2001, **3**, 664.
- 213 H. Lischka, T. Müller, P. G. Szalay, I. Shavitt, R. M. Pitzer and R. Shepard, *Wiley Interdiscip. Rev. Comput. Mol. Sci.*, 2011, **1**, 191–199.
- 214 H. Lischka, R. Shepard, R. M. Pitzer, I. Shavitt, M. Dallos, T. Müller, P. G. Szalay, M. Seth, G. S. Kedziora, S. Yabushita and Z. Zhang, *Phys. Chem. Chem. Phys.*, 2001, **3**, 664–673.
- 215 F. Aquilante, J. Autschbach, R. K. Carlson, L. F. Chibotaru, M. G. Delcey, L. De Vico, I. Fdez. Galván, N. Ferré, L. M. Frutos, L. Gagliardi, M. Garavelli, A. Giussani, C. E. Hoyer, G. Li Manni, H. Lischka, D. Ma, P. Å. Malmqvist, T. Müller, A. Nenov, M. Olivucci, T. B. Pedersen, D. Peng, F. Plasser, B. Pritchard, M. Reiher, I. Rivalta, I. Schapiro, J. Segarra-Martí, M. Stenrup, D. G. Truhlar, L. Ungur, A. Valentini, S. Vancoillie, V. Veryazov, V. P. Vysotskiy, O. Weingart, F. Zapata and R. Lindh, *J. Comput. Chem.*, 2016, **37**, 506–541.
- 216 Newton-X, M. Barbatti, G. Granucci, M. Ruckebauer, F. Plasser, R. Crespo-Otero, J. Pittner, M. Persico and H. Lischka, 2013.
- 217 Newton-X, <http://www.newtonx.org/>, (accessed 1 October 2017).
- 218 M. Barbatti, M. Ruckebauer, F. Plasser, J. Pittner, G. Granucci, M. Persico and H. Lischka, *Wiley Interdiscip. Rev. Comput. Mol. Sci.*, 2014, **4**, 26–33.
- 219 M. Barbatti, G. Granucci, M. Persico, M. Ruckebauer, M. Vazdar, M. Eckert-Maksić and H. Lischka, *J. Photochem. Photobiol. A Chem.*, 2007, **190**, 228–240.
- 220 M. Richter, P. Marquetand, J. González-Vázquez, I. Sola and L. González, *J. Chem. Theory Comput.*, 2011, **7**, 1253–1258.
- 221 G. M. Sheldrick, *Acta Crystallogr. Sect. C Struct. Chem.*, 2015, **71**, 3–8.
- 222 MATLAB, <https://uk.mathworks.com/products/matlab.html>, (accessed 1 October 2017).

- 223 S. Kumar, P. Kumar, M. Gupta and A. K. Nagawat, *Int. J. Comput. Appl.*, 2010, **12**, 27–31.
- 224 C. M. Huntley, D. W. H. Rankin and K. Buildings, *Dalt. Trans.*, 1980, 954–957.
- 225 S. Young, PhD Thesis, University of York, 2015.
- 226 F. Salvat, A. Jablonski and C. J. Powell, *Comput. Phys. Commun.*, 2005, **165**, 157–190.
- 227 FORTRAN 77, <https://docs.oracle.com/cd/E19957-01/805-4939/index.html>, (accessed 1 October 2017).
- 228 ANDOR cameras, <http://www.andor.com/cameras/ixon-emccd-camera-series>, (accessed 1 October 2017).
- 229 A. Heine, R. Herbst-Irmer, D. Stalke, W. Kühnle and K. A. Zachariasse, *Acta Crystallogr. Sect. B*, 1994, **50**, 363–373.
- 230 O. Kajimoto, H. Yokoyama, Y. Ooshima and Y. Endo, *Chem. Phys. Lett.*, 1991, **179**, 455–459.
- 231 Y. Zhao and D. G. Truhlar, *Theor. Chem. Acc.*, 2008, **120**, 215–241.
- 232 Science Imaging Systems,
http://www.bio.huji.ac.il/upload/Imaging_Phosphor_Imager_Brochure_Detailed.pdf, (accessed 1 February 2017).
- 233 L. W. Peng, M. Dantus, A. H. Zewail, K. Kemnitz, J. M. Hicks and K. B. Eisenthal, *J. Phys. Chem.*, 1987, **91**, 6162–6167.
- 234 Raytek, <http://www.raytek.co.uk/bas1800ii.html>, (accessed 1 October 2017).
- 235 M. J. Frisch, G. W. Trucks, H. B. Schlegel, G. E. Scuseria, M. A. Robb, J. R. Cheeseman, G. Scalmani, V. Barone, B. Mennucci, G. A. Petersson, H. Nakatsuji, M. Caricato, X. Li, H. P. Hratchian, A. F. Izmaylov, J. Bloino, G. Zheng, J. L. Sonnenberg, M. Had and D. J. Fox, 2010.
- 236 YARCC, <https://www.york.ac.uk/it-services/services/yarcc/>, (accessed 1 November 2017).
- 237 J. P. Perdew, *Phys. Rev. B*, 1986, **32**, 8822–8824.

- 238 Y. Wang and J. P. Perdew, *Phys. Rev. B*, 1991, **44**, 13298–13307.
- 239 T. M. Henderson, A. F. Izmaylov, G. Scalmani and G. E. Scuseria, *J. Chem. Phys.*, 2009, **131**, 0–9.
- 240 J. Heyd, G. E. Scuseria and M. Ernzerhof, *J. Chem. Phys.*, 2006, **124**, 2005–2006.
- 241 J. Heyd, J. E. Peralta, G. E. Scuseria and R. L. Martin, *J. Chem. Phys.*, 2005, **123**, 174101–174109.
- 242 J. Heyd and G. E. Scuseria, *J. Chem. Phys.*, 2004, **120**, 7274–7280.
- 243 J. Heyd and G. E. Scuseria, *J. Chem. Phys.*, 2004, **121**, 1187–1192.
- 244 M. Ernzerhof and G. E. Scuseria, *J. Chem. Phys.*, 1999, **110**, 5029–5036.
- 245 M. Ernzerhof and J. P. Perdew, *J. Chem. Phys.*, 1998, **109**, 3313–3320.
- 246 T. H. Dunning, *J. Chem. Phys.*, 1989, **90**, 1007–1023.
- 247 R. A. Kendall, T. H. Dunning and R. J. Harrison, *J. Chem. Phys.*, 1992, **96**, 6796–6806.
- 248 D. E. Woon and T. H. Dunning, *J. Chem. Phys.*, 1993, **98**, 1358–1371.
- 249 C. D. Rankine, J. P. F. Nunes, M. S. Robinson, P. D. Lane and D. A. Wann, *Phys. Chem. Chem. Phys.*, 2016, **18**, 27170–27174.
- 250 Clackers toy, <https://www.pinterest.com/pin/464855992768375884/>, (accessed 1 October 2017).
- 251 R. Singh and G. M. Whitesides, *J. Am. Chem. Soc.*, 1990, **112**, 6304–6309.
- 252 H. Ishida, A. Kisanuki and K. Endo, *Polym. J.*, 2009, **41**, 110–117.
- 253 K. Endo, T. Shiroy and N. Murata, *Polym. J.*, 2005, **37**, 512–516.
- 254 A. Schöberl and H. Gräffe, *Justus Liebigs Ann. Chem.*, 1958, **614**, 66–83.
- 255 R. Crespo-Otero and M. Barbatti, *Theor. Chem. Acc.*, 2012, **131**, 1–14.
- 256 R. Peverati and D. G. Truhlar, *Phys. Chem. Chem. Phys.*, 2012, **14**, 16187.
- 257 F. Weigend and R. Ahlrichs, *Phys. Chem. Chem. Phys.*, 2005, **7**, 3297.
- 258 R. Bauernschmitt and R. Ahlrichs, *Chem. Phys. Lett.*, 1996, **256**, 454–464.

- 259 G. A. Petersson, A. Bennett, T. G. Tensfeldt, M. A. Al-Laham, W. A. Shirley and J. Mantzaris, *J. Chem. Phys.*, 1988, **89**, 2193–2218.
- 260 P. Császár and P. Pulay, *J. Mol. Struct.*, 1984, **114**, 31–34.
- 261 N. R. Gunby, S. L. Masters and D. L. Crittenden, *J. Mol. Graph. Model.*, 2017, **77**, 286–294.
- 262 G. Igel-Mann, H. Stoll and H. Preuss, *Mol. Phys.*, 1988, **65**, 1321–1328.
- 263 A. Bergner, M. Dolg, W. Küchle, H. Stoll and H. Preuß, *Mol. Phys.*, 1993, **80**, 1431–1441.
- 264 D. N. Mehta-Hurt, J. A. Korn, P. Navotnaya, A. P. Parobek, R. M. Clayton and T. S. Wier, *J. Chem. Phys.*, 2015, **143**, 74304–74318.
- 265 J. Quenneville and T. J. Martínez, *J. Phys. Chem. A*, 2003, **107**, 829–837.
- 266 B. G. Levine and T. J. Martínez, *Annu. Rev. Phys. Chem.*, 2007, **58**, 613–634.
- 267 J. H. Waite, D. T. Young, T. E. Cravens, A. J. Coates, F. J. Crary and B. Magee, *Science*, 2013, **870**, 870–876.
- 268 R. N. Zare and P. J. Dagdigian, *Science*, 1974, **185**, 739–746.
- 269 D. R. Crosley, *J. Chem. Educ.*, 1982, **59**, 446.
- 270 M. Sharma, J. M. Austin, N. G. Glumac and L. Massa, *AIAA J.*, 2010, **48**, 1434–1443.
- 271 A. F. H. Van Gessel, B. Hrycak, M. Jasiński, J. Mizeraczyk, J. J. A. M. Van Der Mullen and P. J. Bruggeman, *J. Instrum.*, 2012, **7**, 1–8.
- 272 A. H. Zewail, *Science*, 2010, **328**, 187–193.
- 273 D. Shorokhov and A. H. Zewail, *J. Chem. Phys.*, 2016, **144**, 80901–80914.
- 274 E. Schrödinger, *Phys. Rev.*, 1926, **28**, 1049–1070.
- 275 V. Schomaker and R. Glauber, *Nature*, 1952, **170**, 290–291.
- 276 M. Born and R. Oppenheimer, *Ann. Phys.*, 1927, **389**, 457–484.
- 277 F. Jensen, *Introduction to Computational Chemistry*, Chichester, 2nd edn., 2007.
- 278 C. C. J. Roothaan, *Rev. Mod. Phys.*, 1951, **23**, 69–89.

- 279 C. Froese Fischer, *Comput. Phys. Commun.*, 1987, **43**, 355–365.
- 280 C. C. J. Roothaan, *Rev. Mod. Phys.*, 1960, **32**, 179–185.
- 281 J. A. Pople, R. Seeger and R. Krishnan, *Int. J. Quantum Chem.*, 1977, **11**, 149–163.
- 282 R. Krishnan and J. A. Pople, *Int. J. Quantum Chem.*, 1978, **14**, 91–100.
- 283 J. Čížek, *J. Chem. Phys.*, 1966, **45**, 4256–4266.
- 284 R. J. Bartlett and M. Musiał, *Rev. Mod. Phys.*, 2007, **79**, 291–352.
- 285 A. D. Becke, *J. Chem. Phys.*, 1993, **98**, 5648–5652.
- 286 C. Lee, W. Yang and R. G. Parr, *Phys. Rev. B*, 1988, **37**, 785–789.
- 287 B. Miehlich, A. Savin, H. Stoll and H. Preuss, *Chem. Phys. Lett.*, 1989, **157**, 200–206.
- 288 T. Yanai, D. P. Tew and N. C. Handy, *Chem. Phys. Lett.*, 2004, **393**, 51–57.
- 289 N. Yamamoto, T. Vreven, M. A. Robb, M. J. Frisch and H. Bernhard Schlegel, *Chem. Phys. Lett.*, 1996, **250**, 373–378.
- 290 C. J. Cramer, *Essentials of Computational Chemistry*, John Wiley & Sons Limited, Chichester, 2002.
- 291 G. Das, *J. Chem. Phys.*, 1973, **58**, 5104–5110.
- 292 J. Olsen, *Int. J. Quantum Chem.*, 2011, **111**, 3267–3272.
- 293 Molpro, <http://www.molpro.net>.
- 294 H. J. Werner, P. J. Knowles, G. Knizia, F. R. Manby and M. Schütz, *Wiley Interdiscip. Rev. Comput. Mol. Sci.*, 2012, **2**, 242–253.
- 295 P. C. Hariharan and J. A. Pople, *Chem. Phys. Lett.*, 1972, **16**, 217–219.
- 296 J. S. Binkley, J. A. Pople and W. J. Hehre, *J. Am. Chem. Soc.*, 1980, **102**, 939–947.
- 297 M. S. Gordon, J. S. Binkley, J. A. Pople, W. J. Pietro and W. J. Hehre, *J. Am. Chem. Soc.*, 1982, **104**, 2797–2803.
- 298 A. D. McLean and G. S. Chandler, *J. Chem. Phys.*, 1980, **72**, 5639–5648.

- 299 P. T. Brain, B. A. Smart, H. E. Robertson, M. J. Davis, D. W. H. Rankin, W. J. Henry and I. Gosney, *J. Org. Chem.*, 1997, **62**, 2767–2773.
- 300 Allectra GmbH, <http://www.allectra.com/index.php/en/>, (accessed 1 September 2017).
- 301 Thorlabs, <https://www.thorlabs.com/>, (accessed 1 September 2017).
- 302 Edwards, <https://www.edwardsvacuum.com/>, (accessed 1 September 2017).
- 303 Miller groups, <http://www.mpsd.mpg.de/en/research/ard/ard>, (accessed 1 September 2017).
- 304 Laser Loan Pool, <https://www.clf.stfc.ac.uk/Pages/The-Laser-Loan-Pool.aspx>, (accessed 1 October 2017).
- 305 MACOR ceramic, <https://www.corning.com/emea/en/products/advanced-optics/product-materials/specialty-glass-and-glass-ceramics/glass-ceramics/macor.html>, (accessed 1 October 2017).
- 306 Parker pulsed valves, <http://ph.parker.com/us/12051/en/pulse-valves-miniature-high-speed-high-vacuum-dispense-valve>, (accessed 1 October 2017).

Associated Publications

The work performed during my PhD has led to the publications of an article entitled “A theoretical investigation of internal conversion in 1,2-dithiane using non-adiabatic multiconfigurational molecular dynamics” in a peer-reviewed journal. The article has been appended in this Section to aid the examiners.